

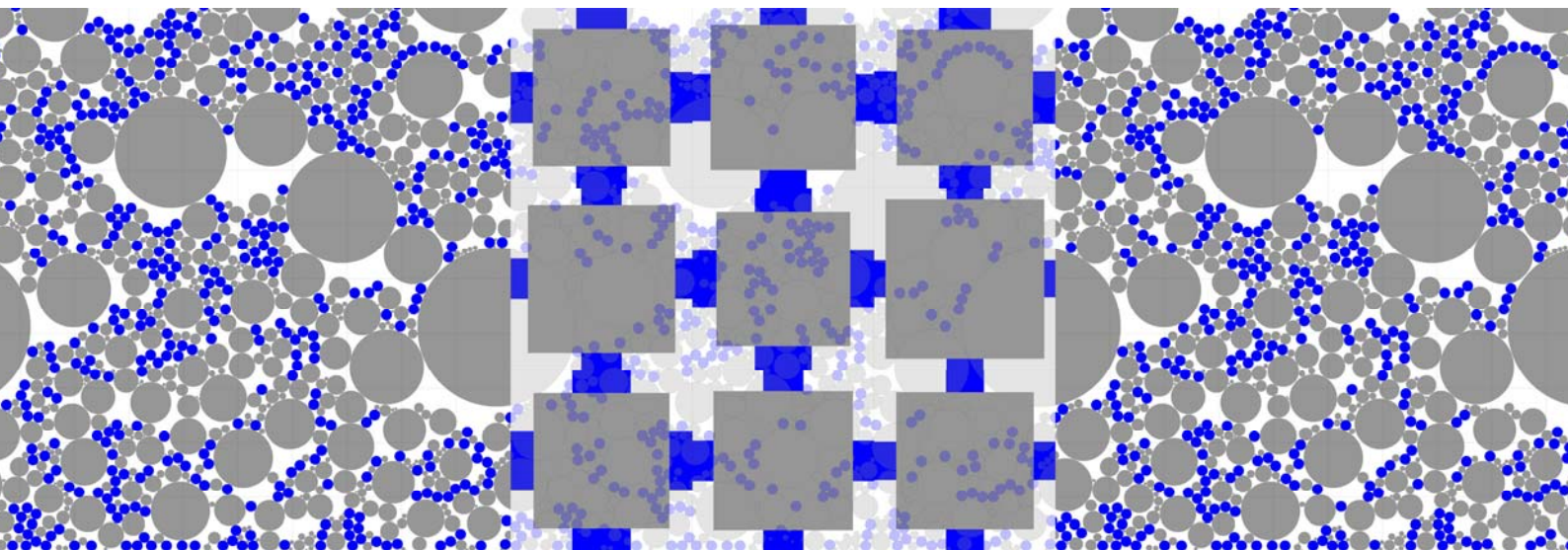
TKK Reports in Forest Products Technology

Series A13

Espoo 2010

HEAT TRANSFER THROUGH POROUS MULTIPHASE
SYSTEMS: measurement, modelling and application in printing of
coated papers

Philip Gerstner



Aalto University
School of Science and Technology
Faculty of Chemistry and Materials Sciences
Department of Forest Products Technology

TKK Reports in Forest Products Technology

Series A13

Espoo 2010

HEAT TRANSFER THROUGH POROUS MULTIPHASE
SYSTEMS: measurement, modelling and application in printing of
coated papers

Philip Gerstner

Dissertation for the degree of Doctor of Science in Technology to be presented with due permission of the Faculty of Chemistry and Materials Sciences, for public examination and debate in Auditorium AS1 at the Aalto University School of Science and Technology (Espoo, Finland) on the 22nd of October, 2010, at 12 noon.

Aalto University, School of Science and Technology
Faculty of Chemistry and Materials Sciences
Department of Forest Products Technology

Aalto-yliopisto, Teknillinen korkeakoulu
Kemian ja materiaalitieteiden tiedekunta
Puunjalostustekniikan laitos

Distribution:

Aalto University, School of Science and Technology
Faculty of Chemistry and Materials Sciences
Department of Forest Products Technology
P.O.Box 16300
FI-00076 AALTO

ISBN: 978-952-60-3376-1

ISBN: 978-952-60-3377-8 (PDF)

ISSN: 1797-4496

ISSN: 1979-5093 (PDF)

URL: <http://lib.tkk.fi/Diss/>

The financial support of Omya Development AG, Oftringen, Switzerland in printing this dissertation is gratefully acknowledged.

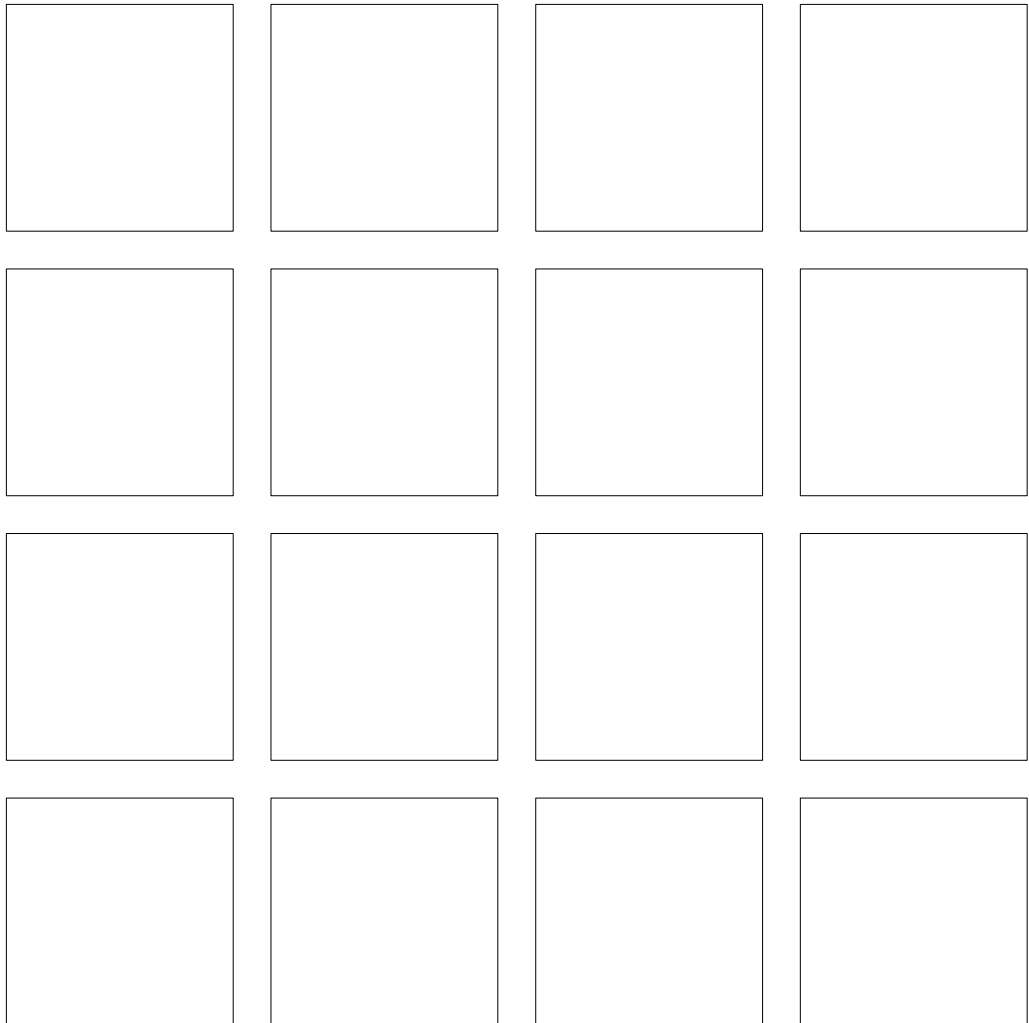
Picaset Oy
Helsinki 2010

ABSTRACT OF DOCTORAL DISSERTATION		AALTO UNIVERSITY SCHOOL OF SCIENCE AND TECHNOLOGY P.O. BOX 11000, FI-00076 AALTO http://www.aalto.fi	
Author: Philip Gerstner			
Name of the dissertation: Heat transfer through porous multiphase systems: measurement, modelling and application in printing of coated papers			
Manuscript submitted: 11.06.2010		Manuscript revised: 20.09.2010	
Date of the defence			
<input type="checkbox"/> Monograph		<input checked="" type="checkbox"/> Article dissertation (summary + original articles)	
Faculty:	Chemistry and Materials Sciences		
Department:	Forest Products Technology		
Field of research:	Printing Technology		
Opponent:	Professor G. Peter Matthews		
Supervisor:	Professor Patrick A.C. Gane		
Instructor:	Professor Jouni Paltakari		
<p>Abstract:</p> <p>This work examines the thermal transfer through porous media by means of measurement of the effective thermal conductivity and modelling of the structural parameters. While most of the work is of a general nature, the porous media in focus are pigment plus latex binder systems as used for paper coatings. As such, the application field of thermal effects in printing is discussed.</p> <p>At first the use of a dynamic measurement method for the thermal conductivity of porous coating pigment binder systems in the form of tablets is evaluated. In addition, a Lumped Parameter Model is developed to analyse the measured thermal conductivities in terms of the material volume fractions and their structural configuration. The model therefore uses two independent structural parameters instead of porosity alone as the governing parameter. This enables a discussion following modelling approaches adopting parameter modelling and structural modelling. A combination of both is used to discuss the solid-solid connectivity of pigment binder systems. It is shown by the model parameter of pigment connectivity that a disruption of the pigment packing already at low concentrations of binder occurs related to surface and colloid chemistry factors which cause the binder to accumulate first at pigment nodal points. The analysis of different pigment binder systems shows that, due to the presence of two interacting solid phases, the effective thermal conductivity cannot be modelled by using porosity and pore structure alone, but also requires the additional parameter of dual solid phase connectivity. It is proposed, therefore, that a combination of pore structure analysis and thermal conductivity measurement can be used to identify and parameterise subtleties in interactive particulate systems.</p> <p>For the application of toner fusing in electrophotography it is shown that a thermally insulating coating layer leads to a concentration of the fusing energy on the surface, thus aiding the fusing/adhesion development of the toner while shielding the base paper from undesired heating. In the heatset web-offset drying process, an insulating precoating in combination with liquid barrier properties can lead to a similar shielding of the base paper and thus helps to maintain an even moisture profile effectively reducing the waving/fluting tendency.</p>			
Keywords: Thermal conductivity, porous media, modelling, energy efficiency, electrophotography, heatset web-offset			
ISBN (printed)	978-952-60-3376-1	ISSN (printed)	1797-4496
ISBN (pdf)	978-952-60-3377-8	ISSN (pdf)	1979-5093
Language	English	Number of pages	193 p. + app. 143 p.
Publisher	Aalto University, School of Science and Technology, Department of Forest Products Tech.		
Print distribution	Aalto University, School of Science and Technology, Department of Forest Products Tech.		
<input checked="" type="checkbox"/> The dissertation can be read at http://lib.tkk.fi/Diss/			

PREFACE



INTRODUCTION



“When you are face to face with a difficulty, you are up against a discovery.”

Sir William Thomson,
British Physicist, 1824-1907

PREFACE

During my Master's thesis work in January 2007, my supervisor Professor Patrick Gane had the idea to publish some of my results. Since my work was still in a very early stage, I didn't have quite enough, or any, data to publish. That way he (probably intentionally) put me on the spot to come up with a new idea. After walking up and down in my office for a distance that must have been close to $1.802 \cdot 10^{15}$ nm, I came up with model modifications and parameterisations that would eventually become the Lumped Parameter Model. I am quite certain that neither one of us had anticipated that this model would follow us for a much longer time, going on into my doctoral studies. I would like to take this opportunity to express my sincere gratitude to Professor Patrick Gane, who went on to be my doctoral supervisor. He is always encouraging, but at the same time always tries to demand a little more than you thought you were capable of doing. Although our offices are exactly 1 802 km away from each other, we have been working together excellently and often our discussions of new ideas and approaches turned into scientific "jam sessions" that ultimately put me away with work for weeks.

I would like to thank my instructor and co-author Professor Jouni Paltalkari for his "open door policy" to have short meetings whenever he is in his office. I also appreciated to be given the opportunity to lecture coating structure in the Master level courses.

Many thanks to Omya Development AG for the initial funding of my doctoral studies and for the support I received from the entire team in Oftringen during my stays for sample preparation and measurements, especially to Dr. Cathy Ridgway who started instructing me in the experimental part and went on to become co-author and good friend.

It was a great pleasure to work with my co-authors Sami Veikkolainen, who was writing the Master's thesis in Printing Technology, and Teemu Grönblom during the coating and printing trials at the Forest Pilot Center in Raisio. Both collected a large amount of data and contributed to the publications.

The financial support of TEKES, the Finnish Funding Agency for Technology and Innovation, is gratefully acknowledged. This work was done as part of the offset printing project "Thermal Effects and Online Sensing" (THEOS), a cooperation of several Finnish universities and industrial partners that I truly appreciated. Support for conferences and travelling was provided by PaPSaT, the International Doctoral Programme in Pulp and Paper Science and Technology.

I would also like to thank all of my colleagues at the Department of Forest Products Technology who have contributed in one way or another to this dissertation. Many thanks go to Kaarlo Nieminen for the assistance and discussions concerning the mathematical issues and to Timo Hartus for the advice regarding the adhesion measurement.

Finally, I would like to thank my parents Gabriele and Jürgen, my brothers Sebastian and Felix for all of their support during my studies as well as all my friends for their support and their patience with me while writing this dissertation.

Espoo, June 2010

Philip Gerstner

TABLE OF CONTENTS

PREFACE & INTRODUCTION

LIST OF SYMBOLS AND ABBREVIATIONS	14
LIST OF PUBLICATIONS.....	16
<i>Contributions</i>	<i>17</i>
<i>Errata.....</i>	<i>17</i>
1 INTRODUCTION.....	19
1.1 <i>Background</i>	<i>19</i>
1.2 <i>Heat transfer in paper and printing applications</i>	<i>20</i>
1.3 <i>Hypotheses and outline of this work</i>	<i>20</i>

PART I

2 MEASUREMENT OF THERMAL CONDUCTIVITY.....	25
2.1 <i>Background</i>	<i>25</i>
2.2 <i>Classification of methods</i>	<i>25</i>
2.2.1 <i>Steady state methods</i>	<i>25</i>
2.2.2 <i>Transient methods</i>	<i>26</i>
2.2.3 <i>Transient contactless methods.....</i>	<i>26</i>
2.2.4 <i>Electrical analogy</i>	<i>27</i>
2.3 <i>Tablet diffusivity measurement.....</i>	<i>27</i>
2.3.1 <i>Background</i>	<i>27</i>
2.3.2 <i>Materials and sample preparation.....</i>	<i>28</i>
2.3.3 <i>Tablet diffusivity measurement device</i>	<i>29</i>
2.3.4 <i>Calculation of thermal diffusivity</i>	<i>31</i>
2.3.5 <i>Evaluation of the measurement technique.....</i>	<i>34</i>
2.3.5.1 <i>Precision</i>	<i>34</i>
2.3.5.2 <i>Accuracy.....</i>	<i>35</i>
2.3.5.3 <i>Measurement limitations</i>	<i>37</i>
2.3.6 <i>Pigment coating structure tablet properties</i>	<i>38</i>
2.3.6.1 <i>Evaluation of the tablet structure isotropy.....</i>	<i>38</i>
2.3.6.2 <i>Relation to real coatings</i>	<i>41</i>
2.4 <i>Calculation of thermal conductivity.....</i>	<i>42</i>
2.5 <i>Summary.....</i>	<i>42</i>
2.6 <i>Measurement thread.....</i>	<i>44</i>
3 MODELLING OF THERMAL CONDUCTIVITY	45
3.1 <i>Background</i>	<i>45</i>
3.1.1 <i>Modelling versus simulation</i>	<i>45</i>
3.1.2 <i>Modelling of effective thermal conductivity.....</i>	<i>45</i>
3.2 <i>Classification of the models</i>	<i>48</i>
3.2.1 <i>Solution of the Heat Diffusion Equation.....</i>	<i>48</i>
3.2.2 <i>Thermal resistance models</i>	<i>49</i>
3.2.3 <i>Unit cell models.....</i>	<i>50</i>
3.3 <i>Introducing the Lumped Parameter Model (LPM)</i>	<i>51</i>

3.4	<i>Discussion of the modelling parameters</i>	52
3.4.1	Grouped Lumped Parameter Model	53
3.4.2	The effect of intrinsic thermal conductivities	55
3.5	<i>Alternate model configurations</i>	57
3.5.1	Pigment surface connectivity	57
3.5.2	2D equivalent porosity	58
3.5.3	Skeletal modes	59
3.6	<i>Model comparison: Lumped Parameter and Composite-Layer</i>	62
3.7	<i>Modelling approaches</i>	64
3.7.1	Parameter modelling	65
3.7.2	Structural modelling	65
3.7.3	Connectivity modelling	65
3.8	<i>Summary</i>	66
3.9	<i>Modelling thread</i>	68

PART II

4	APPLICATION OF THE MODEL TO THERMAL CONDUCTIVITY ...	71
4.1	<i>Background</i>	71
4.2	<i>Non-disruptive system</i>	71
4.2.1	Materials	71
4.2.2	Parameter modelling	72
4.2.3	Comparison of unit cell structure to material structure	73
4.2.4	Relating binder dosage to the model binder variable	75
4.3	<i>Disruptive system</i>	76
4.3.1	Materials	76
4.3.2	Role of porosity for thermal conductivity	77
4.3.3	Parameter modelling	78
4.4	<i>Pigment disruption</i>	80
4.5	<i>Summary</i>	81
4.6	<i>Parameter modelling thread</i>	83
5	APPLICATION OF THE MODEL TO COATING STRUCTURES	85
5.1	<i>Background</i>	85
5.2	<i>Generation of structural master layers</i>	85
5.2.1	Materials	85
5.2.2	Particle deposition (simulated master layers)	86
5.2.2.1	Generating the numerical pigment particle system	87
5.2.3	SEM cross-sectional imaging (microscopy master layers)	90
5.2.4	Modelling on master layers	92
5.2.4.1	Generation of the model parameters	92
5.2.4.2	The effect of sub-domain size	93
5.3	<i>Structural modelling of the effect of binder content</i>	95
5.3.1	Simulated masters	95
5.3.2	Microscopy masters	97
5.4	<i>Connectivity of coating structures</i>	98
5.4.1	Connectivity in simulated master layers	99
5.4.2	Comparing the connectivity of master layers	103
5.4.3	Model connectivity	105

5.5	<i>Connectivity modelling</i>	106
5.6	<i>Modelling using alternate unit cell modes</i>	107
5.7	<i>Summary</i>	109
5.8	<i>Structural modelling thread</i>	110
6	MODELLING THE EFFECT OF PHASE PROPERTIES	111
6.1	<i>Background</i>	111
6.2	<i>Binder conformability</i>	111
6.2.1	Materials.....	111
6.2.2	Effective thermal conductivity and pore structure.....	113
6.2.3	Porosity and particle packing.....	115
6.2.4	Effect of binder on connectivity.....	118
6.3	<i>Liquid saturation</i>	120
6.3.1	Materials.....	120
6.3.2	Effective thermal conductivity.....	122
6.3.3	Modelling of the effective thermal properties.....	123
6.3.4	Thermogravimetric behaviour of liquid saturated media.....	127
6.3.4.1	Mineral Oil.....	127
6.3.4.2	Water.....	129
6.4	<i>Summary</i>	131
6.5	<i>Phase properties thread</i>	133

PART III

7	ELECTROPHOTOGRAPHIC TONER FUSING ON THERMALLY DESIGNED SUBSTRATES	137
7.1	<i>Background</i>	137
7.1.1	General.....	137
7.1.2	Principle of electrophotography.....	137
7.2	<i>Substrate properties in toner fusing</i>	139
7.3	<i>Simulation of electrophotographic toner fusing</i>	140
7.3.1	Substrates and fusing nip.....	140
7.3.2	Simulated temperature responses.....	144
7.3.3	Comparison of printer configurations.....	145
7.3.4	Heat conduction versus heat storage.....	147
7.4	<i>Toner adhesion on coated papers</i>	149
7.4.1	Materials and methods.....	149
7.4.2	Adhesion measurement results.....	151
7.4.3	Surface roughness and surface continuity.....	153
7.5	<i>Toner fusing and improved adhesion development</i>	154
7.5.1	Coating concepts and their thermal properties.....	154
7.5.2	Printing.....	156
7.5.3	Adhesion development.....	157
7.5.4	Full tone adhesion development.....	158
7.5.5	Print gloss development.....	162
7.6	<i>Summary</i>	163
7.7	<i>Electrophotography thread</i>	165
8	THERMAL EFFECTS IN HEATSET WEB-OFFSET DRYING	167
8.1	<i>Background</i>	167

8.1.1	General	167
8.1.2	Theoretical Considerations.....	168
8.2	<i>Materials and Methods</i>	169
8.2.1	Materials.....	169
8.2.2	Measurement of waving.....	170
8.2.3	Liquid permeability	171
8.2.4	Ink-surface interaction (ISIT)	172
8.3	<i>HSWO printing of thermally designed coated papers</i>	172
8.3.1	Basic properties	172
8.3.2	Waving	173
8.3.3	Barrier properties and ink interaction	174
8.4	<i>Summary</i>	176
8.5	<i>Offset thread</i>	178

CONCLUSIONS & OUTLOOK

9	CONCLUSIONS	181
10	FUTURE PROSPECTS.....	185
10.1.1	Optimisation and characterisation.....	185
10.1.2	Homeomorphism.....	185
10.1.3	Skeletal structures	185
10.1.4	Combined heat and mass transport	186
	REFERENCES	187

LIST OF SYMBOLS AND ABBREVIATIONS

Symbols

<i>Symbol</i>	<i>Description</i>	<i>Publication*</i>	<i>Unit</i>
<i>a</i>	Pigment factor	[II - VI]	-
<i>a'</i>	Corrected pigment factor	[IV - VI]	-
<i>A</i>	Area (1 dimensional)	[II]	m
	Permeable area	[IX]	m ²
<i>B</i>	Binder dosage	[II]	w/w%
<i>c</i>	Specific heat capacity	[III - IX]	Jkg ⁻¹ K ⁻¹
	Binder variable	[II - VI]	-
<i>c'</i>	Pigment connectivity	[IV - VI]	-
<i>d</i>	Mesh size	[I, III]	µm
	Particle diameter	[IV]	µm
<i>D</i>	Thermal diffusivity	[I - VIII]	m ² s ⁻¹
	Diameter	[VII]	m
<i>E</i>	Modulus of elasticity	[VII]	Nmm ⁻²
<i>F</i>	Force	[VII]	N
<i>h</i>	Heat loss factor	[I, III, IV]	s ⁻¹
	Polymer thickness	[VII]	mm
<i>H</i>	Histogram segment entropy	[IV]	-
<i>i</i>	Grey level value	[IV, V]	-
<i>k</i>	Thermal conductivity	[I - IX]	Wm ⁻¹ K ⁻¹
<i>l</i>	Tablet thickness	[I, III]	mm
	Sheet pile thickness	[IX]	mm
<i>L</i>	Grey levels	[IV, V]	-
	Length	[VII]	mm
<i>m</i>	Mass	[III, VII]	kg
<i>N</i>	Pixel number	[VIII]	-
<i>p</i>	Pressure	[I, III, IX]	bar
	Probability density function	[IV]	-
<i>P</i>	Histogram	[IV]	-
	Cumulative probability	[IV, V]	-
<i>q̇</i>	Energy rate per unit volume	[III]	Wm ⁻³
<i>q</i>	Heat flux		Wm ⁻²
<i>Q</i>	Specific fusing energy	[VII]	kJm ⁻²
<i>r</i>	Repeatability parameter	[I]	-
	Radial coordinate in cylindrical coordinates	[I]	
<i>R</i>	Radius	[I, III]	mm
	Thermal resistivity	[I, VI]	KmW ⁻¹
	Thermal resistance	[II]	KW ⁻¹
<i>s</i>	Nip smoothing	[VII]	mm
<i>S</i>	Bending stiffness	[IX]	mNm
<i>t</i>	Time	[I - IV, VII]	s
	Grey level threshold	[IV]	-
<i>T</i>	Temperature	[III - IX]	°C, K
<i>V</i>	Liquid permeation volume	[IX]	m ³

* numbering of publications see page 16

Greek Letters

<i>Symbol</i>	<i>Description</i>	<i>Publication*</i>	<i>Unit</i>
β	Binder content	[III - VIII]	w/w%
γ	Contact parameter	[II]	-
	Pigment equivalent connectivity	[V]	-
	Adhesion, cohesion	[VIII]	Jm ⁻²
η	Liquid viscosity	[IX]	kg s ⁻¹ m ⁻¹
κ	Liquid permeability	[IX]	m ²
λ	Conductivity ratio of fluid to pigment	[II, IV - VI]	-
μ	Conductivity ratio of fluid to binder	[II, IV - VI]	-
ν	Log-normal distribution parameter	[IV]	μm
ζ	Particle overlap factor,	[IV]	%
	Toner adhesion	[VII]	%
	Toner area fraction	[VIII]	%
ρ	Density	[I - VIII]	kg m ⁻³
τ	Experimental time	[I]	s
	Log-normal distribution parameter	[IV]	μm
	Relative time	[VII]	-
ϑ	Temperature	[I, II]	°C
ϕ	Porosity	[I - VIII]	%

* numbering of publications see page 16

Abbreviations

<i>Abbreviation</i>	<i>Description</i>
abs	Absolute
CLM	Composite Layer Model
CLSM	Confocal Laser Scanning Microscopy
CPVC	Critical Pigment Volume Concentration
exp	Experimental
eff	Effective
FEM	Finite Element Method
GCC	Ground Calcium Carbonate, also in conjunction with:
v	very
c	coarse
f	fine
b	broad particle size distribution
n	narrow particle size distribution
HSWO	Heatset web-offset
LPM	Lumped Parameter Model
MCC	Modified Calcium Carbonate
num	Numerical
PPS	Parker Print Surf
SEM	Scanning Electron Microscopy
res	Residual / Residence
SA	Styrene acrylate
SB	Styrene butadiene
sim	Simulation

LIST OF PUBLICATIONS

This dissertation is based on the following list of publications. Both the listed conference papers and the journal publications have been peer-reviewed. For all publications, the author was in charge of the experimental plan, sample preparation, execution of the measurements, analysis of the results and first draft of the manuscript. Individual contributions to each publication are provided in a subsequent listing. The focus of the individual papers and how they contribute to the structure of the work at hand will be explained in more detail in section 1.3.

- [I] P. Gerstner, J. Paltakari and P.A.C Gane. A method for the measurement of thermal contact diffusivity of paper coating structures: *Nord. Pulp Paper Res. J.* **23**(4):354-362, 2008.
- [II] P. Gerstner, J. Paltakari and P.A.C Gane. A lumped parameter model for thermal conductivity of paper coatings: *Transp. Porous Med.* **78**(1):1-9, 2009.
- [III] P. Gerstner, J. Paltakari and P.A.C Gane. Measurement and modelling of heat transfer in paper coating structures: *J. Mater. Sci.* **44**(2):483–491, 2009.
- [IV] P. Gerstner, C.J. Ridgway, J. Paltakari and P.A.C Gane. A structural analysis of the thermal conductivity of paper coatings: application of particle deposition simulation to a lumped parameter model. *Proceedings of the 14th Oxford Fundamental Research Symposium*, Oxford, UK, 2009, pp. 1255-1292.
- [V] P. Gerstner and P.A.C. Gane. The effect of latex binder on thermal conductivity of paper coatings. *Proceedings of the 7th International Paper Coating and Chemistry Symposium*, Hamilton, Canada, 2009, pp. 33-42.
- [VI] P. Gerstner, S. Veikkolainen and P.A.C. Gane. Effective thermal conductivity of liquid saturated coatings and their liquid vaporisation behaviour. *Proceedings of the TAPPI 11th Advanced Coating Fundamentals Symposium*, München, Germany, Tappi Press, Atlanta, 2010.
- [VII] P. Gerstner and P.A.C. Gane. Considerations for thermally engineered coated printing papers: focus on electrophotography: *J. Pulp Paper Sci.* **35**(3-4):108-117, 2009.
- [VIII] P. Gerstner and P.A.C. Gane. Fusing of electrophotographic toner on thermally engineered coated paper: *Nord. Pulp Paper Res. J.* **25**(1):100-106, 2010.
- [IX] P. Gerstner, T. Grönblom and P.A.C. Gane. Quality and efficiency enhancement in heatset web-offset drying by adopting thermally designed paper coatings. *Proceedings of the 37th IARIGAI Research Conference of Advances in Printing and Media Technology*, Montréal, Canada, 2010.

Contributions

Initial tablet preparation for publications [I] and [II] was performed under the guidance of Dr. Cathy Ridgway, Omya Development AG.

AFM measurements in publication [V] were made with the assistance of Ritva Kivelä and Dr. Monika Österberg, Aalto University.

Sami Veikkolainen was responsible for the thermogravimetric measurements in publication [VI].

Calculations of the inverse Lumped Parameter Model in publications [IV] to [VI] were formulated with the assistance of Kaarlo Nieminen, Aalto University.

Coating and calendering of the papers used in publications [VIII] and [IX] was conducted at the Forest Pilot Center in Raisio with the assistance of Teemu Grönblom.

The electrophotography trial printing in publication [VIII] was performed at VTT (formerly KCL) in cooperation with Jorma Koskinen and Minna Hakkarinen. The toner adhesion measurements were carried out with the assistance of Mr. Andrew Berry of University of Victoria, BC, Canada, during an exchange student programme whilst visiting Aalto University.

SEM imaging in publication [IX] were performed with the assistance of Silvan Fischer, Omya Development AG.

1 INTRODUCTION

1.1 Background

Before beginning to discuss the heat transfer through porous multiphase systems it is appropriate to describe a porous multiphase system in more detail. A porous medium can be defined as a solid matrix that is permeated by fluid filled pores. The pores may be interconnected to a certain degree or may remain completely non-connected as in foams. In addition, the term composite material is used widely, usually signifying a compound of solid materials, i.e. a matrix and reinforcing component. Originally the term refers to material compounds in which the individual parts remain distinguishable. However, in so called nano-composites this is not given anymore. While both the definition of a porous medium and a composite already imply the presence of multiple phases, we can combine these to define a porous multiphase system or a porous composite material, that is the combination of two or more solid phases and fluid filled void spaces.

Due to the versatile nature of porous multiphase systems, many disciplines deal with their characterisation, starting from the basic materials science going on to process engineering applications and end-user product designs. The following list does not claim to be a complete representation, but should merely illustrate the wide range of applications, of which a few examples are:

- a) Chemical engineering, reactors, paper and printing applications
- b) Environmental, soil or petroleum science
- c) Medical and pharmaceutical products
- d) End-user related processes goods, e.g. food processing, clothing

In all of these fields, the transport properties in general, and the heat transport in particular, may play a significant role. In chemical engineering the thermal conductivity of porous media or packed beds of particles is vital, for example, the design of chemical reactors in which the reaction rate is expressed as a function of temperature by the Arrhenius equation /1/. In the field of paper and printing applications alone there is a wide range of heat transport through multiphase systems. Since this aspect will be part of the focus of this work, it will be discussed in more detail separately in the following section.

The thermal properties of soils are an essential part in determining the energy balance between soil, plant and atmosphere /2/. Therefore, a large amount of research is devoted to the thermal characterisation of soils. However, due to the presence of water in soils, most of this research focuses on coupled effects of heat and mass transfer /3/.

In medical research, it is traditionally dentistry that has paid a lot of attention to characterisation of thermal conductivity /4, 5/. The tooth nerves (pulp) need to remain thermally insulated after restorative procedures to avoid temperature shocks. The naturally porous dentine fulfils this function, so the design of synthetic fillings is made to consider thermal considerations as well. In the case of pharmaceutical products, the thermal properties of, for example, tablets are important during their production process. The compaction of powder material into the tablet shape creates heat which affects the final structure of the tablet, but may also affect the chemical stability of the components /6, 7/.

Processed food products can be categorised as porous and non-porous multiphase systems. They are often subject to thermal processing, for which knowledge of the effective thermal properties is required /8/. Also in the design of clothing, the heat

transport properties play a significant role, while also a certain rate of mass transport through the fabric has to be ensured /9/.

1.2 Heat transfer in paper and printing applications

Thermal conductivity of paper coating structures can be regarded as an important property in many steps of coated paper production (drying) /10/, finishing (thermal calendering) /11/, converting (heat sealing, hot melt gluing) and printing (electrophotography, heatset web-offset) as well as in the end use properties of specially coated grades (thermal papers) and barrier films. The rising costs for energy continue to draw attention to ensuring its most effective use. Processes, as mentioned above, involving the application of thermal energy onto coated papers, may benefit from a better knowledge of the thermal transfer in two identifiable ways. On the one hand, the flow of energy and its local effects should be better understood. This would enable optimisation of the thermal efficiency by adjusting either the process parameters or the coating structure itself, i.e. its structure and/or its components. On the other hand, better knowledge of the thermal response of coatings also creates new possibilities to improve the product quality. Especially in processes where interactions of the interface of the coating layer play an important role, i.e. in printing, it is not only the coating structure itself, but also the thermal response that the structure creates, which ultimately affects the product quality.

Being porous multiphase systems, paper coatings show a complex relationship between thermal conductivity and their structural properties. The binder phase plays an important role in formation of the coating structure /12/ and, therefore, porosity alone is unlikely to be sufficient in describing the thermal conductivity. Hence, a generalised model, which is able to describe the relationship of pigment and binder in the coating structure, would be required.

1.3 Hypotheses and outline of this work

This work combines most of the contents of the listed publications, summarises the most important findings and links them based on the knowledge gained after having completed the individual papers. In addition, information is provided to establish those links and to complement the data given in the papers as well as to give a more general view and outlook on future research.

In principle, the publications, and, therefore, this work can be grouped into three progressive levels of investigation. Figure 1 illustrates them using a “tree” analogy. The first level is the fundamental methodology or ground on which the tree grows. As such, there are no final conclusions or hypotheses, but it is the basis upon which further work, i.e. the tree above ground, can grow. The second level is the stem of the tree signifying the focusing of research to point in a given direction, while still being open to extend in a multitude of further investigation. To extend the biological analogy, this second level can be expressed as phototropism, and would translate to “heat transfer through porous multiphase systems”, while the branches represent the third level consisting of multiple fields of application, as discussed in 1.2, exemplified by the branch of “application in printing of coated papers”. Eventually there is the “fruit” of a supported hypothesis (close to the stem) or an application (at the tip of a branch).

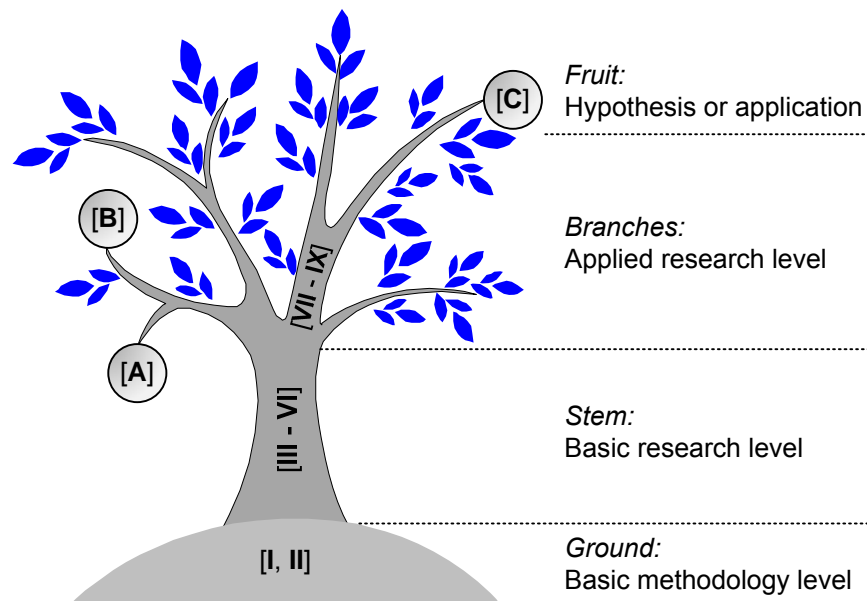


Figure 1. The structure of publications and hypotheses of this work.

The *basic methodology level* is represented in part I of this work. Two important methods on which a significant part of this work builds are introduced. This level is characterised by a broader approach, the findings have an implication for the properties of porous media in general and lay down the basis of further work. Publication [I] introduces the technique for the measurement of thermal diffusivity for samples in the form of macroscopic tablets. This technique will be used for subsequent thermal measurements throughout this work and is therefore an important basis underlying the discussion of the results. The measurement technique is characterised in terms of precision (repeatability and reproducibility) and accuracy. Bias errors of both the measurement technique as well as the tablet sample preparation are discussed. The tablet thermal diffusivity measurement method will be introduced in chapter 2. In addition, publication [II] can be assigned to the fundamental methodology level, since it introduces the model for the calculation of effective thermal conductivity of porous multiphase systems. The use of structural variables instead of porosity is discussed as well as the effect of the phase properties. The modelling of heat transfer in porous media with a focus on the model at hand will be discussed in chapter 3.

Similar to the basic methodology level, the *basic research level* represents a general approach. It is “basic” in a way that the discussion is relevant for porous multiphase systems in general, exemplified with a focus on the specific materials as are found in pigmented coatings and modern, high brightness paper coatings in particular. Publication [III] builds on the previous two methodology papers, and discusses the application of the model to measured data using the tablet diffusivity measurement method. The discussion of the model is based on fitting the model structural parameters (parameter modelling) to the experimental thermal conductivity data. This approach differs to the one taken in publications [IV] to [VI] in that it does not use porosity as the governing model parameter. However, porosity is used initially to point out the role of skeletal connectivity, which will later be used to formulate hypothesis [A]. The approach of fitting the structural model parameters to effective thermal conductivities is discussed in chapter 4. Publication [IV] introduces a different concept of superposing the model onto quasi two-dimensional simulated coating structures. Comparison to real microscopically imaged two dimensional cross-sections, with extensive discussion of both the simulation parameters as well as the modelling parameters, shows the effect of pigment packing disruption effected by colloidal

INTRODUCTION

Hypotheses and outline of this work

forces associated with the introduction of synthetic latex binder. This so called structural modelling is discussed in chapter 5. The disruptive component interaction of binder is then further analysed for binders of different conformability, expressed during coating shrinkage on drying, and in terms of pigment equivalent connectivity in paper [V]. The effect of the liquid saturation on the effective thermal properties as well as vaporisation of liquids from pigment binder structures is added in paper [VI] to provide additional studies on the effect of the phase properties. The effects of binder and fluid are covered in chapter 6. The papers [IV] to [VI] contribute to hypotheses [A] and [B], summarised as follows:

- [A] The parameters of *pore structure* and *skeletal connectivity* are required to model the thermal conductivity of paper coating structures.
- [B] *Measurement* and *modelling* of the thermal conductivity can reveal both colloidal and mechanical interactions of the components acting during formation of the structure.

The *applied research level* adds a practical perspective and discusses the implications of the theoretical work for a specific process. As paper [VI] examines the effective thermal properties of liquid saturated porous media, it is on one hand supporting hypotheses [A] and [B], on the other hand it serves a bridging function to the applied research level. Liquid saturation and the vaporisation of liquids has a direct impact on the print quality in heatset web-offset printing, in which both fountain solution and oil play a part in the ink interaction with the pore structure under the dynamic temperature conditions of the press. The applied research level is represented by papers [VII] to [IX], the specific process being printing on thermally designed coatings, both for electrophotography printing [VII, VIII] and heatset web-offset [IX]. Paper [VII] starts by looking at the theoretical considerations of the temperature conditions in a simulated electrophotography fusing nip for different thermal conductivities of the paper coatings. This, together with measurements of toner adhesion, leads to a general concept for good toner fusing on thermally engineered coatings. This concept is taken further and studied in more detail in publication [VIII]. Both papers are summarised in chapter 7. Print quality effects in drying of heatset web-offset are discussed in chapter 8. Both printing methods on thermally designed substrates respond to hypothesis [C]:

- [C] An insulating paper coating having a surface displaying thermally conductive micro-continuity can provide a beneficial effect in terms of the spatial concentration of heating during thermal transfer.

The publications in relation to the hypotheses are summarised in Table 1.

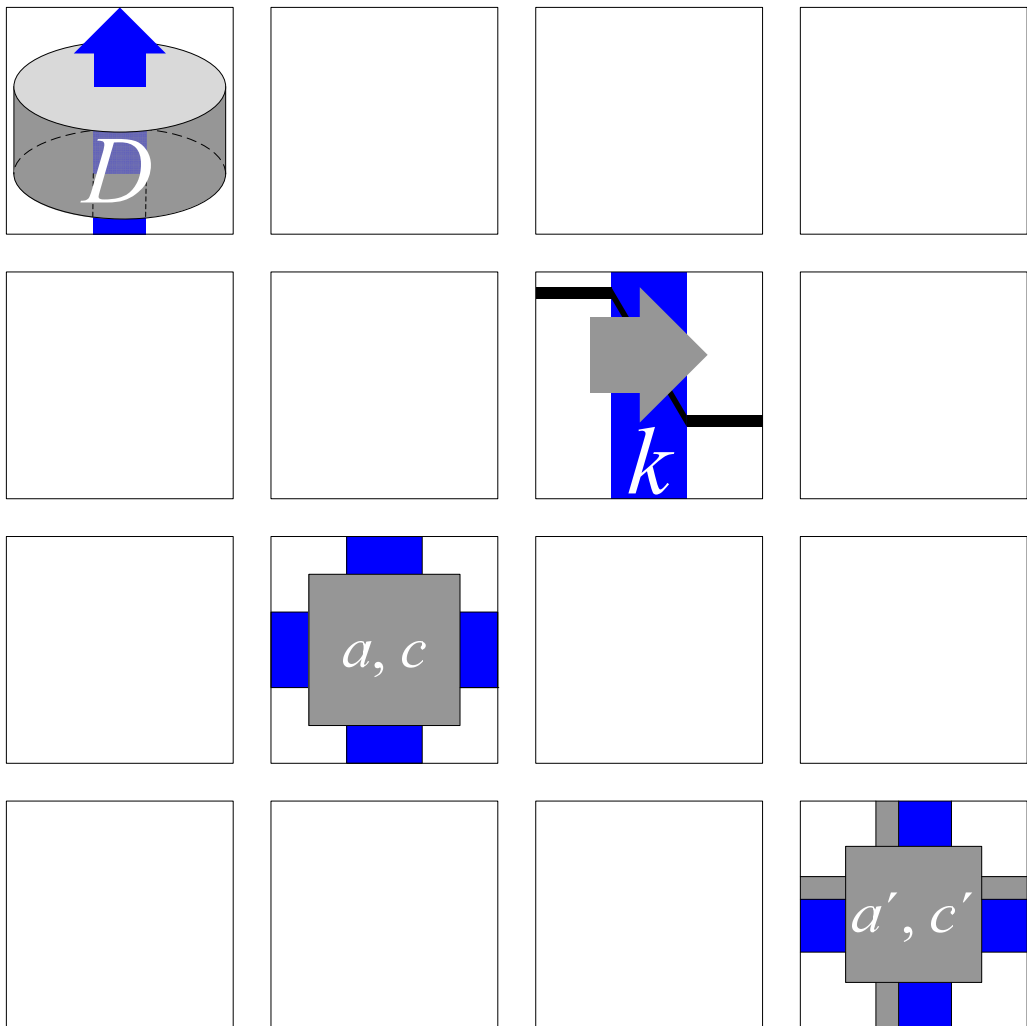
Table 1. Publications and their role in establishing the verity or otherwise of the hypotheses underpinning this work

Paper	Hypothesis		
	[A]	[B]	[C]
[I]	<i>methodology</i>		
[II]	<i>methodology</i>		
[III]	•		
[IV]	•	•	
[V]	•	•	
[VI]	•	•	
[VII]			•
[VIII]			•
[IX]			•

PART

I

BASIC METHODOLOGY LEVEL



*“What we observe is not nature itself,
but nature exposed to our method of questioning.”*

Werner Heisenberg,
German Physicist, 1901-1976

2 MEASUREMENT OF THERMAL CONDUCTIVITY

2.1 Background

Because of the wide range of interest in the thermal properties, the studies of various measurement techniques have been given a great deal of attention over the passage of time, with available publications reaching back to the 1930s. The early works focus more on the theoretical development of techniques, whereas more recent papers tend to refine the existing methods, adapt them to alternate configurations or standardise them, e.g. ISO 22007. A comprehensive summary and classification of the early methods can be found in the review paper of Tsotsas and Martin /13/. This chapter tries to classify some of the measurement methods based on their general approach and give examples of commonly used methods. As the measurement method used in this study, the tablet diffusivity measurement will be introduced in more detail and evaluated regarding its accuracy and precision. In addition, a closer look is taken at the tablet sample material.

2.2 Classification of methods

In their review of thermal conductivity of packed beds, Tsotsas and Martin /13/ suggest a classification of measurement methods based on a) the state of heat flow, i.e. steady state or transient, b) on the direction of heat flow, i.e. radial or axial, and c) on whether the methods are absolute or comparative. Since the state of heat flow is the most characteristic distinction, we adopt the method grouping described under a), and thus separate the following discussion into steady state and transient methods. In addition, contactless (transient) techniques are included and the analogy of measuring electrical resistivity as a comparable property is briefly discussed.

2.2.1 Steady state methods

In the steady state methods, the sample is arranged or insulated in a way that a steady state of heat conduction can be attained. This is often done by “clamping” the sample material in between two surfaces which are heated and cooled, respectively, in order to achieve a defined temperature gradient over the sample thickness, expressed as a distance (depth) z . Thus, under these boundary conditions, the measurement of thermal conductivity can be based on the Fourier equation for unidirectional heat flux across a planar structure /14/:

$$q_z = -k \frac{dT}{dz} \quad (1)$$

The steady state methods, therefore, measure the thermal conductivity directly, rather than the thermal diffusivity, as is the case in many transient methods. This technique can yield an absolute measure for the sample material or a comparative value to the known thermal conductivity of a reference material.

Sanders and Forsyth /15/ discuss an absolute steady state method in which a paper sample is clamped in between two brass columns. The upper column is heated at constant power consumption at its upper side, whereas the lower column is cooled by a steady water flow. The heater power consumption and the cooling water flow rate are adjusted to achieve a steady state for a desired mean temperature. By measuring the temperature gradient in the brass columns, one can extrapolate to the surface temperatures at the sample interfaces. Knowing the power consumption of the heater, it is then possible to calculate the thermal conductivity of the sample.

A comparative steady state method was described by Ofuchi and Kunii /16/. Unidirectional heat flow is created by appropriate insulation and by having a heated side and a cooling side in the device. In their example, the heat is transported serially through the sample and a marble plate of known thermal conductivity. By measuring the temperature gradient across the marble plate one can calculate the total heat flux which also holds for the flux through the sample material. With this heat flux and the temperature gradient through the sample one can in turn calculate the effective thermal conductivity of the sample material.

2.2.2 Transient methods

For transient methods, the sample is subjected to a sudden change of the thermal boundary conditions. This can be a temperature step or a dynamic, e.g. sinusoidal, temperature function control of one interface boundary. Using the temperature-time response to the change of the initial boundary condition, one can calculate the thermal diffusivity by fitting the solution of the heat diffusion equation to the measured dissipation curve. The quality of such a fit may be used to assess the quality of the technique /17/.

The tablet diffusivity, developed here in this thesis study, is an example of a measurement that falls into this latter category of transitory response. It is introduced in part 2.3, and the quality of the temperature response shall be discussed using a mean absolute residual method (see 2.3.4).

Examples of transient contact based methods which are widely used for a broad range of materials are the hot-wire method /18/ and the transient plane source method /19/. Both methods have the advantage that only small temperature gradients and therefore very short experimental times are necessary. For the transient plane source method, commercially available measurement devices exist following the ISO standard 22007.

A different type of transient thermal measurement was utilised by Guérin *et al.* /20/. A stack of sample papers is heated to a constant initial temperature before a thermal mass of lower temperature is brought in contact with the samples. Based on the temperature rise of the thermal mass they calculate the total thermal resistance of the sample stack. By measuring samples of different thicknesses they extrapolated the contact resistance of the thermal mass to the sample stack. The difference of total resistance and contact resistance is the intrinsic sample resistance, which also, in turn, delivers the thermal conductivity. A variation of this technique was employed by Majala *et al.* /21/, in which the device was made up of a symmetrical arrangement of heat source and heat sinks, with the sample materials clamped in between.

A transient method was also used by Rättö and Rigdahl /22/ in order to estimate temperature effects in calendering. The calender was simulated by a pressure pulse from a heated plate. The temperature responses to the heated pressure pulse were measured within a paper sheet and compared to the numerical solutions.

2.2.3 Transient contactless methods

The advantage of contactless methods is the absence of an interface through which the heat is transported from the source to the sample material. Thus, the thermal contact resistance present in relation to the interface can be eliminated.

The flash method /23/ is one example of a transient contactless measurement technique for thermal diffusivity. A light pulse of high intensity, but short duration, is absorbed at the front side of the sample and the resulting temperature response at the backside of the sample is recorded to calculate thermal diffusivity. The flash pulse energy eliminates the heat transfer interface and the short duration of the light pulse minimises heat losses.

Furthermore, the maximum recorded temperature at the sample backside allows calculation of the sample heat capacity. This method was adapted by Zhao and Schabel /24/ for the measurement of the thermal properties of paper. Drawbacks relate to the inhomogeneous nature of the paper samples used. Additionally, the light absorption versus scattering potential of the porous structure of paper, and paper coatings, makes the thermal transfer mechanism via the medium of light energy ill-defined. However, for comparable structures, values obtained can be readily related.

The fundamentals of the thermoacoustic method, also known as thermal radiometry, were initially described by Rosencwaig /25/. In this method, a periodic laser pulse hits the surface of the sample material. The part of the energy of the laser beam that is absorbed by the sample is converted to heat which in turn heats up the surrounding. This causes periodic pressure waves in a closed measurement cell which can be detected. Phase and intensity of the measured pressure waves relative to the laser beam pulse are in direct relation to the thermal properties of the sample. Kartovaara *et al.* /26/ used this method for a comprehensive study of the thermal properties of various paper furnishes. A thermophysical characterisation of copy paper was performed by Mandelis *et al.* /27/ using laser infrared radiometry. Once again, for porous materials there are two immediate drawbacks, i.e. that of the proportion of forward and back light scattering and that of the acoustic response of a porous material, which, although analysed as a composite, responds as a coupled two or multiphase system, having internal resonance and harmonic response according to the pore structure itself and material interfaces constituting it.

2.2.4 Electrical analogy

In the steady state case, both electrical and thermal conductivity can be described by the Fourier equation. Hale /28/ points out the similarity of electric field, magnetic field and the temperature gradient. This translates to the Maxwell relation /29/ analogy for effective thermal conductivity, derived from its original description for electrical conductivity (see 3.2.1). Turner /30/ discusses the Maxwell relation for the case of a dilute dispersion of spheres. Determining the electrical conductivity is often easier and more accurate than temperature measurements. Furthermore, the conductivity of the fluid phase can easily be changed by changing the concentration of an electrolyte solution, e.g. NaCl. This method provides a simple way of studying fluid saturated structures for a wider range of conductivity ratios of fluid and solid phase. A disadvantage of these methods is that certain heat specific effects, such as thermal radiation, pore convection or pressure dependency, cannot be captured.

2.3 Tablet diffusivity measurement

2.3.1 Background

This introduction of the tablet diffusivity measurement is largely based on publication [I]. It summarises the most important aspects of the measurement technique, including the sample preparation and its numerical evaluation. Further information on the data handling and calculation algorithms can be found in ref. /31/.

The technique applied is based on the work of Gane *et al.* /32/ where macroscopic pigment tablets were used to determine the thermal properties. The method can be classified as an absolute, axial and transient one (see 2.2). The use of tablet material representing the porous coating structure brings a set of advantages for both the measurement and the modelling. The pigment or coating tablets are ca. 40 mm in diameter and 14 mm thick. Because of their size they are easy to handle and, more importantly, it is possible to examine various coating structures independently from any carrier material,

such as the base paper, that is normally present. A further advantage of working with macroscopic structures is that the measured data are suitable for modelling. In order to describe the effective properties of porous media as a true composite material, the measured structure needs to be large compared to the internal pore structure (compare discussion in 3.1). In respect to the relevance to paper coatings (also see discussion in 2.3.6.2), however, the representation of coating structure as a homogeneous bulk composite fails to take account of thin layer effects, in which, for example, thin areas of coating application behave in the limit as single particulate material. For example, if the pigment particle size is of the order of, or greater than, the local coating thickness, the thermal conductivity is then that of a single particle or air alternately. In such cases, the opportunity for modifying coating design is greatly limited, and so we consider the case where coat weight application is sufficient to render the coating thicker than the individual component(s) size.

Despite the advantages of using tablets it is important to characterise both the measurement technique and the tablet properties before drawing any conclusions from the measurement results. One aim of this chapter is, therefore, to evaluate the measurement technique in more detail. The quality of the measurement method, including the sample preparation, is described in terms of precision and accuracy. Furthermore, it is important to determine the factors which might affect the measurement result, such as the thermal contact resistance present.

The characterisation of the tablet material is undertaken by measuring internal transient temperature distributions. These measurements allow conclusions to be drawn concerning the degree of isotropy of the tablets. In addition, previous literature data are discussed in order to point out the similarity of tablet structures to real paper coatings.

2.3.2 Materials and sample preparation

The pigment used in the experiments for the evaluation of the tablet diffusivity measurement was a coarse industry standard, polyacrylate dispersed, ground calcium carbonate with a broad particle size distribution (bcGCC¹). The binder used was a medium glass transition temperature, T_g , n-butyl acrylate styrene latex², and coating colours were prepared using doses of 8, 12 and 20 w/w% based on 100 w/w% pigment, respectively. In addition, also binder free pigment slurry was used. The tablets were formed, following the method of Ridgway *et al.* /33/, in which the coating slurry gets dewatered through a membrane (mesh size: $d = 0.025$ mm) by applying a pressure of $p = 20$ bar (Figure 2). All tablets were oven dried for at least 12 hours at 60°C before further processing.

¹ Hydrocarb 60 is a registered trademark of Omya AG

² Acronal S360D is a registered trademark of BASF AG

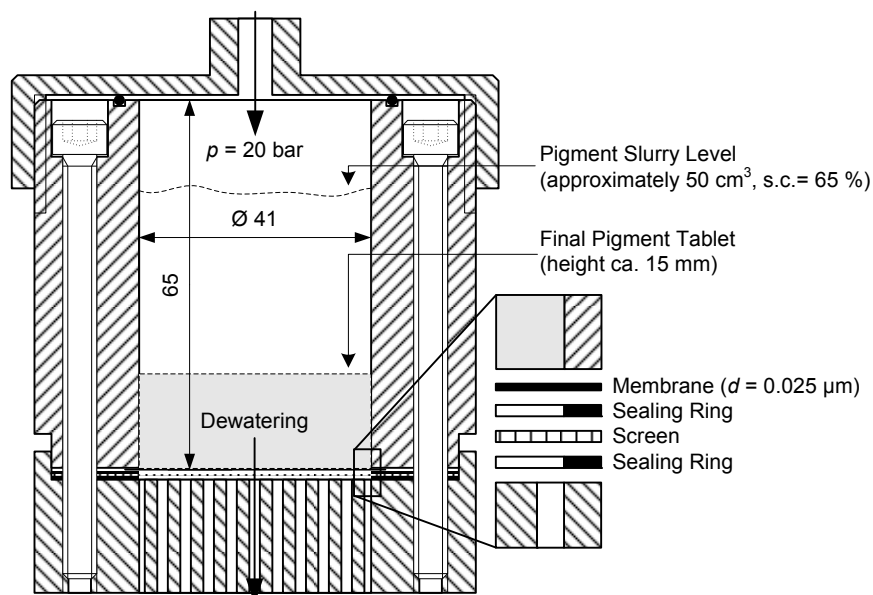


Figure 2. Pressure vessel used to form the pigment tablets. Based on paper [1], Figure 1.

In order to measure the internal temperature profile within the pigment tablets and evaluate their isotropy, thermocouples were embedded at different positions in the thickness direction. For convenience this was done either directly or indirectly during the tablet forming process.

In the vertical method, the thermocouple wires were held inside the pressure vessel while the pigment tablet formed directly around the thermocouples. The horizontal method is an indirect method. Before the coating slurry was added, a “skeleton” with horizontal needles was glued to the inside wall of the pressure vessel. After the tablet forming and drying, the needles were removed and the thermocouples were placed in the remaining pre-formed holes. Both embedding methods showed themselves to be similarly suitable for the measurement.

2.3.3 Tablet diffusivity measurement device

To measure thermal diffusivity, a pigment tablet was insulated around the shell and on top of it by pads of fibreglass wool. The thermal conductivity of fibre glass wool is low (ca. $0.058 \text{ Wm}^{-1}\text{K}^{-1}$ /14/) compared to that of the sample material. The sample is therefore effectively insulated and convection heat losses can be minimised. The insulated tablet was embedded in a further insulating case (Figure 3).

MEASUREMENT OF THERMAL CONDUCTIVITY

Tablet diffusivity measurement

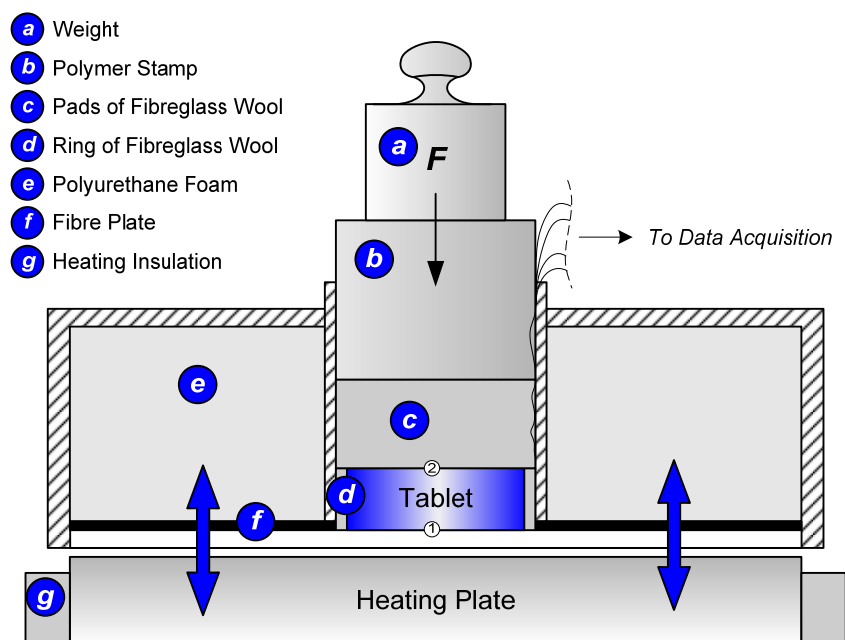


Figure 3. Setup for the heat conduction measurement. The tablet is insulated on top and around the shell by fibreglass wool, and held in an insulating case. This case is put on the heating plate. A weight on top of the tablet ensures consistent contact to the heating plate. Based on paper [1], Figure 3.

The thermally insulated case positions the tablet at a fixed place and brings it into close contact with a heating plate. The contact was facilitated by pressing the sample to the heating plate by a weight. For all measurements taken, there were at least two thermocouples present. One thermocouple at the bottom (No. 1 in Figure 3) to measure the temperature step when bringing the tablet case in contact with the heating plate as well as to measure actual heating temperature during the measurement. Another thermocouple at the top of the tablet (No. 2 in Figure 3) measures the dynamic temperature response (Figure 4). Based on this dynamic temperature response the thermal diffusivity of the tablet material is calculated as described in the following section. If embedded thermocouples would be present in the tablet (not shown in Figure 3) the internal thermal diffusivities could be calculated as well.

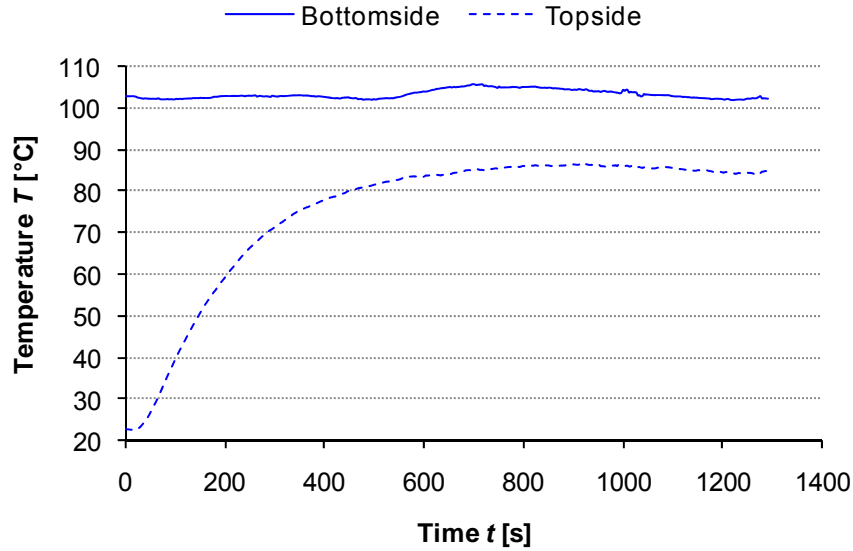


Figure 4. Temperature time curves for the tablet diffusivity measurement. The bottomside temperature is the heating temperature. The temperature response on the topside is used to calculate the thermal diffusivity of the sample.

2.3.4 Calculation of thermal diffusivity

The general form of the heat diffusion equation /14/ is:

$$\nabla \cdot (k \nabla T) - \dot{q}_{\text{loss}} = \rho c_p \frac{\partial T}{\partial t} \quad (2)$$

where:

k	is the thermal conductivity [Wm ⁻¹ K ⁻¹]
T	is the Temperature [K]
\dot{q}_{loss}	is the rate of energy loss per unit volume [Wm ⁻³]
ρ	is the density [kgm ⁻³]
c_p	is the specific heat capacity at constant pressure [Jkg ⁻¹ K ⁻¹]
t	is the time [s]

The heat transfer through a tablet for the given experimental setup can be described as the heat conduction along the axis of a cylinder. We, therefore, choose cylindrical coordinates for the heat diffusion equation and assume that k is independent of the coordinates and constant for the temperature range in question. The general diffusion equation becomes:

$$D \left[\frac{1}{r} \frac{\partial}{\partial r} \left(r \frac{\partial T}{\partial r} \right) + \frac{1}{r^2} \frac{\partial^2 T}{\partial \phi^2} + \frac{\partial^2 T}{\partial z^2} \right] - \frac{\dot{q}_{\text{loss}}}{\rho c_p} = \frac{\partial T}{\partial t} \quad (3)$$

where D is the thermal diffusivity defined as:

$$D = \frac{k}{\rho c_p} \quad (4)$$

For the experiment, we can further assume that the heat flux through the tablet is homogeneous because the radius of the tablet is large compared to its thickness, and the

MEASUREMENT OF THERMAL CONDUCTIVITY

Tablet diffusivity measurement

tablet is insulated in the radial direction. Therefore, we can say that the temperature gradient in the radial direction reduces to zero: $\frac{\partial T}{\partial r} \rightarrow 0$

Because of the tablet shell insulation symmetrical to the cylinder axis and the homogeneous heat source, the heat flux in the circumferential direction further becomes negligible: $\frac{\partial^2 T}{\partial \phi^2} \rightarrow 0$

This means that the heat diffusion equation reduces to its one dimensional transient form. Since the tablet is additionally insulated on the top, the heat losses \dot{q}_{loss} would ideally become zero. However, since this ideal case cannot be reached completely in practice, we need to take some ambient heat losses into account and so the heat diffusion equation becomes:

$$D \frac{\partial^2 T}{\partial z^2} - \frac{\partial T}{\partial t} = h \cdot (T - T_a) \quad (5)$$

where: D is thermal diffusivity [m^2s^{-1}],
 T is temperature [$^{\circ}\text{C}$],
 T_a is ambient temperature [$^{\circ}\text{C}$],
 z is the tablet thickness coordinate [m],
 t is time [s], and
 h is a heat loss term [s^{-1}].

To solve the differential equation, the initial and boundary conditions are given by the experimental setup shown in Figure 3. The tablets were acclimatised to 23°C at least 12 hours before the experiment. Moisture/humidity of the tablet was that of the prevailing room humidity. Since the timescale of the measurement is quite extended, it is assumed that humidity in the apparatus can equilibrate to that defined by the temperature regime in exchange with the surroundings, i.e. a progressive drying effect is expected, which at the highest temperatures can be considered as effectively bone dry. Therefore, the initial condition is that the material has an even temperature T_0 throughout its thickness ($0 < z < l$):

$$T(z, t = 0) = T_0 \quad (6)$$

A two point controller regulates the temperature of the heating plate at the bottom of the tablet and keeps it within a certain interval. Figure 4 shows that the heating temperature does vary to some extent. However, the mean standard deviation of the heating temperatures for the measurements was 1.25°C . Since this is a small variation compared to the temperature step, we can assume that the temperature of the heated side (tablet bottom) is constant around the mean of heating temperature during the experimental time. The boundary condition at $z = 0$ for the total experimental time ($0 < t < \tau$) is given, therefore, by the Dirichlet boundary condition:

$$T(z = 0, t) = \bar{T}_1 \quad (7)$$

The topside of the tablet is insulated, thus no direct heat flux occurs. This is the Neumann boundary condition:

$$\frac{\partial T}{\partial z}(z = l, t) = 0 \quad (8)$$

The initial condition (equation 6) and the boundary conditions (equations 7 and 8) are used to solve the partial differential equation (equation 5). The thermal diffusivity D of equation 5 is calculated from the measured temperature responses by a self adaptive numeric iteration. The experimentally measured temperature response is compared to the calculated one of known parameters D and h . Both parameters are then iterated until there is a minimum difference between the numerical and the experimental temperature response. We call this mean of the absolute temperature difference, the absolute residual res_{abs} :

$$res_{abs} = \frac{\sum_{i=0}^N |T_{num}(t_i) - T_{exp}(t_i)|}{N} \quad (9)$$

The residual can be used as a quality indicator of the iteration, and therefore for the calculation as also for the quality of the experimental result. The residuals for both internal temperature measurements (embedded thermocouples) and topside thermocouples for tablets of different binder concentrations are shown in Figure 5.

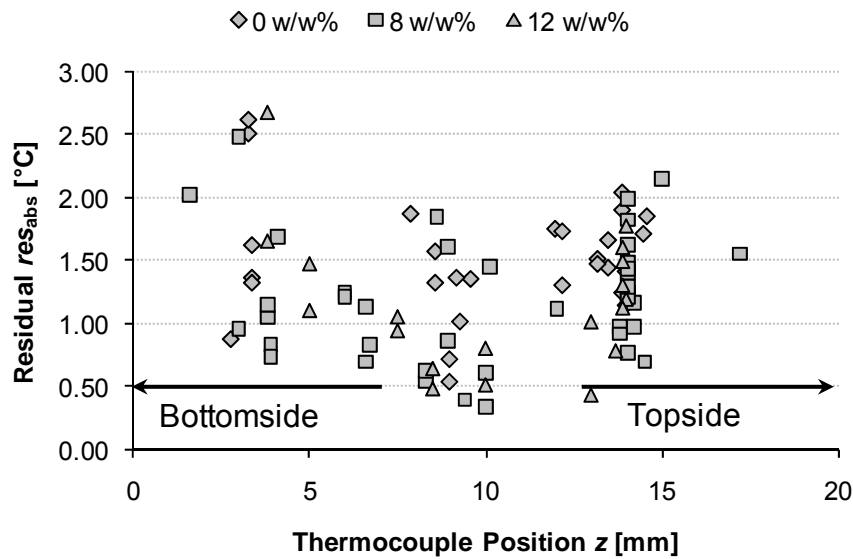


Figure 5. Residual plot for the numerical temperature responses. The residuals for the given binder levels are iterated for each thermocouple position individually. Based on paper [1], Figure 4.

It can be seen that the temperature responses for both the internal and topside temperature measurements, as well as for tablets of all the chosen binder levels, are approximated similarly. In addition it can be seen that the residual is generally smaller than 3 °C, indicating that the experimentally measured temperature response fits the theoretical solution rather well. The calculated thermal diffusivities D_{exp} using this method can, therefore, be the base for further evaluations of the measurement technique.

2.3.5 Evaluation of the measurement technique

Having discussed the calculation of the thermal diffusivity, one needs to evaluate the technique of the measurement itself. This can be done by describing the results in terms of precision and accuracy.

2.3.5.1 Precision

Precision is a general term used to describe the closeness of individually obtained measurements. We separate the term precision into *repeatability* and *reproducibility*. The UIPAC³ /34/ defines *repeatability* as “the closeness of agreement between independent results obtained with the same method on identical material, under the same conditions”. Conditions include operator, measurement apparatus, laboratory and interval of time. In our case repeatability is then defined as the closeness of the measurement results for the diffusivity obtained from a single tablet in several measurements with the same insulation and experimental setup.

We define the repeatability of the measurement as the standard deviation based on the mean diffusivity. Table 2 lists the individual repeatability of tablets for different binder levels as well as the total repeatability. It can be seen that the repeatability values are all roughly around 2 %, so they don't vary significantly and thus show that they are describing the technique independently of the material used.

In addition to repeatability, *reproducibility* is defined /35/ as “the closeness of agreement between independent results obtained with the same method on identical test material but under different conditions”. We adapt this definition to our situation by saying that reproducibility is the closeness of the measurement results for the thermal properties obtained from all tablets of a certain binder level. That way the material as such is the same, but because the tablet and the insulation changes (the radial fibre glass ring is replaced for every new measurement), we can say that the experiment is done under different conditions. Depending on viewpoint provided by these experiments, reproducibility of the measurement is, therefore, a combination of the repeatability of the heat conduction measurement and the repeatability of the tablet forming. We note as a result, that the individual reproducibility may be expected to be lower than repeatability itself because they both include the repeatability of the tablet forming as well. The reproducibilities listed in Table 2 confirm this. While the reproducibility value for the range of tablets without binder is only slightly higher than the repeatability values of the measurement on a single tablet, introducing binder per se seems to reduce the reproducibility more significantly. This indicates that the tablet forming of the binder-containing tablets is not as repeatable as for the pure pigment tablet. We shall see later that this relates at least in part to the interacting colloidal nature of the binder and the pigment dispersion, and not to the experimental method per se, leading to a disruptive packing of the pigment, which can be expected to exhibit a partly chaotic/stochastic behaviour, particularly if the interaction displays criticality.

³ International Union of Pure and Applied Chemistry

Table 2. Repeatability and reproducibility of the measurement.

<i>Binder content</i>	<i>Repeatability</i>	<i>Reproducibility</i>
w/w%	%	%
0	2.20	2.39
8	1.63	4.55
12	2.45	6.27
20	-	4.43
Total:	2.09	4.41

2.3.5.2 Accuracy

Accuracy is defined as closeness of agreement between the result of a measurement and a true value of what is being measured. Therefore, we go on to compare the thermal diffusivity of standard materials measured using this method with their properties established in the literature. Solid cylinders of aluminium, stainless steel (AISI 316) and marble were machined to similar dimensions as those of the pigment tablets. Although their thermal properties are different from the calcium carbonate samples, they are very well known and established in the literature [14]. Furthermore, the advantage of metals is that they are (in the scale of the sample tablets used) very homogeneous and isotropic materials.

The reference material cylinders were placed in the insulating case in the same way as the pigment tablets. However, because the thermal diffusivity of the metal cylinder is in the same order of magnitude as that of the heating plate, the temperature of the heating plate drops when the metal tablets come in contact with it. This occurs for the marble cylinder as well, though to a lesser extent. As a result, the assumption of constant heating temperature is no longer given and the lower boundary condition (equation 7) becomes a function of time. This is taken into account when calculating the thermal diffusivity. Instead of the constant mean heating temperature, a cubic polynomial fitting of the actual measured heating temperature is used to model the lower boundary condition. Figure 6 shows, exemplified for the aluminium reference tablet, the experimentally measured temperature at the heating plate (exp) in comparison with the numeric polynomial (num):

$$T(z = 0, t) = 4.0823 \cdot 10^{-6} t^3 - 0.0026482 t^2 + 0.61276 t + 47.283 \quad (10)$$

as well as the residual (res) difference of both.

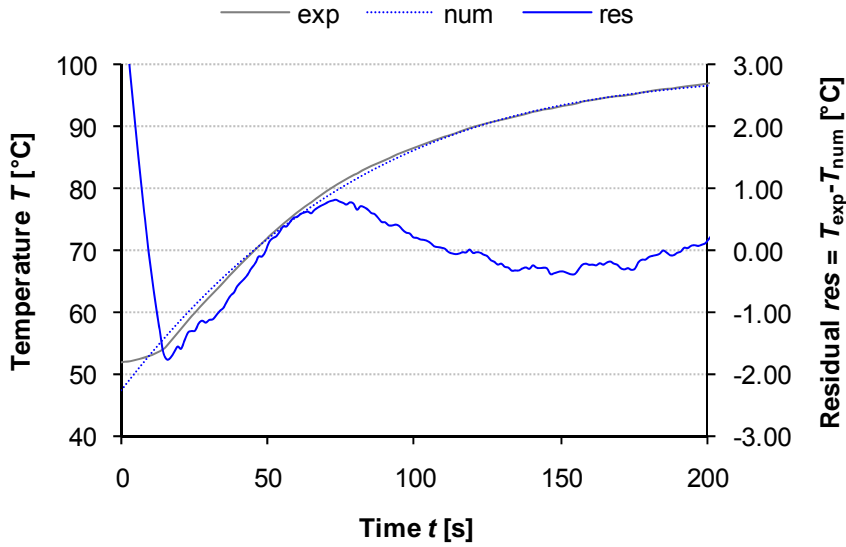


Figure 6. Experimentally measured heating temperature for the aluminium tablet in comparison with a cubic polynomial fit as well as the residual of both curves.

However, the calculated diffusivity value is lower than the literature values would suggest. The same trend was found for the other reference materials as well. The fact that all reference materials show lower diffusivities than their corresponding literature value, suggests that there is a systematic error that leads to the inaccuracy of the measurement. It is suspected that this “error” lies in the interface between heating plate and sample tablet. The heat transfer in that area is dependent on the contact. This can be explained by the concept of thermal resistance. We can say that the total specific resistance or resistivity of the measurement system consists of the tablet’s resistivity and a contact resistivity from the interface between heating plate and tablet:

$$R_{\text{exp}} = R_{\text{tablet}} + R_{\text{contact}} \quad (11)$$

where the resistivities are defined in respect to conductivity, k , as:

$$R = \frac{1}{k} \quad (12)$$

Combining equations 11 and 12 with the definition of thermal diffusivity (equation 4), the total (experimentally measured) thermal diffusivity becomes:

$$D_{\text{exp}} = \frac{1}{\left(\frac{1}{k_{\text{lit}}} + \frac{1}{k_{\text{contact}}} \right) \rho c_{\text{eff}}} \quad (13)$$

This equation can be converted to get the thermal contact conductivity, k_{contact} , from the measured diffusivity, D_{exp} , and the literature values of conductivity, k_{lit} , density, ρ , and effective specific heat capacity, c_{eff} . Table 3 lists the calculated values of thermal contact conductivity for the reference materials as well as for a calcium carbonate tablet without binder. The literature values of thermal conductivity and heat capacity for the calcium carbonate tablet are based on the ratio of pigment tablet density to marble density (74 %).

Table 3. Comparison of contact conductivity k_{contact} calculated from the measured temperature responses and the corresponding literature values /14, 42/.

	D^{exp} m^2s^{-1}	D^{lit} m^2s^{-1}	ρ kgm^{-3}	c_{eff} $\text{Jkg}^{-1}\text{K}^{-1}$	k_{lit} $\text{Wm}^{-1}\text{K}^{-1}$	k_{contact} $\text{Wm}^{-1}\text{K}^{-1}$
Al	9.72E-06	9.72E-05	2700	888	237	25.89
Al*	4.47E-05	9.72E-05	2700	888	237	198.55
AISI 316	2.10E-06	3.48E-06	7960	588	13.4	24.80
AISI 316*	2.95E-06	3.48E-06	7960	588	13.4	90.90
Marble	8.15E-07	1.26E-06	2700	830	2.3-3.0	5.17
Marble ⁺	8.70E-07	1.26E-06	2700	830	2.3-3.0	6.30
Marble* ⁺	1.02E-06	1.26E-06	2700	830	2.3-3.0	11.98
cGCC ^a	3.77E-07	9.39E-07	1997	618	2.09	0.78
cGCC* ^a	3.86E-07	9.39E-07	1997	618	2.09	0.81

* With thermo-conductive paste at the interface of heating plate and reference tablet

⁺ Polished

^a Pigment tablet without binder, diffusivity literature value based on the density ratio compared to marble

It should be noted that the thermal contact conductivity cannot be seen as an absolute value, because of the problem to assign from which part of the interface, the heating plate or the lower side of the tablet, the temperature measurement comes from. The temperature measurement at the interface is, therefore, ill-defined and the contact conductance should be seen more as a number to identify the order of magnitude of how the contact interface might affect the overall measurement.

When comparing the magnitude of the observed contact conductivity with the experimental and literature values of conductivity of the materials, it can be seen that, although the thermo-conductive paste improves the contact conductivity, it is still quite low. The interface plays, therefore, an important role in the outcome of the measurement. It is likely that the experimental results of Gane *et al.* /32/ are affected by the contact conductivity as well. The low contact conductivity could explain the lower thermal conductivity values compared to ones measured by Guérin *et al.* /20/, for example.

Because of the contact conductivity, the experimental diffusivities measured are apparent values, which include the thermal transfer properties of the interface. We assume that, because of the similarity of both bulk material and the surface of the pigment tablets, their measurements are comparable. For the pigment tablet measurements no thermo-conductive paste was used as this would introduce an additional source of variation at the interface. The discussion of thermal conductivity at the interface is, nonetheless, considered to be of great importance when measuring the effective thermal properties of liquid saturated structures or considering the process of toner fusing in electrophotography, as the thermal contact is likely to be similarly disturbed. This effect serves to heighten the relevance of the experimental method.

2.3.5.3 Measurement limitations

The discussion above, regarding the accuracy of the tablet method, showed that it is possible to consider other solid materials than mineral structures as long as they can be shaped into a cylindrical form of the appropriate dimensions. In the case described, metal cylinders of aluminium and stainless steel were used. However, when working with these materials some of the limitations of the method became apparent.

It was explained that because the thermal diffusivity of metal tablets is in the same order of magnitude as that of the heating plate, the assumption of constant heating temperature

was not valid anymore. When bringing the metal tablets in contact with the heating plate, the interface temperature dropped initially and began to recover slowly. While this doesn't fully exclude the use of metals for this method, it creates a significant amount of extra work for each measurement as boundary condition (equation 10) is a function of time, which needs to be modelled mathematically in order to solve the diffusion equation. There is, therefore, a practical upper limiting boundary for the thermal diffusivity of sample materials when considering the suitability of the method.

A lower limiting boundary also exists because the response times for insulating materials can become very long. For a pigment tablet measurement ca. 20 min were taken to record one temperature response curve. During this time the insulation case begins to warm up. If the total experimental time would be significantly longer, the heating of the insulation case could interfere with the thermal insulation of the tablet and therefore rule out the use of the one dimensional diffusion equation (equation 5). The experimental time can be shortened by reducing the sample thickness. However, it was found highly impractical to handle samples thinner than 10 mm.

The limitations, described above, define a practical range of thermal diffusivities measurable using this technique. It was found that thermal diffusivities in the order of $10^{-7} \text{ m}^2\text{s}^{-1}$ seem ideally suited. This is the case for many materials, such as minerals, various wood species or polymers and also includes the porous pigment coating structures as studied in the work at hand /14/.

In addition to the thermal diffusivity range of the sample material, also the applicable temperature can pose limitations. The heating temperatures for the measurement of the pigment tablets were 100 °C on average. Materials like polymers might react to too high temperatures, and, thus, lower heating temperatures would be required, which, in turn, increases the experimental time for a given sample thickness. Therefore, these three parameters of the experimental setup, i.e. heating temperature, sample thickness and experimental time, need to be tuned to the sample material in question.

2.3.6 Pigment coating structure tablet properties

2.3.6.1 *Evaluation of the tablet structure isotropy*

To estimate if there is anisotropy or inhomogeneity in the tablet, we assume initially that the tablet is isotropic and then calculate the overall thermal diffusivity by the topside temperature measurement. Even though the thermal conductivity may be a function of z , it is valid to use equation 5, because we calculate the overall thermal diffusivity as for a quasi isotropic medium. However, instead of calculating the internal diffusivities separately, we use the residual to express how close the internal temperature measurements are in relation to the overall effective thermal diffusivity. In contrast to the residuals expressing the quality of the temperature response approximation (equation 9), the absolute values are not used here, but rather the algebraic sign in the mean of the residual. That way one not only gets information on how well the experimental curve is approximated, but also on whether the numerical curve lies "above" or "beneath" the locally experimentally measured temperature response.

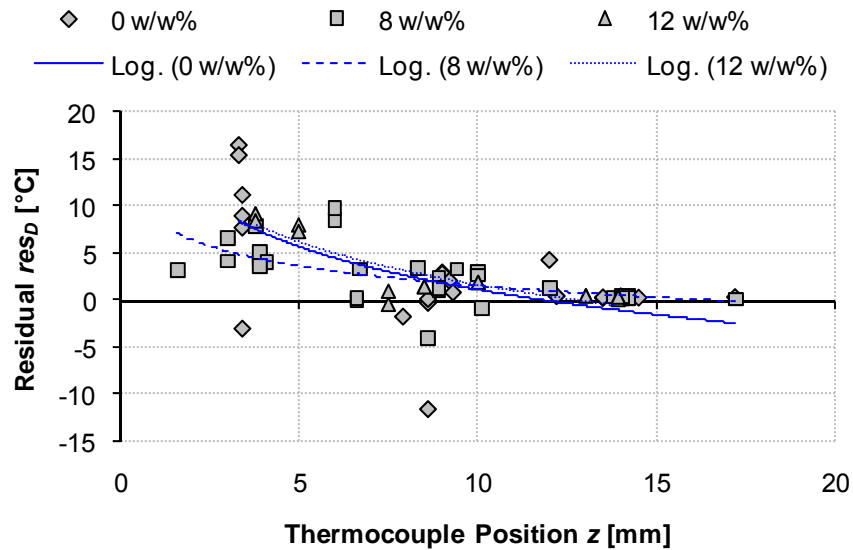


Figure 7. Temperature residual plot, measured as a function of position, when adopting the diffusivity numerically iterated for the top temperature measurement only. Based on paper [1], Figure 10.

The residual res_D in Figure 7 is positive if the calculated overall diffusivity is larger than the locally experimentally measured one and negative if the calculated overall diffusivity is lower. With the exception of a few outliers, the residuals in Figure 7 are positive, which tells us that the local thermal diffusivity is lower than the total effective diffusivity calculated from the topside temperature response. This trend is seen for all binder concentrations, which implies that if the tablet is anisotropic, it is not only due to the binder but also due to an anisotropic structure as such (i.e. density gradient). Niskanen and Simula [36] measured the thermal diffusivity of paper and found that for the more porous grades, the thermal diffusivity is not a material property but increases with increasing sheet thickness. They align this increase with the growing heat diffusion into air channels through the sheet. A similar phenomenon could occur in the porous calcium carbonate pigmented structures. For this reason, further measurements were taken to examine whether there was additional tablet anisotropy. In one experiment, a tablet with 8 w/w% binder and two horizontally embedded thermocouples was measured in the usual way, with the heat flow opposite to the dewatering direction. In a second experiment, after cooling down, the tablet was turned around and the thermal properties were measured again with the heat flow in the direction of previous dewatering.

MEASUREMENT OF THERMAL CONDUCTIVITY

Tablet diffusivity measurement

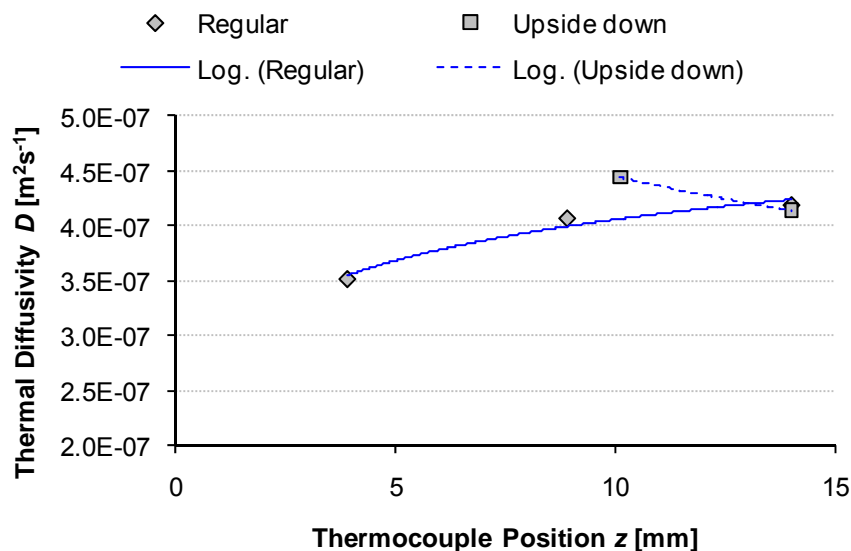


Figure 8. Thermal diffusivities measured for a tablet containing 8 w/w% binder. Heat flow opposite (regular) and in direction (upside down) of the tablet dewatering direction. Based on paper [1], Figure 11.

Figure 8 shows the results for the calculated diffusivities depending on tablet orientation. Note that for the second experiment in the upturned case one thermocouple measurement failed so that there is only one internal measurement available. The tablet thickness is 14.0 mm, so for both experimental runs the topside temperature measurement delivers the thermal diffusivity at this position. After turning the tablet around, the thermocouple which used to be at $z_1 = 3.9$ mm is subsequently at the position $z_1 = 10.1$ mm away from the heated side. The experiment indicates that the thermal diffusivity at the dewatering side of the tablet is lower. This seems to be a material property, because, as the tablet is turned around the internal temperature measurement shows a higher diffusivity opposite to the dewatering side and this cannot be explained by the growing influence of heat diffusion into pores. However, Figure 8 also shows that, for both experimental runs, the measured overall diffusivity of the tablet is practically the same, confirming good repeatability, as discussed in 2.3.5.1.

The anisotropy indicated in the diffusivity is likely due to the cake formation in the filtration step when forming the pigment tablets [37]. This can be further examined by looking at the density distribution in the thickness direction of a tablet. Figure 9 shows the density gradients for a binder free tablet and a tablet containing 2 w/w% binder. They are measured by stepwise grinding of the tablets starting from the dewatering side. The densities were then calculated by the tablet weight and the cylindrical tablet volume of the corresponding tablet thickness after each grinding step. Since the accuracy of the tablet thickness measurement is constantly 0.1 mm, the interval of the calculated densities widens as the tablet grinding proceeds to low thicknesses. This interval is illustrated in the form of grey zones around the measurement values in Figure 9. Despite the reduced accuracy, it can be seen for both tablets that there is a slight increase in the local density towards the topsides of the tablets. This can be attributed to a straining/sieving mechanism found for the flow of small particles through porous media [38]. As a filter cake forms the larger particles act as strainers for fines, thus getting progressively trapped in the upper regions of the filtered structure. This leads to an increase of the density as a function of height of the filter cake, i.e. tablet thickness.

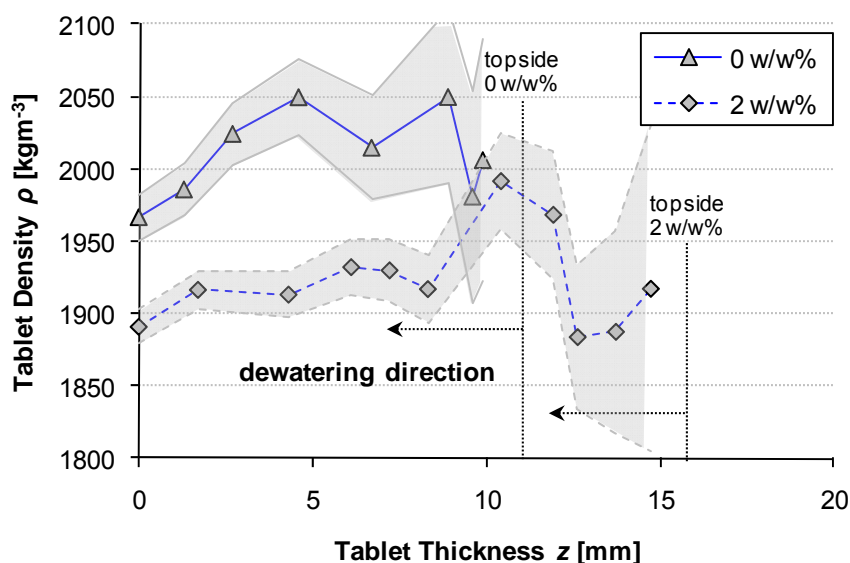


Figure 9. Density distribution over the thickness for a binder free and a 2 w/w% tablet. The density is calculated for the tablet mass and volume of an ideal cylinder. The grey area indicates the measurement accuracy.

2.3.6.2 Relation to real coatings

The tablets formed have been shown to have similar pore structure and porosity values to those of paper coatings /33, 39, 40/.

To study the effective particle size in coatings, Laudone *et al.* /41/ coated thin layers of a bcGCC pigment in combination with a high T_g (23 °C) SA latex binder on aluminium foils. The coat weights were 10 gm⁻² and 20 gm⁻² and the latex dosage was 10 w/w%. The resulting porosities measured by mercury porosimetry were 26.1 % and 24.8 %, respectively. They argued that the lower porosity for the higher coat weight is due to a higher degree of rearrangement of pigment and binder particles upon the drying of the coating. In a thicker coating layer the particles will have more space to rearrange and will therefore form a more closely packed structure.

Experimental data for a comparable hard latex SA binder (also $T_g = 23$ °C) and the very same bcGCC pigment (compare hard latex discussion in 6.2) showed a porosity of 23.5 % for 8 w/w% binder. Extrapolating the experimental data of the tablet material to 10 w/w% latex would return a porosity of 22.2 %. These porosities indicate that, in case of the tablet forming, the pigment and binder particles can reach only a slightly higher degree of packing than in constrained layers, due to the further increased particle freedom.

When considering very thin coating layers on interacting substrates like porous papers, a direct comparison to tablet structures might not be valid. However, this is not a shortcoming of the tablet forming technique, but merely due to the fact that with a layer thickness of, say, < 10 μm, and pigment particles of 40 w/w% > 2 μm, the coating layer cannot be a representative porous structure especially when interacting with the substrate during consolidation, including regions of poor or absent coverage.

One can therefore say that the tablet material structures are indeed similar to high weight coatings in which the coating layer thicknesses are large compared to the internal pore structure.

2.4 Calculation of thermal conductivity

For modelling purposes the effective thermal conductivity k_{eff} will be used. It is calculated based on the density, measured by weight and volume of a tablet, as well as the tablet heat capacity:

$$k_{\text{eff}} = D_{\text{exp}} \cdot \rho_t \cdot c_t \quad (14)$$

The tablet specific heat capacity of the sample material (c_t) is calculated additively for the mass share of the two phases using the specific heat capacities of pigment (c_{s1}) and binder (c_{s2}):

$$m_{\text{tot}} \cdot c_{\text{eff}} = m_{s1} \cdot c_{s1} + m_{s2} \cdot c_{s2} \quad (15.1)$$

The contribution of air in pores to the total heat capacity is neglected because of its very low mass compared to the solid phases. With $m_{\text{tot}} = m_{s1} + m_{s2}$ and $m_{s2} = \beta m_{s1}$, the effective specific heat capacity becomes:

$$c_{\text{eff}} = \frac{c_{s1} + \beta c_{s2}}{1 + \beta} \quad (15.2)$$

where β is the binder dosage in w/w%.

For the individual phases, literature values of $c_{s1} = 880 \text{ Jkg}^{-1}\text{K}^{-1}$ /42/ and $c_{s2} = 559.8 \text{ Jkg}^{-1}\text{K}^{-1}$ /43/ are used for calcium carbonate (pigment) and n-butyl styrene acrylate (binder), respectively.

2.5 Summary

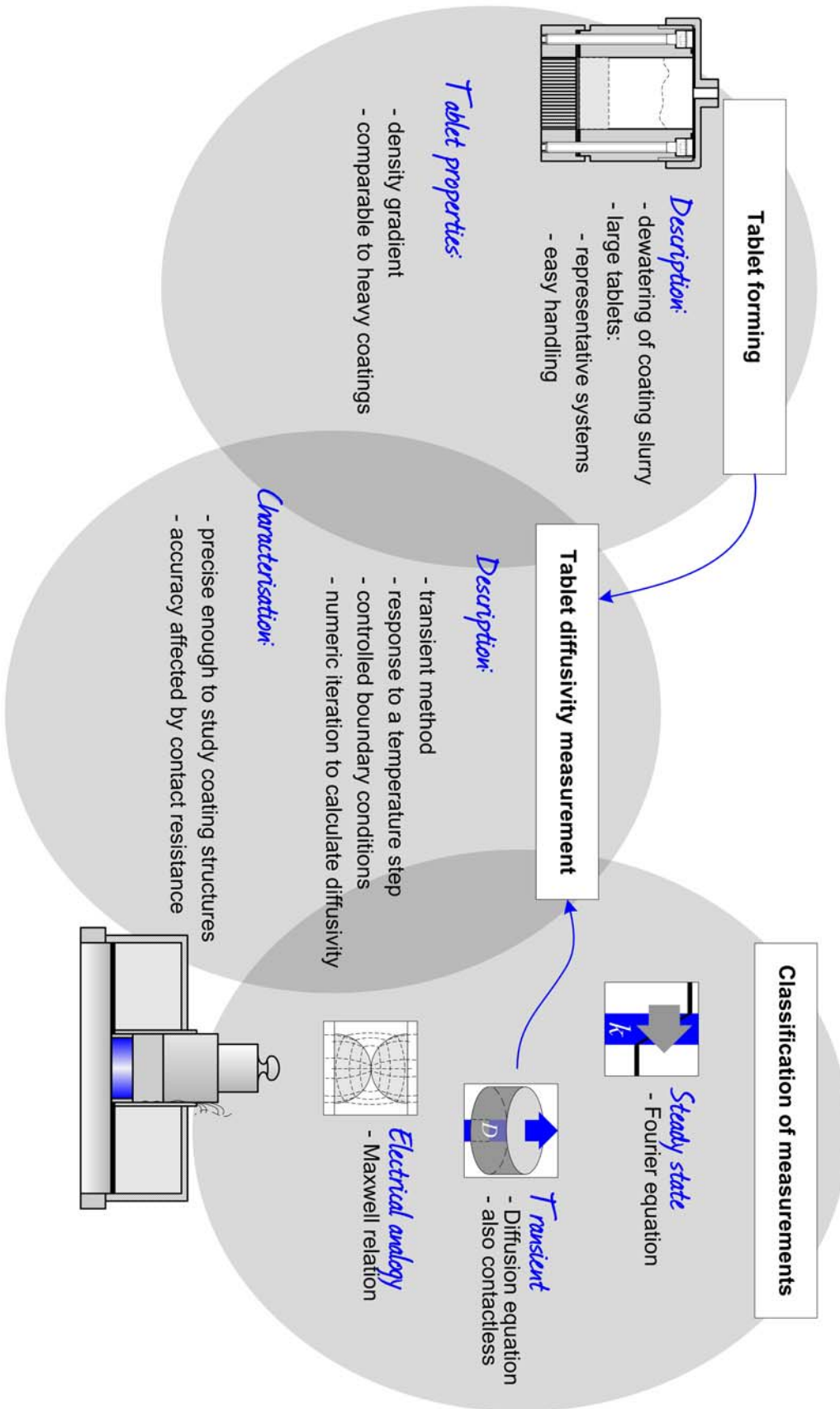
Different methodologies for the measurement of thermal conductivity and thermal diffusivity are reviewed and classified according to steady state methods and transient methods. Examples are given for the basic methodology but also for the practical application of these methods.

As a transient method for the measurement of thermal diffusivity, the tablet diffusivity technique is discussed in greater detail. While it brings several advantages, by using macroscopic sample material, the method is also shown to be precise as it is both repeatable and reproducible. The variation is small enough to allow the statement that heat conduction measurement is precise within the scope required to discuss different pigment/binder tablet materials and structures.

The accuracy of the heat conduction measurement is discussed by comparing measured values of standard materials to their literature values. It was found that there is a notable difference, and that the thermal contact resistivity at the interface of heating plate and specimen plays an important role in creating that difference. All measured thermal properties using this technique are, therefore, apparent values, which include the resistive property of the contact interface. However, this is not seen as a disadvantage provided the experimental thermal transfer process is taken into account for different interface configurations, as, for example, in the case of liquid saturated structures. Furthermore, contact thermal transfer in calendaring, printing and converting will also be dependent on the contact resistance, such that values obtained including it are highly relevant to the applications being considered.

The pigment/binder tablet material used for the measurements was shown to have a slight density gradient due to the forming technique, but the overall properties can be related well to the structures as found in heavy weight paper coatings.

2.6 Measurement thread



3 MODELLING OF THERMAL CONDUCTIVITY

3.1 Background

3.1.1 Modelling versus simulation

Since this work incorporates both modelling and simulation we separate the terms: “*simulation*” being used in the sense of “the imitative representation of the functioning of one system or process by means of the functioning of another”, whereas the term “*model*” relates to “a system of postulates, data and inferences presented as a mathematical description of an entity or state of affairs” /44/.

In this work, the term simulation is used for a Monte Carlo based particle deposition which creates quasi, two-dimensional coating structures (see 5.2.2). These simulated structures function as a master for the modelling of the thermal conductivity. The method itself is not a simulation of the thermal properties or the heat transfer properties of these structures, as opposed to part 7.3, where Finite Element Method simulations of the actual heat transfer in an electrophotography fusing nip are performed. Even though the simulation of heat transfer through porous materials is not the focus of the current work, there is a wide range of studies in this field to be noted. For example, Hunt and Gu /45/ created a two dimensional finite element structure of softwood with different porosities and different plant cell alignments. They simulated the heat flow through these structures in order to calculate their effective thermal conductivities. However, subsequently, Hunt *et al.* /46/ note that the use of such simulations is limited due to the lack of availability of the appropriate software. They, therefore, deduce a mathematical model to describe the finite element simulation results and this is also how modelling is interpreted in this work.

The term modelling, here, refers to the mathematical description of the thermal conductivity of porous media, performed predominantly using the Lumped Parameter Model. The following section gives an overview of early models for the effective thermal conductivity of porous media and elaborates on the Lumped Parameter Model in more detail.

3.1.2 Modelling of effective thermal conductivity

Nozad *et al.* /47/ discussed the theoretical governing equations for a general two-phase system and also extended it for the case of three phases /48/. They start with the general heat diffusion equation:

$$\rho c_p \frac{\partial T_i}{\partial t} = \nabla \cdot (k_i \nabla T_i) \quad (16)$$

in the volume V_i of the phase i , where i can be s_1 , s_2 and f in case of a porous multiphase system as shown in Figure 10, i.e. two solid phases, s_1 and s_2 , and a fluid, f . Furthermore the boundary conditions:

$$T_i = T_j \quad (17)$$

and

$$\vec{n}_{ij} \cdot k_i \nabla T_i = -\vec{n}_{ji} \cdot k_j \nabla T_j \quad (18)$$

apply at the phase boundaries A_{ij} where i and j are s_1 , s_2 and f with $i \neq j$ and \vec{n}_{ij} are the phase interface normal vectors as exemplified in Figure 10. Cheng and Hsu /49/ show

further that by applying a volume averaging process and assuming local thermal equilibrium as well as incompressible phases, equation 16 yields:

$$\nabla \cdot (k_m \nabla T) + \nabla \cdot \left[\frac{(k_i - k_j)}{V} \iint_{A_{ij}} T \vec{n}_{ij} ds \right] = 0 \quad (19)$$

for steady state heat conduction, where k_m is the volumetric average of the thermal conductivities and s is the interphase surface area. While the first part of equation 19 is the standard steady state heat conduction equation, the second term signifies the tortuosity effect, a term which takes the thermal path through the phase interface area A_{ij} of the porous structure into account.

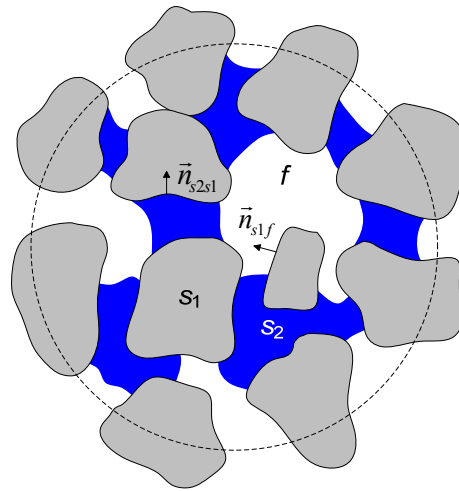


Figure 10. Porous multiphase system consisting of two solids, s_1 and s_2 , and a fluid, f . Adapted from /48/.

The closure of equation 19 for a two phase system and three phase system can be found in /47, 49/ and /48/, respectively. Both result in a term of the form:

$$\bar{\nabla} \cdot (\mathbf{K}_{\text{eff}} \cdot \bar{\nabla} T) = 0 \quad (20)$$

which is the standard heat conduction equation with an effective thermal conductivity tensor \mathbf{K}_{eff} . This equation can be seen as a basic law for heat conduction in porous media, showing that an effective thermal conductivity can be used. However, determining the effective properties often requires detailed knowledge of particle size, shape and location in the system /50/. The following discussion will focus on the mechanisms for effective thermal conductivities and available models.

Balakrishnan and Pei /51/ reviewed the heat transfer through gas-solid packed bed systems. Even though the focus of the review tends more towards the fluid flow related phenomena, they initially point out the six possible dominant modes of heat transport (illustrated in Figure 11):

1. convective heat transfer from the walls to the fluid
2. convective heat transfer from the particles to the fluid
3. conduction heat transfer from the walls to the particles
4. conduction heat transfer from particle to particle
5. radiant heat transfer
6. heat transfer by mixing

Although the authors point out that for many industrial applications two or more mechanisms may take place simultaneously and may also interact with each other, for given properties of the phases in a given temperature range, and so their impact might change significantly.

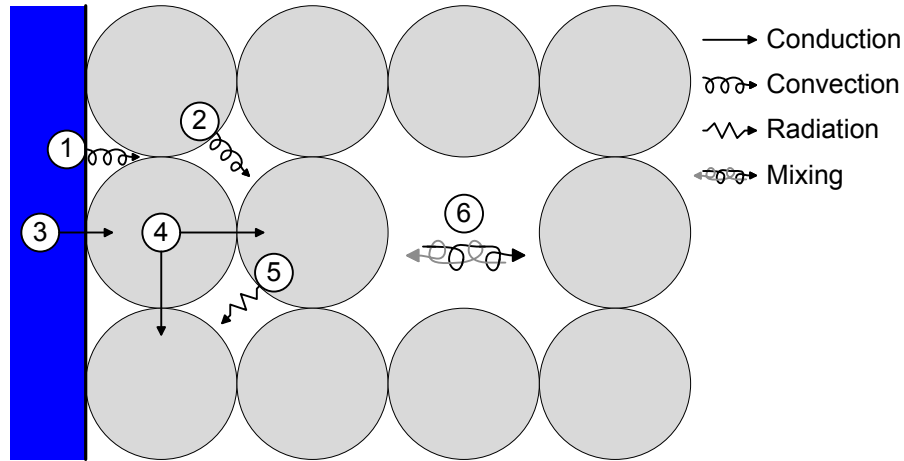


Figure 11. Theoretical heat transfer modes in packed beds. Adapted from /51/.

To summarise the different heat transport mechanisms, the thermal properties of porous multiphase systems are usually expressed in terms of “effective” properties for the whole system as if the porous medium can be regarded as homogeneous. This is based on the theoretical discussion above and is valid if the scale used to describe the effective thermal properties is large compared to the scale of the porous structure itself. Many theoretical models assume that the effective thermal conductivity of a porous medium k_{eff} can be defined additively by the convective transport mechanisms k_c (1. and 2.), by the conductive heat transport of the solids k_s (3. and 4.) as well as the by radiation (r) in pores (5.):

$$k_{\text{eff}} = k_c + k_s + k_r \quad (21)$$

whereas the heat transport mechanisms from the wall (1. and 3.) relate to the contact properties of the porous medium. Such an additive expression, however, would imply that these transport processes are taking place independently of each other. Therefore, Tsotsas and Martin /13/, refine the parameters determining the effective thermal conductivity of porous media and divide into primary and secondary effects. Primary effects are:

- a) thermal conductivity of the disperse or solid phases (k_s)
- b) thermal conductivity of the continuous or fluid phase (k_f)
- c) porosity, i.e. volume fractions of components (ϕ_i)
- d) spatial distribution of phases

In porous media where particles are in close contact to each other, the distinction between the continuous and discontinuous phase vanishes, but the connectivity of a single phase remains an important parameter as we shall see in 3.5.1. For isotropic media, or quasi-isotropic media in the scale of the analysis, the spatial distribution can be neglected. The secondary effects are:

- i. thermal transfer due to radiation (k_r)
- ii. thermal transfer due to convection (k_c)
- iii. thermal transfer by area contact of particles
- iv. particle shape and particle size distribution

MODELLING OF THERMAL CONDUCTIVITY

Classification of the models

Since the radiation energy is proportional to the fourth power of the temperature (Stefan's Law for black body radiation /14/), the thermal transfer by radiation depends highly on the temperature level itself. In many cases this effect can be neglected, and here this is the case since neighbouring particles are approaching very similar temperatures. In media where the pore size is on the scale of the mean free path of the gas molecules, the thermal conductivity of the gas becomes also a function of pore size. If the pore sizes are on a scale of less than 3 to 4 mm, free convection in the pores is considered to become negligible /28/. However, particle shape and size distribution play an important role. On the one hand, because the packing density depends strongly on the particulate shape characteristic and common porous media do not consist of ideally monodisperse particles, and on the other hand, because the particle area contact affects the connectivity of the whole.

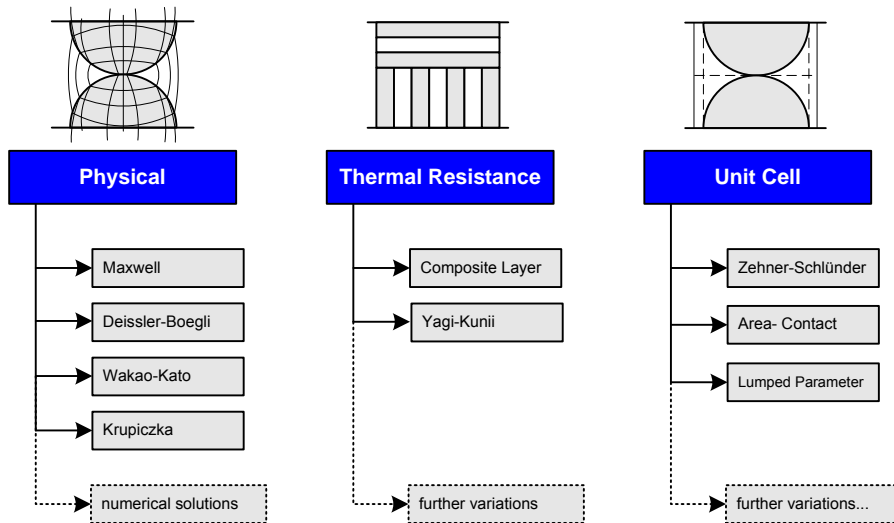


Figure 12. Overview of selected models for thermal conductivity of porous media. Models are grouped into analytical or numerical solutions of the heat diffusion equation, models using the concept of thermal resistance and models based on a unit cell.

The common aim of adopting any model is to describe the effective thermal conductivity as a function of the identifiable primary and secondary effects. One can separate the existing models into three groups according to their approach (Figure 12). The first group of models provides either an analytical or numerical solution of the heat diffusion equation. The second group follows the concept of thermal resistance, where the whole resistance is described as a combination of resistances for the different phases. The third group of models consists of different unit cells which represent the effective porous medium and thus construct the thermal properties directly from the combination of the geometrical equivalences. The following will briefly review selected models from each group.

3.2 Classification of the models

3.2.1 Solution of the Heat Diffusion Equation

The history of modelling the effective properties begins with Maxwell's (and independently also Lorenz' /52/) work on the conduction in heterogeneous media /29/. However, this model is based on the assumption that particles in a continuous medium are at "such distances from each other that their effects in disturbing the course of the current may be taken as independent of each other". In denser packed media this might not be the case, and the interaction at the phase interfaces needs to be taken into account. However,

by using relaxation methods, Deissler and Boegli /53/ created similar models for a cubic packing of spheres ($\phi = 0.476$), Wakao and Kato /54/ for orthorhombic packing ($\phi = 0.396$) and Krupiczka /55/ for a bundle of cylinders.

3.2.2 Thermal resistance models

One of the most common models in use is the composite layer model, also called Kriescher-Esdorn model /56/. It is one of the simplest models to describe heat transfer through porous structures by representing the structure of the porous medium in two extreme cases by an arrangement of either parallel or serial layers of liquid and solid. Figure 13 illustrates the two situations as well as the combination of both.

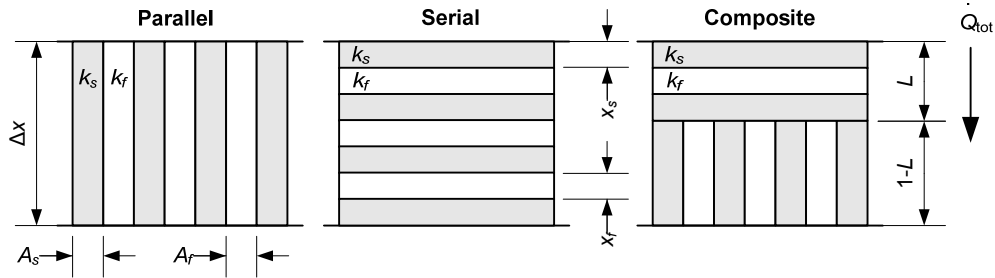


Figure 13. Arrangement of two phases in parallel, serial and composite layers. Adapted from /56/.

The parallel arrangement (heat flux \dot{Q}_{tot} is parallel to the layers) represents a maximum in thermal conductivity. The serial arrangement (heat flux is perpendicular to the layers) represents the minimum conductivity. The calculation is based on the concept of thermal resistance of each layer. As an example, the total heat flow through the parallel arrangement is the sum of the heat flows through each layer of area A_n :

$$\dot{Q}_{\text{tot}} = \sum_n \dot{Q}_n = \sum_n (k_n A_n) \frac{\Delta T}{\Delta x} \quad (22.1)$$

$$\dot{Q}_{\text{tot}} = \left(k_s \sum_n A_{s,n} + k_f \sum_n A_{f,n} \right) \frac{\Delta T}{\Delta x} \quad (22.2)$$

In order to get the effective thermal conductivity, the whole system can be described as the heat flow through a “wall” representing the end combination of the descriptions above:

$$\dot{Q}_{\text{tot}} = k_{\text{eff}} A_{\text{tot}} \frac{\Delta T}{\Delta x} \quad (23)$$

Keeping in mind that porosity is defined as the fraction of the fluid volume and that the same is to be assumed by the area fraction of the parallel arrangement:

$$\phi = \frac{V_f}{V_f + V_s} = \frac{\sum_n A_{f,n}}{A_{\text{tot}}} \quad (24)$$

One can combine equations 22 and 23 to get the effective thermal conductivity for the parallel arrangement:

$$k_{\text{eff, parallel}} = \phi k_f + (1 - \phi) k_s \quad (25)$$

Similarly, for different Δx_n of the layers, the equation of the serial arrangement can be derived:

$$\frac{1}{k_{\text{eff, serial}}} = \frac{\phi}{k_f} + \frac{1 - \phi}{k_s} \quad (26)$$

In a next step, those two extreme cases can be combined to the composite structure (also see Figure 13) in order to describe porous media better in practice. The parallel and serial share of the structure is weighted by a factor L , which is a material property and needs to be determined accordingly:

$$k_{\text{eff, tot}} = \frac{1}{\frac{1 - L}{k_{\text{eff, parallel}}} + \frac{L}{k_{\text{eff, serial}}}} \quad (27)$$

Another, but less commonly used version of the composite layer model was published by Yagi and Kunii /57/, which uses a parallel plate, which, in turn, holds perpendicular ribs. The heat conductivity is then adjusted by the thickness of the ribs.

3.2.3 Unit cell models

Zehner and Schlünder /58/ developed a model that included the effect of porosity and the form of particles in random particle beds (secondary effects iii. and iv.). They used a unit cell of cylindrical shape for their model. The outer part of the unit cell consists solely of fluid phase, whereas the inner part consists of both fluid and solid phases. Zehner and Schlünder derived the total effective thermal conductivity by integrating over the particle shape for the inner part of the unit cell:

$$\frac{k_{\text{eff}}}{k_f} = 1 - \sqrt{1 - \phi} + \frac{2(\sqrt{1 - \phi})}{1 - \frac{k_f}{k_s} B} \left[\frac{\left(1 - \frac{k_f}{k_s}\right)^B}{\left(1 - \frac{k_f}{k_s} B\right)^2} \ln\left(\frac{k_s}{k_f B}\right) - \frac{B + 1}{2} - \frac{B - 1}{1 - \frac{k_f}{k_s} B} \right] \quad (28)$$

The deformation factor B can be approximated by the relative volume fractions of the unit cell (equivalent to porosity), adopting a form factor, C , for the particles as follows:

$$B = C \left(\frac{1 - \phi}{\phi} \right)^m \quad (29)$$

with $m = 10/9$. The value of C was determined from existing literature for the shape of particles. They recommend form factors of $C = 1.25, 1.4, 2.5$ for spheres, broken particles and cylinders, respectively.

A drawback of the Zehner- Schlünder model is that for higher thermal conductivity ratios between solid and pore fluid, the thermal conductivity is predicted lower than the experimental data showed /59/. Hsu *et al.* /60/ therefore postulated that this is due to a lack of finite contact area in the Zehner- Schlünder model. For that reason they introduced another factor, α , which allows truncating the idealised particle sphere in addition to the deformation by factor B . This creates a finite contact area between the unit cells. Hsu *et al.*

/60/ show that this matches the experimental data better than the original Zehner-Schlünder model.

The Lumped Parameter Model introduced by Hsu *et al.* /61/ is another one belonging to the unit cell model category. The advantage of the original model is the easy use of porosity and a connectivity factor to describe the unit cell. This model will be further developed and discussed in more detail in the following part.

3.3 Introducing the Lumped Parameter Model (LPM)

The Lumped Parameter Model (LPM) introduced by Hsu *et al.* /61/, combines the thermal resistance approach with the unit cell approach. By working with a structural unit cell one can link the structure of the porous medium to the visual representation of the model. This is one main advantage of the LPM.

At first, a type of unit cell is defined having either a square or cylindrical central solid phase. This cell is then split up into layers of solid and fluid phase, so that the unit cell becomes a combination of serial and parallel thermal resistors. This approach allows the use of a contact parameter that describes the interconnection of solid phases of different unit cells. This is a second major advantage of the model which may be used to include the secondary effects like particle shape and contact area according to Tsotsas and Martin /13/ (see discussion in 3.1).

We now adapt this model (see Figure 14) using a square solid phase (k_{s1}), representing the pigment, and introduce a second solid phase (k_{s2}) for the connecting plates, representing the binder, the fluid phase being air when representing a dry medium or a chosen liquid when considering a saturated medium. The width of the binder bridge is c and can be related to the pigment size a as the contact parameter $\gamma = ca^{-1}$. The unit cell can be split up into three parallel layers (Figure 14, I.-III.), consisting of the relative combinations of solid phases and each solid phase with the fluid phase, respectively.

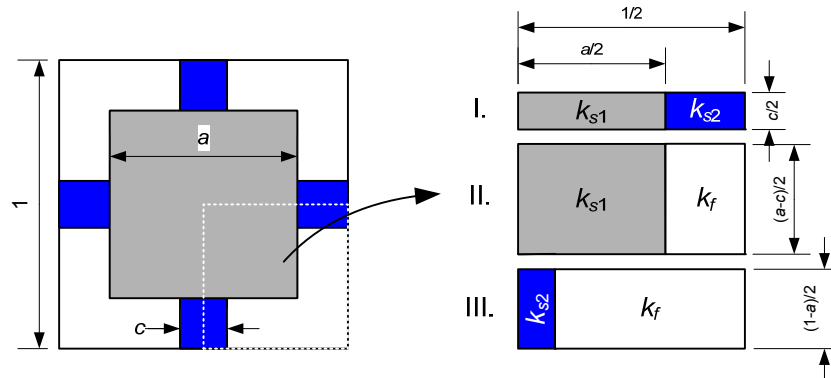


Figure 14. Modified three phase unit cell based on the lumped parameter model /61/ and its decomposition into serial and parallel layers (I.-III.) of thermal resistors. Based on paper [II], Figure 1.

The total thermal conductivity of a unit cell can be calculated using the analogy of thermal and electrical resistance, wherein the thermal resistance of a single phase within a layer of the unit cell is defined as:

$$R = \frac{\Delta x}{kA} \quad (30)$$

where, Δx is the length of the thermal resistor, k its thermal conductivity and A the area (or width in this two dimensional case) perpendicular to the heat flow. By combining the thermal resistance of each phase in each layer (analogous to electrical resistors), one gets the overall effective thermal conductivity of the unit cell:

$$\frac{k_{\text{eff}}}{k_f} = \frac{\gamma a}{(\lambda - \mu)a + \mu} + \frac{(1 - \gamma)a}{(\lambda - 1)a + 1} + \frac{1 - a}{(\mu - 1)\gamma a + 1} \quad (31)$$

where: k_{eff} is the effective thermal conductivity of the unit cell,
 k_f the thermal conductivity of the fluid phase,
 $\lambda = k_f/k_{s1}$ the conductivity ratio of the fluid phase to the pigment phase,
 and
 $\mu = k_f/k_{s2}$ the conductivity ratio of the fluid phase to the binder phase.

It has been shown /62/ that the uncertainty of a model often depends on the differences of the thermal conductivity of the phases involved. It is, therefore, common to give the model equations (see Zehner- Schlünder model equation 28) in the form of thermal conductivity ratios.

3.4 Discussion of the modelling parameters

When discussing properties of porous media it is common to use the porosity of the medium as the governing parameter. In Figure 14 it can be seen that the porosity of the unit cell is defined as:

$$\phi(a, c) = 1 + 2ac - 2c - a^2 \quad (32)$$

To use porosity as a parameter, Equation 32 needs to be converted to $c = f(a, \phi)$ or approximated (since nonlinear) to $a = g(c, \phi)$, where f and g are appropriate functions. This relationship means that neither a nor c are independent parameters but are mutually dependent, i.e. Equation 32 is not defined for all positive values of c as it does not cover the whole porosity range defined by the variable c alone. In practice this means that it is not possible to model a coating with a given average pigment particle size by setting the particle size parameter a as a constant and using only the binder amount (given by c or γ) to model porosity. For that reason it is better to use the latter and approximate a for a given porosity and contact parameter. It should be noted that the contact parameter itself affects porosity. Therefore, increase in the contact parameter leads not only to the assumption of more binder, but also to less pigment in the unit cell. Figure 15 shows that there is a maximum in thermal conductivity at a given porosity defined by an optimal contact value, such that if the contact parameter rises above this certain value thermal conductivity again drops. However, this theoretical curve is based on a constant porosity, which is not given in practice when increasing binder contents.

In the experimental data of a packing disruptive system, described later in respect to real coating colour structures as latex binder is added to pigment (4.3), we shall see a very similar trend of a maximum conductivity for a given connectivity of binder, but, in this case, additionally, structure dependent.

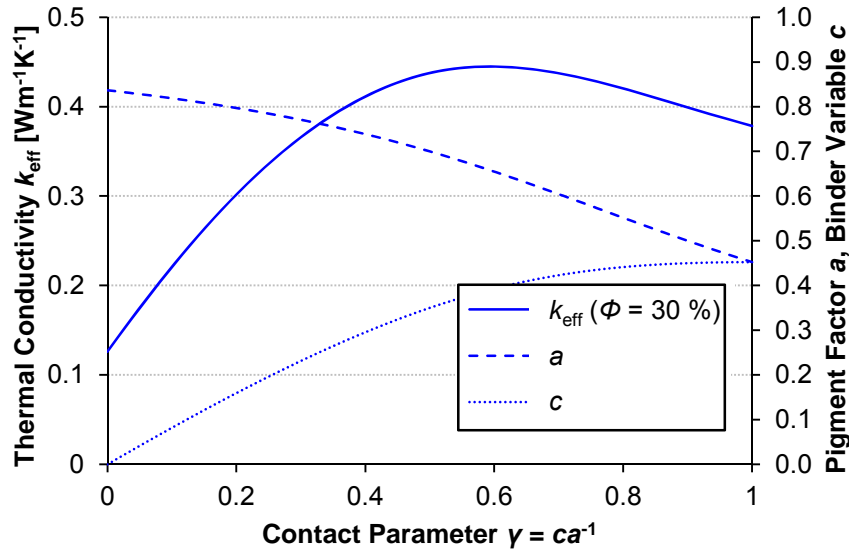


Figure 15. Thermal conductivity according to the Lumped Parameter Model for a constant unit cell porosity of 30 % as a function of the contact parameter γ of the two solid phases. The unit cell variables a and c are given for comparison. Based on paper [II], Figure 2.

The interconnection of the parameters porosity and two solid phase contact is a limitation of the model with respect to real coatings. It would be favourable to replace both porosity and contact parameter by a single parameter, like binder dosage. This enables us to change the binder amount c in a unit cell independently of the pigment particle size parameter a , and therefore allows for further increase of the contact beyond the pigment particle size ($\gamma > 1$). In this way, we enable a discussion of binder dosage at different dose stages, as will be illustrated in the following section. For a given pigment particle system, it is essentially the binder that affects porosity and contact parameter. However, the distribution of binder is currently assumed homogeneous, and this is frequently not the case. To model the effect of binder dosage, we would need to discuss its model equivalent in more detail, which, given the likely complexity, may not bring too much extra value to the results. Rather it will be illuminating to understand the role of binder amount and then to recognise that binder rich areas will behave differently from binder poor areas.

3.4.1 Grouped Lumped Parameter Model

The model should be able to cover the whole porosity range starting from a pure air unit cell to pure pigment as well as the whole range of possible binder dosages from no binder to coatings of pure binder. To overcome the limitations of equation 31, as discussed above, this is done by splitting up the lumped parameter model by defining three stages (see Figure 16), each depending on the amount of binder. For the binder amount, we choose the width of the connections c as a “running” variable for all stages.

In the first stage ($0 < c \leq a$), the pigment in the unit cell is first surrounded by air ($c = 0$). For increasing values of c , connectivity between unit cells and, therefore, thermal conductivity increase by the increasing width of the forming binder bridges. The limit is reached when the binder bridges equal the pigment particle size ($c = a$). This first stage is identical to the previous model:

MODELLING OF THERMAL CONDUCTIVITY

Discussion of the modelling parameters

$$\left(\frac{k_{\text{eff}}}{k_f} \right)_{0 < c \leq a} = \frac{c}{(\lambda - \mu)a + \mu} + \frac{a - c}{(\lambda - 1)a + 1} + \frac{1 - a}{(\mu - 1)c + 1} \quad (33.1)$$

In idealised non-disruptive media, increasing binder amount would continue to fill up the void spaces. This is done in the second stage ($a < c \leq 1$). The parameter c increases towards the size of the unit cell and replaces the remaining air in layer III (see Figure 14) by binder. The thermal conductivity increases further, by replacing the low conductive air with binder:

$$\left(\frac{k_{\text{eff}}}{k_f} \right)_{a < c \leq 1} = \frac{a}{(\lambda - \mu)a + \mu} + \frac{1 - a}{(\mu - 1)c + 1} \quad (33.2)$$

Note, that this replacement of air by binder can only affect layer III (Figure 14) of the unit cell because the model needs to remain decomposable into parallel and serial thermal resistors. For this reason, the unit cell in stage 2 ($a < c \leq 1$) becomes asymmetric. This is seen in the illustration of stage 2 in Figure 16. There is a horizontal binder bridge with constant size equal to the pigment width and a vertical binder bridge that increases with increasing c . This is no problem as many thermal resistance models are in fact asymmetric (see model introduction in 3.2), but it should be noted for the application of the model that the orientation of the unit cell in stage 2 matters. Furthermore, one needs to be aware that due to the use of c as a common running variable throughout the stages, it does not represent a binder bridge from this stage on.

The limit of stage 2 is reached when layer III of the unit cell is filled with binder and the unit cell becomes then nonporous. In practice, this occurs at the critical pigment volume concentration (CPVC). When continuing to increase the binder amount (stage 3), the share of pigment to binder in a unit cell decreases. Therefore, the difference of unit cell width and binder amount ($c - 1$) is used to lower the “effective” pigment particle size from a to \hat{a} , i.e. where $\hat{a} = a - (c - 1)$. Since binder has a lower thermal conductivity, the total conductivity decreases because of the increasing influence of binder:

$$\left(\frac{k_{\text{eff}}}{k_f} \right)_{1 < c \leq (1+a)} = \frac{1 + a - c}{\lambda(1 + a - c) + \mu(c - a)} + \frac{c - a}{\mu} \quad (33.3)$$

The limit is reached when the share of pigment to binder becomes infinitely small, i.e. unit cell consists of binder only:

$$\left(\frac{k_{\text{eff}}}{k_f} \right)_{c > (1+a)} = \frac{1}{\mu} \quad (33.4)$$

The LPM in all three stages combined shall be referred to as “grouped” Lumped Parameter Model.

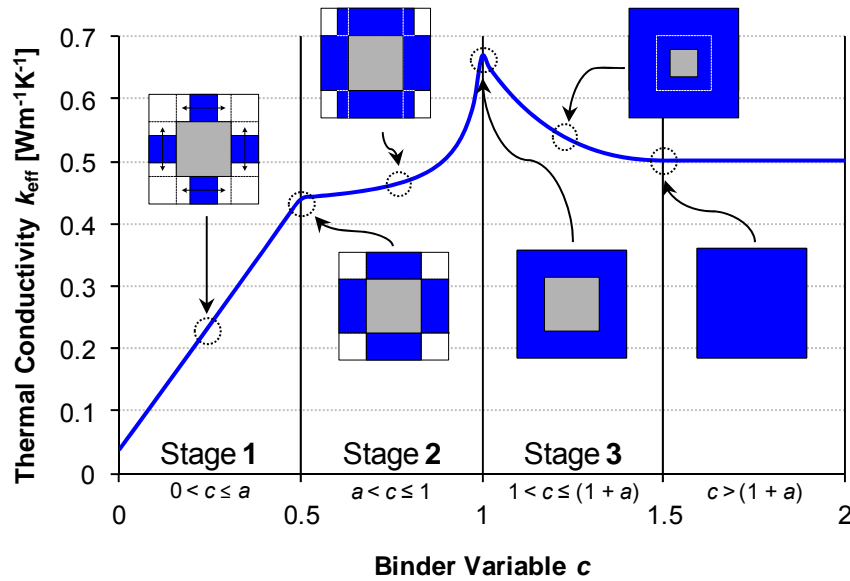


Figure 16. Three stages of the grouped Lumped Parameter Model. In stage 1 binder bridges form, in stage 2 porosity goes to zero and in stage 3 the share of binder to pigment increases. Based on paper [II], Figure 3.

3.4.2 The effect of intrinsic thermal conductivities

Figure 17 exemplifies the effect of the thermal conductivity of pigment on the modelled effective thermal conductivity of the grouped LPM unit cell as introduced in the previous section. The left graph shows the entire binder dosage range of the unit cell behaviour for three thermal conductivities of pigment. All data are given for a pigment factor of $a = 0.8$, which is an approximate value for the calcium carbonate structures used in the experimental part of this study (see discussions in chapters 4 and 5). The right side shows the effective thermal conductivity of what we shall call a “reference unit cell”, for a range of material values for the pigment, whilst keeping binder level and porosity constant. The reference unit cell in this graph is also defined for $a = 0.8$, having the binder variable chosen to be $c = 0.25$, again to exemplify a bcGCC system with a porosity of 26 %. The unit cell parameters of a and c for actual experimental structures are further discussed in sections 4.2, 4.3 and 5.3.

It can be seen in Figure 17 that for lower pigment thermal conductivities the slope in stage 1 (see Figure 16) of the effective thermal conductivity is lower. This leads to a lower level of thermal conductivity in stage 2, but the difference diminishes with higher doses of binder. For the reference unit cell we can see that the thermal conductivity of pigment has very little impact in the range of the material property used for calcium carbonate ($k_{s1} = 2.7 \text{ Wm}^{-1}\text{K}^{-1}$) and does not alter the effective thermal conductivity of the porous medium significantly when applying higher values.

MODELLING OF THERMAL CONDUCTIVITY

Discussion of the modelling parameters

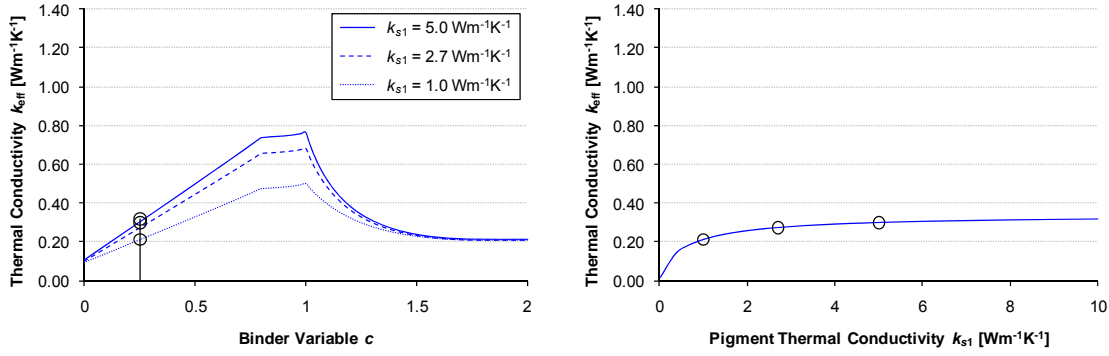


Figure 17. Left: effective thermal conductivity as a function of the unit cell binder variable for different thermal conductivities of the pigment phase. Right: reference unit cell showing the effect of pigment conductivity at constant binder and porosity levels. In both cases, the fixed parameters are $a = 0.8$, $k_{s2} = 0.21$ Wm⁻¹K⁻¹ and $k_f = 0.025$ Wm⁻¹K⁻¹.

In contrast to the material property of the pigment, the binder conductivity has a much greater effect, since it acts as the connecting material. Figure 18 illustrates that a different thermal conductivity of binder leads to a distinctly different level of the effective thermal conductivity of a unit cell in all stages of binder addition. This is to be kept in mind, especially when discussing the parameter fitting approach of the model (3.7.1) in chapter 4. It should be noted, though, that the thermal conductivities of binder in Figure 18 depict a rather wide interval, ranging broader than might be expected in practice. For example, the latex binders chosen in this work have a thermal conductivity of 0.21 Wm⁻¹K⁻¹ and 0.25 Wm⁻¹K⁻¹ for the SA and SB latices, respectively.

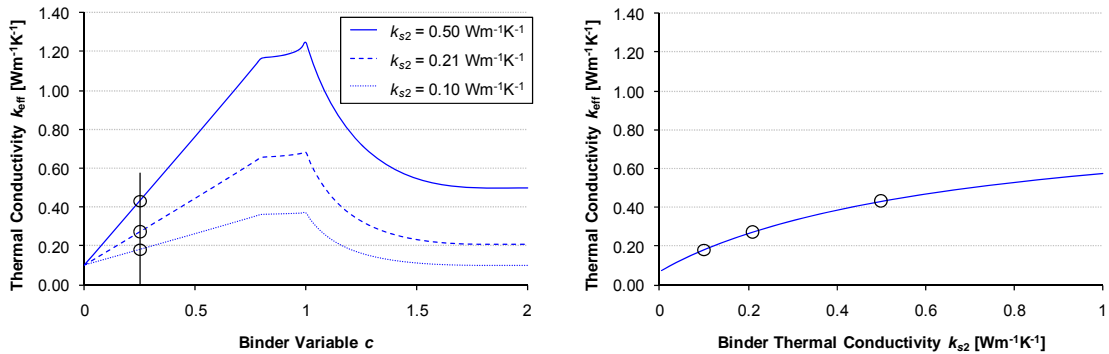


Figure 18. Left: effective thermal conductivity as a function of the unit cell binder variable for different thermal conductivities of the binder phase. Right: reference unit cell showing the effect of binder conductivity at constant pigment and porosity levels. In both cases, the fixed parameters are $a = 0.8$, $k_{s1} = 2.7$ Wm⁻¹K⁻¹ and $k_f = 0.025$ Wm⁻¹K⁻¹.

A strong effect can also be seen for the fluid phase in Figure 19. It shows the effective thermal conductivities for an air filled unit cell as well as for mineral oil and water filled unit cells, both of which are typical liquids present in the standard offset printing process. The corresponding thermal conductivities of the fluids are listed in Table 12. The influence of the fluid is of course dependent on the amount of fluid in a unit cell, and therefore most significant in stage 1, where a sufficient fluid volume fraction is present to manifest its effect. For $a = 0.8$, stage 1 in Figure 19, the cell represents fluid volume fractions from 36 % ($c = 0$) down to 4 % ($c = 0.8$). Even for the reference unit cell, with an available fluid volume fraction of 26 %, the effective thermal conductivity of the unit cell almost doubles for oil and quadruples for water, compared with air.

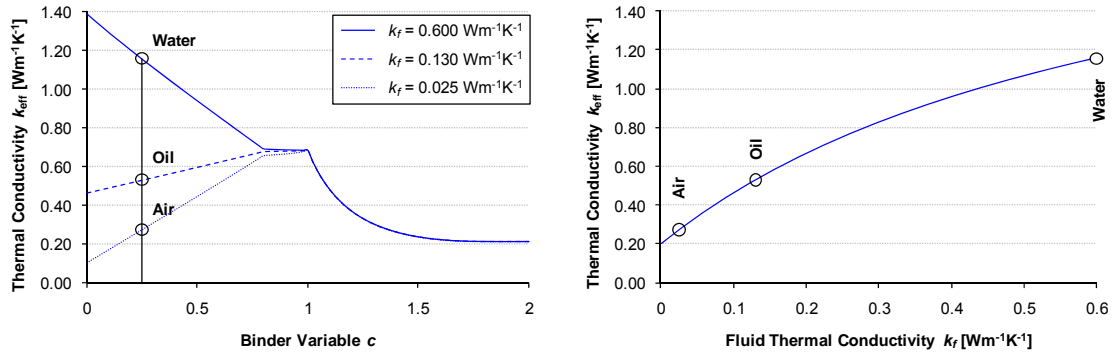


Figure 19. Left: effective thermal conductivity as a function of the unit cell binder variable for thermal conductivities of the fluid phase ranging from air to mineral oil and water (increasing). Right: reference unit cell holding the parameters for pigment, binder and porosity level constant. Fixed parameters in both cases are $a = 0.8$, $k_{s1} = 2.7 \text{ Wm}^{-1}\text{K}^{-1}$ and $k_{s2} = 0.21 \text{ Wm}^{-1}\text{K}^{-1}$.

Figure 17 through Figure 19 illustrate the qualitative effect of the intrinsic thermal conductivities of the materials for the given structural representation in an LPM unit cell. This information will help in further discussions of the unit cell parameters and the relevance of the material properties, and deviations in practice from the idealised non-interacting structural relationship of pigment and binder discussed so far, will become highlighted.

3.5 Alternate model configurations

3.5.1 Pigment surface connectivity

In the original approach of the Lumped Parameter Model, connectivity is restricted to the role of the binder phase alone. If no or little binder is present, there are no connecting bridges to take account of any connectivity provided by pigment-pigment contact. Real pigment particles are usually irregularly shaped, and, in the cases studied here, have a layer of adsorbed dispersant polymer (polyacrylate) on their surface. Both factors can effectively create a pigment-pigment interface, or pigment connectivity. This was discussed in the general considerations of models in 3.1 as mode 4 of heat transfer.

The absence of any means to connect the unit cells of binder free systems can lead, as we shall see in the discussion in chapter 5, to an underestimation of thermal conductivity compared to real systems. We therefore introduce “pigment bridges” to connect the unit cells instead of, or in addition to, the binder bridges. Equation 33, for stage 1 of the model, then extends to:

$$\frac{k_{\text{eff}}}{k_f} = \frac{c'}{\lambda} + \frac{c}{(\lambda - \mu)a' + \mu} + \frac{a' - c' - c}{(\lambda - 1)a' + 1} + \frac{1 - a'}{(\lambda - 1)c' + (\mu - 1)c + 1} \quad (34)$$

where c' is the new pigment connectivity and a' is the corrected pigment factor.

Furthermore, the definition of unit cell porosity (equation 32) changes to:

$$\phi(a', c') = 1 + 2a'(c' + c) - 2(c' + c) - a'^2 \quad (35)$$

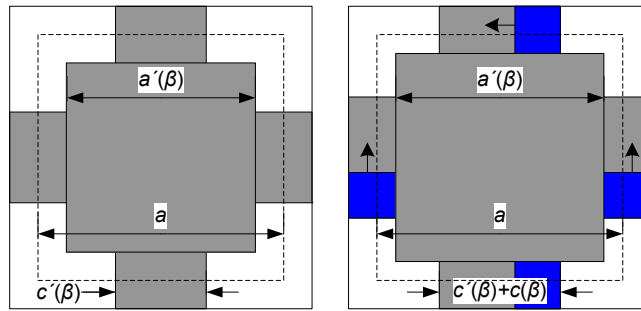


Figure 20. Left: corrected pigment factor a' and new pigment connectivity variable c' . Right: Addition of binder connectivity c to pigment connectivity c' . Based on paper [IV], Figure 17.

3.5.2 2D equivalent porosity

It is clear that there are fundamental differences between a three dimensional pore volume fraction, i.e. the porosity of a material structure, and the two dimensional void area fraction, i.e. the porosity in a cross-sectional representation of that structure. Gane *et al.* /40/ showed the non-trivial topological relationship of the three dimensional pore volume as measured by mercury intrusion curves and the two dimensional projected void area fractions as observed in cross-sectional SEM images for the special case of pigment-latex coatings, where it could be shown that the structures at different latex doses can be considered homeomorphic.

It is possible to expand the two dimensional unit cell of the LPM to a three dimensional one. This approach was already described in the original paper by Hsu *et al.* /61/ and it can be applied to the modified version as well. The central pigment phase is then surrounded by six binder bridges, which in turn define the porosity of the three dimensional system analogue to the two dimensional one given in equation 32:

$$\phi_{3D}(a, c) = 1 + 3ac^2 - 3c^2 - a^3 \tag{36}$$

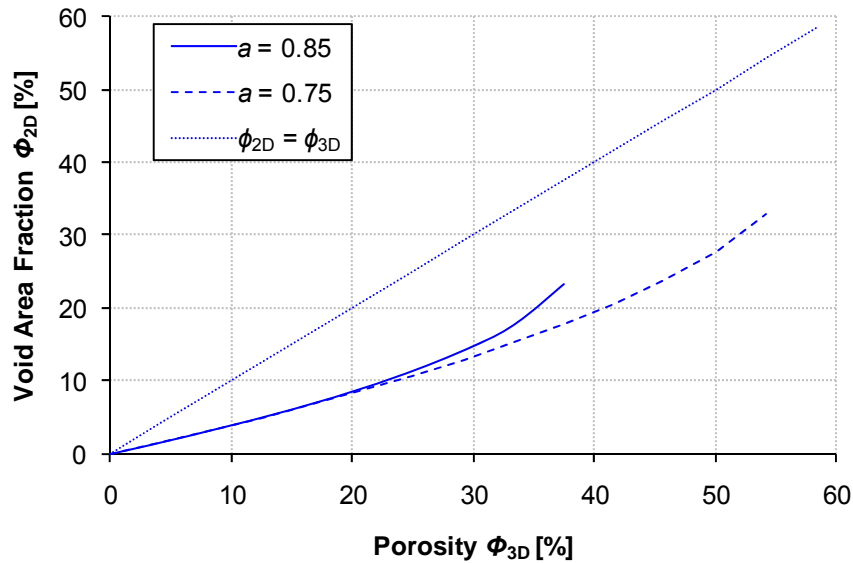


Figure 21. Nonlinear relationship between 3D pore volume fraction and 2D void area fraction in the case of LPM unit cells with $a = 0.75$ and 0.85 .

Figure 22 exemplifies equivalent unit cells for both 3D and 2D cells with porosities of 46 % and 28 %, respectively. The 2D unit cell, using the very same model parameters as in the 3D case, therefore representing a “cross-section”, shows a significantly lower porosity when represented directly as the area fraction. However, vice versa, it means that, when trying to express the porosity of a three dimensional structure by building the 3D value into a two dimensional unit cell, the effective pore volume will be overestimated. This difference will have to be examined further when applying the model either to measurement data (using parameter modelling) or to coating structures (adopting structural modelling). The two different modelling approaches will be introduced in 5.6.

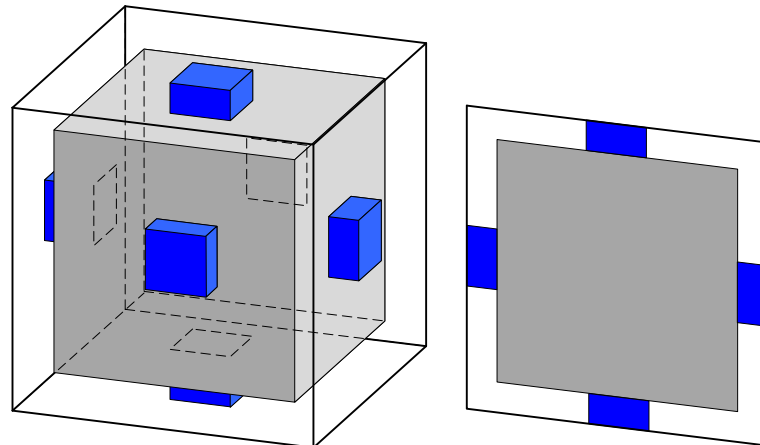


Figure 22. Comparison of a three dimensional LPM unit cell and its two dimensional equivalent. Unit cell parameters are $a = 0.8$, $c = 0.2$ and $c' = 0$.

3.5.3 Skeletal modes

Besides the effect of the intrinsic material properties as described in 3.4.2, the effective thermal conductivity of a unit cell will also depend on its skeletal structure, i.e. the configuration of the phases. We shall call this the unit cell mode. So far, the discussion has focused on unit cells based on a central pigment phase and connecting binder bridges (mode I). In addition to this configuration, five further theoretical unit cell modes are

possible. The volume fractions (area fractions in 2D) of the components of a unit cell are defined by:

$$\phi_1 = a^2 \quad (37.1)$$

$$\phi_2 = 2c(1 - a) \quad (37.2)$$

$$\phi_3 = 1 + 2c(a - 1) - a^2 \quad (37.3)$$

where ϕ_1 is the volume fraction of the central phase, ϕ_2 of the bridge phase and ϕ_3 of the corners (see Figure 23).

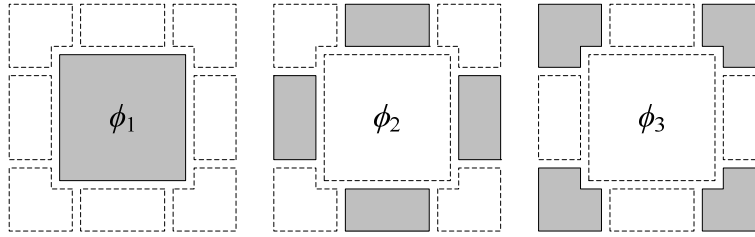


Figure 23. Components of a unit cell with ϕ_1 being the central phase, ϕ_2 the bridge phase and ϕ_3 the corners.

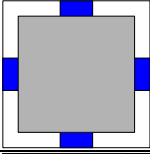
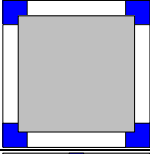
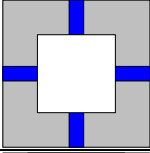
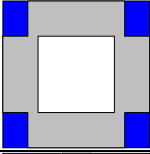
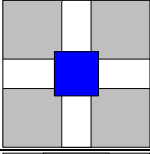
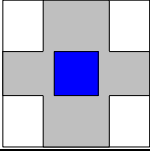
For the materials, the pigment volume fraction for the binder dosage β is defined by the porosity and the density ratio of solids by:

$$\phi_{s1} = \frac{1 - \phi_f}{1 + \beta \frac{\rho_{s1}}{\rho_{s2}}} \quad (38)$$

By assigning the volume fractions of the materials to the volume fractions of a unit cell in each mode (see mode column in Table 4) it is possible to calculate the effective thermal conductivities using equations 33.n. The conductivity ratios of λ and μ , required for equations 33.n, will change as well. The new material fractions for each of the modes are listed in Table 4. It should be noted that for the modes IV and VI, $c > a$ means that the unit cell is in stage 2 of binder filling, as discussed in 3.4.1. This is not due to the unit cell mode itself, but because of the given pigment volume fraction in the depicted example.

Figure 24 shows the effective thermal conductivities for equivalent unit cells of each mode. It can be seen that for the given porosity and binder concentration, modes III and IV deliver the highest thermal conductivity. These are the inverse skeletal structures of mode I and II. The pore volume is represented by the central phase, whereas both pigment and binder have a connecting function. For this reason, binder addition will have a distinctly different effect on the effective thermal conductivity. This shall be discussed in further detail and in comparison with experimental results in section 5.6.

Table 4. Parameters for the modes of the Lumped Parameter Model equations 33.n. The left side of the equation is denoted as ξ . The unit cells are shown for a porosity of 28 % and a binder content of 6 w/w%. * Modes IV and VI are in stage 2 of the model definition.

Mode	Unit Cell	ξ	λ	μ
I $\phi_1 = \phi_{s1}$ $\phi_2 = \phi_{s2}$		$\frac{k_{\text{eff}}}{k_f}$	$\frac{k_f}{k_{s1}}$	$\frac{k_f}{k_{s2}}$
II $\phi_1 = \phi_{s1}$ $\phi_2 = \phi_f$		$\frac{k_{\text{eff}}}{k_{s2}}$	$\frac{k_{s2}}{k_{s1}}$	$\frac{k_{s2}}{k_f}$
III $\phi_1 = \phi_f$ $\phi_2 = \phi_{s2}$		$\frac{k_{\text{eff}}}{k_{s1}}$	$\frac{k_{s1}}{k_f}$	$\frac{k_{s1}}{k_{s2}}$
IV* $\phi_1 = \phi_f$ $\phi_2 = \phi_{s2}$		$\frac{k_{\text{eff}}}{k_{s2}}$	$\frac{k_{s2}}{k_f}$	$\frac{k_{s2}}{k_{s1}}$
V $\phi_1 = \phi_{s2}$ $\phi_2 = \phi_{s1}$		$\frac{k_{\text{eff}}}{k_{s1}}$	$\frac{k_{s1}}{k_{s2}}$	$\frac{k_{s1}}{k_f}$
VI* $\phi_1 = \phi_{s2}$ $\phi_2 = \phi_{s1}$		$\frac{k_{\text{eff}}}{k_f}$	$\frac{k_f}{k_{s2}}$	$\frac{k_f}{k_{s1}}$

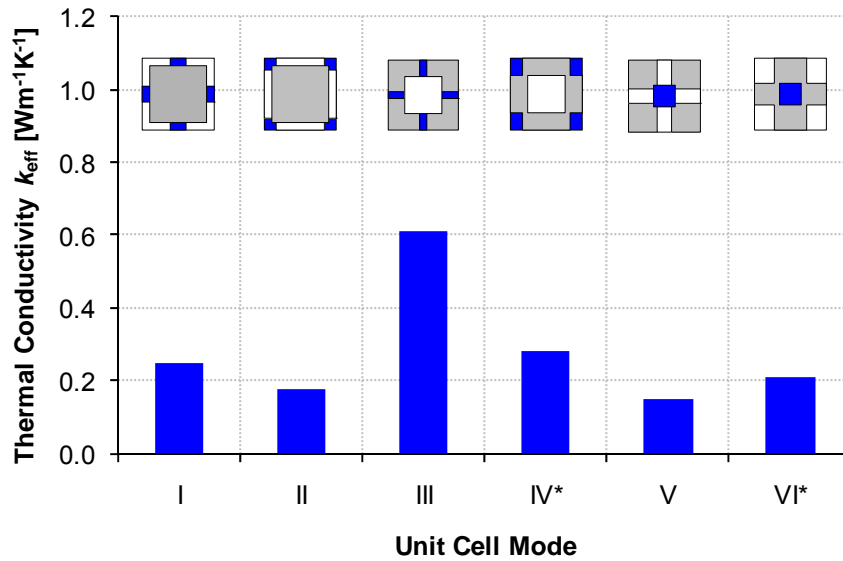


Figure 24. Effective thermal conductivities for different modes of the LPM. All data are based on a theoretical porosity of 28 % and a binder content of 6 w/w%.

3.6 Model comparison: Lumped Parameter and Composite-Layer

The Composite-Layer Model (CLM) as introduced in 3.2.2 describes the porous medium as a simple arrangement of serial or parallel layers of thermal resistors of solid and fluid phase. This was shown for two phases, but it can also be extended to include a second solid phase for binder (Figure 25).

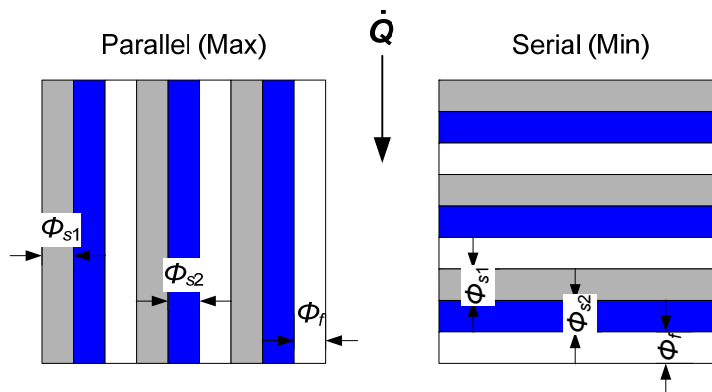


Figure 25. Composite layer model for a three phase porous medium. The left side illustrates the arrangement of thermal resistors parallel to the heat flow (maximum thermal conductivity). The right side shows the serial arrangement of thermal resistors (minimum effective thermal conductivity). Governing parameters of the model are the volume fractions of the phases. Based on paper [V], Figure 5.

By the use of volume fractions of the materials as governing parameters, the composite layer model allows calculation of the effective thermal conductivity. Where the purely parallel arrangement represents the maximum possible thermal conductivity $k_{\text{eff, parallel}}$ for given volume fractions ϕ of pigment (s_1) binder (s_2) and air (f):

$$k_{\text{eff, parallel}} = \phi_{s1}k_{s1} + \phi_{s2}k_{s2} + \phi_f k_f \quad (39)$$

The serial arrangement of thermal resistors describes the minimum possible thermal conductivity $k_{\text{eff, serial}}$:

$$\frac{1}{k_{\text{eff, serial}}} = \frac{\phi_{s1}}{k_{s1}} + \frac{\phi_{s2}}{k_{s2}} + \frac{\phi_f}{k_f} \quad (40)$$

A simple approximation of the maximum and minimum limits can, therefore, be reached, in which interval the thermal conductivity of a porous medium is to be expected, and by adjusting the share of parallel and serial heat conduction, the effective conductivity of the medium can be modelled. This was shown for different paper furnishes by Gu erin *et al.* /20/ or for drying of paper when moisture is present /63/. However, Gu erin *et al.* stated that while it is possible to model the thermal conductivity of different pulps, it is not possible to model the thermal conductivity of paper coatings to sufficient precision.

For the LPM unit cell, the pigment variable a is given by the square root of relative pigment volume (compare equation 37.1):

$$a = \sqrt{\phi_{s1}} \quad (41)$$

and the binder variable c can be calculated by the definition of the unit cell porosity, i.e the fluid volume fraction (see equation 32 or 37.3):

$$c = \frac{\phi_f - 1 + a^2}{2(a - 1)} \quad (42)$$

Equations 41 and 42 enable calculation of the effective thermal conductivity for the porous LPM unit cell using equation 33.1 ($c \leq a$). Figure 26 shows the model values for both the CLM and LPM, respectively. The modelled values are calculated for the measured porosities of the material and the volume fractions based on the density of pigment and binder.

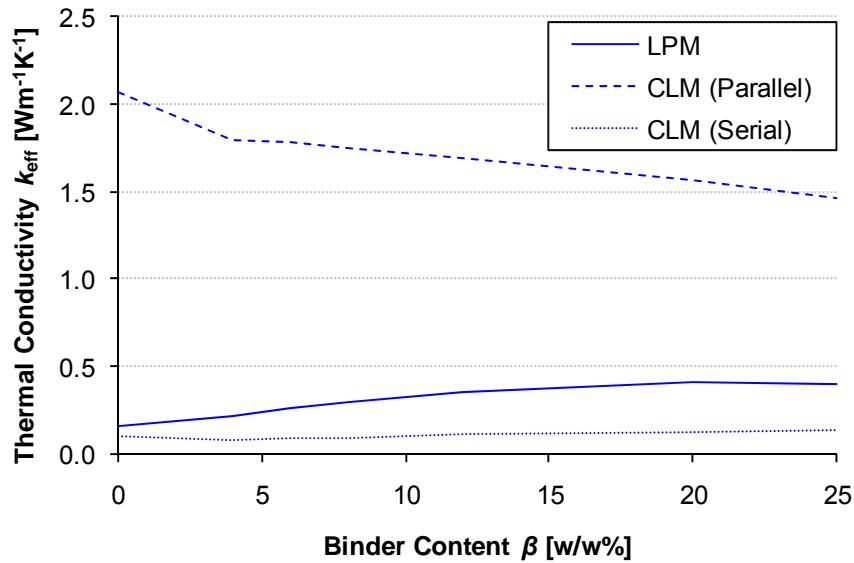


Figure 26. Comparison of the model extrema of the Composite Layer Model with values of the Lumped Parameter Model.

The easy calculation of the boundaries of the CLM in Figure 26 is an advantage of this approach. It allows a simple estimation of the effective thermal conductivity range that is to be expected. However, one can see that this range is rather large, and, as we shall discuss later when considering the experimental structures, they differ more than the experimentally observed material-dependent values. Because of the inter-link of modelling parameters and structural parameters, the LPM will be shown to come significantly closer to the experimental values, using the same given parameters of porosity and binder content.

3.7 Modelling approaches

As described earlier, in contrast to other models for effective thermal conductivity, the LPM unit cell is a simplified structural representation of a porous medium. Working with such a structural model, two modelling approaches readily present themselves. On the one hand, one can get the model structural parameters by fitting the model thermal conductivities to experimental data (parameter modelling). On the other hand, one can fit the unit cell structure to a given “template” or material structure (structural modelling). Figure 27 illustrates both approaches and points out their interrelation for comparison.

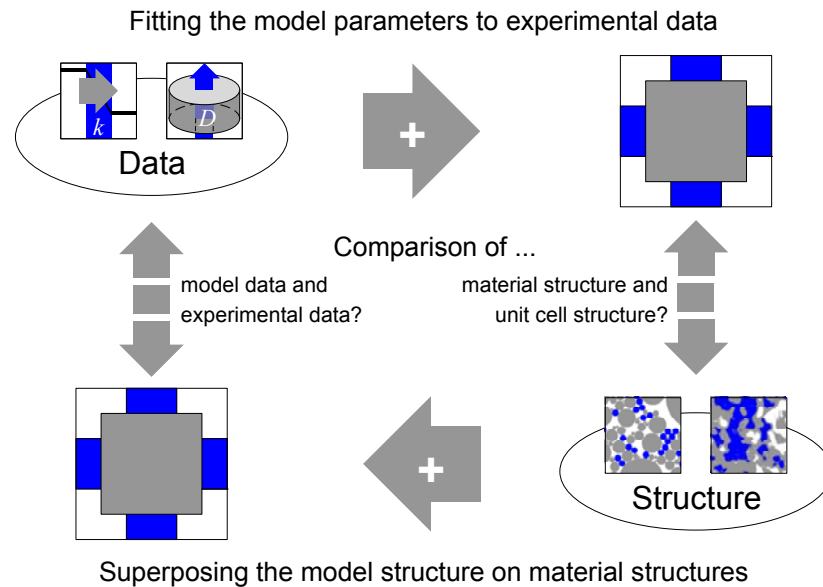


Figure 27. Approaches of modelling either experimental thermal conductivity data or structural data and their interaction.

3.7.1 Parameter modelling

Using the least squares fitting method, one can correlate the theoretical effective thermal conductivity curve of the model for a given pigment factor to the measured thermal conductivities. The binder variable becomes the resulting fitting parameter, and together they define a unit cell of the model that represents a certain two dimensional structure. This describes adequately the porous medium in terms of its thermal conductivity, but it may in fact differ from the actual porous medium. Examining the difference between the LPM construction, the values it delivers, and the actual measurable information regarding the medium itself, could reveal details regarding the structural formation and the role of the material factor(s) underlying the effective properties of the porous medium, e.g. effective pore network characteristics, such as nodal points, connectivity etc. This approach will be discussed in chapter 4 of this work.

3.7.2 Structural modelling

The structural modelling is based on the idea that the material fractions in a unit cell should equal the material fractions of a cross-section or a quasi-two dimensional representation of the medium. For pigment factor a , the equation 41 holds and the binder variable c can be deduced with equation 42. The effective thermal conductivity of a unit cell using these structural parameters is compared to the measured property. The structural fitting approach will be discussed in chapter 5.

3.7.3 Connectivity modelling

While in parameter modelling the unit cell parameters are adapted to fit the thermal conductivity data and in structural modelling the unit cell structures are fitted to match a cross-sectional structure, connectivity modelling can be seen as a combination of both. In connectivity modelling the alternate unit cell configuration including pigment connectivity (see 3.5.1) is used to match both the thermal conductivity data and cross-sectional structures. This results in a description of pigment and binder connectivity (Figure 28) that can be used as a tool in assessing the role of the phase properties in chapter 6.

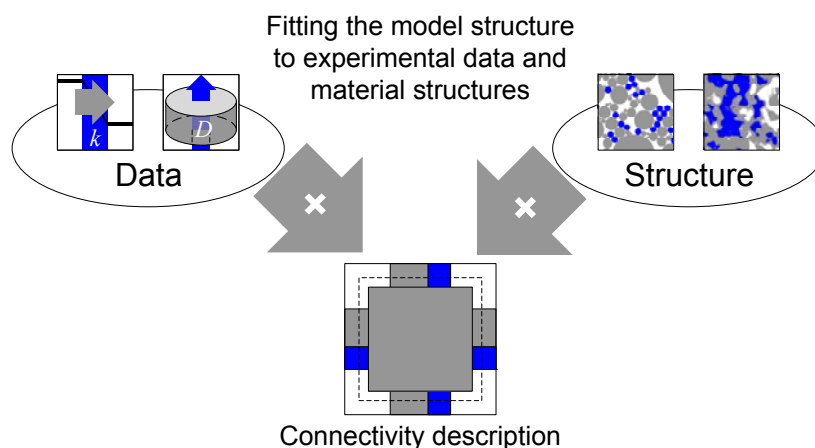


Figure 28. Connectivity modelling by fitting the model unit cell to both the experimental data and the material structure.

3.8 Summary

General considerations for modelling by using effective thermal conductivities have been presented, and various examples of such models for porous media or packed beds have been introduced and discussed. Special attention was paid to the Composite-Layer Model, to illustrate its simplicity and to demonstrate that it has certain drawbacks, although in some fields it remains a widely used model.

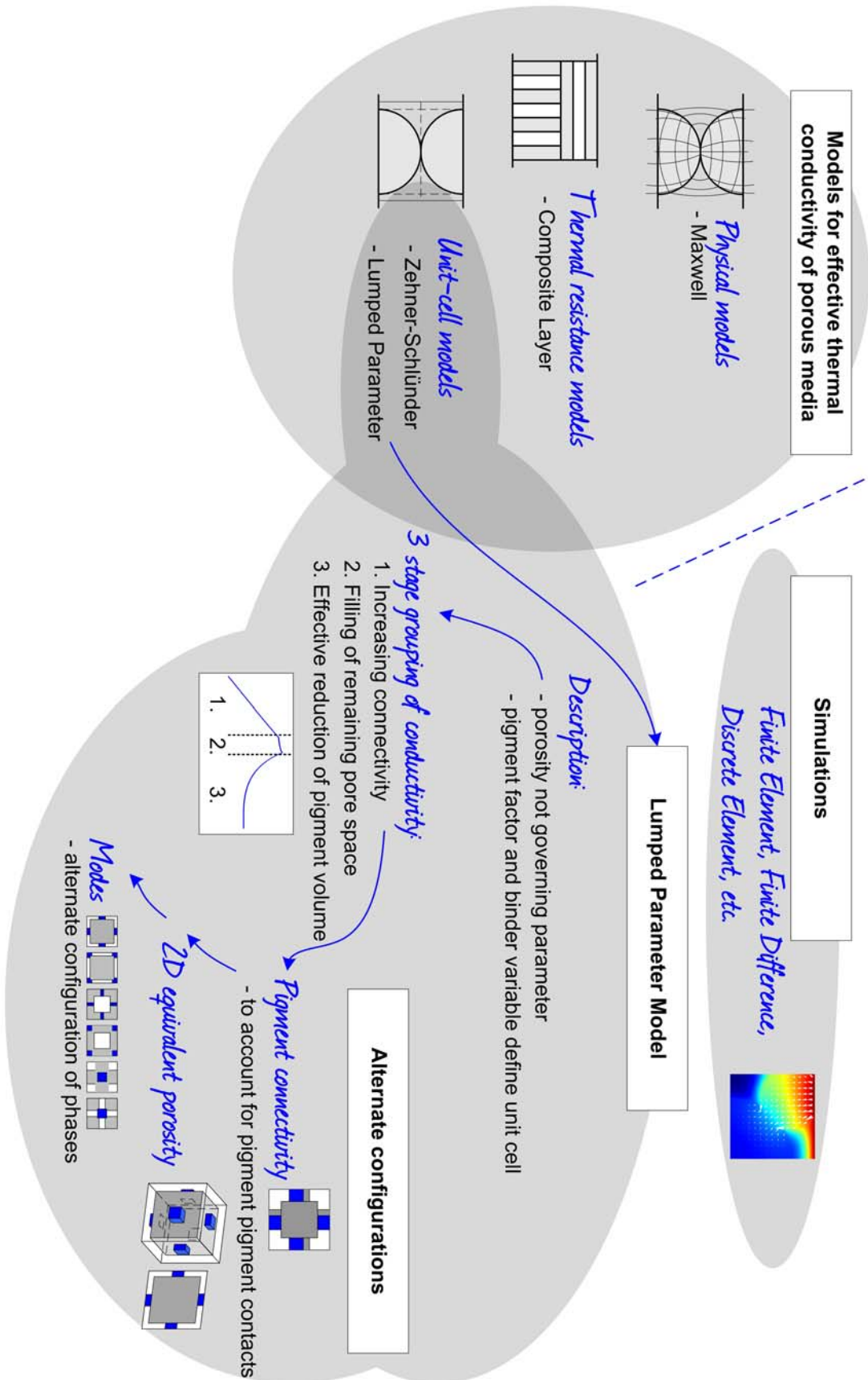
A modified Lumped Parameter Model (LPM) was proposed as providing a conceptually good option within the category of unit cell models, and discussed in detail in respect to the individual material parameters and proportions in relation to porosity and volume fractions of the components. The model adopts a unit cell resembling the structure of simple porous media. In its initial form it includes a central pigment phase and, in our case, the binder phase forming connecting “bridges”. The model distinguishes between three stages of binder dosage in relation to pigment amount. Initial discussion of the parameters of the model suggested that it is favourable to use the binder variable and a pigment volume fraction factor together instead of porosity as the governing parameter. In addition, the modelling parameters and the material parameters of the three phases, solid, binder and fluid, were discussed. It was seen that, because of its connecting function, the material property of binder can have a distinct impact on the total effective thermal conductivity, as does the change of fluid from air to typical liquids, as are found in printing processes.

In light of the fact that the model connectivity is merely provided by binder, it was recognised that, especially in cases of low or zero binder content, thermal conductivity would be grossly underestimated or zero, respectively. Therefore, additional pigment connectivity was included in an alternate model description of the unit cell, to account for the pigment to pigment heat conduction mode provided for by particle irregularities and adsorbed dispersant polymer acting similarly to the binder phase. Furthermore, the direct use of a 2D equivalent porosity was suggested to account for the fundamental difference of the three dimensional pore volume versus the two dimensional void area fraction. Different configurations of the materials constituting a unit cell showed that the skeletal structure, i.e. its mode, affects the effective thermal conductivity. This shall be discussed further in comparison with experimental results.

A comparison between the traditional Composite-Layer Model (CLM) and the LPM showed that the maximum and minimum conductivity boundaries of the CLM are rather wide and, so, likely to fail to capture the subtleties underlying effective thermal

conductivities in a pigment binder system. Using the same given volume fractions the LPM was considered to provide the opportunity to come much closer to the actual thermal conductivities, because of the structural description provided by its unit cell. Further, it was considered, that, because of the structural representation of the LPM, two different modelling approaches, that of parameter modelling and structural modelling, respectively, present themselves as being applicable depending on whether one starts from a combination of compositional and measured property data, or from compositional and structural information. Both modelling approaches in combination can be used to assess the connectivity of pigment binder systems. The following part II of this work will include these approaches as applied to practical coatings.

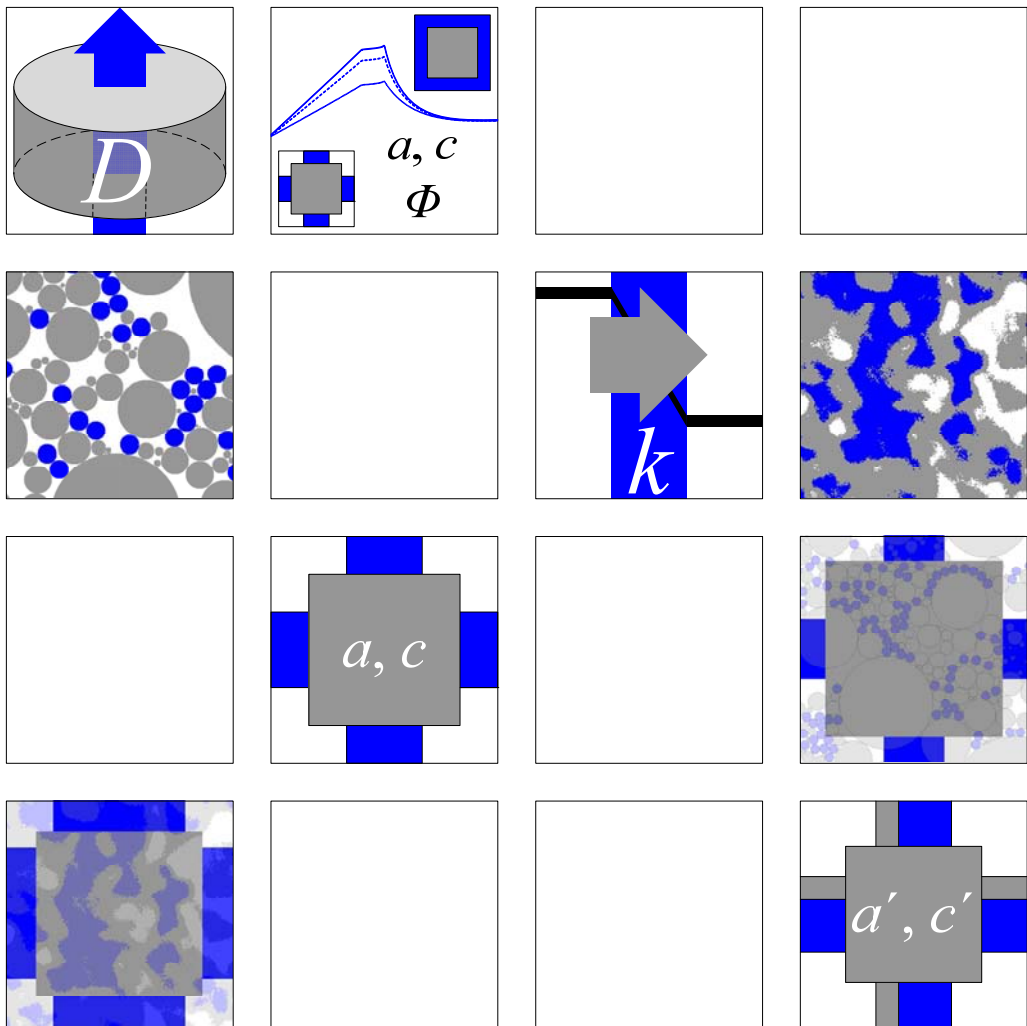
3.9 Modelling thread



PART

II

BASIC RESEARCH LEVEL



“Basic research is what I'm doing when I don't know what I'm doing.”

Wernher von Braun,
German Engineer, 1912-1977

4 APPLICATION OF THE MODEL TO THERMAL CONDUCTIVITY

4.1 Background

One motivation for the use of the independent structural binder dosage variable c and the pigment variable a in the grouped Lumped Parameter Model is to avoid the use of porosity as the governing parameter. This is, on the one hand, because the term binder dosage is more tangible in terms of coating colour recipes, but, on the other hand, as we shall see in this chapter, because porosity alone is not sufficient to describe the thermal behaviour of such multiphase systems. This chapter takes a look at existing literature data of talcum pigment systems and newly measured thermal conductivities for a calcium carbonate pigment system adopting the tablet diffusivity measurement. They are classified as non-disruptive and disruptive, respectively, based on the following discussion regarding the effect of binder addition.

4.2 Non-disruptive system

4.2.1 Materials

Guérin *et al.* /20/ measured the thermal conductivity of thin talcum coatings with SB latex binder in dosages from 5 to 50 w/w% (see Table 5). They used a method measuring the temperature rise of a thermal mass through a sample pile. This method was introduced in 2.2.2 as being based on transient contact.

Table 5. Summary of particle data and thermophysical properties of the talcum pigment binder systems /20/.

Component:		
Latex	SB	SB
Dosages [w/w%]	5-50	5-50
Thermal conductivity [$\text{Wm}^{-1}\text{K}^{-1}$]	0.25	0.25
Specific heat capacity [$\text{Jkg}^{-1}\text{K}^{-1}$]	454.8	454.8
Pigment	Talcum 1	Talcum 4
Thermal conductivity [$\text{Wm}^{-1}\text{K}^{-1}$]	3.1	3.1
Composition:		
Talcum [%]	85	95-96
Chlorite [%]	13	4-5
Dolomite [%]	2	(magnesite)
d_{50} (weight median) [μm]	3.2	2.2

Table 6 lists the measured thermal conductivities as well as the porosities of two talcum pigment coatings. They were chosen from the measurement data available because of their high talcum content. Guérin *et al.* noted that the coatings with 25 w/w% binder are at the critical pigment particle volume concentration (CPVC). The remaining porosity for higher binder concentrations, as determined from density, was attributed to entrapped air bubbles in the coating slurry, which they reported could also be observed in cross-sectional microscopy images.

Table 6. Thermal conductivity and porosity of talcum model coating layers /20/.

Binder Content w/w%	Talcum 1		Talcum 4	
	Th. Cond. $Wm^{-1}K^{-1}$	Porosity %	Th. Cond. $Wm^{-1}K^{-1}$	Porosity %
5	0.56	37.0	0.48	32.0
10	0.62	28.5	0.56	22.0
15	0.68	19.5	0.58	12.0
20	0.65	8.0	0.65	13.0
25 ⁺	0.90	1.5	0.73	7.0
30*	0.72	4.0	0.78	11.0
50*	0.60	2.0	0.63	12.0

⁺CPVC

* remaining porosity attributed to entrapped air bubbles

Figure 29 shows the thermal conductivity as a function of porosity for the increasing binder dosage, exemplified for Talcum 1. If one regards the point with 20 w/w% binder as an outlier, one can see that the thermal conductivity increases quite linearly for reducing porosities below the CPVC. However, above the CPVC a different mechanism is affecting the effective thermal conductivity, and it is clear that it cannot be described by porosity or the binder dosage alone unless there would a structural relationship. The following section will, therefore, discuss the measurement data in relation to the LPM.

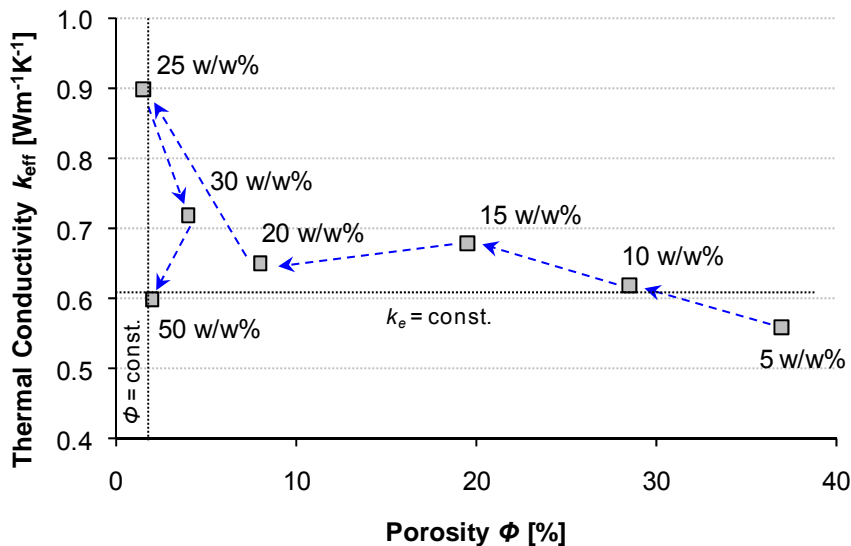


Figure 29. Thermal conductivity of Talcum 1 as a function of porosity. The labels and arrows indicate the increasing binder dosage.

4.2.2 Parameter modelling

In order to compare the thermal conductivity data of the measurement to the model, we need to find an empirical relationship of the physical binder dosage of the coating colour to the binder variable of the model. The CPVC refers to point $c = 1$ in the grouped Lumped Parameter Model definition (see 3.4.1). It signifies the point when the unit cell becomes non-porous. In the case of the talcum coatings this equals a binder dosage of 25 w/w%. We initially use a quadratic correlation between the binder variable c and the binder dosage β , the latter being given in w/w%:

$$c(\beta) = x_0 + x_1\beta + x_2\beta^2 \quad (43)$$

where $x_0 = 0.29$, $x_1 = 0.04$ and $x_2 = -5 \cdot 10^{-4}$. Figure 30 shows the experimental data obtained by Guérin *et al.* as well as the model prediction for pigment factors of $a = 0.75$, 0.80 and 0.85 .

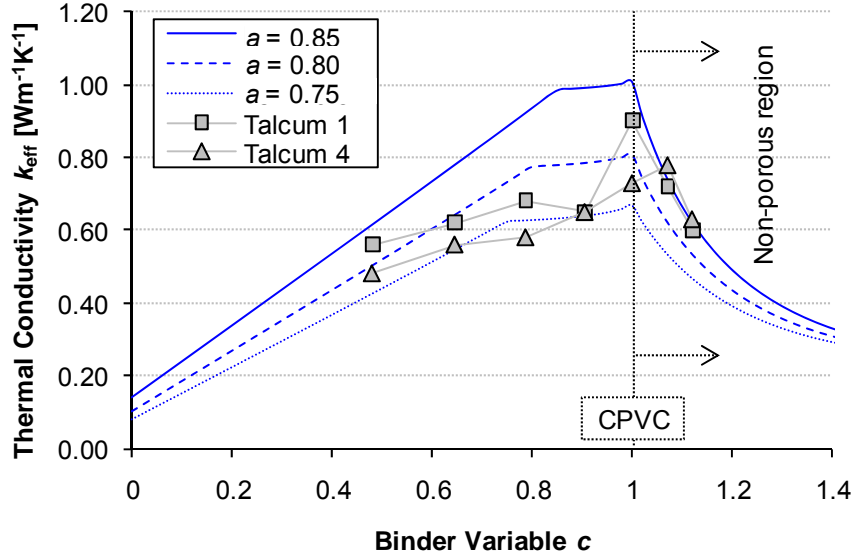


Figure 30. Thermal conductivity predicted by the model as a function of the binder variable c with $a = 0.75$, 0.80 and 0.85 . Thermal conductivities of the phases are $k_{s1} = 3.1$, $k_{s2} = 0.25$ and $k_f = 0.025 \text{ Wm}^{-1}\text{K}^{-1}$. Results by Guérin *et al.* /20/ for Talcum 1 and 4 are given for comparison. Based on paper [II], Figure 4.

Despite the simple assumption of a quadratic relation between c and binder dosage, the model solution fits the experimental data rather well. There might be some scattering of the results found in Guérin *et al.*, but it should also be kept in mind that the measurements were made for thin coating layers. One precondition for modelling of porous media is that the measured structure for the effective properties is large compared to the pore structure (see 3.1.2). The measurement of thin coating structures might, therefore, induce some errors due to boundary effects. Furthermore, given the plate-like crystal symmetry of talc particles, thin layer structures will inevitably be preferentially aligned along the basal planes of the particles. This is a cause for divergence from the cubic symmetry assumed by the model, and in practice would mean a different thermal conductivity across/through the coating from that in the plane of the coating. Additionally, at high binder dose levels, the spherical nature of a latex binder will disrupt the pigment alignment somewhat and lead to a change from highly aligned structures to less aligned more homogeneous/isotropic structures, during which the clearer transitions seen in the model will become smeared out. Nonetheless, the correspondence is promising.

4.2.3 Comparison of unit cell structure to material structure

The data given in Figure 30 allows the determination of a pigment factor a for each binder concentration of both talcum coatings (Table 7). Together with the given binder variable c this allows calculation of the unit cell void area fraction, i.e. 2D porosity ϕ_{UC} , (equation 32) that effectively represents the thermal conductivity. A comparison of these theoretical 2D unit cell porosities of the model and the measured coating porosities ϕ_C is shown in Figure 31. It can be seen that the correlation is quite linear even though for measured porosities $< 13\%$ one can observe a step where the entrained air bubbles lead to

a higher measured porosity at binder concentrations where the unit cells are perfectly non-porous. However, one can observe that, in general, the unit cell porosities underestimate the measured porosities. This is an interesting connection considering the theoretical relationship of 2D void area fraction and a 3D porosity discussed earlier in 3.5.2 and shown Figure 21.

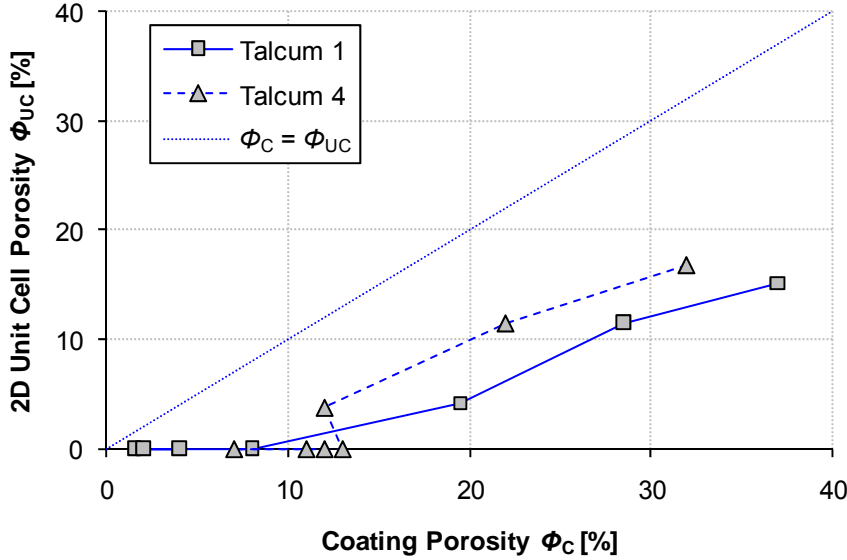


Figure 31. Comparison of the measured talcum coating porosities /20/ and the theoretical 2D unit cell porosity resulting from parameters a and c given in Figure 30.

Table 7. Theoretical void area fractions (2D) and porosities (3D) of talcum 1 and 4 for the unit cell parameters a and c .

Binder Content w/w%	c	a	2D		3D		
			Talcum 1	Talcum 4	Talcum 1	Talcum 4	
			%	%	%	%	
5	0.480	0.825	0.800	15	17	32	35
10	0.645	0.750	0.750	11	11	27	27
15	0.787	0.725	0.700	4	4	11	10
20	0.905	0.775	0.750	0	0	0	0
25	1.000	0.825	0.775	0	0	0	0
30	1.070	0.850	0.850	0	0	0	0
50	1.120	0.850	0.850	0	0	0	0

When using the very same pigment factors and binder variables of Table 7, but applying the three-dimensional porosity definition of the unit cell (equation 36), one gets a significantly better agreement between the theoretical case and the measurement (Figure 32). This shows that, in the case of the talcum systems, there is homeomorphism between the 2D topology of the unit cells and the three dimensional topology, where the homeomorphic function is given by the 2D-3D relationship of the porosities of the unit cells:

$$\phi_{2D}(a, c) = f(\phi_{3D}(a, c)) + C \tag{44}$$

where f and f^{-1} are defined for all pairs in the set $\{\phi_{2D}, \phi_{3D}\}$ and C is a constant.

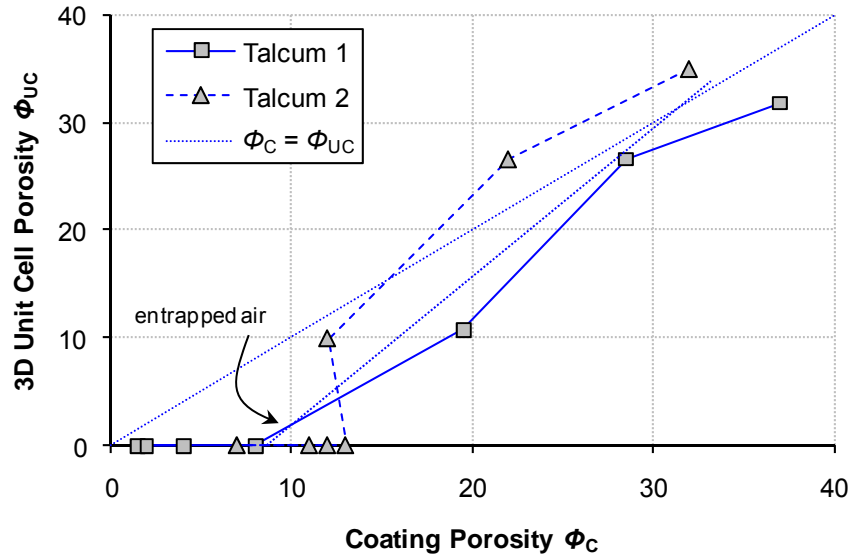


Figure 32. Comparison of the measured talcum coating porosities [20] and the theoretical 3D unit cell porosity resulting from parameters a and c given in Figure 30.

4.2.4 Relating binder dosage to the model binder variable

The use of a quadratic correlation between binder dosage and binder variable (equation 43) showed good agreement between the measurement data and the model behaviour. However, the assumption of such a correlation was purely empiric. The addition of more binder to the coating colour, i.e. a higher relative volume of binder, would mean in a physical sense, when translated to the model, that the area fraction of binder in the unit cell increases linearly, provided the binder density remains constant. And since the area fraction of binder in a unit cell ϕ_{s2} is also merely a linear function of the binder variable c (see equation 37.2 with $\phi_2 = \phi_{s2}$), it means in turn that there should be a linear correlation between the binder dosage of the coating and the binder variable of the unit cell. To investigate this we can fit the data points of, say, Talcum 1 to the model curve of a constant pigment factor. Figure 30 showed that the maximum thermal conductivity of Talcum 1 lies between a pigment factor of $a = 0.80$ and 0.85 . We therefore choose $a = 0.825$, in order to match the general level of the pigment influence on thermal conductivity of this series and discuss the correlation of binder dosage β and binder variable c by fitting the rest of the data points to the corresponding curve (Figure 33.a). Keeping the pigment factor constant, for this discussion, implies that the role of the pigment itself doesn't change upon binder addition. However, it allows us to retain the possibility that the role of binder changes with respect to the pigment, i.e. void filling or disrupting. In other words, the pigment factor is defined by the maximum thermal conductivity of the data and the binder variable describes the way binder addition changes the unit cell.

Figure 33.b shows the correlation of the binder variable c of this fit to match the curve in Figure 33.a and the corresponding binder dosage. With the exception of the outlier of 20 w/w% (compare also Figure 30), the points closely match a stepwise linear function. For $c < 1$ there is a higher gradient of binder addition than there is for $c > 1$. Below the CPVC the binder fills the structure and contributes directly to connectivity. As a result there is a strong increase in c since in that stage it is describing the binder bridges. As the system is filled, a comparatively high binder amount in the coating colour is required to further disrupt the filled structure and thus lower, by replacement, the relative amount of pigment (stage 3). This is observed as the lesser gradient in the correlation above the CPVC.

APPLICATION OF THE MODEL TO THERMAL CONDUCTIVITY

Disruptive system

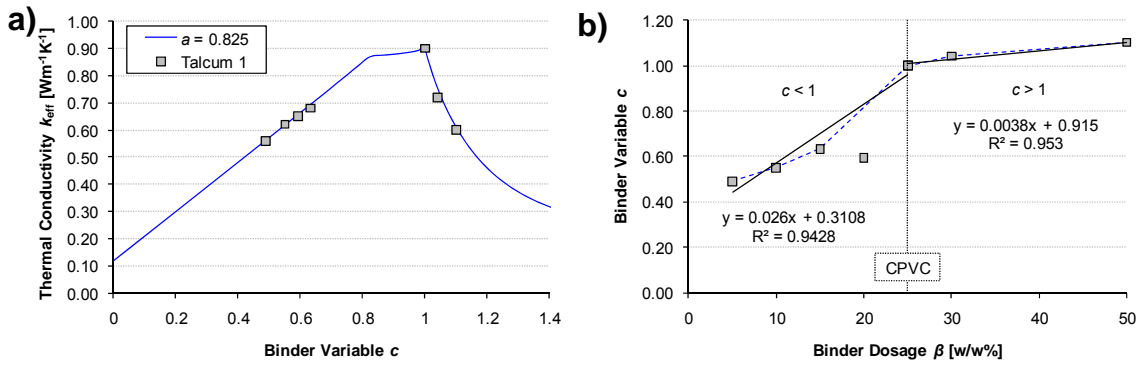


Figure 33. a) Thermal conductivities of Talcum 1 fitted to the model curve for $a = 0.825$. b) Correlation of the resulting binder variable and the corresponding binder dosage.

This discussion shows that by using a stepwise linear function instead of the quadratic correlation, on the one hand, the physical meaning of binder dosage is directly translated to the model unit cell, and, on the other hand, the role of binder in the system can be examined more closely, albeit that Figure 34 shows there is very little difference between either approach. Because of the advantages in discussing the role of binder, the stepwise linear fitting shall be used for the following bcGCC system and also for a comparison of both pigment systems.

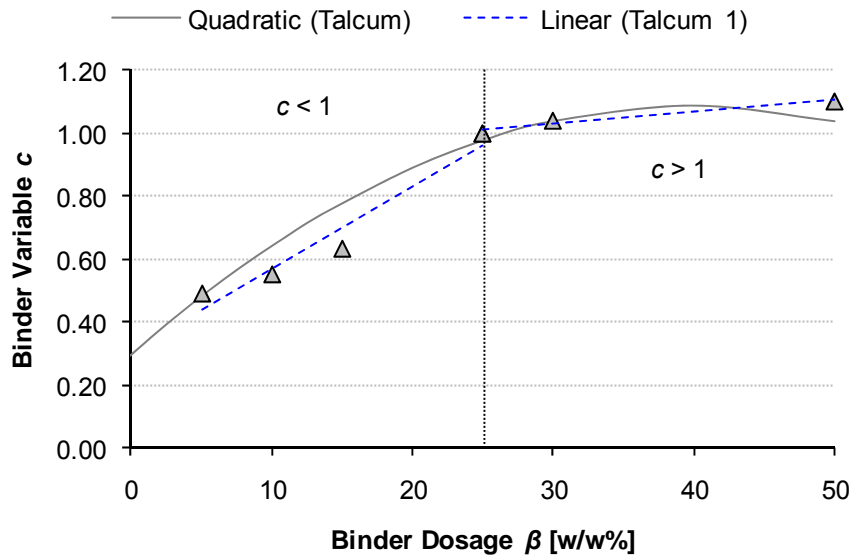


Figure 34. Comparison of the quadratic correlation with the stepwise linear correlation of binder variable and binder dosage.

4.3 Disruptive system

4.3.1 Materials

The pigment used was a coarse calcium carbonate with a broad particle size distribution (bcGCC) in combination with a medium T_g styrene-acrylate latex binder in dosages of 4, 6, 8, 12, 20 and 25 w/w% in relation to 100 w/w% pigment. The materials were prepared and measured in the form of pigment tablets as described in section 2.3. Table 8 lists the material properties of the pigment binder system, the pore size distributions can be found in Figure 36.

Table 8. Summary of the pigment binder system.

<i>Component:</i>	
Latex	SA
Dosages [w/w%]	0-25
Glass transition temp. [°C]	5
Particle size [μm]	0.20
Thermal conductivity [Wm ⁻¹ K ⁻¹]	0.21
Specific heat capacity [Jkg ⁻¹ K ⁻¹]	559.8
Density [kgm ⁻³]	1 100
Pigment	bcGCC
Thermal conductivity [Wm ⁻¹ K ⁻¹]	2.7
Specific heat capacity [Jkg ⁻¹ K ⁻¹]	454.8
Density [kgm ⁻³]	2 700
PSD [w/w%]	
< 5 μm	93
< 2 μm	60
< 1 μm	40
<i>d</i> ₅₀ (weight median) [μm]	1.6

4.3.2 Role of porosity for thermal conductivity

It was stated earlier, that porosity alone is not sufficient to describe the thermal behaviour of a pigment/binder system. This can be seen in two ways in Figure 35. Although the systems of 0 w/w% and 8 w/w% binder have very similar porosities, the thermal conductivity of the 8 w/w% binder-containing structure is higher than the binder-free one. At the same time, the 4 w/w% and 8 w/w% binder structures share similar thermal conductivity, while their porosities are different.

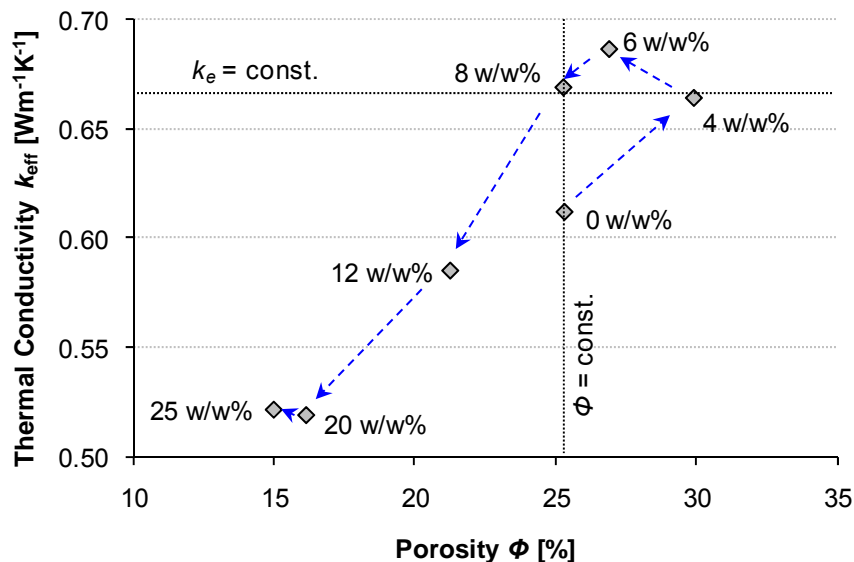


Figure 35. Thermal conductivity as a function of porosity. The labels and arrows indicate the increasing binder dosage. Based on paper [III], Figure 10.

Intuitively, introducing more binder, which is a material with lower inherent thermal conductivity than the pigment phase, it would be expected to observe a decrease in the total effective thermal conductivity. The fact that, for the same porosity (0 and 8 w/w%), the modal pore size is changed from 0.1 μm to 0.2 μm (compare Figure 36), shows that the number of pores is less, and, therefore, the connectivity of the skeletal structure is higher.

The higher skeletal connectivity is compensating for by the lower inherent thermal conductivity of the binder phase. Once a concentration of 8 w/w% is reached, this effect is replaced by one of greater insulation. Thus, the binder acts initially by contributing to the effective thermal conductivity by the mechanism of particle to particle conduction (mode 4. in the form of the secondary effect iii. described in 3.1.2) whereas higher binder amounts lower the effective thermal conductivity due to the growing influence of the intrinsically lower thermal conductivity of the binder (primary effects a) and c) in 3.1.2). This illustrates that pore volume and skeletal connectivity are not necessarily directly related, and, therefore, both of them must be considered independently in respect to the effective thermal conductivity.

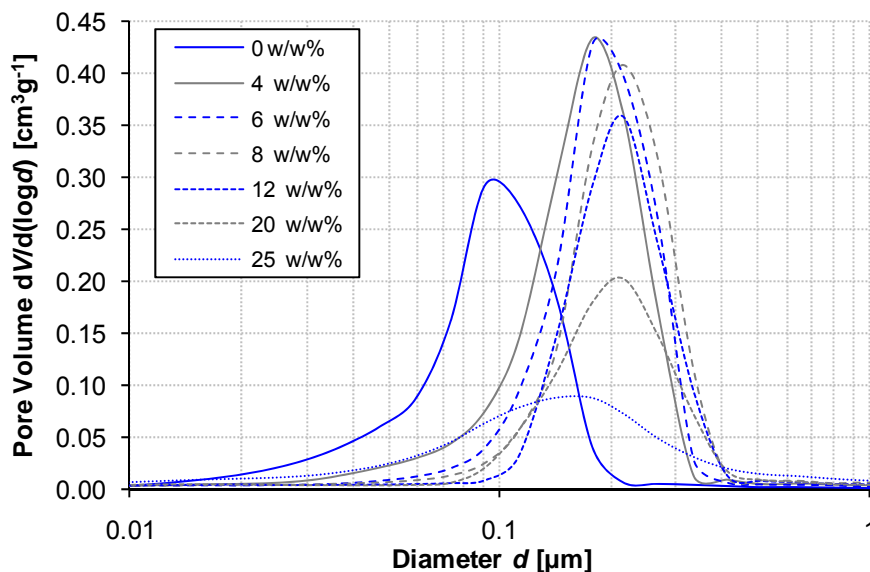


Figure 36. Pore size distribution for the bcGCC pigment with increasing dose of SA latex binder. Based on paper [III], Figure 9.

4.3.3 Parameter modelling

Translated to the grouped Lumped Parameter Model (LPM), the point of the maximum thermal conductivity ($c = 1$) is given for the binder concentration of 6 w/w%. For the lower binder concentrations, the skeletal connectivity is smaller, and for higher binder concentrations the lower inherent thermal conductivity of the binder, as well as the disruptive interactions of binder particles and pigment, acts to lower the effective thermal conductivity. This trend is shown in Figure 37 for the theoretical curves of the Grouped Lumped Parameter Model, fitted to the curve of $a = 0.80$. The connection of binder dosage and binder variable c was made by using the same fitting approach as described in 4.2.4. Figure 38 shows the resulting correlation of binder dosage and binder variable.

It should be noted that the mechanisms evoked in this bcGCC pigment-binder system differ from the original approach of the model. The talcum system discussed in 4.2 showed a very consistent behaviour with the initially constant pigment volume approach, in which the critical pigment volume concentration of the coating was reached at a binder dosage of 20 w/w%. The binder variable c was then correlated to the completely filled unit cell of the model ($c = 1$). The lower binder concentrations maintained porous coatings and also porous unit cells in the model, whereas higher binder concentrations showed the increasing influence of the binder with respect to the pigment phase for the coating, the binder filling the voids, which in turn shrank in relation to binder dose in the unit cell of the model.

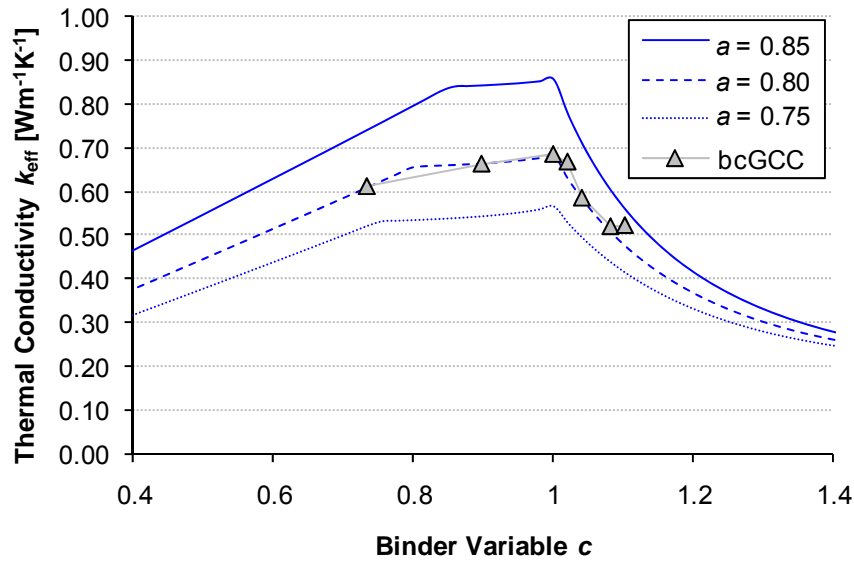


Figure 37. Theoretical curves of the Modified Lumped Parameter Model and experimental data of thermal conductivity.

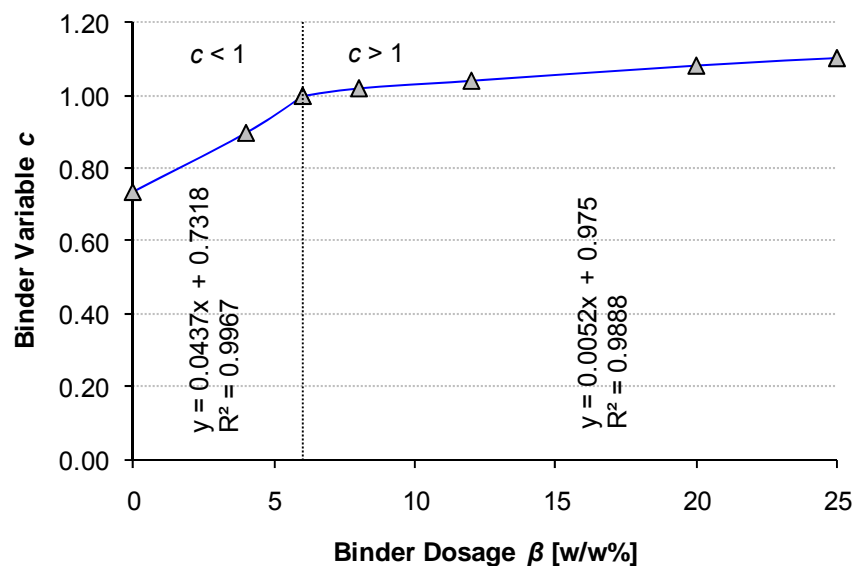


Figure 38. Stepwise linear relationship of binder dosage and binder variable.

In this calcium carbonate system, there are several differences that distinguish it from the previously studied talc coating, and the mechanisms of their effective thermal behaviour. The calcium carbonate pigments with a shape factor between one and two (low aspect ratio) are quite blocky compared to the very platy (high aspect ratio) talcum particles. The talc particles, when aligned, pack more densely, with particle thickness being the main controlling parameter, which in talc is rather uniform, compared with the more random packing of the carbonate. This results in a slightly lower value for the pigment variable ($a \approx 0.80$ for the calcium carbonate, versus $a \approx 0.825$ for the talcum system) showing that the influence of the pigment material properties is greater if it is more densely packed.

The difference between a blocky and a platy pigment can also be observed when studying the comparison of how the binder addition translates to the LPM binder variable c in Figure 39. As discussed for the parameter modelling of both systems, the maximum

thermal conductivity equals the point of $c = 1$, i.e. 6 w/w% and 25 w/w% for bcGCC and Talcum 1, respectively. It is seen that the Talcum systems require a comparatively small binder variable at the same binder concentration. Adding, e.g. 6 w/w% of binder to the Talcum system translates to a binder variable of ca. 0.5 and 0.9 for Talcum 1 and bcGCC, respectively. Since both correlations are given for the constant pigment factor of each system, this difference describes the role of binder in relation to pigment. A given binder amount provides, therefore, a much higher relative skeletal connectivity for an isometric pigment compared to a platy pigment when normalised to the pigment size.

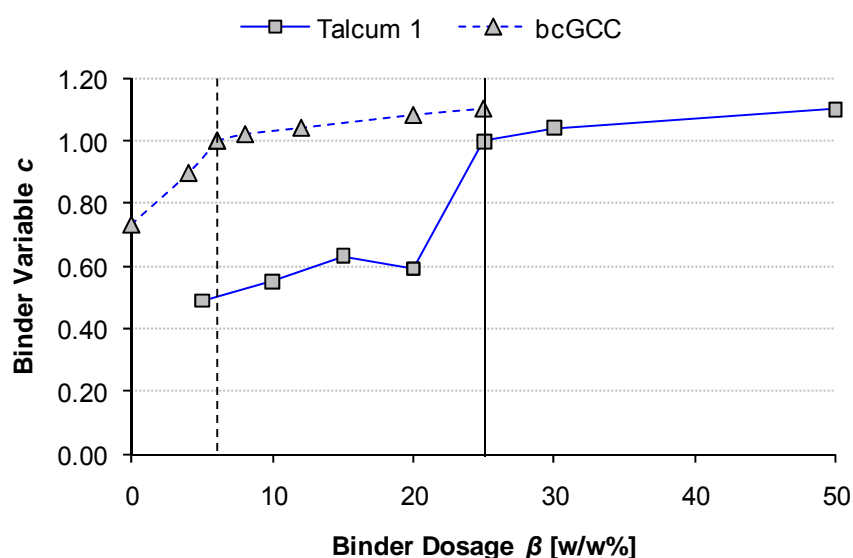


Figure 39. Comparison of the Talcum 1 and bcGCC system in terms of the behaviour for the addition of binder.

A second difference between both systems is the binder used. The styrene butadiene latex used for the talcum system is assumed to be softer and easier film forming than the higher glass transition temperature (T_g) acrylic latex in the calcium carbonate system. The more rigid binder spheres in combination with the blocky particles of the pigment, having its rather broad particle size distribution, increase the tendency for disruptive packing interactions. For that reason, the porosities of the calcium carbonate coating are generally quite high, even for the higher binder concentrations. This is in contradiction to the originally proposed three stages approach of unit cells in the model. The following section takes a look at the disruptive nature of the binder, whereas the role of the latex binder material properties is studied in section 6.2.

4.4 Pigment disruption

The unit cells after the point where $c = 1$ are, by definition, non-porous, and this fails to reflect the effect of the binder disrupting the pigment packing before it finally fills the remaining voids and becomes non-porous. The model unit cell, therefore, would have to follow an alternative set of transitions through the stages of binder dosage to maintain a relation of the model to the practical “thermal porosity”. The model porosity at this stage is defined naively by the solid phase fractions in the unit cell, whereas the “structural porosity” is measured by porosimetry. One approach would be to effectively lower the amount of pigment in a unit cell when increasing the binder content (Figure 40). This would reduce the total effective thermal conductivity of the unit cell before it becomes non-porous. However, there is no a priori reason to accept this as a realistic representation. While the difference between the measured porosity of the system and the unit cell

porosity could relate to the connectivity of solids, it is clear at this point that a more detailed analysis of the model structure in relation to the coating structure is required. In the following chapter the model will therefore be applied based on the structural information of the coating, i.e. structural modelling.

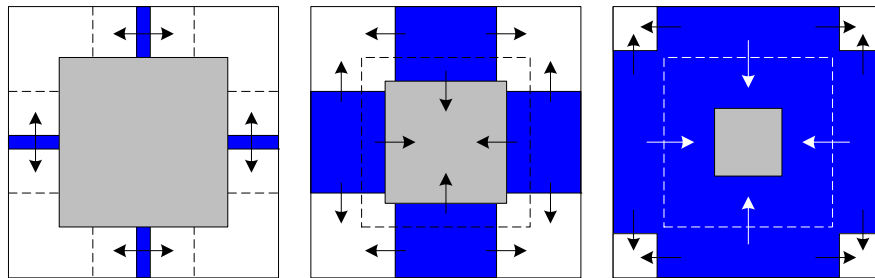


Figure 40. Three stages of alternate unit cell behaviour for the addition of disruptively interacting binder. Based on paper [III], Figure 12.

4.5 Summary

At first, existing literature values for the thermal conductivity of a talcum pigment coating with various doses of SB latex binder were examined. It was shown that the thermal conductivity increases as a function of latex dose below the critical pigment volume concentration (CPVC) due to a reduction of porosity (void filling). Above the CPVC, the increasing influence of the binder phase compared to pigment lowers the effective thermal conductivity. As such, this behaviour agreed well with the original definition of the Lumped Parameter Model where the maximum thermal conductivity is observed at the critical pigment volume concentration. A comparison of the model unit cell void area fraction and the real coating porosity showed an underestimation of the latter by the model. However, by using the very same model configuration in a 3D unit cell agreement between model and structure could be found. This suggests a topological homeomorphic relationship between the 2D model and the 3D pore structure. The relationship of binder dosage and the model binder variable was initially expressed as a quadratic function, although in a physical volume addition sense there should be a linear relationship. The discussion showed that the quadratic correlation can also be expressed as a stepwise linear function where the different gradients reflect the void filling and disrupting behaviour of binder below and above the CPVC, respectively.

The thermal conductivities of a bcGCC system with SA latex exhibited similar behaviour in respect to the thermal conductivity going through a maximum. In contrast to the talcum coating, this occurs, however, at binder concentrations well below the CPVC. This indicates that the binder, in combination with the broad particle size distribution pigment, is not void filling as in the talcum system, but disrupts the pigment packing already at low binder concentrations. The relationship between binder dosage and model binder variable showed that in comparison to the talcum system, binder addition to the bcGCC system has a stronger relative influence on skeletal connectivity. Since the binder is disrupting the pigment packing before the system becomes nonporous, to provide a match between model and observation, it is required to describe alternative model stages of binder dose, e.g. the use of an effective thermal porosity. Since such a thermal porosity would differ from the structural porosity, a more detailed look at the coating structure in relation to the model structure is required. This shall be addressed in the following chapter.

Besides the structural differences observed for the talcum and bcGCC system, it became clear that the thermal conductivity cannot be described by either the pore structure volume change or the binder level alone. This supports hypothesis [A] and also emphasises

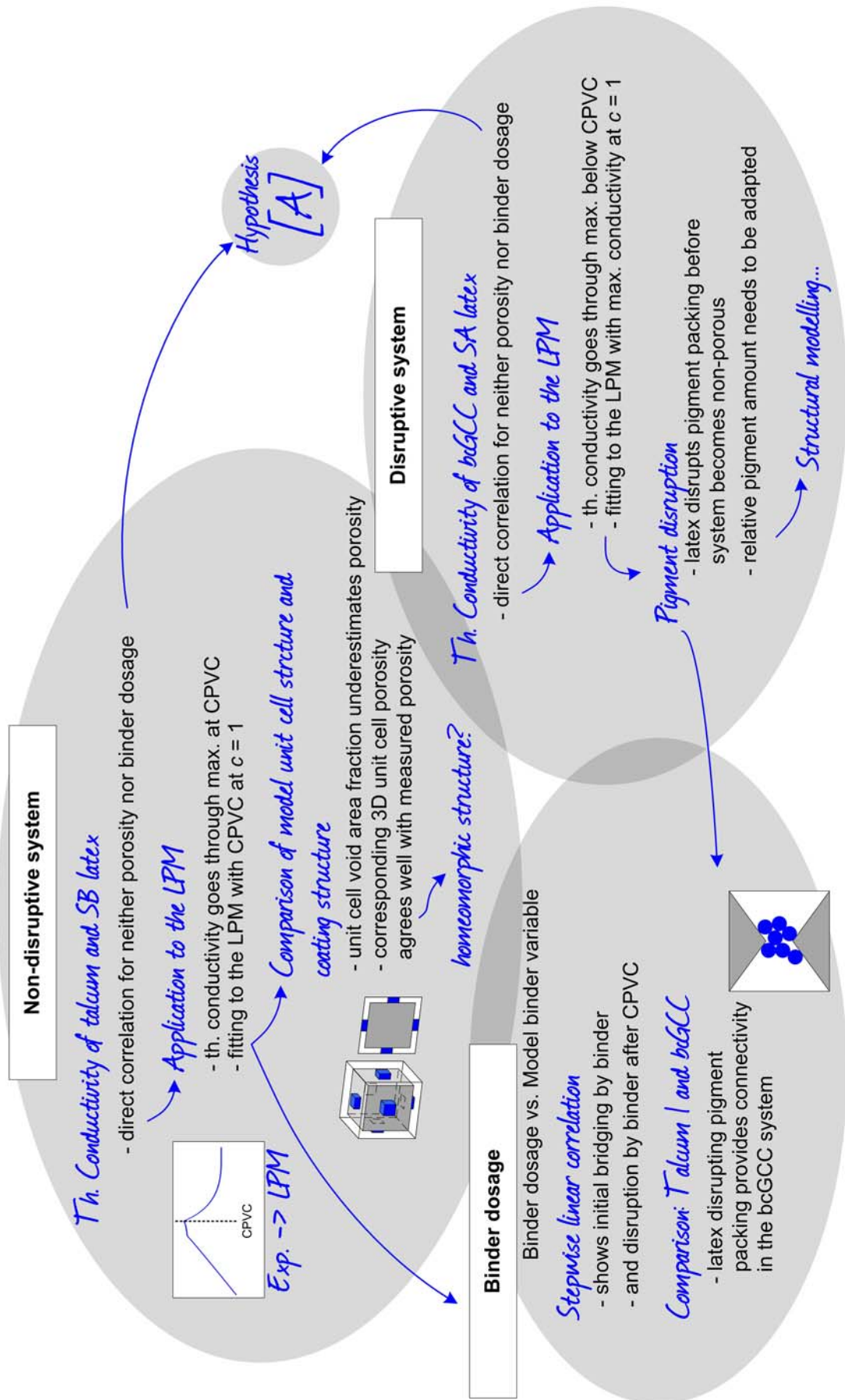
APPLICATION OF THE MODEL TO THERMAL CONDUCTIVITY

Summary

the need for the model to establish a link between material components and their mutually interactive role in the structure:

- [A] The parameters of *pore structure* and *skeletal connectivity* are required to model the thermal conductivity of paper coating structures.

4.6 Parameter modelling thread



5 APPLICATION OF THE MODEL TO COATING STRUCTURES

5.1 Background

In general, porosity is the most commonly used parameter to describe porous media. However, it was shown in chapter 4 that porosity alone is not sufficient to describe the thermal conductivity of multiphase systems. Since there are at least two solid phases present in a paper coating, i.e. pigment and binder, at least two parameters are required for an accurate description. The Lumped Parameter Model uses a pigment factor and a binder variable independently to define the solid content of a unit cell. This allows a more flexible modification of the unit cell and shall be used to follow a structural modelling approach, i.e. fitting the unit cell structure to a given coating structure, the so called “master layer”.

5.2 Generation of structural master layers

5.2.1 Materials

The same pigment-binder system as in 4.3 was studied in comparison with SEM cross-sectional image data from a previous study adopting a similar range of latex addition /40/. The pigment in this latter study was a finer ground calcium carbonate having a narrow particle size distribution (nfGCC), and the latex was styrene butadiene (SB). A summary of the materials involved is given in Table 9.

Table 9. Summary of particle data and thermophysical properties of the pigment binder systems.

<i>Component:</i>	<i>Experimental, Simulation</i>	<i>SEM imaging /40/, Simulation</i>
Latex	SA⁴	SB⁵
Dosages [w/w%]	0-25	2-14
Glass transition temp. [°C]	5	20
Particle size [µm]	0.20	0.14
Thermal conductivity [Wm ⁻¹ K ⁻¹]	0.21	0.25
Specific heat capacity [Jkg ⁻¹ K ⁻¹]	559.8	454.8
Density [kgm ⁻³]	1 100	1 025
Pigment	bcGCC⁶	nfGCC⁷
Thermal conductivity [Wm ⁻¹ K ⁻¹]	2.7	2.7
Specific heat capacity [Jkg ⁻¹ K ⁻¹]	880	880
Density [kgm ⁻³]	2 700	2 700
PSD [w/w%]		
< 5 µm	93	100
< 2 µm	60	95
< 1 µm	40	75
d₅₀ (weight median) [µm]	1.6	0.6

By studying the comparison between particle packing simulation and the SEM images of nfGCC, it is possible to derive the level of confidence, or shortfall, for the simulation. Using the simulation then for the bcGCC, correlations with experimental diffusivity determined for the bcGCC could be established. The thermal properties of the constituent

⁴ Acronal S 360D (SA) is a registered trademark of BASF AG

⁵ DL966 (SB) is a registered trademark of Dow AG

⁶ Hydrocarb 60 (bcGCC) is a registered trademark of Omya AG

⁷ Covercarb 75 (nfGCC) is a registered trademark of Omya AG

components, i.e. pigment and latex, are identical for the calcium carbonate component and only differ slightly for the two latices used in the coating structure series.

Both the measurements of thermal diffusivity and the simulation of the particle deposition (see 5.2.2.1) were made for the binder-free pigment system as well as for binder concentrations of 4, 6, 8, 12, 20 and 25 w/w% based on pigment. The additional SEM data were from a particle system containing SB binder and was simulated accordingly for binder concentrations of 2, 6, 10 and 14 w/w% based on pigment.

5.2.2 Particle deposition (simulated master layers)

The simulated particle deposition is a simplified, two dimensional version following the Monte Carlo approach by Vidal *et al.* /64/. At first, a virtual domain is created. The height of the domain is the thickness of the wet coating layer and is based on a specified target coat weight and the specified initial solids content for pigment and latex. For the domain sides, periodic boundary conditions apply. The width of the domain is defined in advance, and comprises a balance of two considerations: on the one hand, the domain must be large enough to provide a sufficient number of particles to follow the pigment particle size distribution and also to be larger than the biggest particle present, on the other hand, a small domain reduces the total number of particles and therefore can greatly reduce the calculation demand. It was found that a domain size of $d_D = 10 \mu\text{m}$ is an acceptable compromise for both aspects. A particle deposition containing ca. 2 000 particles was calculated in less than four hours on a standard office PC.

Table 10 summarises some basic domain data.

Table 10. Standard data for the domains used in the simulations.

	Domain
Width	10 μm
Initial solids content	65 w/w%
Target coat weight	20 gm^{-2}
Binder concentrations	0-25 w/w%
Number of particles	~ 1-3k

The numerical generation of particles is discussed in 5.2.2.1. The generated pigment and binder particles are placed evenly at random in the domain as in an idealised dispersed coating colour (Figure 41.a), i.e. ignoring any species interactive effects. The actual particle deposition algorithm applies a minimisation of the particle potential energy in respect to height. Each particle is moved by a small distance in a random, downward oriented direction. In the first series of simulations, the move is accepted if no overlapping with other particles occurs, thus describing the rigid sphere approximation. This iteration is followed for each particle until no particle can be moved for two consecutive iterations; the system is then regarded as deposited (Figure 41.b). The resulting two dimensional quasi “cross-sectional” structures are used as the basis (master template) for the parameter generation of the general Lumped Parameter Model to be used subsequently to calculate the thermal diffusivity.

In order to study the effective thermal connectivity of the structure, identified as being necessary when compared with the experimental data, a slightly different approach was followed in a second series of simulations by allowing slight overlapping of the particles (soft sphere model). This takes account of the irregular shaped pigments, the adsorbed polymer layer (dispersant) and of the action of the consolidation of latex spheres. This approach will be considered in more detail when considering the role of connectivity in initiating transferring thermal contact.

Since both the generation of the pigment particles and the particle deposition process are of a statistical nature, four replicates were calculated for each configuration.

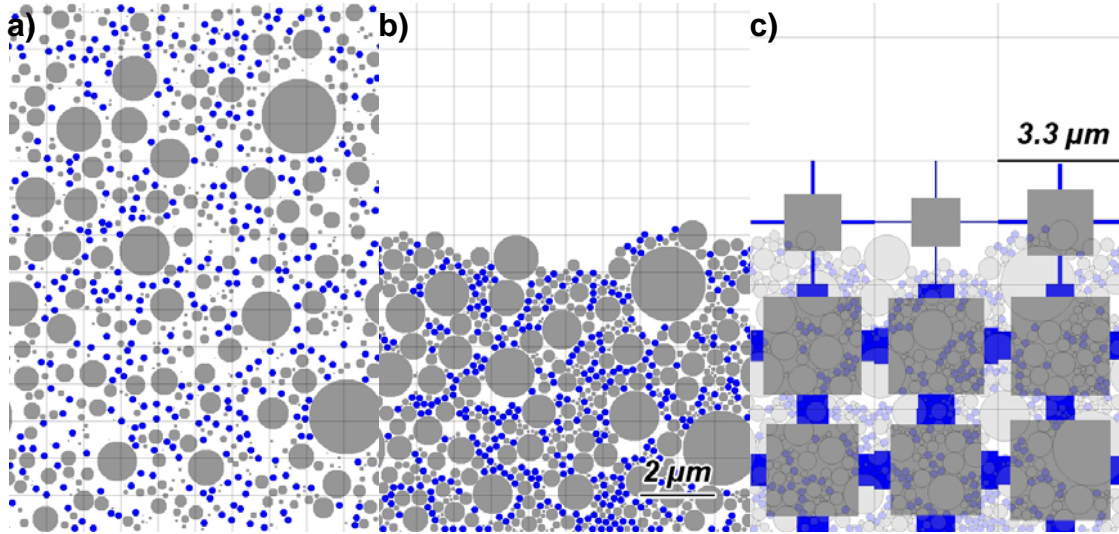


Figure 41. a) Initial domain ($d_D = 10 \mu\text{m}$) with randomly distributed particles (8 w/w% binder). b) The same domain after particle deposition and c) the domain split into three lateral sub-domains ($d_{SD} = 3.3 \mu\text{m}$) with a superposed lumped parameter unit cell developed for each sub-domain. Based on paper [IV], Figure 4.

After deposition of the particles in the domain, it is split into several sub-domains. For each sub-domain a LPM unit cell is superposed, thus permitting the calculation of the effective thermal conductivity of the coating structure. The superposition of the model on the master layer will be discussed in 5.2.4.

5.2.2.1 Generating the numerical pigment particle system

For the simulations of particle deposition, the particle size distributions of both pigments were expressed as the log-normal distribution, having the cumulative probability distribution function, $P_w(d)$, of particle diameter, d :

$$P_w(d) = \frac{1}{2} + \frac{1}{2} \operatorname{erf} \left[\frac{\ln(d) - \nu}{\sqrt{2\tau}} \right] \quad (45)$$

for which $\operatorname{erf}(x)$ is the Gauss error function, defined as:

$$\operatorname{erf}(x) = \frac{2}{\sqrt{\pi}} \int_0^x e^{-t^2} dt \quad (46)$$

The parameters ν and τ were determined from the weight based particle size distributions of the pigment data sheets. Because of the isometric nature of calcium carbonate, the pigment particles could be assumed to be spherical for the conversion of mass (volume) to number occupancy. The number based distribution function becomes then:

$$P_N(d) = \frac{1}{2} + \frac{1}{2} \operatorname{erf} \left[\frac{3\tau^2 + \ln(d) - \nu}{\sqrt{2\tau}} \right] \quad (47)$$

The fitting of the log-normal distribution to the particle size distribution measured by the Sedigraph method, was done using the two points of the logarithmically distributed

APPLICATION OF THE MODEL TO COATING STRUCTURES

Generation of structural master layers

mean particle size (d_{50} – the weight median particle size, i.e. the size at which 50 wt% of the material is finer) and the top cut (d_{98} – the size at which 98 wt% of the material is finer). A comparison of the experimentally measured particle size distribution and the fit for the bcGCC is given in Figure 42 and Figure 43. It shows that the regular fitting using median and top cut, results in a good fit for particles larger than 2 μm . However, for smaller particle sizes the fitting underestimates the weight percentage, i.e. the gap between the log-normal curve and the Sedigraph measurement curve widens. Nonetheless, for reasons of computational tractability, as we go on to elucidate, this distribution has been chosen for the simulations.

Alternatively, one can make a second fitting of a log-normal distribution to only the measurement data finer than 2 μm . This results in a better approximation of fines, but provides a considerably worse replication of coarser particles. Theoretically, a weighted combination between both fittings would be possible. However, the very large number of fine particles requires further consideration.

When using the parameters of the fines fitting ($\nu_{\log\text{-normal}} = 0.397662$, $\tau_{\log\text{-normal}} = 1.48027$) to generate a particle system for simulation, this results in a computationally unreasonable large number of particles. Compared to the particle system of the coarse particle fit, containing a number of ca. 1 000 to 2 000 particles (see Table 10), the fines fit particle system contains ca. 300 000 particles. Since the calculation demand of the particle deposition simulation increases by approximately 2^N for N particles, it leads to unfeasible calculation times for today's PC systems, and is even laborious for super or cluster computing solutions (compare /64/).

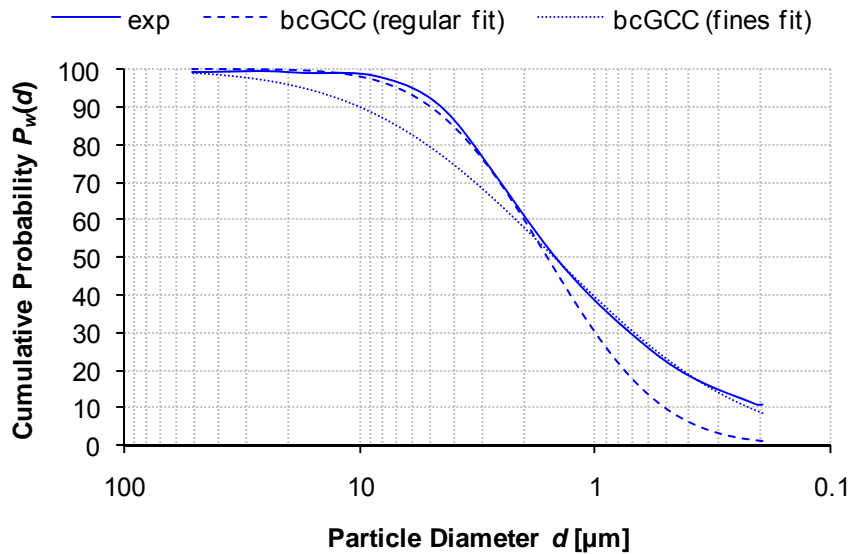


Figure 42. Sedigraph data of the bcGCC (exp) compared to the log-normal cumulative weight, w , distribution, $P_w(d)$, based on top cut ($\nu_{\log\text{-normal}} = 0.47000$ and $\tau_{\log\text{-normal}} = 0.89231$) and the log-normal cumulative distribution fitted to the fines fraction ($\nu_{\log\text{-normal}} = 0.397662$ and $\tau_{\log\text{-normal}} = 1.48027$). Based on paper [IV], Figure A2.a.

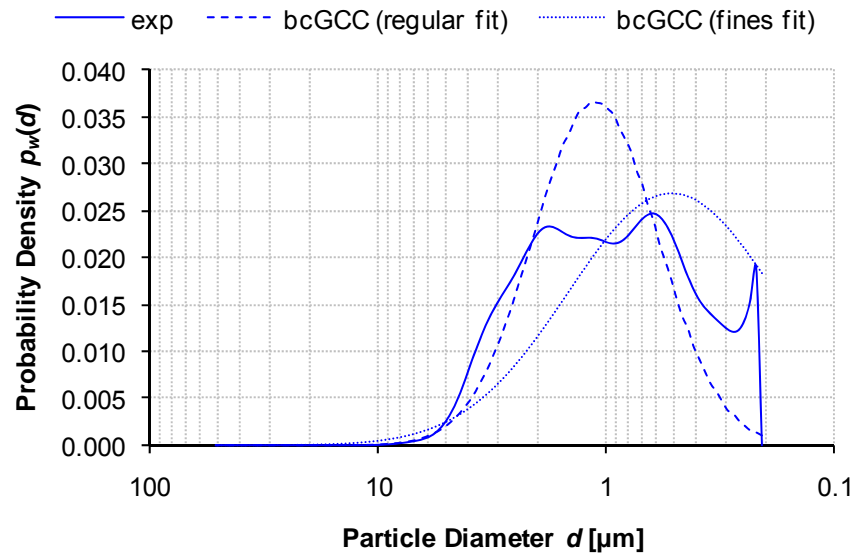


Figure 43. Probability density functions, $p_w(d)$ corresponding to Figure 42. Based on paper [IV], Figure A2.b.

In addition to the computational reasons for choosing the coarse particle fitting size distributions, there are further geometrical considerations. In two dimensional packing simulations the difference to real three dimensional systems, in which additional interactional forces are also present, is likely to be large in itself, irrespective of the goodness of fit for the particle size distribution. This holds particularly true for the simulations in this study, because of the absence of any surface chemical forces in the simulations (see discussion in 5.2.2). For simulating the surface chemical forces, the fines become increasingly important because of their large specific surface.

Figure 44 summarises the cumulative probability distribution functions of the actual pigment systems as used in the simulations, containing 818 and 791 particles for the bcGCC and nfGCC, respectively. The fitted parameters were $v_{bc} = 0.47000$ and $\tau_{bc} = 0.89231$ for the bcGCC pigment and $v_{nf} = -0.5108$ and $\tau_{nf} = 0.9237$ for the nfGCC pigment. Because of the very large number of fine particles in the nfGCC systems, the smallest particle diameter for the simulation of those systems was limited to $d_{\min} = 0.1 \mu\text{m}$ in order to keep the calculation demand within an acceptable range. The pigment was initially simulated as hard spheres following the derived size probability distribution function.

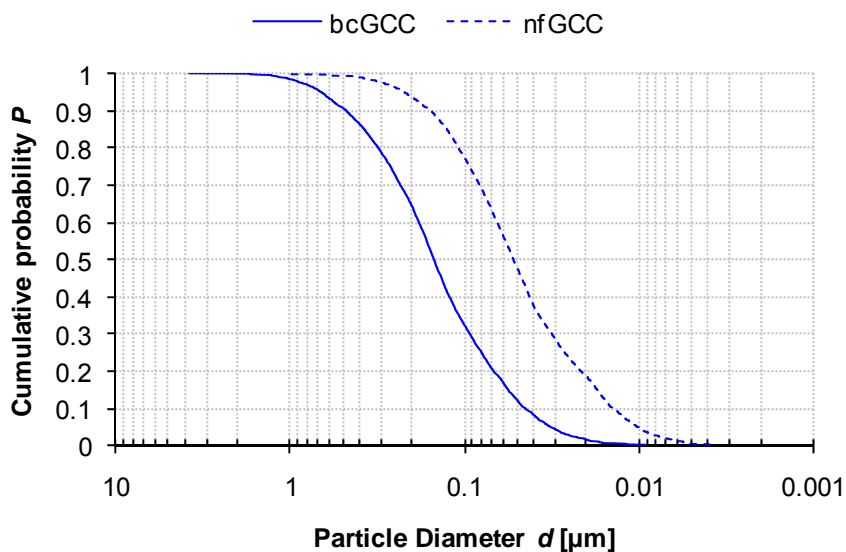


Figure 44. Cumulative probability plot for the number based particle size distributions of the bcGCC and nfGCC pigments. The plotted particle systems contain 818 and 791 pigment particles, respectively. Based on paper [IV], Figure 1.

In the discussion in section 4.3, the SA binder used had been shown to act disruptively on the pigment packing in the bcGCC pigment and also to the nfGCC pigment at certain low to medium dose ranges, and acting as a hard sphere during consolidation. For the simulations, the binder was, therefore, first described as mono-size rigid spheres.

5.2.3 SEM cross-sectional imaging (microscopy master layers)

The SEM cross-section images were provided from a previous study /40/ as a means to compare the simulated particle structures to real cross-sectional data. The methodology and equipment used is described in /65/. A high resolution field emission scanning electron microscope (FE-SEM, Jeol JSM 6335 F) was used in the element contrast mode (backscattered electron detection). The samples were prepared using the same tablet forming techniques as described in 2.3.2. The SB latex was made visible by a treatment with osmium tetroxide. Figure 45.a shows a cross-sectional image of a tablet containing 6 w/w% binder. In this image, the pores are distinguished as dark areas whereas the stained latex appears bright. Thresholding was used to identify clearly the three different phases.

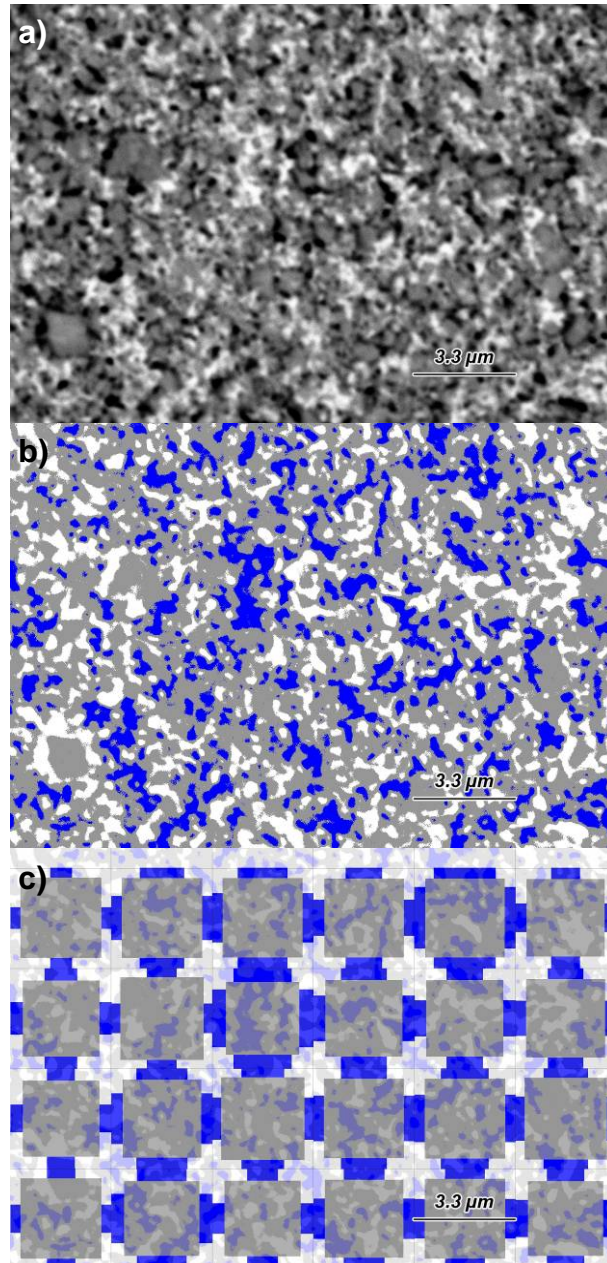


Figure 45. a) Original SEM image of a 6 parts latex tablet structure. The OsO_4 stained latex appears in a brighter tone. b) Threshold image. For a better comparison, the phases are colour coded as in the simulated structures. c) Unit cell image. Superposition of LPM unit-cells onto the SEM threshold image. Based on paper [IV], Figures 9-11.

Many different thresholding techniques exist, not least because of the great variety of application fields and their individual requirements. For the thresholding of the SEM images a one-dimensional maximum entropy based algorithm based on the work of Kapur *et al.* [66] was used. Because of the three phases present, two thresholds need to be found: the air-pigment threshold t_1 and the pigment-binder threshold t_2 . Let P_i be the normalised histogram of the grey level image, where $0 \leq i \leq L-1$ for $L = 256$ grey levels, then the total entropy f_2 of the histogram, segmented by t_1 and t_2 , is given by:

$$f_2(t_1, t_2) = H(0, t_1) + H(t_1, t_2) + H(t_2, L) \quad (48)$$

where the entropy $H(a, b)$ of a histogram segment from a to b is:

$$H(a,b) = -\sum_{i=a}^b \frac{P_i}{\omega(a,b)} \ln \frac{P_i}{\omega(a,b)} \quad (49)$$

where

$$\omega(a,b) = \sum_{i=a}^b P_i \quad (50)$$

The optimal thresholds are the grey levels that maximise the total entropy of equation 48. The normalised histogram P_i is based on the grey level data of a single SEM image. For each binder level, 25 cross-sectional images were analysed. Figure 45.b shows the threshold image for an air-pigment threshold of $t_1 = 77$ and a pigment-binder threshold of $t_2 = 163$.

After identifying the phases of pigment, binder and air in the SEM images, the unit-cells of the Lumped Parameter Model were superposed onto the cross-sectional image, analogous to the superpositioning on simulated layers. Figure 45.c shows the same cross-section with the unit cells. The following section will describe the generation of the LPM parameters in superpositioning.

5.2.4 Modelling on master layers

5.2.4.1 Generation of the model parameters

The original master layer (simulated or microscopy) is divided into several square sub-domains for each of which the LPM variables a and c are calculated individually. Both of them are given by the local area fractions of pigment and binder, respectively. Equations 37.n defined the three area fraction components of a unit cell. The pigment factor a is given by:

$$a = \sqrt{\phi_{s1}} \quad (51)$$

and the binder variable c can be calculated subsequently using the pigment factor a and the binder area fraction:

$$c = \frac{\phi_{s2}}{2(1-a)} \quad (52)$$

In this way, the porosities of the model unit cells equal the porosities of the structural sub-domains. The resulting unit cells can then be assigned to the according sub-domain in the coating structure (Figure 41.c and Figure 45.c) to calculate the overall porosity and effective thermal conductivity.

In order to exclude effects of surface roughness and surface porosity of the simulated structures, when calculating the overall properties of the coating structure, the top or boundary layer in the coating structure (compare Figure 46.a) is determined as the uppermost row of unit cells with a porosity of not larger than 35 %. In Figure 41.c, for example, only the two lower rows of unit cells would be used for calculation of the overall properties.

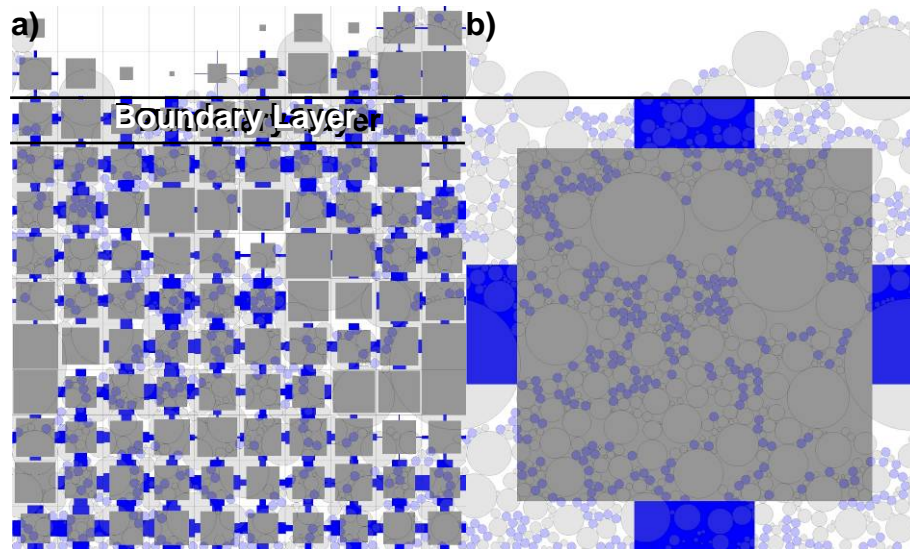


Figure 46. a) Domain split into ten lateral sub-domains and unit cells for each sub-domain. b) The same domain with a single sub-domain and unit cell. Based on paper [IV], Figure 6.

5.2.4.2 The effect of sub-domain size

The number of lateral sub-domains in both a simulated structure and SEM cross-sections, and therefore the number of unit cells, does have an influence on the calculation of specific values of thermal conductivity. A large number of sub-domains (smaller sub-domains, Figure 46.a, generates more information on the homogeneity and isotropy of the coating structure but it is more susceptible to those irregularities, whereas larger sub-domains can even out inhomogeneities (Figure 46.a).

Figure 47 shows the calculated effective thermal conductivity of the simulated coating structure, i.e. the entire domain ($d_D = 10 \mu\text{m}$), as a function of the sub-domain size d_{SD} . For large sub-domains (one, two, three or four lateral sub-domains), the calculated thermal conductivity is fairly constant. When the sub-domain size is of the order of the pigment particle size ($d_{SD} = 2 \mu\text{m}$, 5 lateral sub-domains), there is a distinct drop in the calculated values. Another drop occurs at the general size of the binder particles, confirming that sub-domains smaller than the present particle sizes are more susceptible to “weak spots” in the structure. This can be observed in Figure 46.a, where the sub-domain size is $d_{SD} = 1 \mu\text{m}$. Some sub-domains are entirely filled by pigment, whereas others show a high binder amount or, conversely, a high porosity.

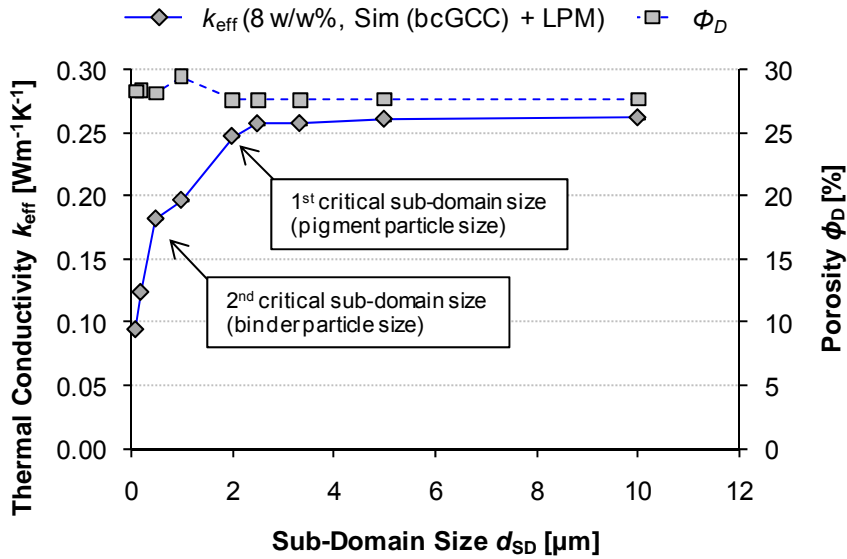


Figure 47. Effective thermal conductivity and porosity of a simulated coating structure obtained in combination with the Lumped Parameter Model as a function of the sub-domain size. Based on paper [IV], Figure 7.

Similar to Figure 47, Figure 48 shows the calculated effective thermal conductivity of the microscopy master layer. The same trend as in Figure 47 can be observed, although the drop in the thermal conductivity does not occur as distinctly as for the simulated structure. This is most likely due to the more random nature of the pigment and binder areas in the cross-sectional cuts, compared to the mathematically defined particle size distribution of the simulated structures. However, both figures show that a sub-domain size of $d_{SD} = 3.3 \mu\text{m}$ (three and six lateral sub-domains for simulation and SEM images, respectively) is above the critical sub-domain size. For future calculations a sub-domain size of $d_{SD} = 3.3 \mu\text{m}$ will be used.

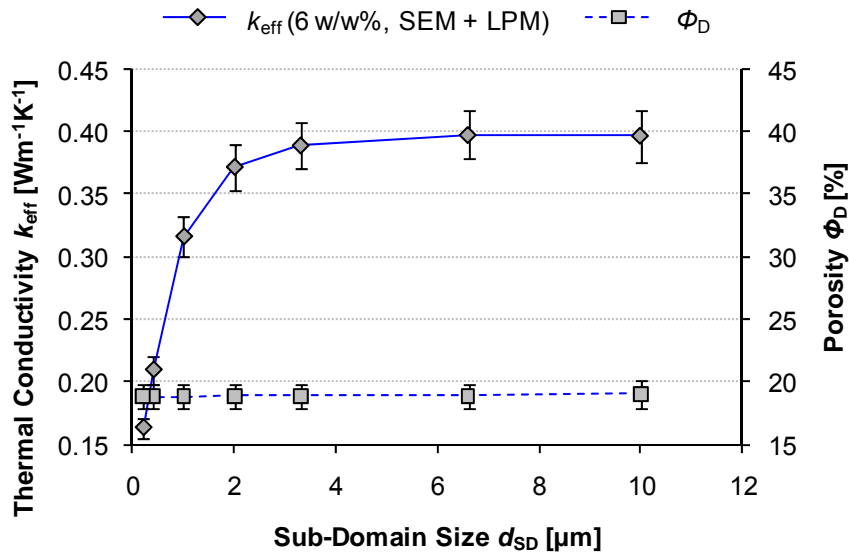


Figure 48. Effective thermal conductivity obtained by SEM imaging in combination with the Lumped Parameter Model as well as porosity as a function of the sub-domain size. The porosity is determined as the average void area fraction of the unit cells in an SEM cross-section image. Based on paper [IV], Figure 8.

Furthermore, Figure 47 and Figure 48 show the porosities calculated as the void area fractions of the simulated and of the SEM cross-sectional structures. The simulated porosity remains largely independent of the sub-domain size. As it is the porosity of the simulation domain, it is quite clear that the simulated pore area in the domain does not change by decreasing the sub-domain size. However, by changing the sub-domain size in simulated domains, the position of the boundary layer changes slightly. This is the reason for the kink in the porosity curve of Figure 47.

5.3 Structural modelling of the effect of binder content

5.3.1 Simulated masters

Figure 49 shows the thermal conductivities calculated from the thermal diffusivity measurement of the tablet material (experimental) as well as the numeric effective thermal conductivity calculated for the lumped parameter unit cells of six (2x3) sub-domains in the equivalent hard sphere simulated coating structure. There is a clear difference in the general level of thermal conductivity. This difference can be only partially accounted for by the porosity differences between the simulated two-dimensional structures and the experimental porosity (Figure 50). This finding reconfirms the non-trivial relationship between the two dimensional void area and the three dimensional pore structure /40, 65/, but, despite the better agreement on porosity at binder levels below 10 w/w% the difference in conductivity in this region is at its greatest. This initial gap between experimental and numeric will be given special attention as it relates to the connectivity differences between perfect spheres and the real situation of pigment particle asymmetries and the important role of adsorbed dispersant polymer (polyacrylate) used during the pigment slurry manufacture.

APPLICATION OF THE MODEL TO COATING STRUCTURES

Structural modelling of the effect of binder content

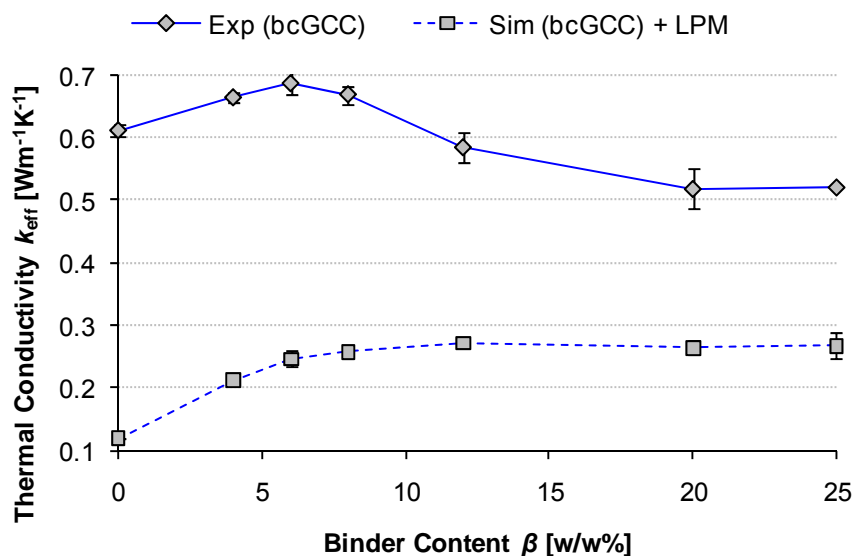


Figure 49. Effective thermal conductivity of the bcGCC coating structures measured experimentally from tablet material and calculated numerically by application of the lumped parameter model to a simulated deposited hard sphere particle system. Based on paper [IV], Figure 12.a.

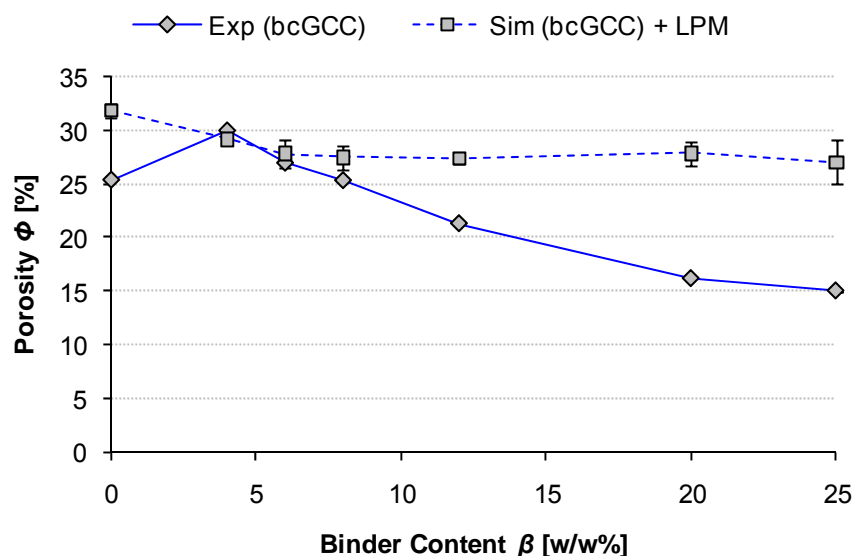


Figure 50. Porosity of bcGCC coating structures measured experimentally by mercury porosimetry, and porosity calculated as the simulated void area fraction over all sub-domains as a function of binder content. Based on paper [IV], Figure 12.b.

While the experimental conductivities show the peak at 6 w/w%, as discussed already in section 4.3, the numeric values show a monotonic increase in thermal conductivity up to a binder concentration of 12 w/w%. This difference is most likely initially due to the missing connectivity in the simulation between the pigment particles, but which occurs in real systems due to particle anisotropy and adsorbed dispersant polymer. In the simulation, therefore, conductivity keeps increasing upon adding binder until the maximum connectivity (of the unit cell) is reached at very high binder levels, and from thereon conductivity reduces by adding more binder. The generally large difference between the

simulation and the experimental results requires further discussion including the addition of necessary reality-driven corrective factors. The next step is to investigate, whether the difference is due to the nature of the simulated master layer and/or the superposed model. This can be done in the following section by replacing the simulated master layer with the real system of the SEM cross-sectional images.

5.3.2 Microscopy masters

Figure 51 and Figure 52 show the results obtained by superposition of the Lumped Parameter Model unit-cells onto the thresholded SEM cross-sectional images. It should be kept in mind, however, that, in this case, different types of particle systems are compared: the experimental values are from the bcGCC system with SA latex and the SEM images relate to the nfGCC system with SB latex. Since the material properties of both the experimental and the modelled SEM system should be identical for the pigment and very similar for the binders concerned (see Table 9), three possible reasons for the difference of the curves in Figure 51 and Figure 52 come to mind:

- The two experimental coating structures are fundamentally different, especially in the lower range of binder dosages.
- There is a general discrepancy caused by the interpretation of the coating structure by the LPM.
- The literature material values chosen for modelling differ from the actual material properties.

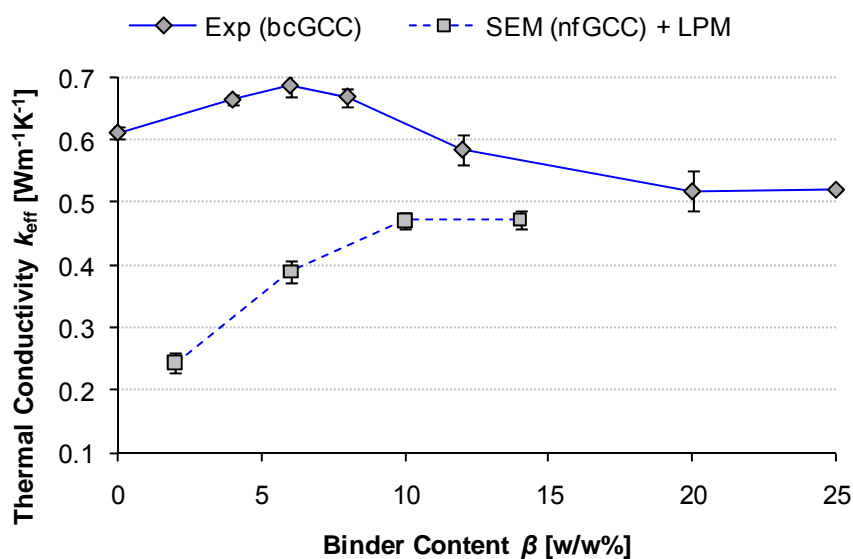


Figure 51. Effective thermal conductivity of the coating structure measured experimentally from tablet material (bcGCC, SA latex) and calculated numerically by application of the lumped parameter model compared to that applied to SEM cross-sectional images (nfGCC, SB latex). Based on paper [IV], Figure 13.a.

In contrast to Figure 49, no particle simulation is involved. Rather, it is merely the application of the model to a real coating structure (microscopy master). It can be noted in Figure 51 that the predicted thermal conductivities by the model are initially still lower than the experimentally measured ones. Also the cross-sectional porosities, or void areas, shown in Figure 52 are lower than the ones measured by mercury porosimetry, even though the trend of decreasing as a function of higher latex dose is followed very well.

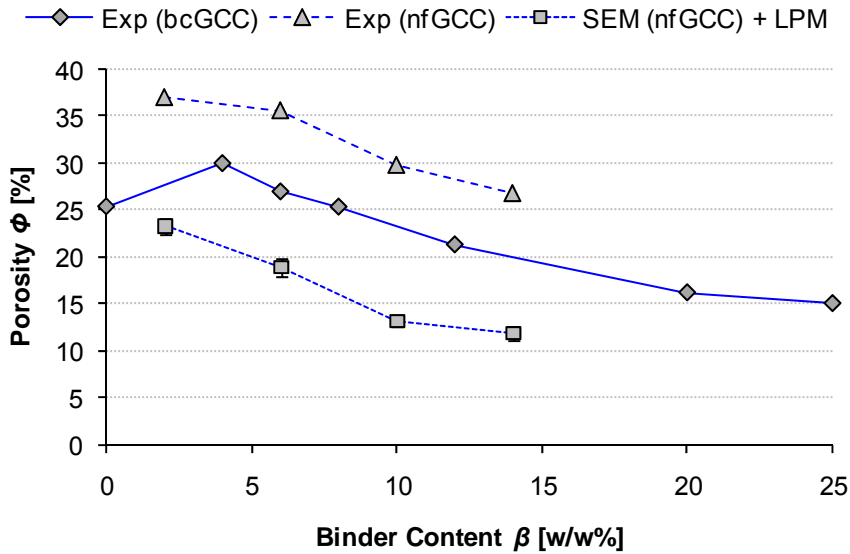


Figure 52. Porosity measured experimentally by mercury porosimetry (both bcGCC and nfGCC) and porosity calculated as the void area fraction over all sub-domains as a function of binder content from the SEM images (nfGCC, SB latex). Based on paper [IV], Figure 13.b.

It is unlikely that the difference of bcGCC and nfGCC (point a)) is accountable for the large difference in thermal conductivity seen in Figure 51. Especially since the difference is even larger in Figure 49 for the same pigment/binder system.

As for point c), one can see for the higher binder contents in Figure 51 that both curves are approaching a common level of ca. $0.5 \text{ Wm}^{-1}\text{K}^{-1}$. This is a good indication that the material value for binder in the model is of the right magnitude. This was not obvious, since Figure 49 showed a very large difference even for higher binder contents. Neither can the initially large difference in thermal conductivity be accounted for by the material value of pigment, since it is identical. Assuming an infinitely high conductivity of pigment, equation 33.1 reduces to:

$$\frac{k_{\text{eff}}}{k_f} = \frac{c}{\mu(1-a)} + \frac{c-a}{a-1} + \frac{1-a}{(\mu-1)c+1} \quad (53)$$

The point for 6 w/w% binder in the SEM data has an average LPM pigment factor of $a = 0.7884$ and binder variable $c = 0.3600$. For these unit cell properties, the maximum effective thermal conductivity (for a superconductive pigment) becomes $k_{\text{eff}}^{\text{max}} = 0.4156 \text{ Wm}^{-1}\text{K}^{-1}$. This is still significantly lower than the experimental value. The discussion about the intrinsic material values in 3.4.2 already showed that the pigment has only minor influence on the effective thermal conductivity for high intrinsic thermal conductivities. In fact, this example illustrates the great influence of the connecting phase (binder bridges in this stage of the LPM) in the effective thermal conductivity. As the interpretation of connectivity by the model is crucial, point b) of the possible reasons seem most plausible and a further discussion on skeletal connectivity is required in order to improve the simulation and to understand better the role of pigment and binder addition.

5.4 Connectivity of coating structures

The previous discussion regarding the simulated and experimental values showed a significant difference in thermal conductivity between observed and the LPM modelled

structure, mainly at low binder concentrations or binder free systems. It was hypothesised that this difference is due to the differences in connectivity of the structures. Figure 53 shows a hard sphere simulated binder free particle system; the domain alone is seen in Figure 53.a, the domain and the superimposed LPM unit cells shown in Figure 53.b. This illustrates that the problem of connectivity is twofold.

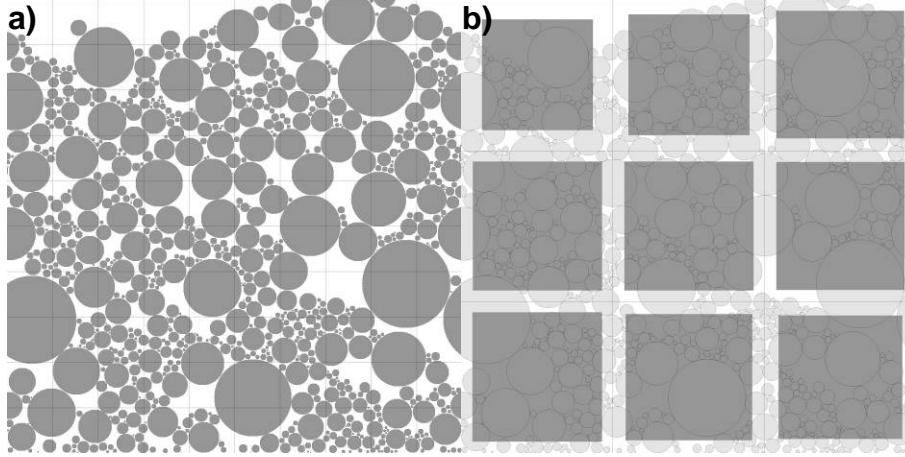


Figure 53. a) Domain of a simulated binder free coating structure. b) The same domain with superposition of the LPM unit cells. The lack of connectivity in the model is responsible for the zero value of calculated conductivity. Based on paper [IV], Figure 14.

At first, we note that the particles in the simulations are ideal circles; they only have point contacts to other particles, which is theoretically equivalent to no contact area at all. This is in contrast to real pigment particles having irregular particle shapes and shape distributions as well as adsorbed dispersant polymer on the pigment surface. Both factors effectively create a larger pigment-pigment interface, or pigment connectivity. This difference in connectivity of a binder free system is due to the nature of the simulation using rigid, ideal spheres. It is the zero conductivity difference of the simulation, Δk_0^S .

The second difference in connectivity is directly due to the nature of the Lumped Parameter Model. The original approach restricts connectivity to the binder phase alone. If no or little binder is present, there are no connecting bridges per se to take the pigment connectivity into account (see Figure 53.b), even if there were area contact between simulated pigment particles. As the previous discussion showed, this difference can be quite significant and it is not related to the cross-section (whether it is simulated or it is an SEM image), but to the model. It is the zero conductivity difference of the model, Δk_0^M . The total initial difference in conductivity, Δk_0 , (for the binder free system) in Figure 49.a, is thus:

$$\Delta k_0 = |k_{\text{eff}}(0) - k_s(0)| \quad (54)$$

and can be expressed as:

$$\Delta k_0 = \Delta k_0^S + \Delta k_0^M \quad (55)$$

The following sections will first examine ways to quantify the connectivity differences of simulated coating structure and model for binder free systems before the connectivity of binder will be further discussed.

5.4.1 Connectivity in simulated master layers

It was pointed out that the difference in structural connectivity is due to the irregular shape of real pigment particles as well as the presence of adsorbed dispersants on the

APPLICATION OF THE MODEL TO COATING STRUCTURES

Connectivity of coating structures

pigment surfaces. With a certain amount of overlapping, the point contacts between the particles will extend to contact areas. This contact area approach can be done without modifying the deposition algorithm. Merely a modification of the overlapping condition is required to make the particles seem smaller due to a “soft” surface layer. The thickness of the soft layer s_A is based on the absolute size, the radius, r_A , of a particle A :

$$s_A = \xi_A \cdot r_A \quad (56)$$

where ξ_A is the overlap factor, a coefficient of softness. Larger pigment particles appear therefore “softer” to account not only for the adsorbed poly-dispersant but also for the irregular shape of pigment particles. The overlapping condition for two particles A and B becomes then:

$$\sqrt{(x_A - x_B)^2 + (z_A - z_B)^2} \leq r_A(1 - \xi_A) + r_B(1 - \xi_B) \quad (57)$$

where $\xi_A = \xi_B$ if A and B are of the same material.

While soft particles will have a contact area, the porosity will also be reduced because the particles will form a denser packing. Porosity can therefore be used as the control parameter to identify the overlap factor of pigments. Figure 50 shows an experimentally measured porosity of 25 % versus a simulated area porosity of 32 % for the simulated structure. The question is what overlap factor (softness of pigments) would be required to match the experimental porosity at zero binder level. By performing a series of particle depositions with varying overlap factors, it was found that for a pigment overlap factor of $\xi_{s1} = 3\%$ the porosity of the binder free simulated packing largely matches the experimental porosity. Figure 54 illustrates both the hard sphere approach a) and the soft sphere approach b).

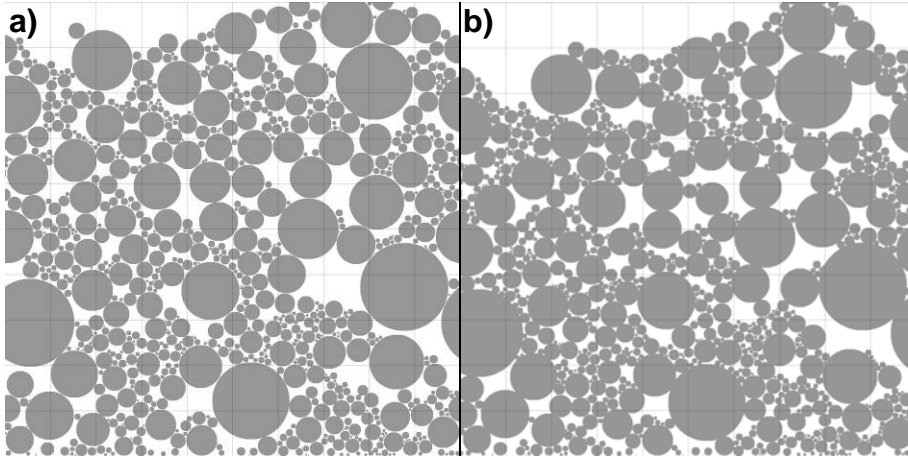


Figure 54. a) Domain of a simulated binder free coating structure using the hard sphere approach. b) The same domain with a pigment overlap factor $\xi_{s1} = 3\%$ to match the experimental porosity.

Figure 55 shows the calculated effective thermal conductivities for the simulation with rigid spheres and with a soft sphere packing to match the experimental porosity as well as the experimentally measured conductivity. It is seen that the zero binder conductivity difference of the simulation Δk_0^S is much smaller compared to the remaining difference Δk_0^M accounted for by the model connectivity. It is, therefore, vital to discuss the pigment connectivity and its role in the LPM, but it is also necessary to look at the role of soft binder in the particle packing.

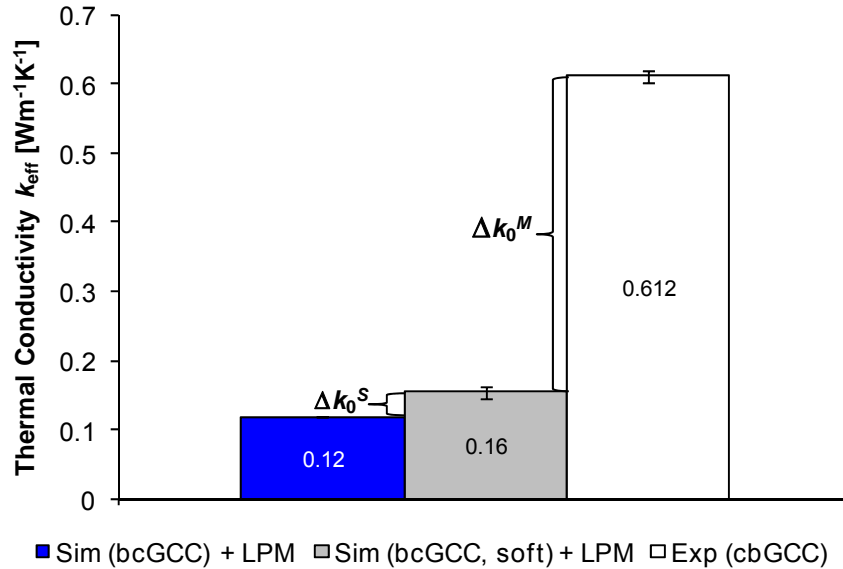


Figure 55. Effective thermal conductivities for simulations with rigid pigment spheres and soft pigment spheres ($\zeta_{s1} = 3\%$) as well as the experimental thermal conductivity for the binder free pigment structure. Based on paper [IV], Figure 15.

In addition to the soft sphere approach for pigments, it can be extended to the binder as well. The binder phase is much softer and is likely to form interdiffused layers where binder particles touch. To reflect this, the binder would need a higher overlapping factor compared to pigment. To be able to form an almost nonporous structure for binder to binder contact, an overlap factor of $\zeta_{s2} = 40\%$ would be required.

Figure 56 shows the same comparison of experimental values and simulated values for the bcGCC as in Figure 49, but the particle deposition is now made allowing an overlap of $\zeta_{s1} = 3\%$ for pigment and $\zeta_{s2} = 40\%$ for binder, the hard sphere curve is given for reference. While the general shape of the simulated thermal conductivity curve does not change compared to the hard sphere approach, the thermal conductivities of the higher binder levels come close to the experimental values and are similar to the level seen in Figure 51. This reconfirms the choice of the material value for binder and points out that the large conductivity difference (of higher binder levels) in Figure 49 is due to the deficiencies of the hard sphere approximation simulated structure.

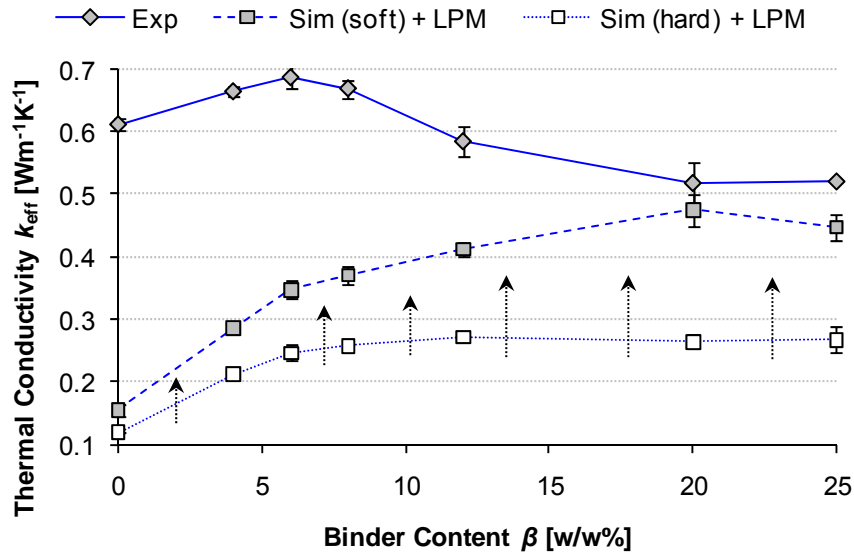


Figure 56. Effective thermal conductivity of the coating structure measured experimentally from tablet material and calculated numerically by application of the lumped parameter model to simulation deposited particle system with the soft sphere approach ($\zeta_{s1} = 3\%$, $\zeta_{s2} = 40\%$). Based on paper [IV], Figure 16.a.

Figure 57 shows that the porosities for the system allowing particle overlap agree better with experimental values, especially at higher binder levels. Despite the generally better agreement for higher binder contents, the thermal conductivities of lower binder levels are still distinctly less than the experimental values. Because the conductivity difference of the simulated structure should be accounted for in this curve, the remaining difference would be that caused by the connectivity interpretation of the Lumped Parameter Model alone. This can be examined by comparing directly the two types of master layers to each other.

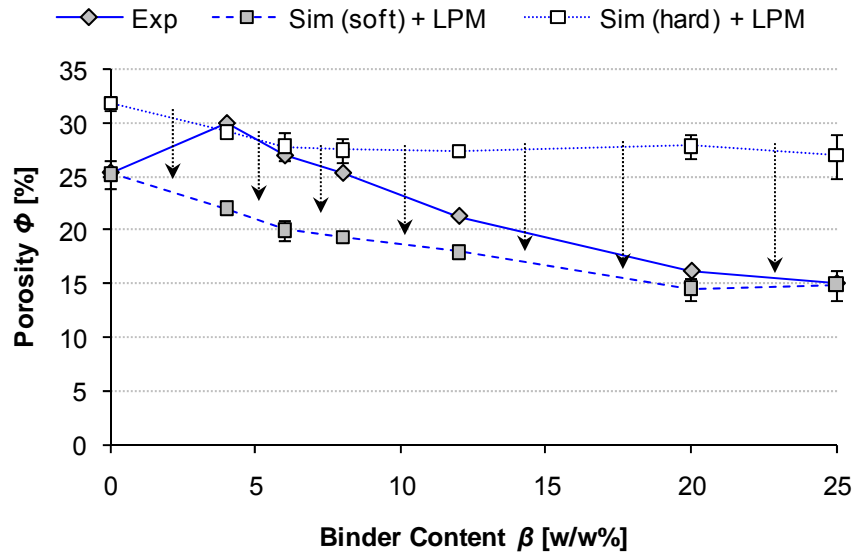


Figure 57. Porosity measured experimentally by mercury porosimetry and porosity calculated as the void area fraction over all sub-domains for the soft sphere approach as a function of binder content. Based on paper [IV], Figure 16.b.

5.4.2 Comparing the connectivity of master layers

So far the discussion has focused on the calculated values of the Lumped Parameter Model for the simulated structures and the SEM cross-sections in relation to the experimental values. However, in order to characterise the particle deposition simulation independently of the model, it is required to compare the model data for the SEM cross-sectional images directly with the model data of the corresponding simulated structures. This comparison is given in Figure 58 for the thermal conductivity and in Figure 59 for porosity.

The simulations were done using the same overlapping parameters as for the bcGCC system ($\zeta_{s1} = 3\%$ for pigment and $\zeta_{s2} = 40\%$ for binder) and, for the model calculation, the original LPM approach allowing merely binder connectivity was used. With the exception of the 10 w/w% binder point, the thermal conductivities for calculated SEM cross-sections and simulated structures, as shown in Figure 58, agree remarkably well. The calculated porosities, shown in Figure 59, differ slightly more for 10 and 14 w/w%.

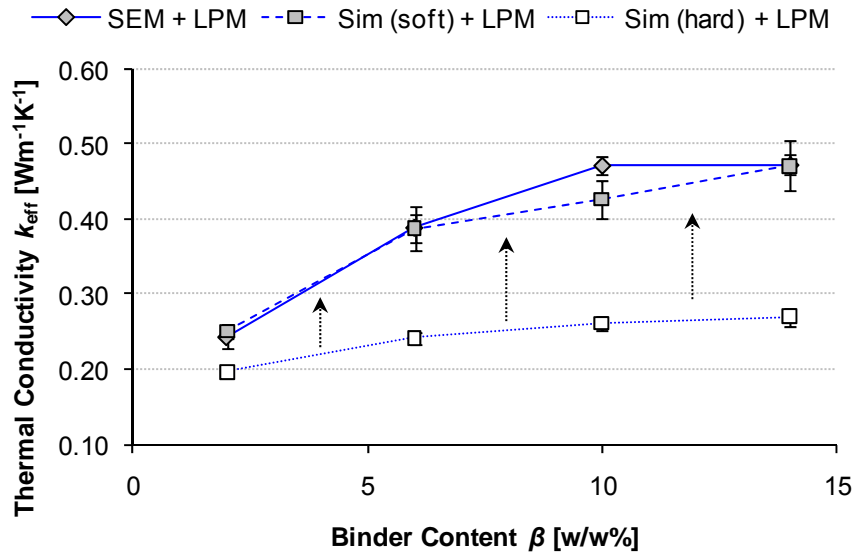


Figure 58. Effective thermal conductivities calculated with the Lumped Parameter Model for both the SEM cross-sectional images and for the corresponding simulated domain with the soft sphere approach ($\xi_{s1} = 3\%$, $\xi_{s2} = 40\%$). Based on paper [IV], Figure 18.a.

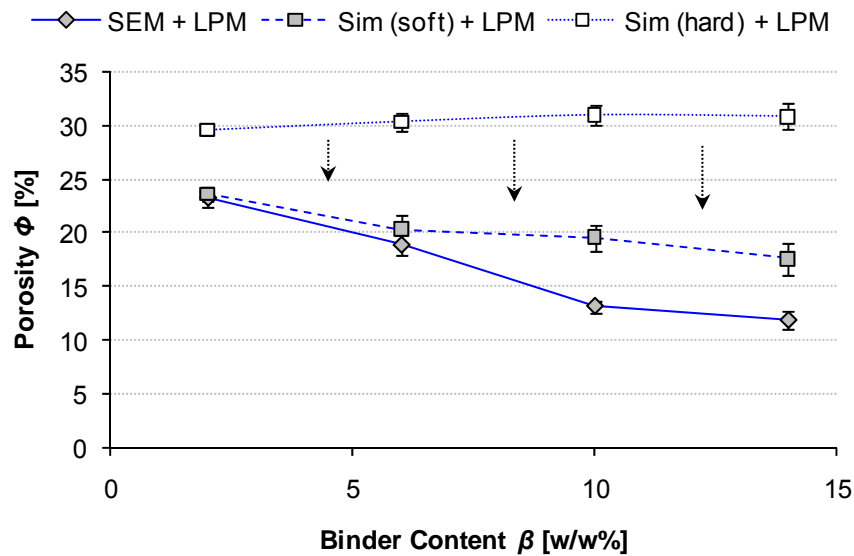


Figure 59. Porosity calculated as the void area fraction over all sub-domains for the SEM cross-sectional images and the simulated domain using the soft sphere approach. Based on paper [IV], Figure 18.b.

The previous discussions illustrated the great influence of the binder connection phase on effective thermal conductivity. The fact the thermal conductivities agree so well for both master layers is, therefore, an indication that, on the one hand, the binder amount in the SEM cross-sectional images was correctly identified by the thresholding algorithm and, on the other hand, that softening of the simulated particles leads to a structure close to the case of a real coating cross-section.

The softening of particles can also be regarded as “out of plane” movement. This is illustrated in Figure 60 for the case of pigment a) and binder b). In case of a zero binder system, the softening effectively simulates the lateral movement of particles under the action of meniscus forces during real-case coating structure drying, as investigated by

Laudone *et al.* /67/. The limit of the out of plane movement for pigment is defined by the closest nearest neighbour packing of hard spheres in 3D (Figure 60.a). That the softening of pigment applies across the range of binder dosages fitting the simulation/model and reality, suggests that final packing in a dried coating layer is defined by a hard sphere constraint model, thus supporting the work of Laudone *et al.* /67/.

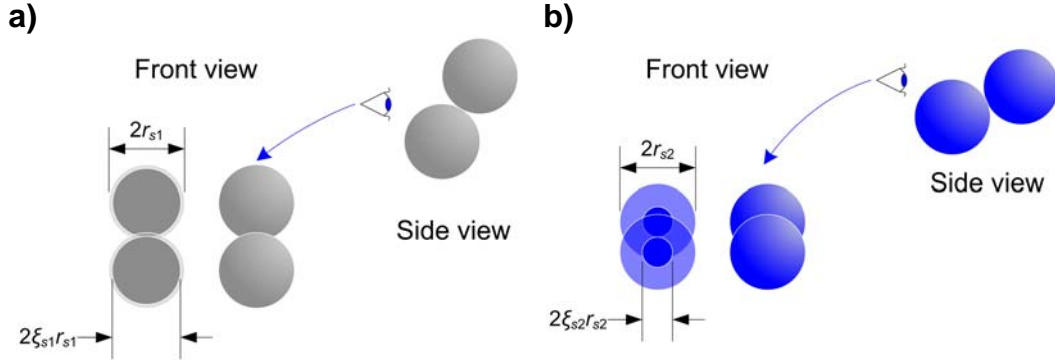


Figure 60. Soft sphere approach regarded as an out of plane movement of particles - showing the front view (as in the simulation) and side view (quasi 3D) of soft sphere particles for a) pigment and b) binder.

5.4.3 Model connectivity

The previous discussion showed that by allowing particle overlap during the particle deposition, the simulated masters and the real cross-sections can be regarded as equivalent. The remaining conductivity difference Δk_0^M is therefore the missing pigment connectivity. The discussion on alternate model configurations in 3.5.1 introduced the use of “pigment bridges” to connect the unit cells instead of, or in addition to, binder bridges. Finding the model pigment connectivity becomes an inverse mathematical problem of the system of equations 34 and 35, which need to be transposed to $a' = f_a(k_e, c')$ where $c' = f_c(\phi, a')$, so that for a given effective thermal conductivity k_{eff} (equal to the experimental value, k_{exp}) and a given unit cell porosity ϕ the new pigment factor a' and the pigment connectivity variable c' are returned. In other words, it is the question of what amount of pigment needs to be shifted from the central pigment phase a to the bridging function c' in order to get the measured thermal conductivity while maintaining the unit cell porosity:

$$a^2 = a'^2 + 2c'(1 - a') \quad (58)$$

This is illustrated qualitatively in Figure 61. The calculations involve solving a fourth degree polynomial equation. Hence, there will be four different solutions, of which at least one should be physical.

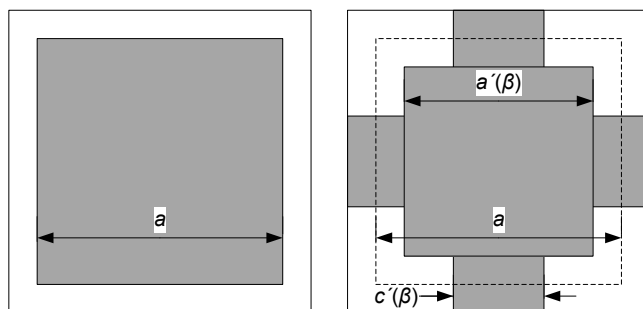


Figure 61. Shift of pigment from the central phase to the bridging phase while maintaining the area fractions of the unit cell.

When using the soft sphere approach for the bcGCC system, and allowing a pigment overlap of $\xi_{s1} = 3\%$, the sub-domains of the binder free structures have an average porosity of ca. 25 % and an average pigment factor of $a = 0.8643$ for the original unit cells. To reach the experimentally measured thermal conductivity of $k_{\text{exp}} = 0.6 \text{ Wm}^{-1}\text{K}^{-1}$ at constant porosity, the corrected pigment factor becomes $a' = 0.8225$ along with the new pigment connectivity variable of $c' = 0.1926$. This is merely the initial pigment connectivity of the binder free system since both a' and c' are a function of the binder dosage. When increasing the binder dosage, the total connectivity increases. In terms of the unit cell it means that the width of the connecting bridges increases. However, while doing so, part of the pigment connectivity is being replaced by binder connectivity, effectively shifting some of the connecting pigment back to the central pigment phase. This could be an explanation for the maximum of thermal conductivity observed for the experimental values. Starting with pigment connectivity only, the binder-induced connectivity, and therefore the total conductivity, is increasing when adding binder. Since, at the same time, the pigment connectivity is continuously replaced by binder, the thermal conductivity goes through a maximum when the inherently lower conductivity of binder begins to dominate the total connectivity of the structure. Further addition of binder acts to increase the connectivity (width of the bridges in the unit cells), but it lowers the conductivity because of the insulating nature of binder compared to pigment. However, as we shall see in the following section, this proposal does not account totally for the local magnitude of the maximum.

5.5 Connectivity modelling

Both equations 34 and 35 form a fifth order polynomial system, which can be solved numerically to fit the effective modelled thermal conductivity of a unit cell to the experimentally measured thermal conductivity. The unit cell is defined by the void area fraction (porosity) as well as the area fractions of pigment and binder. With the given area fraction of binder that forms the binder connectivity, one can calculate the pigment connectivity c' required to achieve the experimentally measured thermal conductivity for the corresponding pigment and void area fractions of the unit cell. This so called connectivity modelling approach shall be used in chapter 6 to further investigate the structural role of the binder and fluid phase.

Figure 62 shows the calculated pigment connectivity c' along with the given binder connectivity c of the unit cells for different binder dosage. It can be seen that, in contrast to the earlier prediction, the pigment connectivity c' decreases for binder concentrations up to 8 w/w% and then levels at higher binder contents. The fact that the pigment connectivity at the initial addition of binder is lowered reconfirms the observations made by Gane *et al.* /40/. For low concentrations of binder, colloidal forces can drive the latex particles away

from the bulk water phase of the forming pores towards the pigment contact points. This effective rejection of the binder from the liquid phase of the pigment could be one reason for causing a disruption of the pigment packing for lower concentrations of latex particles and thus a decrease in pigment connectivity factor c' for those concentrations. For higher concentrations of binder, the phase separating placement of latex particles at pigment contact points reduces, as the colloidal force imbalance of latex particles in presence of other latex particles will be smaller as the environment contains more binder. Pigment connectivity will therefore stabilise itself at higher binder contents.

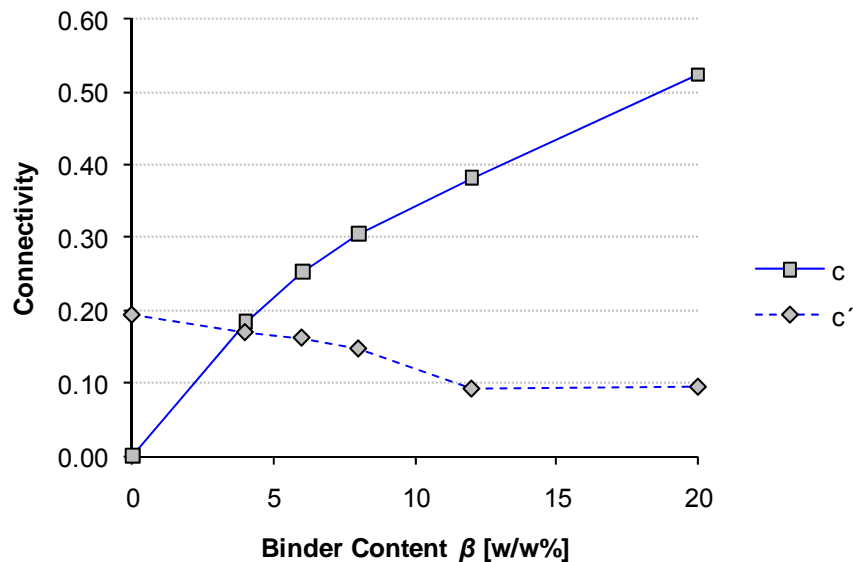


Figure 62. Extended unit cell pigment connectivity c' and binder connectivity c as a function of binder content. Based on paper [IV], Figure 19.

5.6 Modelling using alternate unit cell modes

Aside from describing pigment connectivity as an additional parameter in connecting the unit cells, one could also refer to a different skeletal structure, i.e. configuration of phases, within a unit cell. This concept was introduced in 3.5.3 and shall now be discussed in comparison with the experimental data. Figure 63 shows the experimental data of the bcGCC as well as the theoretical curves for the unit cell in Mode I (Figure 64.a) and Mode III (Figure 64.b). The theoretical curves are based on the measured porosities as well as the densities and volume fractions of the solids.

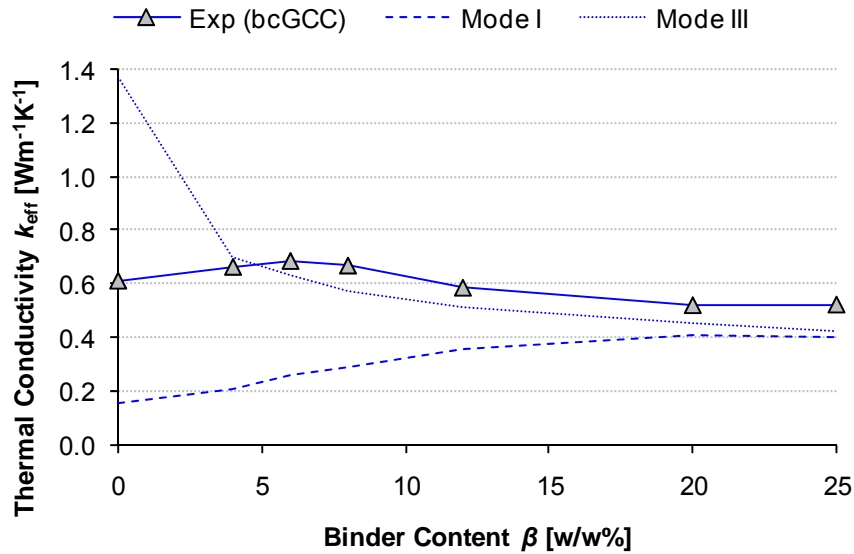


Figure 63. Experimentally measured thermal conductivities in comparison with the theoretical model curves for mode I and III.

As the discussion in 5.3 showed, Mode I displays the expected monotonic increase in thermal conductivity for an increasing binder content. In contrast to this development, Mode III shows a decrease in thermal conductivity for increasing binder contents, however, on an initially distinctly higher level. In this way, the thermal conductivities for binder dosages of 4 w/w% and higher, come much closer to the experimentally measured values. This would indicate that for these binder concentrations the pigment has a more dominant role in forming the skeletal structure and thus in determining the effective thermal conductivity. While at the binder concentration of 25 w/w% both modes can be regarded as equivalent, for the binder free system the thermal conductivity of Mode III is overestimated because the pigment is forming the continuous phase. In this case, Mode III is the “inversion” of Mode I and one can combine both modes in a weighted composite structure to balance the role of pigment as a skeletal material and the interconnected pores. Figure 64.c exemplifies a binder containing composite of Mode I and Mode III. The binder free data shown in Figure 63 would yield a share of 62 % conduction in Mode I and 38 % conduction in Mode III.

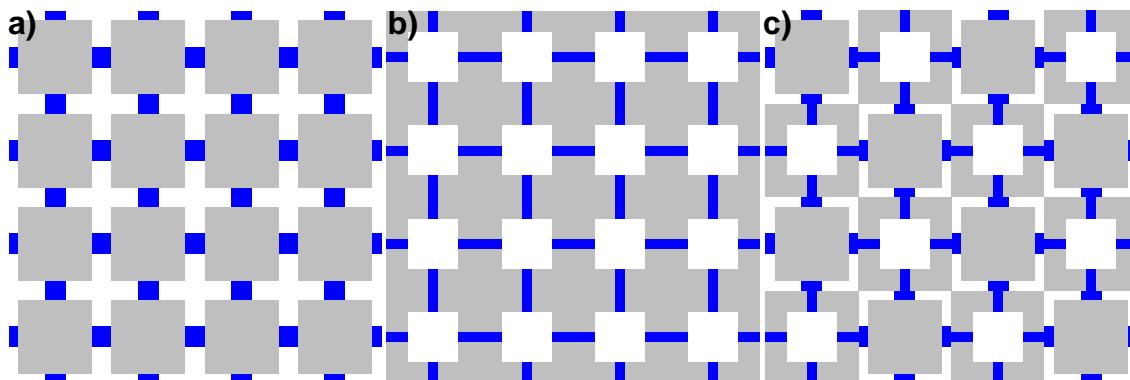


Figure 64. Skeletal structure of unit cells in a) Mode I, b) Mode III and c) a composite structure of 50 % Mode I and III.

While it is visually very tangible to describe the pigment-pigment connectivity and the interconnection of pores in a porous medium as a combination of unit cell modes, the approach using a pigment connectivity parameter, while keeping the unit cell in a fixed

configuration, is more powerful in separating and quantifying both pigment and binder connectivity. Therefore, the latter approach will be followed in connectivity modelling to assess the role of the phase properties.

5.7 Summary

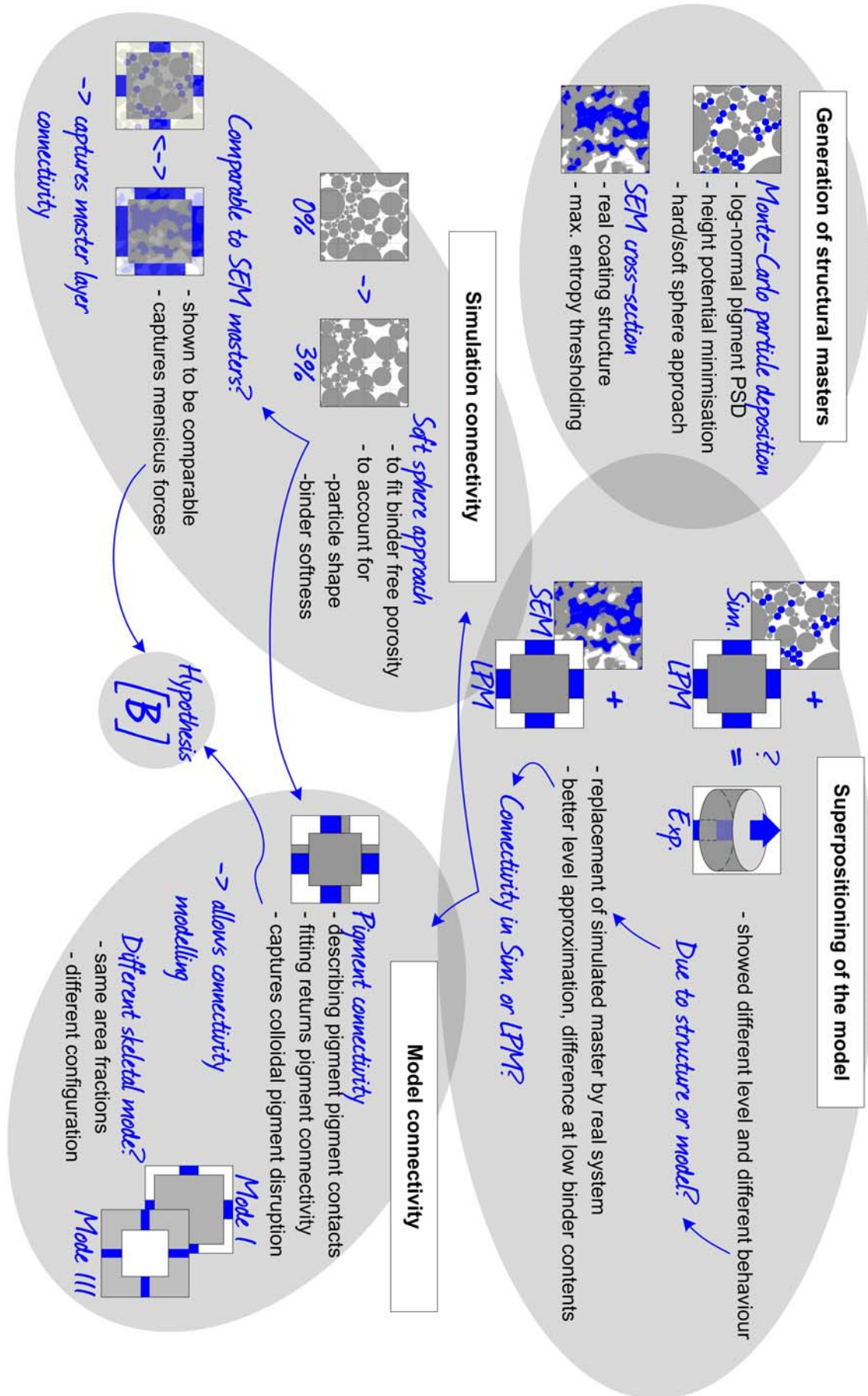
A Monte Carlo simulation-based particle deposition was applied to create two-dimensional coating structures. In addition, real coating structures in the form of cross-sectional SEM images were examined utilising a maximum entropy thresholding algorithm to identify the phases. Both systems, simulated and microscopy-derived, acted then as master layers for the generation of parameters of the Lumped Parameter Model. This provided information concerning the limitations in correlation between the modelled thermal conductivities of the simulated structures and the corresponding measured values. In direct comparison with both the connectivity derived from the microscopy master data and from the simulated masters, it was seen that the model interpretation of connectivity is also an essential factor. Identifying that the hard sphere particle simulation underestimates the contact area of pigment, due to it ignoring the adsorbed polymer dispersant layer and particle surface irregularity, it was possible to define a pigment particle overlap for the case when no binder was present and a binder particle overlap to account for its softness. Adopting the particle overlap in the simulation, it was shown that the soft sphere simulated master layers can be regarded as equivalent to the microscopy cross-sections. It was further discussed that the softening effectively simulates the lateral movement of particles under the action of meniscus forces during drying of real coatings, where the final packing is defined by a hard sphere constraint model. This can be seen as one element in contributing to hypothesis [B].

Furthermore, the equivalence of the master layers showed that the remaining difference between model and experimental values is due to the model interpretation of the master layer. A modified set of parameters was defined for the LPM, which incorporated the factor of pigment connectivity. It was discussed that surface and colloid chemistry factors cause binder to accumulate first at pigment nodal points, which acts to disrupt the pigment packing at binder doses up to 8 w/w%. It was shown, by fitting the modelled thermal conductivities to the experimental values, that the pigment connectivity is in fact lowered at the binder concentrations for which pigment disruption occurs.

It is proposed, therefore, that these methods of imaging, pore structure analysis and thermal conductivity can be used to identify and parameterise subtleties in skeletal connectivity in real colloiddally interactive particulate systems, based on deviations between simulations and modelling, and experimental values. This is the second element in completing support for hypothesis [B].

- [B] *Measurement and modelling* of the thermal conductivity can reveal both colloidal and mechanical interactions of the components acting during formation of the structure.

5.8 Structural modelling thread



6 MODELLING THE EFFECT OF PHASE PROPERTIES

6.1 Background

The discussion in chapter 5 showed that the effective thermal conductivity of porous multiphase systems is not only defined by the thermal conductivities of the materials involved, but, even more importantly, by the structural interaction of the components. Since the materials themselves, particularly the binder phase /12/, can have a distinct effect on the coating structure, this chapter further examines the role of latex binder on the coating structure and its resulting influence on the effective thermal conductivity.

This comparison is carried out in three ways. At first, the thermal diffusivities of the model coatings with different lattices are measured. Subsequent calculation of the corresponding thermal conductivities initiates a discussion regarding the role of connectivity in these systems. Secondly, with the assistance of mercury porosimetry measurements of the model systems, the role of porosity and colloidal forces in consolidation are further investigated. Simulations of idealised two dimensional particle packings are also undertaken to complement and compare with the porosimetry data. The role of connectivity can be further developed by fitting the Lumped Parameter Model to the measured thermal conductivities and porosities (connectivity modelling). This permits separation of the effects of porosity and particle packing characteristics from that of the connectivity formed by the binder. While the discussion in this chapter focuses on thermal conductivity, the elucidation of coating structure using these techniques is of fundamental general interest.

While the binder has an effect on the coating structure and thus on the effective thermal conductivity, the fluid phase of the final coating structure becomes an important factor in processes where interaction with liquids are common. For drying operations, whether in the coating process, in heatset web-offset, or other printing processes, liquid needs to be evaporated from the porous coating layer. This requires basic knowledge of the effective thermal properties of liquid saturated, or partially saturated, coatings, and, on the other hand, also an understanding of how the vaporisation of liquids from a porous paper coating takes place, both at its initiation and its progress to completion within the porous network structure and its interface with the surrounding environment.

The second part of this chapter therefore examines how liquids, e.g. mineral oil as an ink component or water as in fountain solution, change the effective thermal conductivity when air, the fluid in the pores of the dry coating, is replaced by a given liquid. A further aim is also to discuss the use of the Lumped Parameter model to describe the thermal conductivity of liquid saturated structures and to determine the liquid vaporisation behaviour as a function of the corresponding coating structure.

6.2 Binder conformability

6.2.1 Materials

The pigment binder system, as discussed both in section 4.3 and chapter 5, is now compared in structures of the same pigment (bcGCC) using latex binders of different glass transition temperatures (T_g). Three types of latex binders are studied, each independently at dose levels of 0, 4, 6 and 8 w/w% based on pigment. The binders were chosen to cover a range of glass transition temperature, labelled “soft”, “medium” and “hard”, and had slightly different particle sizes. Furthermore, the medium and hard were based on styrene acrylate, whereas the soft was based on styrene butadiene. For the purposes of this study, the impact on packing and consolidation related primarily to the physical and interactional

responses of the binders, and not their internal polymer chemistry. Table 11 lists the particle data and the thermophysical properties of the materials.

Table 11. Summary of particle data and thermophysical properties of the pigment binder systems.

Component:	Soft	Medium	Hard
Latex	SB⁸	SA⁹	SA¹⁰
Dosages [w/w%]	4, 6, 8	4, 6, 8	4, 6, 8
Glass transition temp. [°C]	-7	5	23
Particle size [µm]	0.13	0.20	0.15
Thermal conductivity [Wm ⁻¹ K ⁻¹]	0.25	0.21	0.21
Specific heat capacity [Jkg ⁻¹ K ⁻¹]	454.8	559.8	559.8
Density [kgm ⁻³]	1 025	1 100	1 040
Pigment	bcGCC	bcGCC	bcGCC
Thermal conductivity [Wm ⁻¹ K ⁻¹]	2.7	2.7	2.7
Specific heat capacity [Jkg ⁻¹ K ⁻¹]	880	880	880
Density [kgm ⁻³]	2 700	2 700	2 700
PSD [w/w%]			
< 5 µm	93	93	93
< 2 µm	60	60	60
< 1 µm	40	40	40
<i>d</i>₅₀ (weight median) [µm]	1.6	1.6	1.6

The particle packing simulations were performed adopting the method introduced in 5.2.2. For the simulations, the binders were expressed as mono-size rigid spheres. Deviation in observation from this idealised hard sphere simulation is subsequently used to provide the understanding of the physical deformation properties. Figure 65 shows examples of deposited particle systems for the three different types of binder used. The deposition simulation is subsequently modified to provide for latex softness in respect to a proportional “liquefaction”, effectively differentiating between latex-filled pore space and that remaining void.

⁸ Soft: DL 980, Trademark of the Dow Chemical Company

⁹ Medium: Acronal S 360 D, Trademark of BASF AG

¹⁰ Hard: Acronal S 728, Trademark of BASF AG

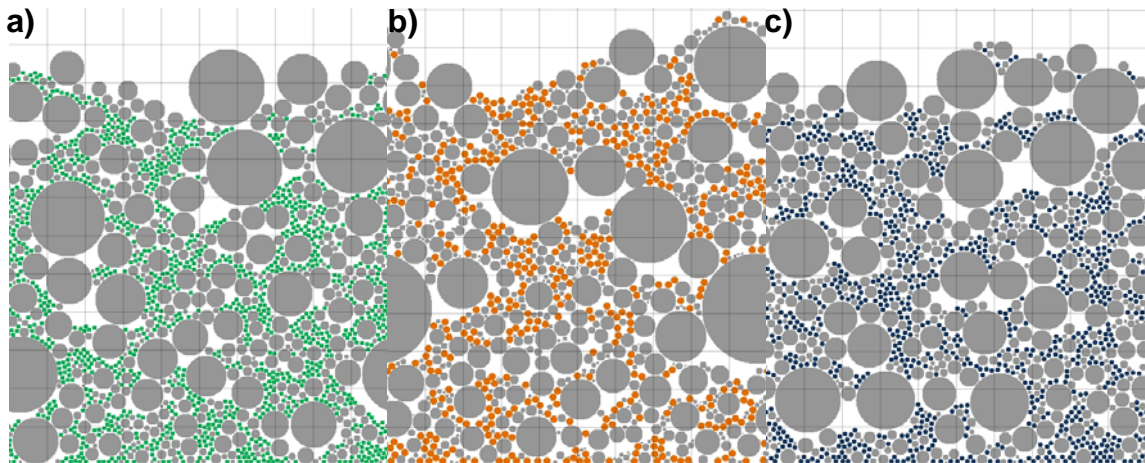


Figure 65. Samples of the 2 dimensional hard sphere particle packing simulation domains containing bcGCC pigment as well as a) soft, b) medium and c) hard latex particles. Based on paper [V], Figure 2.

6.2.2 Effective thermal conductivity and pore structure

Figure 66.a shows the thermal conductivities calculated from the measured thermal diffusivities. One can see that the thermal conductivities of hard latex containing structures are generally higher than those of the medium and soft latex structures.

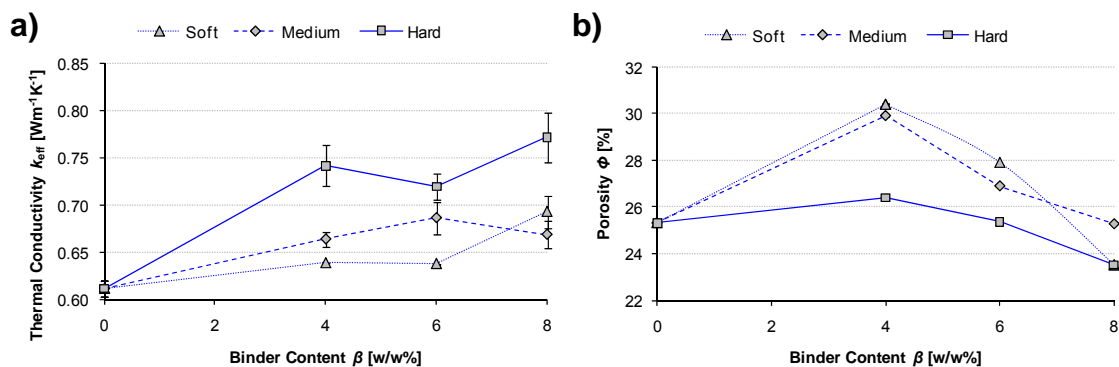


Figure 66. a) Thermal conductivity as a function of binder content for soft, medium and hard latex. Based on paper [V], Figure 11. b) Porosities measured by mercury porosimetry for tablets with soft, medium and hard latex. Based on paper [V], Figure 12.

The same general trend can be seen in the porosities shown in Figure 66.b. The hard latex structures show a lower porosity. The level of thermal conductivity depends, therefore, to some extent on the packing density of the system. However, Figure 66.a also shows that there is a local extremum in the curves of hard and medium latex, which cannot be explained by porosity only.

The discussions in 4.3.3 and 5.4.3 showed that the local maximum of the thermal conductivity for the medium latex at a binder concentration of around 6 w/w% is due to improved connectivity of the structure. This is generated by binder addition acting colloiddally to disrupt the pigment packing, centring itself between the pigment particle contact points, and becoming partly compressed at these structural nodes under the high capillary consolidation pressures, thus providing disproportionately greater connectivity. When adding yet more binder, the inherently lower thermal conductivity, compared to pigment, becomes more dominating and the effective thermal conductivity of the system is lowered.

The hard latex behaves differently amongst the trio. When initially adding small quantities of the hard latex, there is a large increase in thermal conductivity because there is the least disruption of the pigment packing. This is observed as the lowest increase in porosity shown in Figure 66.b. A feature studied further in the later modelling of connectivity. Adding more of the hard sphere latex now lowers the pigment to pigment contact, and, therefore, acts disruptively as hard latex spheres are placed at the nodal points of pigment contact. While the hard latex thus far behaves similarly to the medium latex, it is, however, not conformable under the consolidation forces, and therefore acts as a hard sphere, which, by definition, has little or zero connectivity to a neighbouring hard particle. Therefore, in contrast to the medium latex acting at pigment nodal points to increase the connectivity of pigment particles, even though disruption of the packing might occur, the hard sphere latex, because of its low contact to pigment, reduces connectivity, thus reducing thermal conductivity at this structural configuration.

In terms of porosity, the soft latex behaves very similarly to the medium one. However, the thermal conductivity increases slower upon latex addition and reaches the level of the maximum thermal conductivity shown by the medium latex at a level of 8 w/w%. Further data would be required to say whether there is truly a maximum at this concentration or if conductivity can rise even further by adding soft latex, rather unlikely in the limit of high binder dose given the insulating nature of the material. A reason for the slower increase in thermal conductivity could be that it begins to insulate the system more efficiently as well as providing connectivity between the pigment particles at the same porosity, i.e. it begins earlier to “fill” the system. When comparing the pore size distributions of soft and medium latex tablets (shown in Figure 67), one can see that while having similar total porosities (also compare Figure 66.b), the soft latex addition initially creates more fine pores and then progressively reduces the volume associated with the larger pores, converting many to medium-sized pores – note the larger volume of smaller pores in the range of ca. 0.02-0.1 μm . The same porosity, but a larger number of fine pores, in turn means a more tortuous path for the transport of heat, and most likely through more of the binder as it is conformed by extrusion and compression to distribute itself throughout the structure. Therefore, though connectivity is a necessary factor for conductivity it is not a sufficient controlling factor, in that the complexity of the skeletal structure and the resultant pathway length (tortuosity) is the final structural deciding parameter, which, in combination with the material properties and their relative arrangement, defines the conductivity.

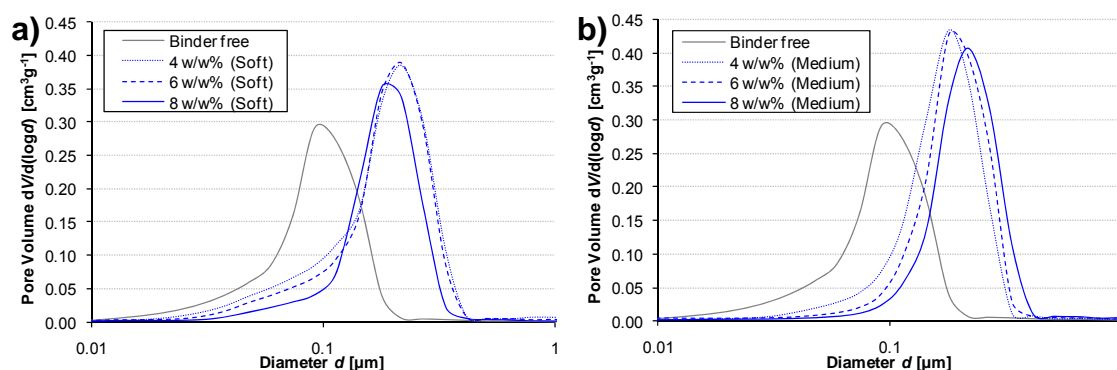


Figure 67. Pore size distribution for a binder free pigment tablet as well as distributions for tablets containing 4, 6 and 8 w/w% of a) soft latex binder (based on paper [V], Figure 13) and b) medium latex binder (based on paper [V], Figure 14).

This discussion shows that both the particle packing (porosity) and the connectivity are important in determining the effective thermal conductivity of the coatings. Therefore, both parts will be discussed in further detail in the following sections.

6.2.3 Porosity and particle packing

Performing simulations of hard sphere particle depositions elucidates the study of the effect of the different latex particle sizes on the particle packing, whilst separating this from the effect due to compression. Since the deposition algorithm is merely based on a minimisation of the height potentials of ideally rigid particles, the role of colloidal interactions and particle dispersion in forming the packing structure of real systems cannot be captured, but the role of latex softness can be studied further.

Figure 68 shows the simulated porosity data in comparison to the measured values. It is observed that the simulations for the binder free particle system greatly overestimate porosity. It should be noted that there is a fundamental difference in the packing density and resulting porosity for two-dimensional systems, as in the simulations, compared with three-dimensional systems as in the consolidation of real coating colours. Two-dimensional close packing shows a comparatively higher packing density. The highest packing densities are achieved for hexagonal close packing. A 2D close packing of monodisperse circular particles would show a minimum porosity of ca. 10 % while a close packing of spheres in 3D delivers a minimum porosity of 26 %. For random close packing of spheres the porosity increases to ca. 36 %. This difference between the hexagonal close packing and the real packing is a measure of the randomness of the system. The same holds for the two-dimensional case, such that 2D relative effects are 3D indicative.

The fact that the simulated porosity of the two-dimensional binder free particle system delivers a higher porosity than the measured three-dimensional system (Figure 68), even though in an ordered system a higher packing density would be theoretically possible in 2D, suggests that there is less randomness in the real system, resulting in improved packing density. This less random behaviour of the real system can also be seen as an indication of the presence of an “ordering force”. Since the simulations completely neglect the dispersion forces present in coating colours, it seems likely that these create improved particle packing during consolidation of a pigment system.

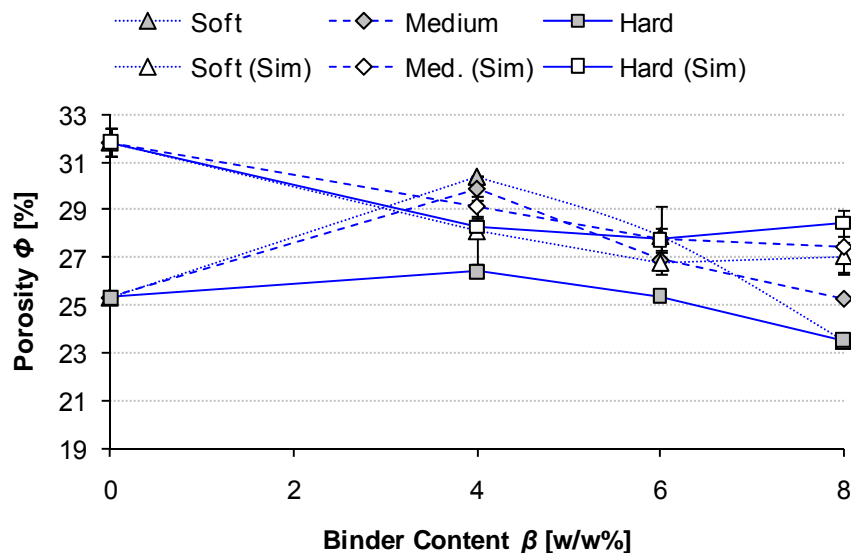


Figure 68. Porosities measured by mercury porosimetry as well as porosities calculated for simulated domains of 2D deposited pigment and latex particles. Based on paper [V], Figure 14.

A similar overestimation of porosity is found for the hard latex, indicating a similar role for the hard sphere latex as for the ideally dispersed pigments. The hard latex spheres add only little to the randomness of the particle packing.

Figure 68 also shows that the simulated porosities, particularly of the medium latex, are closer to the measured values. This means that the medium latex system is similar in its random nature as the simulated two-dimensional structure. Gane *et al.* /40/ showed previously that due to colloidal forces, latex particles tend to be placed between pigment nodal points. This observed effect of pigment disruption creates a more random structure in the particle packing, and the coating structure expands to a state that now can be found to show similar porosities as in the two-dimensional random packing. This confirms both the stronger pigment disruption resulting in generally lower thermal conductivity for the medium latex, but also the more important role of binder connectivity in creating an extremum in thermal conductivity for a critical binder concentration.

The particle deposition simulation of pigment binder systems uses ideally hard spheres for latex. This might not be the case in practice for the soft or medium latex. We therefore consider the effect of “liquefaction” of latex on the porosity of the simulations. Before the deposition of particles in the simulation (Figure 69.a) a certain percentage of random binder particles is removed from the domain (Figure 69.b) and combined to the volume of liquefied latex (Figure 69.c). This volume is subtracted from the final simulated porosity. Thus, liquefaction can be seen as a parameter of the latex conformability and its ability to ideally fill pores.

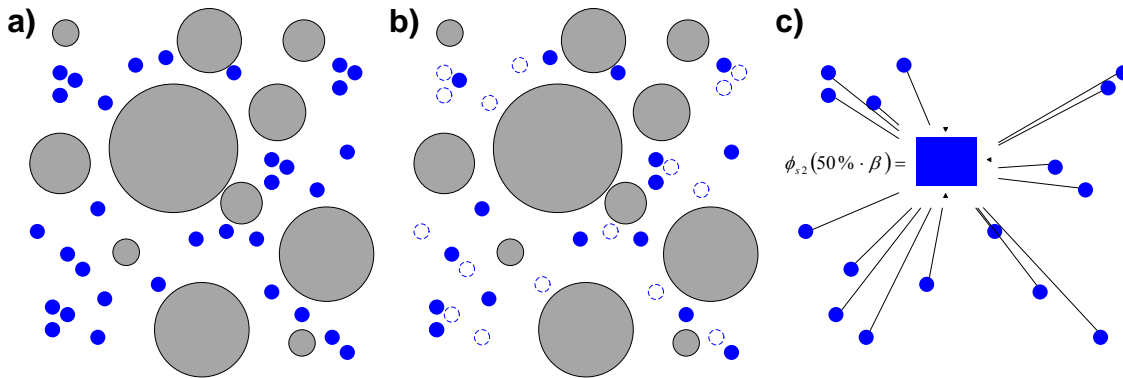


Figure 69. Liquefaction of latex: from the original domain a) $x\%$ of binder particles are removed b) and combined to a volume liquefied latex c). This figure illustrates 50 % liquefaction.

For the soft latex, we take the simulated porosity of the binder free particle system and subtract the volume fraction of binder for a given dosage. This equates to complete liquefaction of latex and the simulated porosity for liquefied latex becomes:

$$\hat{\phi}_f(\beta) = \phi_f(0) - \phi_{s_2}(\beta) \tag{59}$$

Figure 70 presents the measured mercury porosimetry data, the simulated porosity for the random packing of latex particles and the calculated porosity for full liquefaction of the soft latex. As expected, the liquefied latex lowers the porosity compared to the particle simulation. While the general values are not as close to the mercury porosimetry data as for the latex particle simulation, they better reflect the linear decrease in porosity for higher binder dosages.

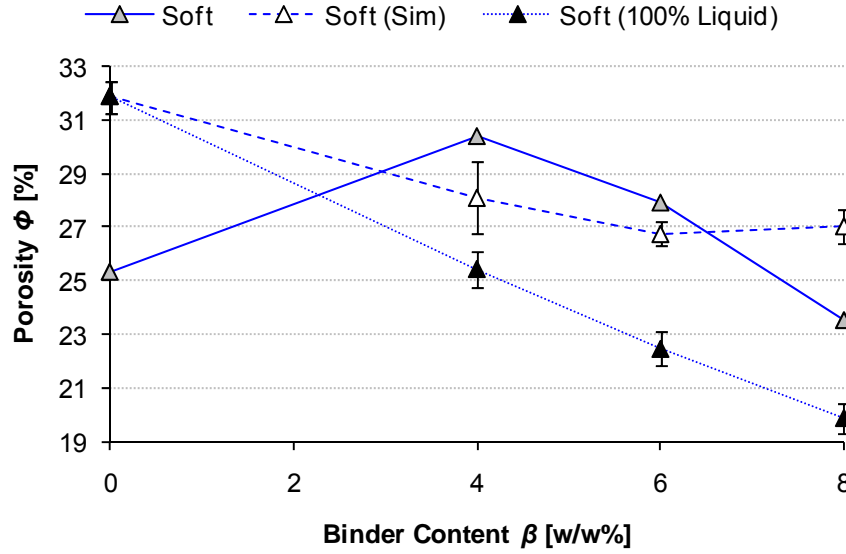


Figure 70. Porosity as a function of soft binder content. The simulated porosities follow the rigid sphere model. Also given are the simulated porosities based on the binder free simulated porosity minus the binder volume fraction. Based on paper [V], Figure 16.

Similar to the complete liquefaction of the soft latex, the medium latex is adapted by allowing, as a first approximation, half of the latex volume to be liquefied, whereas the other half of latex remains as particles in the simulations. The simulated porosity for semi-liquefied latex is:

$$\hat{\phi}_f(\beta) = \phi_f(50\% \cdot \beta) - \phi_{s_2}(50\% \cdot \beta) \quad (60)$$

Figure 71 shows the result for porosity of semi-liquefied latex. Very similarly to the soft latex in Figure 70, the porosities show lower values, but nonetheless seem to reflect the decreasing trend of porosity quite well. The liquefaction effect, however, seems to be disproportionately less than for the soft latex, and we can assume that probably much less than 50 % of the medium latex is acting as a liquefied component within the structure formation despite the drying temperature of 60 °C.

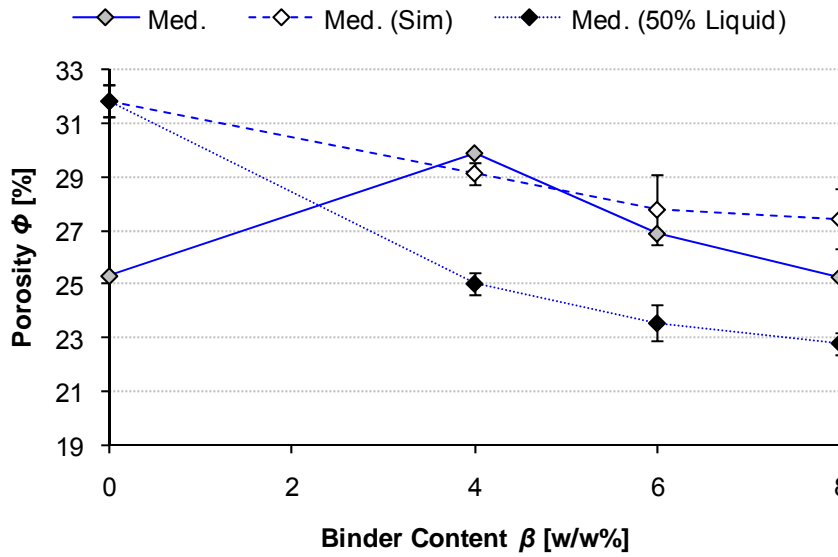


Figure 71. Porosity as a function of medium T_g binder content. The simulated porosities follow the rigid sphere model. Also given are the simulated porosities with 50 % binder as rigid spheres and 50 % of the binder volume fraction subtracted from the simulated porosity. Based on paper [V], Figure 17.

6.2.4 Effect of binder on connectivity

As already pointed out in the comparison of the Composite-Layer and Lumped Parameter Model (3.6), the Composite-Layer model can be used to define the upper and lower limit of the thermal conductivity of a porous medium for a given volume fraction of phases. Figure 72 shows the limits for the medium latex system as already seen in Figure 26. The boundaries are calculated for the measured porosities as the fluid (air) volume fractions, ϕ_f , and the volume fractions of pigment and binder, ϕ_{s1} and ϕ_{s2} , respectively. The upper limit is obtained by parallel arrangement of thermal resistors; the lower limit is defined by serial thermal resistors. Figure 72 adds the experimental data in relation to the limits imposed by the CLM showing that there is theoretically a wide interval of possible thermal conductivities. The experimental values lie well within this interval, but in order to be able to describe the mechanisms that lead to the experimentally observed thermal conductivities this model alone is clearly not satisfactory.

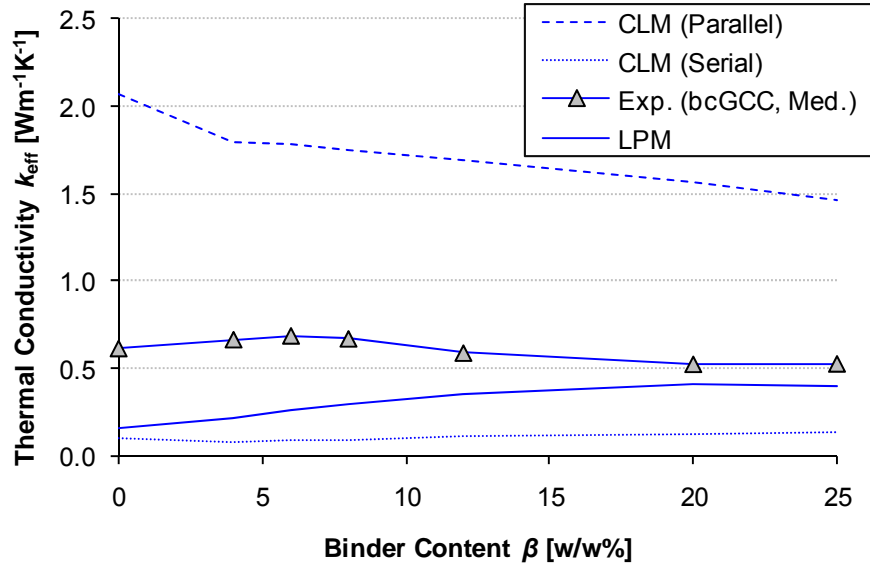


Figure 72. Theoretical limits for thermal conductivity of a pigment-binder-air system encompass the experimentally measured values for the medium latex system. Based on paper [V], Figure 18.

A more representative modelling approach is adopted by fitting the experimentally measured thermal conductivities and porosities to the Lumped Parameter Model unit cell. The unit cells, as described previously, consist of a central pigment phase and connecting bridges for pigment and binder. By fitting the model parameters one can get information on the role of pigment connectivity c' and binder connectivity c . Because of the intrinsically higher thermal conductivity of pigment, connectivity formed by pigment can have a bigger influence on the effective thermal conductivity than binder connectivity. One can, therefore, create a combined connectivity factor γ , composed of the thermal conductivity weighted components of the pigment connective and binder connective factors in relation to the maximum possible conductivity of the system, i.e. a combined connectivity factor acting as if it were consisting of pigment alone:

$$\gamma = c' + \frac{k_{s2}}{k_{s1}} c \quad (61)$$

Figure 73 shows the pigment-equivalent combined connectivity of the three latex bound systems. For the hard sphere latex, the maximum connectivity is reached at 4 w/w% binder content, even though this is not the point of maximum thermal conductivity of that system. This shows that the addition of hard latex does not foremost improve the thermal conductivity by increasing connectivity, i.e. it approximates well to the theoretical limit of a hard sphere, having effectively little or no contact area, but more by the particle packing and by replacing low conductive air in pores by binder (Figure 74.b).

For the medium latex system, the maximum connectivity coincides with the maximum thermal conductivity. This is the critical point where latex forms the highest connectivity between the pigment nodes at initial disruption (Figure 74.c), but before it is outweighed by the insulating effect of increasing binder. This is manifest by a decrease in effective pigment-equivalent combined connectivity.

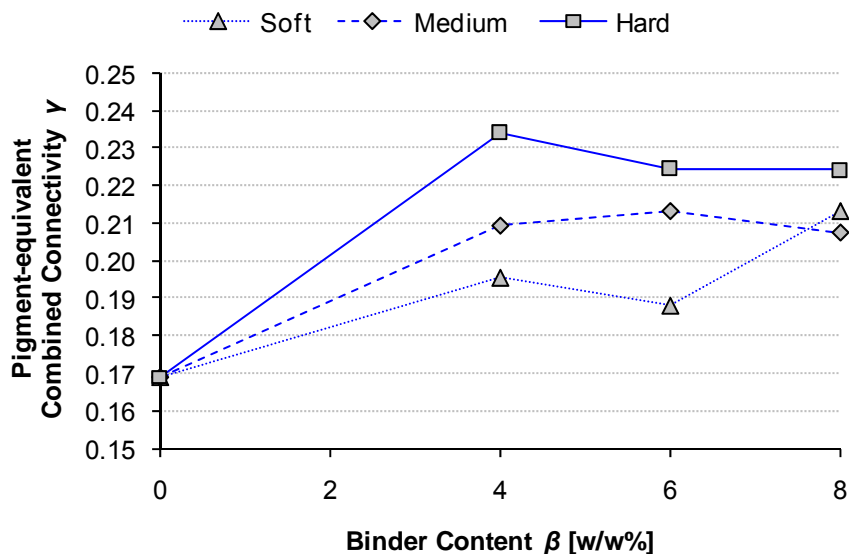


Figure 73. Total connectivity of pigment and binder, weighted by their relative thermal conductivity based on pigment. Based on paper [V], Figure 19.

The soft latex behaves rather similarly to the medium latex, but creates finer pores. Therefore, the connectivity at low binder concentrations is less, and the pigment disruption in combination with the low binder connectivity creates a local minimum at 6 w/w% binder concentration. For higher binder concentrations, the number of fine pores reduces and connectivity increases (Figure 74.d).

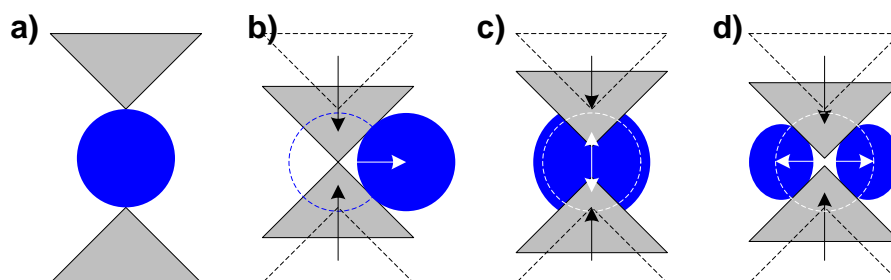


Figure 74. Effect of latex conformability on connectivity and pigment disruption during consolidation. a) initial state, b) hard latex rejection, c) medium latex disruption and connectivity increase, d) soft latex creation of fine pores.

6.3 Liquid saturation

6.3.1 Materials

In this section we consider the effect of liquid having entered the pore structure on the thermal conductivity. The coating formulations studied consist of a single pigment and latex binder at various dosage levels. The materials used are the same bcGCC pigment and SA latex as are listed 4.3.1 and 5.2.1. Tablets were formed following the procedure in 2.3.2 and measured according to 2.3.

Since the objective was to simulate the effect of typical fluid printing process components in the coating structure, in addition to the porous air filled (unsaturated) pigment tablets, both tap water and mineral oil¹¹ were used to saturate the tablet structures. The mineral oil in question can be found as a diluent in heatset offset inks. Its distillation

¹¹ PKWF 4/7 is a registered trademark of Haltermann Products

range is between 240-270 °C at 1 bar. Tap water was used to demonstrate the effect of a dampening solution, though it is to be noted that no surface active agents were included, such as isopropanol or non-ionic surfactant, as might be found in typical commercial fountain solutions. For the thermal diffusivity measurements, tablets with 6 and 8 w/w% latex were particularly of interest due to the prior knowledge of the disruptive effect on pigment packing of typical latex binder addition at this transition dose level (see discussion in 4.3 and 5.5). The choice of SA latex in this case was deliberate, in that, amongst typically used latices, it displays a minimal interaction with mineral oil. Thus, these samples were soaked both in the oil and water, whereas the other tablets in the series were only measured with air. The thermal properties of fluids and solids are summarised in Table 12.

Table 12. The thermal properties of fluids and solids used in this study /43, 68, 69/.

	Air	Oil	Water	Pigment	Binder
Density [kgm ⁻³]	1.2	824	1 000	2 700	1 100
Specific heat capacity [Jkg ⁻¹ K ⁻¹]	1 000	1 670	4 180	880	559.8
Thermal conductivity [Wm ⁻¹ K ⁻¹]	0.025	0.130	0.600	2.700	0.210

In order to absorb the liquids fully, the tablets were placed vertically, but slightly askew from the base, in a decanting glass filled with the respective liquid. Tilting the tablets allowed the absorbing liquid to get underneath the tablets, thus facilitating the capillary forces drawing the liquid into the tablets. When the tablets were taken out of the decanting glass, excess liquid was wiped away with an inert cloth and the tablets were analysed immediately.

Utilising the measured pore volume and the density of the absorbed liquids, Table 13 shows that the absorption of both mineral oil and water into the pores of the tablets is very close to complete, as measured gravimetrically, which provides for good comparison between the liquids.

Table 13. Comparison of the gravimetrically measured relative volume of absorbed liquid to the relative pore volume measured by porosimetry.

Fluid	Binder Concentration	Relative Pore Volume	Relative Volume of Absorbed Liquid	Residual Pore Volume
	[w/w%]	[%]	[%]	[%]
Oil	6	26.90	25.44	1.46
Oil	8	25.28	23.62	1.66
Water	6	26.90	25.92	0.98
Water	8	25.28	26.36	-1.08*

* the relative pore volume and the relative volume of absorbed liquid were measured from different tablets.

To study the liquid vaporisation behaviour, thermogravimetric measurements were made on a Perkin Elmer TGA 7 using a constant heating rate of 1 °Cmin⁻¹ for temperatures from 35 °C up to 250 °C. For these measurements a smaller sample size was required. Therefore, the macroscopic pigment tablets were cut down to smaller pellets of defined surface area (ca. 6 mm in diameter and 1 mm thick). Before any measurements were conducted, it was confirmed that the unsaturated pellet structures were thermogravimetrically stable in the relevant temperature range. The thermal degradation of the latex binder does not take place under 300 °C.

6.3.2 Effective thermal conductivity

Figure 75 shows the thermal conductivity values of both saturated and unsaturated samples, calculated from the measured thermal diffusivities, the densities and the literature values /43, 69/ of heat capacities. As seen in Table 12, the thermal conductivity of the air, mineral oil and water are very different. The thermal conductivity of water is almost 25 times higher, and that of mineral oil approximately 5 times higher than that of air. However, despite this clear difference in the thermal conductivities of the fluids themselves, one may not expect to see a change of this magnitude in the effective thermal conductivity of a liquid saturated porous medium due to the moderating nature of the skeletal material. The available pore volume is roughly one quarter of the total volume, whereas the remaining three quarters of the volume, consisting of solids, has a thermal conductivity that is at least comparable or even higher than that of the liquids (compare Table 12).

For the unsaturated system we see the maximum in thermal conductivity at around 6 parts binder as the binder improves the connectivity of the system, but at the same concentration acts to disrupt the pigment packing centring itself between the pigment contact points and not in the voids. The thermal conductivity of the water saturated samples is about double that of the corresponding samples with air filled voids. The maximum difference between measured binder concentrations for unsaturated samples is $\sim 0.2 \text{ Wm}^{-1}\text{K}^{-1}$, whereas the difference between the unsaturated and the water filled tablets is $\sim 0.8 \text{ Wm}^{-1}\text{K}^{-1}$. This shows that the effect of binder concentration on thermal conductivity is much smaller compared to the effect of fluid, and supports the theory that the water becomes more of a constitutive part of the skeletal structure compared to binder.

This is an interesting finding in regards to offset printing, where water-based dampening solution and oil-based ink are used to separate the non-image and the image areas from each other. The differing thermal conductivities of the printed areas and the unprinted areas might have an effect on the dimensional stability of the paper, e.g. its tendency to fluting. However, conclusions are difficult to make as the drying phenomenon in the heatset offset process is complex and not clearly defined.

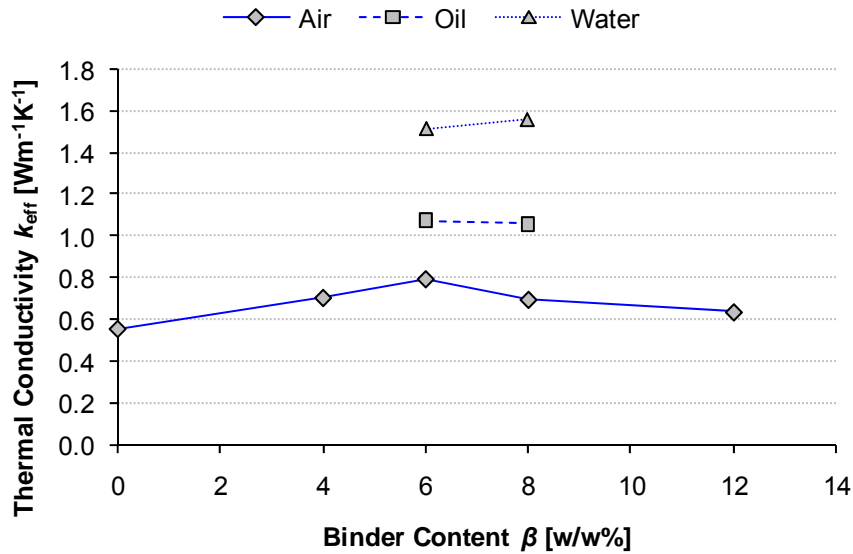


Figure 75. Effect of the void filling fluid on the thermal conductivity of coating. Based on paper [VI], Figure 3.

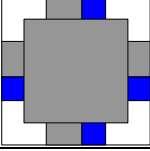
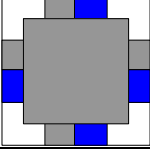
6.3.3 Modelling of the effective thermal properties

It was shown in 5.4 that the original form of the Lumped Parameter Model underestimates the effective thermal conductivity because of its inability to include pigment surface connectivity, as found in real coating structures due to the irregular particle shape of pigments and the surface layer of adsorbed polymer (dispersant). For this reason, pigment connectivity c' was included in the model and it was shown that in this way the model captures colloidal interactions present in the formation of coating structures, which also have an effect on their thermal conductivity (see Figure 62).

In order to model the effect of the fluid on the effective thermal conductivity, we first fit the experimentally measured porosity and thermal conductivity of the unsaturated system to get the appropriate model parameters a' and c' of such a structure. This requires solving the equation describing the combined system of thermal conductivity (equation 34) and is described in 5.4.3. Given that the absorbed water or mineral oil doesn't change the skeleton of the structure, the same unit cell structures can then be used to calculate the effective thermal conductivity of the liquid saturated structures. This is simply done by replacing the thermal conductivity of the fluid air in equation 34, i.e. k_f , λ and μ , by the appropriate literature value (Table 12) for the liquid in question. This allows a comparison of experimental values and model values and thus enables a discussion of how the effective thermal conductivity is affected by the fluid phase.

The measured thermal conductivities and measured porosities of the unsaturated structures for 6 and 8 parts binder, modelled by adopting an LPM unit cell configuration including pigment connectivity, are listed in Table 14. Figure 76 compares the measured thermal conductivities and the model prediction of the liquid saturated structures.

Table 14. Measured values of the unsaturated system and the corresponding LPM unit cell parameters.

Measurement (Air):	6 w/w%	8 w/w%
Porosity ϕ_{3D} [%]	26.90	25.28
Thermal Conductivity k_{eff} [$Wm^{-1}K^{-1}$]	0.79	0.69
Unit Cell Parameters:		
Pigment Factor, a'	0.70058	0.71865
Pigment Connectivity, c'	0.24438	0.19212
Binder Connectivity, c	0.15670	0.21795

Even though it can be seen that, just like the experiments, the model predicts the effect of the fluid to be stronger than that of the binder amount, it fails to capture the full impact of liquid saturation on the thermal conductivity. Given that liquid can infiltrate into the smallest voids, it will act as a more effective connectivity agent than latex/dispersant polymer between the pigment particles, ensuring a more complete connection between the more highly conducting pigment particles making up the skeletal structure. To illustrate this, we could iterate the model increasing the value for the pigment connectivity until equivalency is reached between the model and the experimental value. However, for the given material properties of the components, such liquid enhanced pigment connectivity, e.g. for the water saturated structure, would be $c' = 11.588$ for 6 parts and $c' = 20.995$ for 8 w/w% binder. Since all the unit cell parameters for stage 1 and 2 (see 3.4.1), need to be in the interval of $a', (c'+c) \in \{0,1\}$ this clearly exceeds the physical boundaries of the model. The reason for the difference in the modelled and experimental thermal conductivity must therefore have other reasons as well. These may have their origin in both the measurement and the functioning of the model.

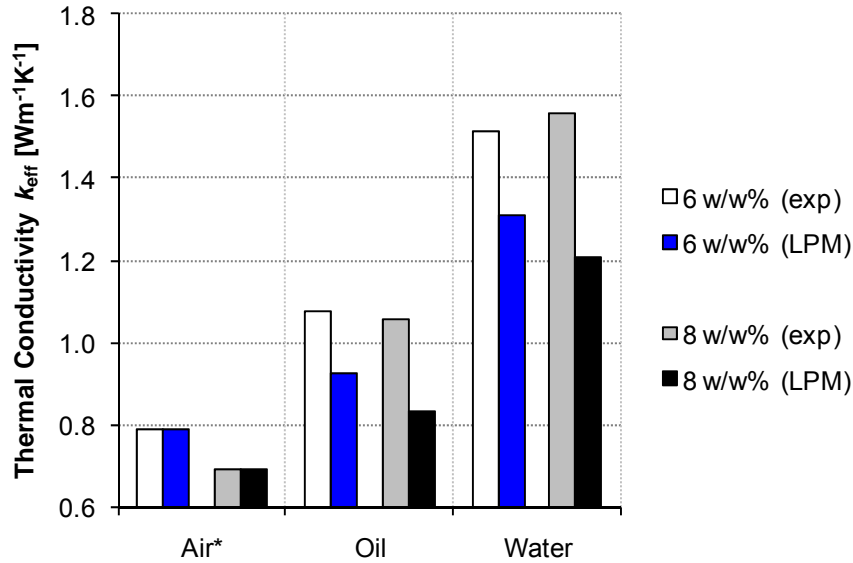


Figure 76. Comparison of the measured thermal conductivities and the model prediction (LPM) of the liquid saturated structures. *The model parameters are determined by a fit to the unsaturated (air) structure. Based on paper [VI], Figure 4.

We need to consider also the physical heat transfer to the sample more closely. For the measurements of thermal diffusivity, a macroscopic pigment tablet is brought into contact with a heated plate. It was discussed in the evaluation of this technique (see 2.3.5.2), that the resulting values therefore include the contact resistivity of the interface heating plate to tablet.

By comparing the measured values of the structures directly, we implicitly assume the contact resistivity remains constant. While this might be the case for unsaturated structures of different binder contents, a liquid at the interface will certainly improve the contact (Figure 77), thus lowering the contact resistivity, $R_{contact}$, and therefore increasing the apparent measured value (equation 11).

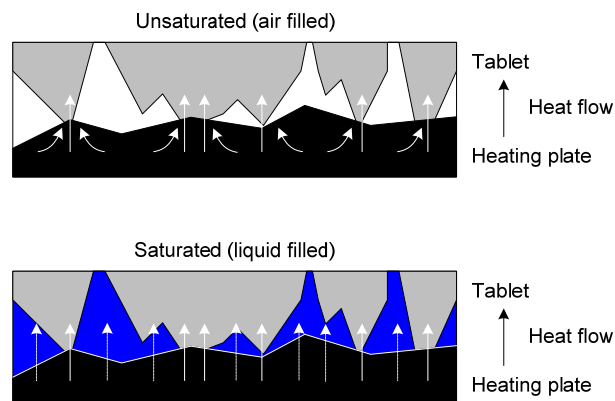


Figure 77. Microscopic contact interface of tablet and heating plate for an air filled and liquid filled system, respectively. Based on paper [VI], Figure 5.

Since the modelled conductivities shown in Figure 76 for oil and water-filled structures are based on the same contact resistivity as was implied by the unit cell parameters for the unsaturated system, the difference between the modelled thermal conductivities for oil and water saturated systems compared with the measured unsaturated system must therefore be the model prediction for the effect of saturation with liquid alone, independent of the change in contact resistivity. The higher thermal conductivities of the measured saturated

systems likely relate in part at least to the improved contact conductance (lower contact resistance) at the heating interface. In other words, one can say that the measured value is “artificially” raised because it includes the higher contact conductivity of the liquid-containing interface system. Because the intrinsic thermal resistivity (without contact resistivity) of the tablets is unknown for both saturated and unsaturated systems, one cannot quantify the exact contact resistivity for these measurements. However, by dividing equation 11 for both the modelled and the experimental values,

$$\frac{R_{\text{contact, model}}}{R_{\text{contact, exp}}} = \frac{k_{\text{exp}}}{k_{\text{model}}} - 1 \quad (62)$$

one can estimate that the experimental contact resistivity of the oil-filled tablets would be ca. 3-4 times lower than that of the modelled interface. This value is consistent with that given in the earlier discussion regarding the contact resistivity in which a thin layer of oil-based thermoconductive paste was used to change the interface properties (see Table 3).

A third origin of the model versus measured difference, as mentioned above, is the functioning of the model itself, in particular the fact that it is a 2D projection of a 3D structure. To model the conductivities of the saturated system we nonetheless fitted two-dimensional model parameters to the measured conductivity and porosity of a three-dimensional system based on the thermal transmission being essentially a one dimensional transit through a two-dimensionally layered structure. This was discussed using a 2D equivalent porosity in 3.5.2 and this simple example shows that the parameters of the two-dimensional unit cell may not necessarily reflect the ones of the three-dimensional system in respect to the effective quantities of each component present, and vice versa.

To examine whether the 2D equivalent porosity of a unit cell, i.e. the void area fraction that would equal the three-dimensional pore volume fraction, is related to the effective porosity, we transform the three-dimensional pore volume fraction to a two-dimensional void area fraction. If such a link exists as a continuous function, the structures are topologically equivalent, i.e. homeomorphic, and the homeomorphic function can be used for the conversion while preserving the topological properties. This criterion was applied previously by Gane *et al.* /40/. This is the case for the LPM unit cell in 3D and 2D. The homeomorphic function for the fluid phase is depicted in Figure 21. Using this transform function, one can create LPM unit cells having a 2D equivalent porosity. The new unit cell parameters are listed in Table 15, the analogue to Table 14.

Table 15. Measured values of the unsaturated system and the corresponding LPM unit cell parameters for the 2D equivalent porosity.

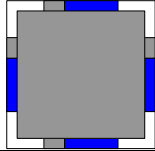
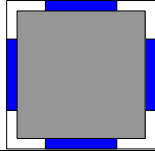
Measurement (Air):	6 w/w%	8 w/w%
Void Area Fraction ϕ_{2D} [%]	12.74	11.52
Thermal Conductivity k_{eff} [Wm ⁻¹ K ⁻¹]	0.79	0.69
Unit Cell Parameters:		
Pigment Factor, a'	0.84732	0.84848
Pigment Connectivity, c'	0.13955	0.06475
Binder Connectivity, c	0.36681	0.47921

Figure 78 compares the measured thermal conductivities of the 6 w/w% binder structure and the model prediction of the liquid saturated structures. The model values using

porosity (LPM, 3D) are given for reference as they were shown in Figure 76. It is seen that the model values using the equivalent area fraction (LPM, 2D) show a higher thermal conductivity, as in the 3D case, yet don't reach the experimentally measured value. This increase is likely directly due to the lower porosity and, therefore, the smaller relative influence of fluid in a unit cell. This indicates that the difference, compared to the experimental value, is not due to the two-dimensional nature of the model alone, but more related to the mechanisms discussed above, i.e. the change of the interface properties and improved thermal transfer (reduced contact resistivity) and an apparent increase in pigment connectivity, effectively filling the very fine pigment-pigment voids with liquid (the acting connectivity agent). For a description of the apparent pigment connectivity, the concept of a "thermal porosity" was discussed in 4.3.3 that would differ from the actual porosity, but better describes the thermal transfer. The link between the thermal porosity and the 2D equivalent porosity would then be the connectivity of solids, which takes us to our first consideration of a likely explanation for the difference, as discussed above.

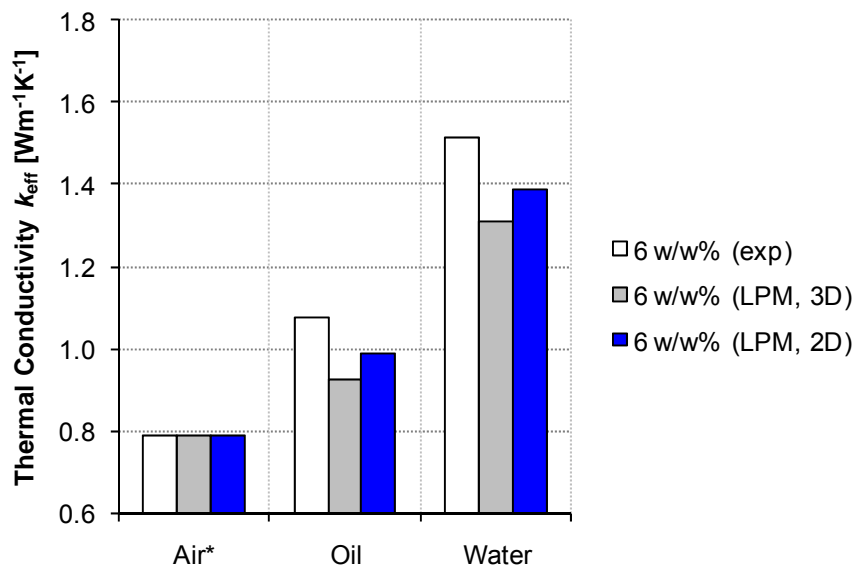


Figure 78. Comparison of the experimental thermal conductivities and the model prediction (LPM) of the liquid saturated structures for unit cells using both the 3D pore volume fraction and the equivalent 2D void area fraction. *The model parameters are determined by a fit to the unsaturated (air) structure. Based on paper [VI], Figure 8.

6.3.4 Thermogravimetric behaviour of liquid saturated media

6.3.4.1 Mineral Oil

Figure 79 shows the relative weight loss of oil for the saturated pellets as temperature is raised in the thermogravimetric measurement. The vaporisation of mineral oil in the binder-free pellets occurs slightly faster than for the binder containing ones. The pellet containing 12 w/w% binder "dries" slower, while it is difficult to differentiate any of the other curves for the different binder levels. Therefore, a look at the derivatives of the curves in Figure 79, i.e. the rate of relative weight change with respect to temperature change as a function of temperature is more illuminating, as provided in Figure 80.

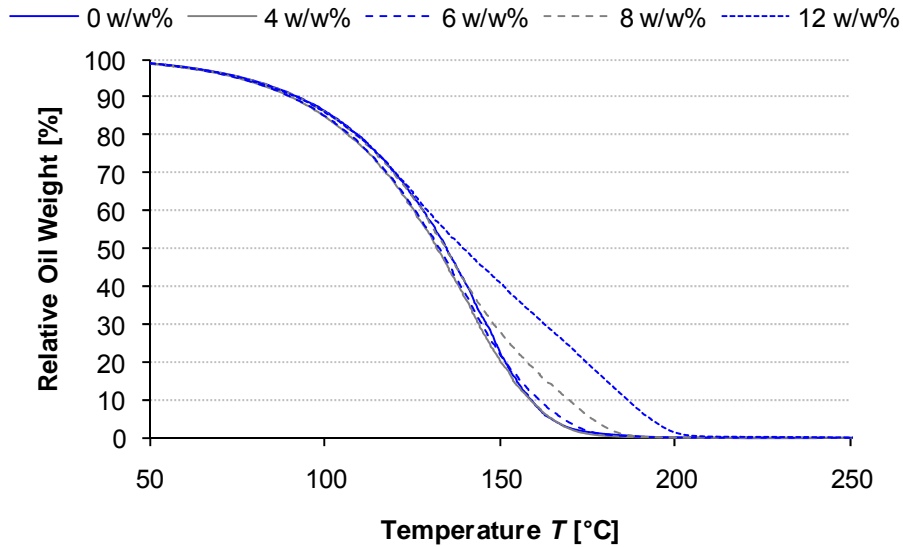


Figure 79. Relative oil weight loss from saturated coating pellets having 0 to 12 w/w% binder. Based on paper [VI], Figure 9.

The more binder the pellet structure contains, the lower is the maximum achieved evaporation efficiency, and the temperature range required to ensure complete removal becomes extended, especially at the higher binder levels. It seems as if the latex “binds” the oil or blocks its vapour removal, i.e. reduces the evaporation rate during the heating regime studied. This effect, however, is not seen for the change of 4 to 6 w/w% binder, and so is unlikely to be a strong direct interaction between the oil and latex binder, though it could be due to the compensatory increase toward the maximum thermal conductivity of the coating structure at the binder concentration of 6 w/w% (as seen in Figure 75).

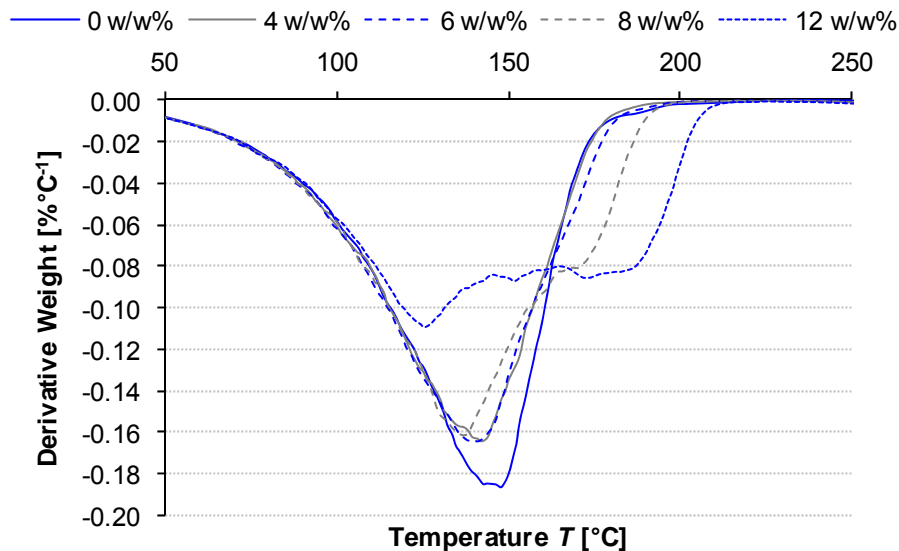


Figure 80. Mineral oil vaporisation rate for coating pellets containing 0 to 12 w/w% binder. Based on paper [VI], Figure 10.

If a too fast heating rate had been used, one could argue that the optimal thermal conductivity in the coating structure of 6 w/w% binder improves the heat transport to such an extent that it compensates for the higher binder effect (compared to 4 w/w% binder), but since sufficient residence time is given in the air containing case for conduction to occur

(the slowest conducting fluid system), this cannot be the case. Similarly, conductivity lag can be discounted when using 8 w/w% binder (or higher), as both the thermal conductivity of the structure decreases and the oil vapour retention capability would be expected to increase. Therefore, although we may expect the evaporation speed to be lowered in practice at high heating rates, in this idealised experiment it cannot be the case. We recall at this point the disruptive packing nature of the latex on the pigment packing at this critical binder amount of 6-8 w/w%, i.e. despite the addition of latex, the porosity increases slightly, and this could suggest that permeability of the coating is playing the major role in determining the likely retention of oil vapour /40, 70/

The overriding factor controlling the evaporation rate in this case of oil saturating the structure is specific surface area available for vapour transport, which controls the surface area of liquid-vapour interface. Addition of latex from 0 to 4 w/w% is seen in Figure 36 to increase both pore size and pore volume. Between 4 and 8 w/w% latex, the coating structure becomes disrupted, the pore size distribution is very similar and the surface area is more or less constant, which also results in an observed constant evaporation rate.

As can be seen in Figure 36, the binder-free tablets have more fine pores. The large number of fine pores also creates a high specific surface area, leading to a comparatively high localised evaporation rate. However, the large number of fine pores leads to an effective increase in the vaporisation pressure of the liquid entrained in those pores (Gibbs-Thomson effect), whilst, at the same time, the geometry of diffusion becomes more tortuous.

The Gibbs-Thomson effect, if present, diminishes as the pore size is increased, which is confirmed by the narrow peak at maximum evaporation as a function of temperature (see Figure 80). If the latex would actually bind the oil, the difference between rate of oil loss peaks would be much larger. Especially, the curve for the 8 w/w% latex structure would be closer to the curve for 12 w/w%. Since it is known that the given liquids do not interact strongly with latex /71/, the apparent “binding” of liquid is better explained by the limiting of pore cross-sectional area available for vapour transport, with the Gibbs-Thomson effect playing a potential role for the binder-free system when many small pores are present. Higher latex concentrations decrease pore volume and permeability - the well-known “closure” effect of binder, renowned in the case of heatset blistering, - but pore size remains similar. Therefore, the surface area of liquid per volume decreases, which results in a decline of the evaporation rate.

The potential effects, described above, of specific cross-sectional surface area affecting diffusion plus potential Gibbs-Thomson confinement combine to result in a broad peak of the maximum evaporation as a function of temperature, as can be observed in Figure 80.

6.3.4.2 *Water*

Figure 81 shows the relative weight loss for the water saturated pellets within the binder content range of 4 to 12 w/w%. Measurement of binder free systems was not possible as the structure becomes unstable when exposed to water. In contrast to the relative weight change for oil soaked pellets, it can be seen more clearly in Figure 81, for the water saturated pellets, that at 6 w/w% binder material, which happens to have the maximum thermal conductivity of the skeletal material, the fastest vaporisation occurs.

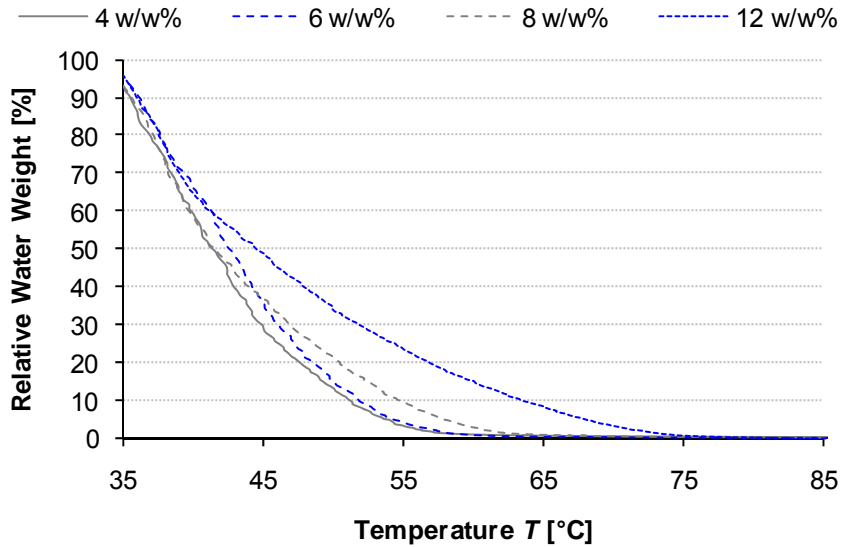


Figure 81. Relative weight change for the vaporisation of water from coating structure pellets with 4 to 12 w/w% binder. Based on paper [VI], Figure 12.

The oil, discussed in the previous section, was a mineral oil with a natural range of molecular weight components and, thus, had a relatively ill-defined vaporisation. Water is seen, on the other hand, to vaporise more readily at a well-defined temperature, within the temperature range of study. The water data suggest, therefore, that an important parameter also in the case of water is the permeability of the coating to allow for vapour escape without raising local vapour pressure. A similar problem was discussed by Gane and Ridgway [72]. Therefore, there is less apparent constraint for water within the binder-related pore structure, thus the effect of thermal conductivity as related to the connectivity function between pigment particles becomes more visible. Because the vaporisation is initially very high it is not possible to draw any conclusions from the derivative weight change shown in Figure 82. Despite the different maximum evaporation temperature and the evaporation time of the oil and water, the effect of the addition of binder is similar.

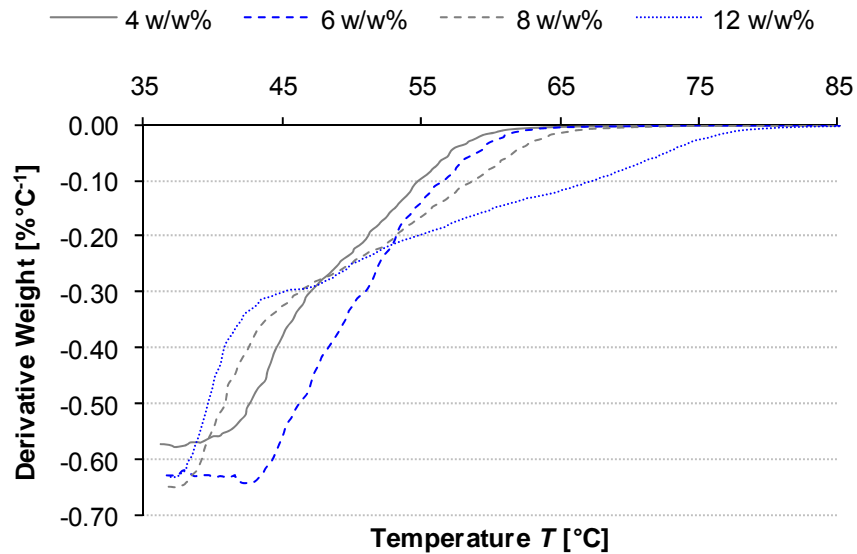


Figure 82. Vaporisation rate of water from coating structure pellets with 4 to 12 w/w% binder. Based on paper [VI], Figure 13.

6.4 Summary

The effect of different T_g latex binders in the formation of pigmented coating structures and the resulting thermal conductivity were studied by means of mercury porosimetry, particle packing simulations and modelling, including parameters for connectivity of binder and pigment.

It was shown that hard latex structures show a generally higher thermal conductivity because of low porosity and very little pigment packing disruption, i.e. high packing density. This was confirmed by particle packing simulations, showing that using hard latex avoids the introduction of further randomness in the packing structure. Therefore, in the case of hard latex, the thermal conductivity is not primarily influenced by the connectivity of binder, but by the optimised packing of particles (observed as high pigment connectivity). This is in contrast to the medium and soft latex where colloidal forces lead to a placement of latex particles at pigment nodal points. This could be observed comparing measured porosities to those from particle packing simulations. The addition of binder acting disruptively creates a more random packing, thus porosities of random packing simulations and real systems were very similar. In case of disruptive binder, the thermal conductivity is a result of the balance between pigment packing disruption caused by binder and the connectivity between pigments formed by binder having undergone conformation at the same time. For the medium latex, the maximum thermal conductivity is, therefore, observed at the maximum connectivity. The action of soft binder as an extrusive component, shown by atomic force adhesion microscopy, is to increase fine pore content and so to increase the connective tortuosity of the skeletal material, thus maintaining a relatively low thermal conductivity.

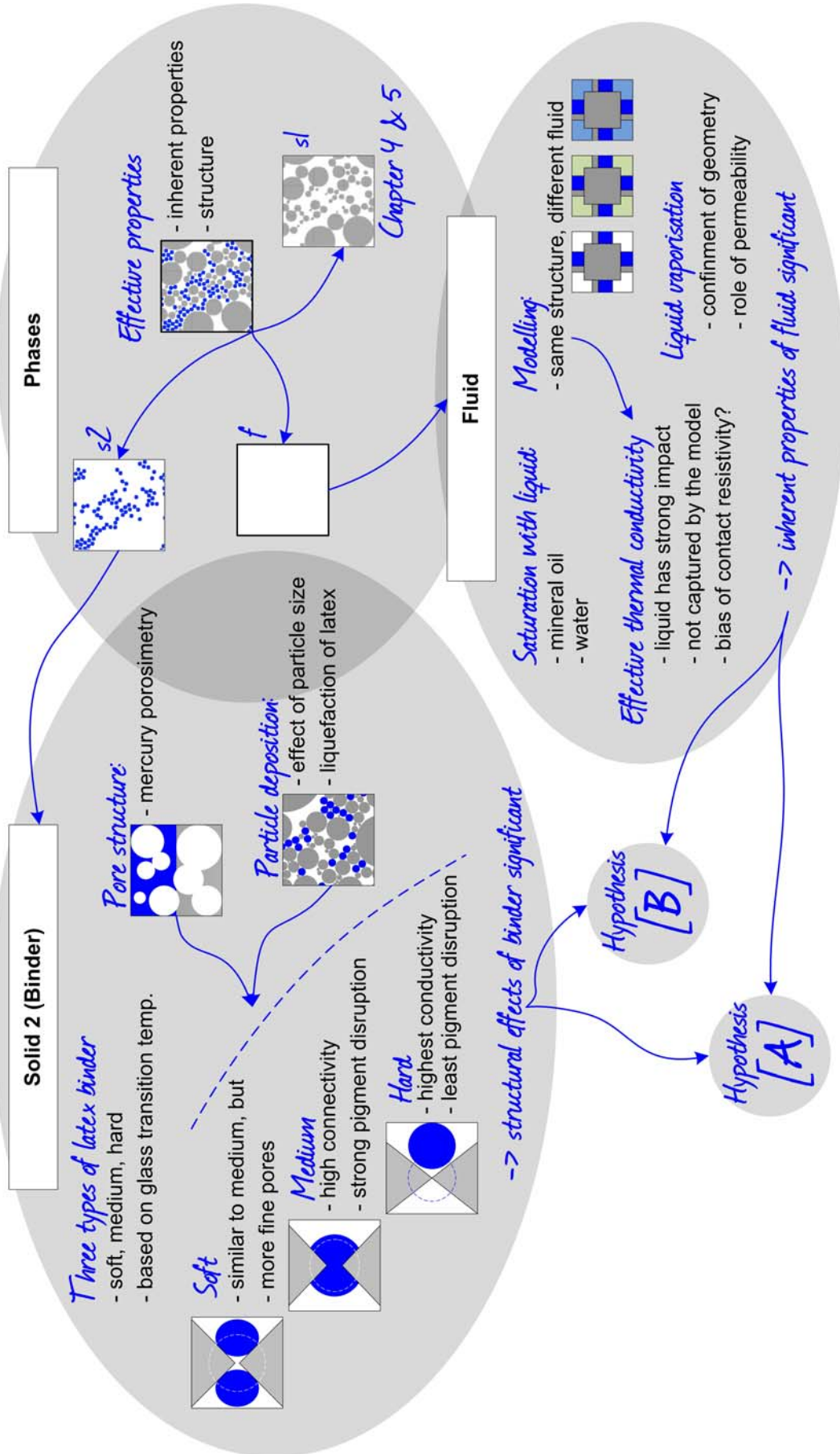
The effective thermal conductivities of mineral oil and water saturated coating structures were studied and compared to the unsaturated case, where air filled the pores. It was shown that the void filling fluid has a strong impact on the total effective thermal conductivity. For water filled pores, the thermal conductivity almost doubles compared to the unfilled structure, and is also distinctly higher for oil filled pores compared to air filled structures. This can have implications for the drying process in heatset web-offset, in which both water in unprinted areas and mineral oil in the ink are present. The differing

thermal conductivities can be expected to lead to a locally different temperature response in printed and unprinted areas, and thus might have an effect on, for example, fluting/waviness.

Modelling of thermal conductivity of the unsaturated structure in comparison with the liquid filled coatings showed a distinct difference between the experimental values and the model prediction. Even though a liquid increases the inter-particle pigment connectivity, which leads to a higher thermal conductivity, it was further discussed that the thermal contact resistance present in the measurement of thermal diffusivity can have a significant impact on the effectively measured properties. In addition, the measured porosity, which was used as a basic modelling parameter, was shown to differ from the model porosity when comparing the 2D model and the 3D parameter-equivalent real case. However, by using a transform function, it was shown that it is unlikely that the 2D-3D relationship is a dominant element in causing the model deviation from the experimental results. Thus, we conclude that the contact resistance and the inter-particle pigment connectivity are more influential. For improving the results from the two-dimensional modelling, the latter could be described by a “thermal” porosity, responsible for thermal transfer.

The vaporisation behaviour of liquids saturating the porous structures was studied using thermogravimetry. It was seen that, despite the different maximum evaporation temperatures and evaporation rates, the effect of the addition of binder was similar for both oil and water. Since it is known that there is little or no interaction between the given liquids and the binder in question, it is concluded that the confinement of geometry, i.e. increased local curvature as pores become finer, and reduced diffusional cross-section area (permeability reduction), result in elevated vapour pressure within the structure, according to the relative contributions from modified phase transition (potential Gibbs-Thomson effect) in the finest pores and restricted diffusion pathway (reduced permeability).

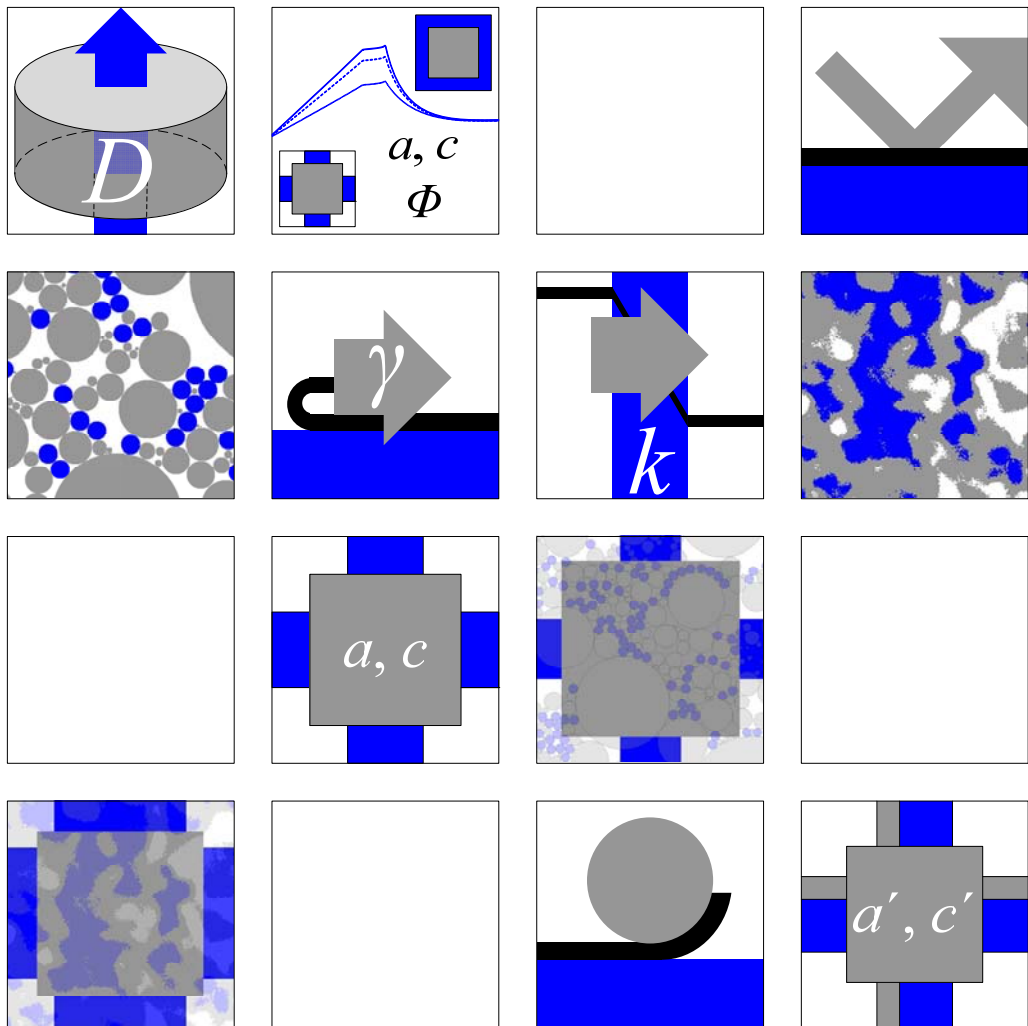
6.5 Phase properties thread



PART

III

APPLIED RESEARCH LEVEL



“There does not exist a category of science to which one can give the name applied science. There are sciences and the applications of science, bound together as the fruit of the tree which bears it.”

Louis Pasteur,
French Microbiologist, 1822-1895

7 ELECTROPHOTOGRAPHIC TONER FUSING ON THERMALLY DESIGNED SUBSTRATES

7.1 Background

7.1.1 General

Even though Lichtenberg /73/ already experimented with the deposition of fine particles on electrically charged surfaces (Lichtenberg figures) in 1778, it was not until 1939 that this idea was combined with a suitable imaging method to turn it into an electrophotographic reproduction process. Electrophotography was invented by Chester Carlson /74/, who described it as an improved method of photography and its main two advantages were already stated in the original patent: firstly, its simplicity, and, secondly, reusability. The lack of any chemical development enables the production of a copy within seconds, and, furthermore, because the process is merely a sequence of mechanical actions, it can be automated easily. Today's electrophotography printers can achieve printing speeds of hundreds of pages per minute. The second advantage stated in the patent is the possibility to reuse the photographic plate by discharging, cleaning, recharging and exposing it to a new master.

The original concept, shown in Figure 83, was an analogue reproduction system. The master is described as a translucent film material. This limits the flexibility of the process because of the requirement of a permanent master. In digital printing, however, no master is required. In digital electrophotography the imaging step is done by directly controlling a discharging light source using the image data file and creating a latent charged retained image accordingly. Thus, the advantage of being able to re-use the photoconductor can be fully utilised.

Both the simplicity of the process and the advantages of a digital printing method in combination with relatively high print quality have made electrophotography into a mature printing process over the years. With the current emergence of greater usage of digital printing in the market place, this is reflected in high predicted growth rates of up to 15 % /75/. This growth is supported by new media applications, such as personalised print runs or online print-on-demand solutions /76, 77/, both of which are characterised by smaller numbers of copies. In addition, strong growth will also put electrophotography more and more in competition to offset printing methods in markets with comparatively larger circulation numbers. Also increasingly active in this field is the development of high speed inkjet technology, and the competition between inkjet and electrophotography will be strong. However, both methodologies either already do or are likely to adopt thermal transfer in one form or another, either to enhance drying (inkjet) or, as an integral part of the process, to fuse applied toner (electrophotography). In order to grow successfully in new small circulation number markets, low specific cost, i.e. an economical process per unit copy, is required, whereas to compete with offset, high image quality and speed are vital. Both factors are addressed in the development of improved printing processes, but also the printing substrate can have a decisive influence. Before discussing the substrate perspective in respect to the economy and quality of an electrophotography print transfer, we describe the principle and process steps in more detail.

7.1.2 Principle of electrophotography

Figure 83 shows selected figures of Carlson's original patent application to illustrate the basic principle of electrophotography. At first (Figure 83: *Fig. 1*) a photographic plate (20), consisting of photoconductive layer (21) and a metal plate (22), is charged by rubbing with a soft cotton handkerchief (23). The original master (27), i.e. a translucent material, is then

ELECTROPHOTOGRAPHIC TONER FUSING ON THERMALLY DESIGNED SUBSTRATES

Background

placed on the charged photoconductor where a light source (26) releases the charge in non-image areas (Figure 83: *Fig. 2*). After removal of the master, the exposed plate is then sprinkled with fine toner dust (31), consisting of, for example, pulverised gum (Figure 83: *Fig. 3*). The particles adhere to the remaining charged image areas. They are then transferred to a sheet substrate by pressing it with a rubber pad against the toner (Figure 83: *Fig. 4*). Part of the toner will transfer to the sheet and is fixed subsequently by heat, causing the polymeric particles to melt on the substrate (Figure 83: *Fig. 5*).

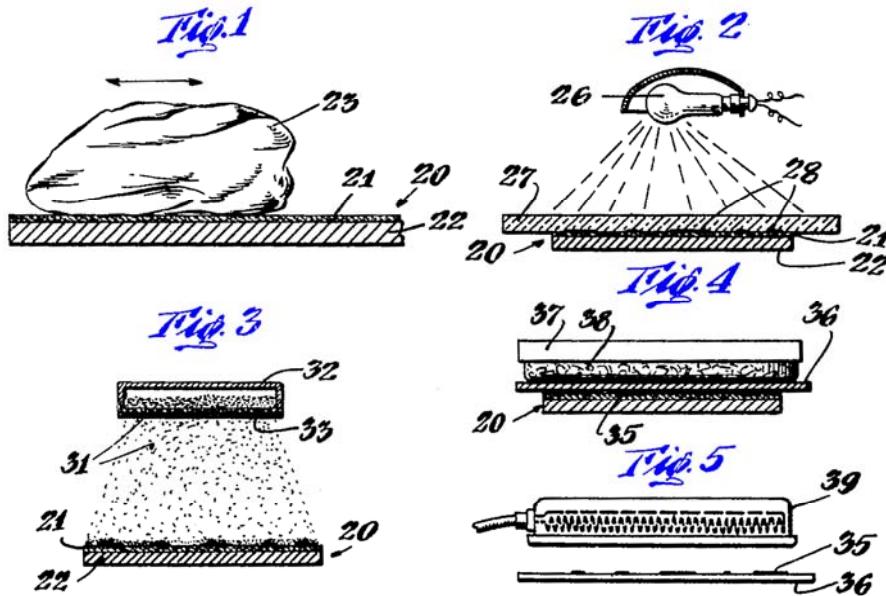


Figure 83. Five steps of electrophotographic printing according to the original patent: 1. charging, 2. imaging, 3. inking, 4. transfer and 5. fusing. Adapted from /74/.

These five steps can be found even in modern electrophotographic printing systems, as shown schematically in Figure 84. The numbering is analogous to Figure 83, beginning with the charging step (1). This is usually done by corona treatment of the photoconductor drum, followed by the imaging step (2) in which the charge is locally released by exposition to a light source, usually laser or light emitting diode (LED) light. The pulsing light beam scans across the revolving photoconductor drum, constantly deleting areas of surface charge and so creating a latent image on the charge-retained surface. In the inking step (3) the charged toner particles are brought in contact with the photoconductor drum, and in step 4 they are transferred to the substrate by an external electric field.

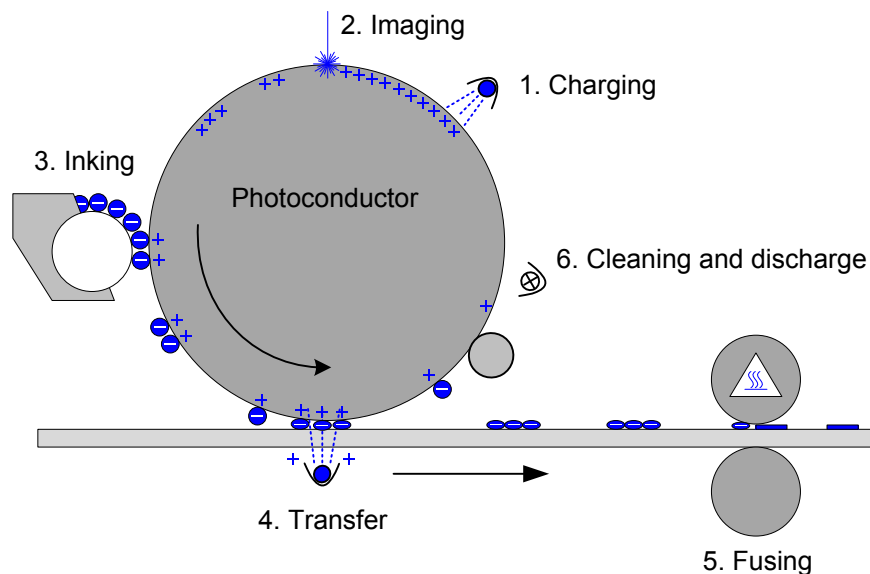


Figure 84. Steps of modern digital electrophotographic printing process, analogue to Figure 83. Adapted from /78/.

At this point, prior to fusing, the toner particles and, therefore, image on the substrate are still loosely arranged. The image needs to be fixed permanently to provide resistance against abrasion due to mechanical sheet processing, surface contact or human handling. Image fixation is also a critical property for forgery proof security documents /79/. There are, in principle, two types of techniques: contact fusing and non-contact fusing /80/. In non-contact fusing, the toner is heated by absorbing radiation in the near infrared range, whereas in contact fusing (as depicted in step 5 of Figure 84) there is a pressure contact to a heated roll, and thus conduction heat transfer to the toner and underlying substrate is the dominating mechanism.

The fixing process has a distinct influence on print quality such as gloss and print density /81/. Essentially three groups of parameters affect the fusing: the toner properties, the substrate properties and the process parameters. The latter are defined by the given printer configuration and printing speed. The toner properties are usually designed for a given printing system /82/, thus allowing more flexibility in the choice of the substrate. The following will take a short look at the role of the substrate in the fusing process.

7.2 Substrate properties in toner fusing

A number of properties of the printing substrate may affect the thermal fusing behaviour /81/. We can separate them into three categories:

1. thermal properties (thermal conductivity and specific heat capacity)
2. structural properties (mass, density and porosity)
3. surface properties (roughness and chemistry)

As toner fusing is a surface critical process, the third category has gained most attention in research on toner adhesion while the structural properties are usually defined by a given paper grade. The surface roughness is known to play an important role in mechanical adhesion mechanisms, thus dominating for uncoated papers, while surface chemistry can have a decisive effect for the chemical adhesion mechanisms, e.g. adsorption /83/. In this work special attention is paid to the category of the thermal properties. Even though the governing properties of thermal conductivity and specific heat capacity are intrinsic

properties of the materials, both have an effect, as we shall see, on the surface temperature in a fusing process.

To satisfy the demand for high print quality, the use of coated papers is required, even in digital electrophotography [84, 85, 86]. In fact, it has been observed [75] that recent trends in the development of digital printing methods tend towards the design and engineering of new materials rather than the development of new machinery. The underlying consideration for designing a coating from a thermal perspective is whether and how it can affect either the print quality or the process efficiency in terms of the energy consumption, as mentioned above, in respect of lowering specific cost.

The thermal energy Q required to raise the temperature of a coated and fully printed sheet of paper to the toner fusing temperature is given by the mass and specific heat of each component i :

$$Q = \Delta T \sum_{i=1}^3 m_i c_i \tag{63}$$

where ΔT is the temperature difference between ambient temperature and the required fusing temperature.

Table 16 lists the material values and also provides the share of thermal energy for each component, assuming homogeneous heating of the printed substrate. It shows that even for the fully printed sheet only a small fraction of the fusing energy is required for the heating of the toner. For text printed sheets (ca. 20 % toner area) this share would be even smaller. The majority of the energy heats the substrate paper, a necessary action in order to raise the temperature of the toner-paper surface interface such that the toner adheres by fusing to the surface. This illustrates the great savings potential if the thermal energy in the fusing nip could be more focused on the heating of the toner and the immediate interface layer only. The next step is, therefore, to analyse further the role of the thermal properties of the coating layer in determining the temperature conditions in a fusing nip.

Table 16. Thermal energy required to raise the temperature of a three layer A4 sheet (toner, coating, base paper) from ambient temperature 23 °C to a homogenous toner fusing temperature of 125 °C. The thermal properties are assumed to be constant for the temperature range.

<i>i, Component</i>	<i>Mass*</i> m_i [g]	<i>Spec. heat capacity*</i> c_i [Jkg ⁻¹ K ⁻¹]	<i>Temperature</i> ΔT [K]	<i>Energy</i> Q_i [J]	<i>Energy</i> <i>share:</i>
1, Toner	1.11	1 255	102	142.09	11.04 %
2, Coating (vfGCC)	2.12	851	102	184.02	14.30 %
3, Paper	6.06	1 554	102	960.56	74.65 %
Total:				1286.67	

*based on the thermophysical properties listed in Table 18

7.3 Simulation of electrophotographic toner fusing

7.3.1 Substrates and fusing nip

The introduction of the principle of electrophotography showed the main components of a fusing system to be:

- a) the toner printed substrate,
- b) a polymer backing roll, and
- c) a heated metal fusing roll.

In our case, the printed substrate a) is a layered structure consisting of base paper, coating and, prior to the fusing nip, toner (Figure 85). We perform simulations for three different kinds of coating pigments while retaining the same properties of the toner layer and the base paper layer in each simulation. To study the effect of the thermal conductivity of the coating layer, the pigments chosen reflect the range of a low, medium and a higher thermal conductivity. They are modified calcium carbonate (MCC¹⁴), vfGCC and talc, respectively. The MCC pigment forms a very porous and therefore effectively insulating structure because of an almost monodisperse particle size distribution in combination with intraparticle pores /87/. vfGCC¹³ was chosen as a medium conductivity carbonate material, whereas talc was known, e.g. Guérin *et al.* /20/, to have a higher conductivity than calcium carbonate.

The thermal diffusivity of the pigment binder formulations was measured using the tablet diffusivity technique (see 2.3). The measured diffusivities along with the literature values of specific heat capacity are used as the material parameters for the simulation of the coating layer. The pigment binder formulations are listed in Table 17. Table 18 provides the material properties and dimensions of the substrate. The length of the simulation substrate is 10 mm for all configurations. In order to investigate the thermal properties alone, these dimensions are kept constant during the simulation.

Table 17. Summary of the material size data for the three systems used

Component:	SA¹²	SA¹²	SA¹²
Latex			
Glass transition temp. [°C]	5	5	5
Particle size [µm]	0.20	0.20	0.20
Thermal conductivity [Wm ⁻¹ K ⁻¹]	0.21	0.21	0.21
Specific heat capacity [Jkg ⁻¹ K ⁻¹]	559.8	559.8	559.8
Density [kgm ⁻³]	1 100	1 100	1 100
Pigment			
	vfGCC¹³	MCC¹⁴	Talc¹⁵
Thermal conductivity [Wm ⁻¹ K ⁻¹]	2.7	2.7	
Specific heat capacity [Jkg ⁻¹ K ⁻¹]	880	880 ⁺	
Density [kgm ⁻³]	2 700	2 700	
PSD [w/w%]			
< 5 µm	100		82
< 2 µm	98		46
< 1 µm	90		
<i>d</i> ₅₀ (weight median) [µm]	0.4	5.1*	2.4
Latex dose [w/w%]	10	15	12

⁺ Assuming CaCO₃ as main component

* Particle size determined by SEM

The heat transfer through the interfaces of the substrate layers is assumed to be ideal, i.e. without heat losses. For the following discussions, the temperatures are numbered consecutively starting from the toner surface: *T*₁ is, therefore, the interface temperature of fusing roll and toner layer, *T*₂ the toner-coating interface temperature and so on.

¹² Acronal S 360D (SA) is a registered trademark of BASF AG

¹³ Setacarb HG (vfGCC), Omya AG

¹⁴ MCC564, 5 µm, 64 m²g⁻¹ (MCC), Omya AG

¹⁵ Finntalc C10, Mondo Minerals Oy

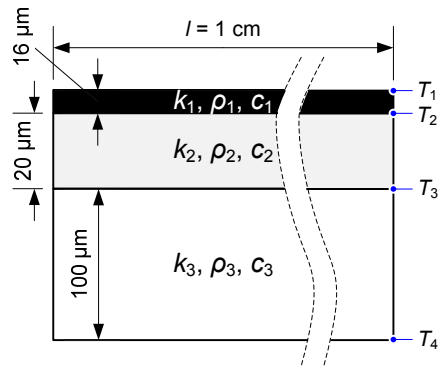


Figure 85. Layered structure of the model printing substrate. Based on paper [VI], Figure 5.

The substrate passes the nip formed by the fusing and backing roll. For the simulation, instead of passing the substrate through the nip, the nip “moves” along the surface with the printing speed v . It can, therefore, be defined merely by the transient boundary conditions of the substrate.

Table 18. Thermo physical properties of toner, coatings and base paper as used in the calculations. The thermal diffusivities of the coatings are measured using the tablet diffusivity measurement (see 2.3)

Layer	Thickness $d [\mu\text{m}]$	Density $\rho [\text{kgm}^{-3}]$	Spec. Heat Capacity $c_p [\text{Jkg}^{-1}\text{K}^{-1}]$	Th. Cond. $k [\text{Wm}^{-1}\text{K}^{-1}]$	Th. Diff. $D [\text{m}^2\text{s}^{-1}]$	Ref.
1, Toner*	16	1 115	1 255.00	0.120	0.85E-7	/43, 88, 89/
2, vfGCC	20	1 703	850.89	0.566	3.90E-7	/42, 43/
2, MCC	20	825	838.23	0.115	1.67E-7	/42, 43/
2, Talc	20	1 670	842.12	0.848	6.03E-7	/42, 43/
3, Paper	100	971	1 445.00	0.101	7.20E-8	/26/

* values for ambient temperature

The fusing nip itself is formed by a polymer backing roll and a heated metal roll. It is simulated in a simplified two dimensional version, using commercially available finite element software¹⁶, where thermal transmission through each finite element in each layer of the substrate is defined by the general heat diffusion equation (equation 2) without heat losses. The nip description excludes effects of surface roughness or surface chemistry, as these can be evaluated initially separately by comparison of observed deviation with experiment.

Because of the insulating behaviour of the polymer backing roll b), and low temperature gradient in respect to the air boundary, there is a zero heat flow condition applied for the lower boundary of the substrate.

The transient upper boundary condition of the substrate is imposed by the moving heated metal roll c). The heating temperature in the nip is believed to be constant because of the comparatively large thermal mass of the aluminium fusing roll. Before the substrate enters the fusing nip, the surface is at ambient temperature, T_a (Figure 86).

¹⁶ Comsol Multiphysics, Version 3.4

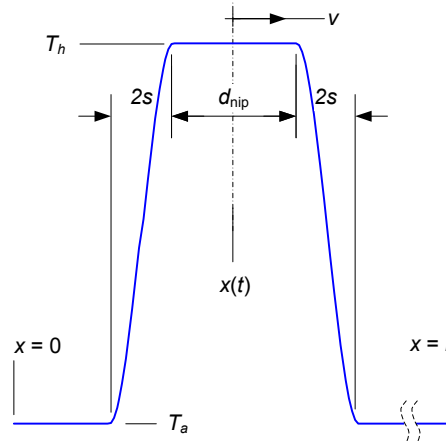


Figure 86. Temperature boundary condition for the fusing nip imposed on the surface of the toner layer. Based on paper [VI], Figure 5.

It was found that such a temperature step boundary condition, shown in Figure 86, simulates the temperature response beneath the toner layer (T_2) quite well. Figure 87 shows a comparison of the experimentally measured temperature response to the simulated behaviour using a temperature step boundary condition for the nip simulation. To remove absolute timescale differences, the relative time is used, based on the time when the temperature in the nip is at its maximum.

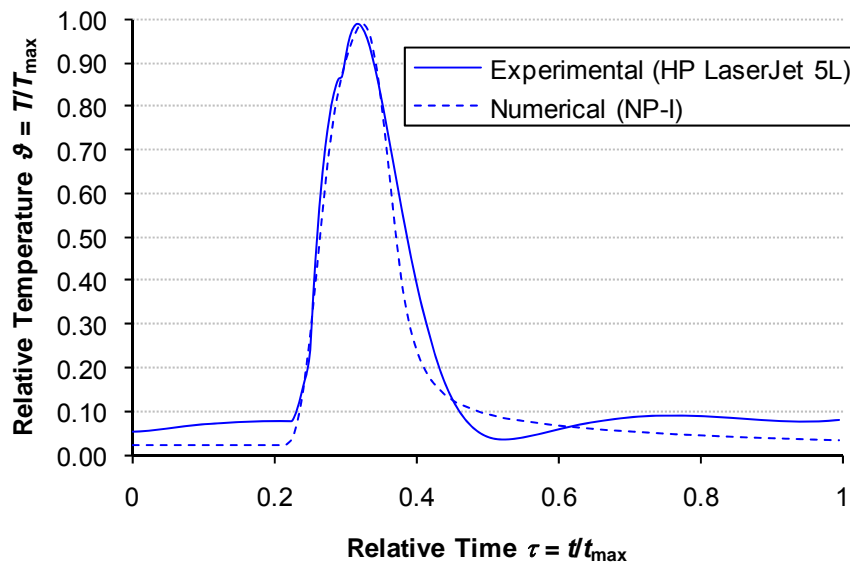


Figure 87. Experimentally measured temperature response beneath the toner layer (T_2) on a talc coated sheet in the printing nip of an HP LaserJet 5 in comparison with a simulated temperature response using a temperature step boundary condition. Based on paper [VI], Figure 7.

The conditions imposed at the boundaries of the substrate are, therefore, a constant ambient temperature, T_a , and a defined step to the constant heating temperature, T_h , of the fusing roll in the nip (see Figure 86) for the upper boundary, and a zero heat flow condition at the lower boundary.

For the simulation, the temperature step in the upper boundary condition is smoothed by the factor $2s$ at both sides. This serves two purposes: at first, the finite element method requires a step of finite gradient (continuous first derivative) to avoid convergence problems. Secondly, the nip pressure is in practice lower at the outer parts of the nip, and

ELECTROPHOTOGRAPHIC TONER FUSING ON THERMALLY DESIGNED SUBSTRATES

Simulation of electrophotographic toner fusing

therefore the contact resistance to the substrate is higher and the thermal transfer lower. Figure 88 shows the simulated nip, drawn to scale.

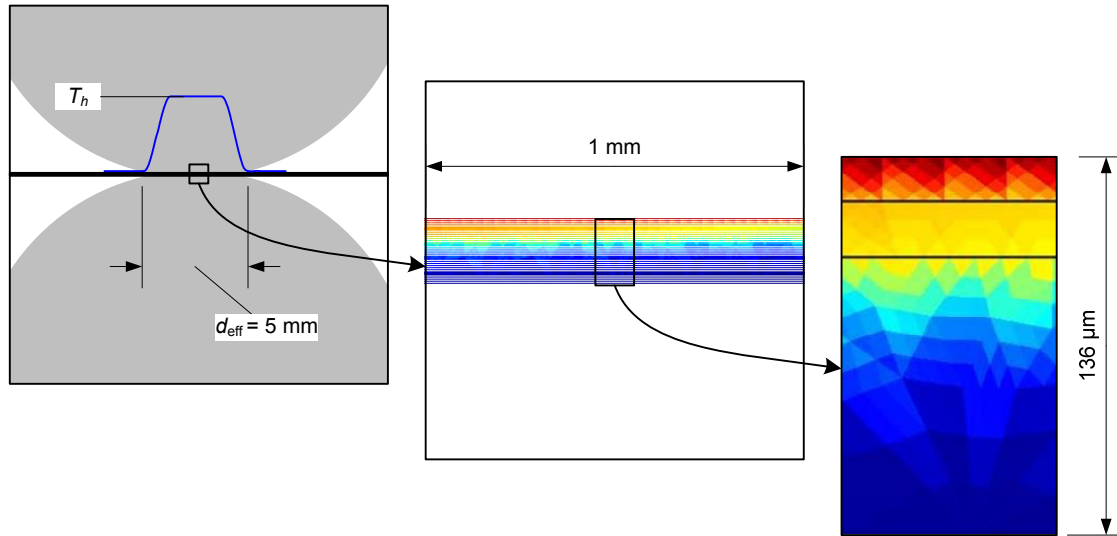


Figure 88. Fusing nip and layered substrate drawn to scale. For the colouring of the substrate, no interpolation was used in order to emphasise the finite elements.

A summary of the simulated “numeric printer” configurations studied is given in Table 19. NP-I resembles a hypothetical current laser printer model. NP-II and -III are variations of this typical printer having lower specific fusing energy, achieved by either reduced fusing temperature or by higher printing speed, respectively.

Table 19. Parameters of the “numeric printers” used to simulate the nip conditions

	NP-I	NP-II	NP-III
Heating temperature T_h	180 °C	140 °C	180 °C
Ambient temperature T_a	23 °C	23 °C	23 °C
Printing speed v	10 cms ⁻¹	10 cms ⁻¹	20 cms ⁻¹
Effective nip length d_{eff}	5 mm	5 mm	5 mm
Nip residence time t_{res}	50 ms	50 ms	25 ms
Spec. fusing energy q^*	10.17 kJm ⁻²	7.48 kJm ⁻²	7.35 kJm ⁻²
Fusing energy Q^{**}	634.30 J	466.53 J	458.42 J

*calculated from the net heat flux into an MCC coated substrate

**for the size of an A4 sheet

Note that the fusing energies Q given in Table 19 are lower than the total energy listed in Table 16, even though the heating temperature of the fusing roll in the simulations are higher than the toner fusing temperature (125 °C) considered in equation 63. It indicates that the substrate heats inhomogeneously, or, in other words, there remains a temperature gradient in the substrate, indicating a degree of thermal shielding. This will become clearer in the following discussion about the internal temperature responses.

7.3.2 Simulated temperature responses

Figure 89 shows the temperature-time responses at the given position $x = 5$ mm (middle of the simulated substrate length) for the printer configuration NP-I. The left side shows the temperatures at the interface toner and coating (T_2), the right side the temperatures between coating and base paper (T_3). It can be observed that, despite their different thermal diffusivity, both the vfGCC and the talc coating show very similar calculated temperature responses at both interfaces. However, the MCC coating displays different behaviour. The temperature T_2 rises notably faster at the interface between toner and coating on the MCC coated surface, whereas at the base paper-coating interface the temperature T_3 is affected much slower. Therefore, the MCC layer, with its rather low thermal conductivity, acts as a

thermal insulator in front of the base paper, but, also, importantly provides a rapid surface temperature rise and a higher maximum temperature in contact with the toner. From the viewpoint of energy efficiency, the shielding properties of the MCC layer can be seen as an advantage. At a given time in the printing nip, the heat does not penetrate so deeply into the substrate structure; the energy remains more at the interface of toner and coating. As a consequence, the surface temperature rises quicker, which provides potential for improvement in either printing speed or optimisation of the heating temperature of the fuser roll. Both of which are important factors for the print economy.

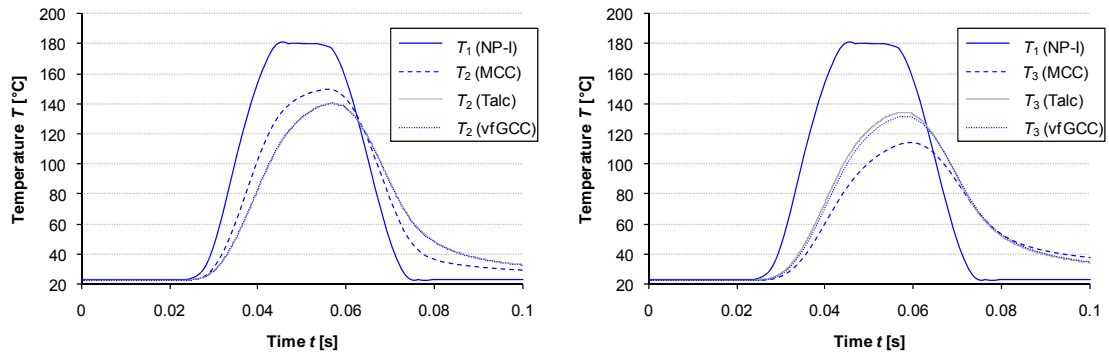


Figure 89. Left: temperature-time responses beneath the toner layer (T_2). Right: temperature-time responses beneath the coating layer (T_3). Both figures are given for the position $x = 5$ mm on the substrate for the printer configuration NP-I. Based on paper [VI], Figure 12.

7.3.3 Comparison of printer configurations

To illustrate the energy saving potential of insulating coatings, Figure 90 shows the temperature responses for two proposed model “improved” printers NP-II and NP-III on an MCC coated substrate (left) and on a vfGCC coated substrate (right). As discussed earlier, a talc coated substrate would show very similar behaviour to that of the vfGCC coated substrate. Especially for the printer NP-III (higher printing speed) the benefits of the thermally insulating MCC coating can be seen. The temperature at the interface of toner and coating layer (T_2) rises quite quickly up to 140 °C. Therefore, the temperature of the entire toner layer is higher than this, allowing the toner to melt readily. At the same time, the temperature at the base paper interface (T_3) never goes above 100 °C. This prevents unnecessary energy losses into the base paper, and, in addition, this limiting of temperature in the base paper might also help to avoid curl, induced by an uneven moisture profile, which can be a result if parts of the base paper temperature rise above the vaporisation point of water. On the right side of Figure 90, we see that, because the vfGCC coating structure is less insulating, the temperature gradient within the coating is quite small compared to the MCC coating. It is also small compared to the temperature gradient in the toner layer. Therefore, both the beneficial effects, as discussed for the MCC, are now reduced in the case of the finer denser product (vfGCC). The temperature, especially in the lower region of the toner layer, is lower, and part of the base paper temperature rises above 100 °C.

ELECTROPHOTOGRAPHIC TONER FUSING ON THERMALLY DESIGNED SUBSTRATES

Simulation of electrophotographic toner fusing

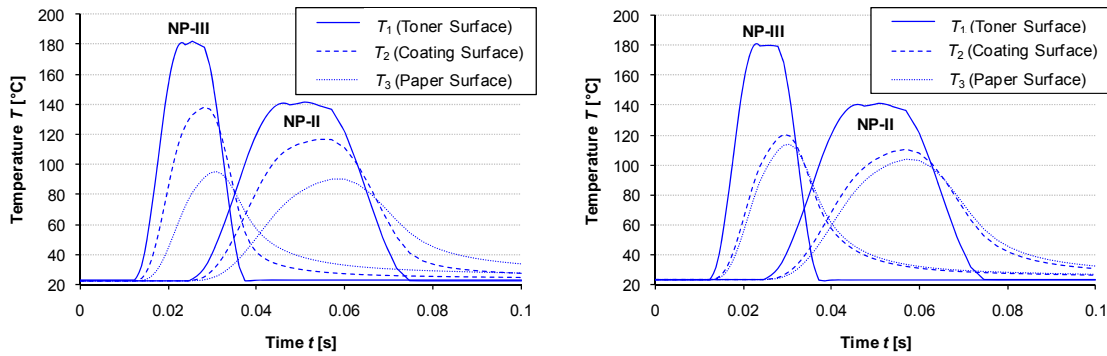


Figure 90. Temperature-time responses on MCC (left) and on vfGCC (right) coated substrate for the printer with reduced fusing temperature NP-II and the faster printer NP-III. Based on paper [VI], Figure 13.

The net heat flux into the substrate, and therefore the specific energy per unit area depends not only on the printer configuration, but also on the thermal properties and the resulting temperature gradient of the substrate. Table 19 gave the specific energies for the printer configurations exemplified for the MCC coated substrate simulation. It was seen that the specific energy is very similar for both NP-II (7.48 kJm^{-2}) and NP-III (7.35 kJm^{-2}). Calculations for the same printer configurations on the vfGCC coated substrate reveal that the energy amount penetrating into the structure is almost 30 % higher than in the MCC case, i.e. 9.72 kJm^{-2} and 9.55 kJm^{-2} for NP-II and NP-III, respectively. This further illustrates that, if the coating is more conducting, then not only is the temperature gradient within the substrate less favourable for the process of fusing but also the consumed energy is higher. As a result, an insulating coating layer can therefore help to concentrate the energy at the place where it is more beneficial for both the process and the substrate.

In a study of the toner fusing by means of discrete element modelling, Azadi *et al.* [90] observed very similar behaviour in terms of the effect of the fusing roll temperature. They showed that an increase in the fusing roll temperature from $160 \text{ }^\circ\text{C}$ to $180 \text{ }^\circ\text{C}$ can reduce the required dwell time to achieve a certain fusing temperature by a factor of two. This effect can also be observed in Figure 90, right. The printer NP-II, which has fusing roll temperature of $140 \text{ }^\circ\text{C}$, requires the time of $t_{\text{NP-II}} = 31 \text{ ms}$ to reach the maximum coating surface temperature of $110 \text{ }^\circ\text{C}$, whereas NP-III, with its heating roll temperature of $180 \text{ }^\circ\text{C}$, reaches this temperature already after $t_{\text{NP-III}} = 13 \text{ ms}$. Azadi *et al.* further stated that the fusing time is a weak function of the thermal conductivity of the coating layer. Their data indicates a 20 % increase in the fusing time for a fourfold increased thermal conductivity of the coating. Figure 91 summarises the temperature responses on the vfGCC and MCC coating surfaces for the NP-III printer configuration. The maximum temperature of $120 \text{ }^\circ\text{C}$ on the vfGCC is reached approximately $\Delta t = 6 \text{ ms}$ faster on an MCC coating layer. This equals an improvement of ca. 37 % in the fusing time to reach that temperature. However, it should be noted that it is not only the fusing time which improves, but also the absolute maximum of the fusing temperature for a given roll temperature.

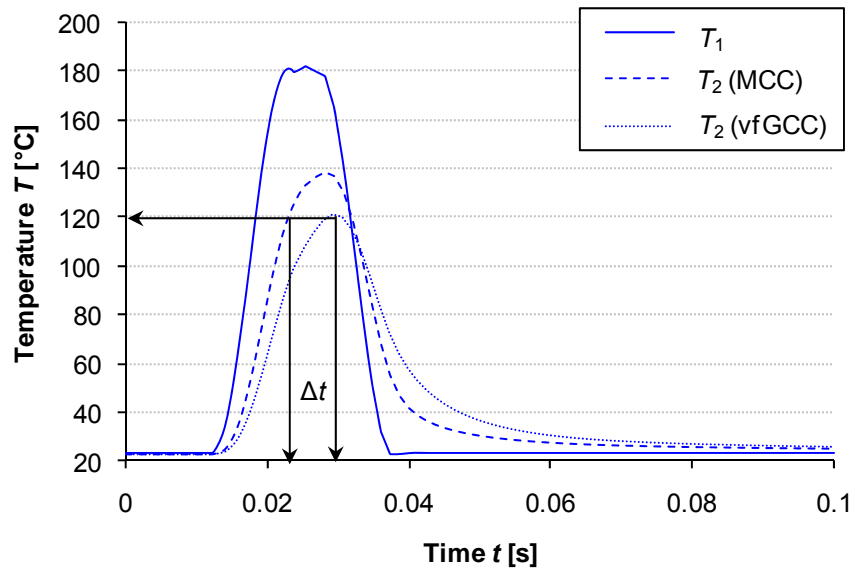


Figure 91. Surface temperature responses of the vfGCC and MCC coating for the NP-III printer configuration. Based on paper [VI], Figure 14.

7.3.4 Heat conduction versus heat storage

The discussion above showed that the thermal conductivity of the coating layer can have a significant effect on the dynamic temperature response on its surface. A perfectly insulating layer would concentrate the entire thermal energy on its surface, leading to a maximum temperature equal to the fusing roll temperature. However, as heat is conducted through the layers, it is its heat capacity, defined also by the materials it contains, that describes the unit of energy per unit temperature and mass required to heat up the material. It is therefore important to consider the role of heat conduction through the coating as well as the heat storage behaviour of the coating layer in determining the maximum fusing temperature. The thermal diffusivity (equation 4), being the ratio of thermal conductivity and volumetric heat capacity, expresses this relationship.

To study these effects, we use the thermal properties of the vfGCC pigment as an example, representing the medium thermal conductivity. We then perform a number of fusing nip simulations for a range of thermal diffusivities. This is done either by changing the thermal conductivity (numerator of diffusivity) or the volumetric heat capacity (denominator of diffusivity) and plot the effect on the maximum achieved coating surface temperature ($T_{2, \max}$). Figure 92 shows that thermal diffusivity does not describe the maximum fusing temperature unambiguously since a certain thermal diffusivity can be given by changing thermal conductivity or volumetric heat capacity accordingly, and each of these has a different effect on the maximum fusing temperature. The intersection of the curves in Figure 92 represents the vfGCC material. On the one hand, if the thermal diffusivity is increased by decreasing the volumetric heat capacity, the maximum fusing temperature response may improve slightly, but the improvement is very small, even for very low volumetric heat capacities. On the other hand, if the thermal diffusivity is increased by increasing the thermal conductivity, the maximum fusing temperature response is reduced, even though the reduction is negligibly small for high diffusivities. The other direction of decreasing thermal diffusivity by increasing volumetric heat capacity or decreasing thermal conductivity becomes more interesting as both have a significant but contradictory effect on the maximum fusing temperature response.

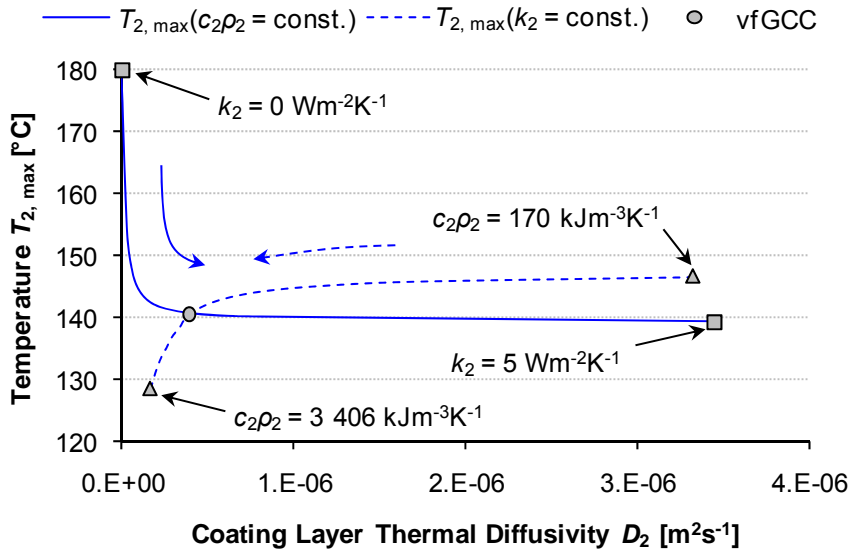


Figure 92. Maximum fusing temperature response as a function of thermal diffusivity resulting from either changing thermal conductivity or volumetric heat capacity.

Figure 92 shows that it is not thermal diffusivity of the coating that directly affects the temperature response, but the individual balance of thermal conduction versus thermal storage capacity of the material. We therefore need to discuss both parameters independently for the complete substrate.

The left side of Figure 93 displays the maximum temperature response as a function of the coating layer thermal conductivity, whereas the right side shows it as a function of the coating layer volumetric heat capacity. In addition, the temperatures are given for the hypothetical cases of an underlying base paper having half of its original heat capacity ($c_3 = 0.5c_{\text{paper}}$) and a base paper without any heat capacity ($c_3 = 0 \text{ Jkg}^{-1}\text{K}^{-1}$). It can be seen that by lowering volumetric heat capacity of the base paper, the maximum temperature response is increased to some extent. However, in the extreme case of no volumetric heat capacity of the coating layer, the maximum temperature response is still limited due to the thermal storage of the underlying base paper. Only if this would be significantly reduced as well, would the maximum fusing temperature response improve notably. The left side of Figure 93 illustrates that the thermal conductivity has very little effect if it is above $0.2 \text{ Wm}^{-1}\text{K}^{-1}$. This explains, on the one hand, why the temperature responses of talc and vfGCC, as discussed in 7.3.2, were so similar. Note, that the initial drop in the maximum temperature response for $c_3 = 0$ is because of the dynamic heat transport into the coating layer alone. Since for the base paper, by definition $c_3 = 0$ cannot take up heat, the response is constant if the thermal conductivity of the coating is high enough to thermally “saturate” the coating layer (steady state) during the dynamic fusing process. Thus, also here, the heat capacity of the base paper influences the general level of the temperature response. However, a difference to changing the volumetric heat capacity of the coating alone is that the influence of the base paper can be significantly reduced if the thermal conductivity of the coating is low enough to act as a shield. Lowering the volumetric heat capacity of the coating will merely reduce the influence of the coating layer itself and not of the base paper, while lowering thermal conductivity of the coating reduces both the influence of the coating and the base paper.

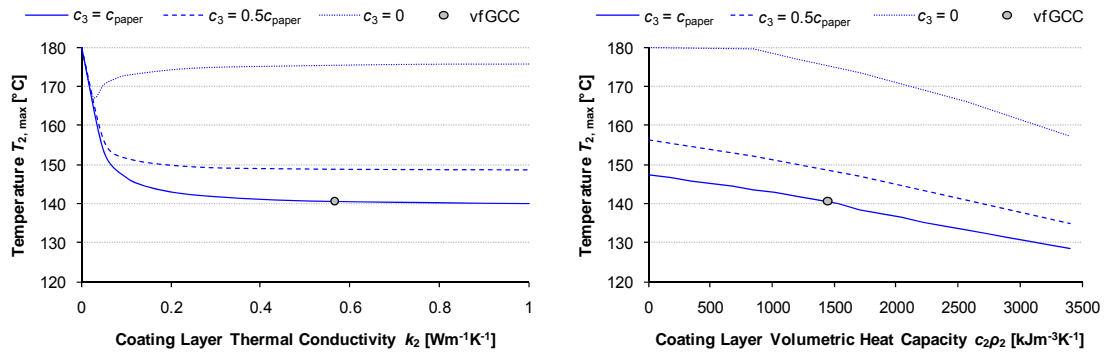


Figure 93. The effect of the coating layer thermal conductivity (left) and coating layer volumetric heat capacity (right) on the maximum coating layer surface temperature in the simulated fusing nip. The maximum temperatures are given for three heat capacity levels of the underlying base paper.

The simulations of the temperature responses for different coating layer properties show that designing the thermal conductivity of the coating layer does have a positive effect on the fusing temperature response, and, therefore, provides more energy for the toner to be fused on the substrate. Alternatively, this would allow faster printer configurations or lower fusing roll temperatures for equal fusing temperature responses. Furthermore, simulations of the thermal conduction versus thermal storage behaviour showed that it is foremost a low thermal conductivity that creates a shielding effect and, thus, improving the fusing temperature response.

To study the practical implications on toner adhesion by modifying the thermal conductivity of the coating layer, the following section will move on to a real fusing process, in which substrates are coated papers using the same formulations as in the simulations.

7.4 Toner adhesion on coated papers

7.4.1 Materials and methods

Standard 80 gm⁻² copy paper was used as a base for laboratory coating using the same pigments as in the simulations above. The binder for all coatings was n-butyl acrylate styrene latex¹⁷ in dosages of 10, 15 and 12 pph, based on 100 parts by weight of pigment for vfGCC, MCC and talc, respectively. In order to have different roughness levels for comparison for each coating type, a set of sheets was calendered in a single nip laboratory calender at a temperature of 80 °C, a load of 100 kNm⁻¹ and a speed of 10 mmin⁻¹. Burnside and Crotofino /91/ showed that for calendering of newsprint, the thermal conductivity increases from 0.10 Wm⁻¹K⁻¹ to 0.12 Wm⁻¹K⁻¹ for a bulk of 3.0 cm³g⁻¹ and 1.5 cm³g⁻¹, respectively. Because of the generally low thermal conductivities of both calendered and uncalendered paper, and the discussion in 7.3.4 that showed that the base paper thermal conductivity merely changes the level of the fusing temperature response, we presume that the densification of the base paper in calendering does not affect the subsequent discussion since we focus on the transmission of heat into the coating layer.

The sheets were printed with a test pattern on a compact commercial laser printer¹⁸. The test pattern, as shown in Figure 93, consisted of areas to measure toner adhesion on full-tone black (100 % black) printed surfaces and on half tone (40 % black) surfaces which

¹⁷ Acronal S360D is a registered trademark of the BASF AG

¹⁸ HP LaserJet 5L

were arranged in a matrix of three columns (1- 3) and three rows (A- C). This allowed evaluation of the evenness of the fusing both lengthwise and crosswise. Because of the diameter of the fusing roll, the fields in row C were fused on the second turn of the fusing roll, and therefore the fusing temperature might have been lower than on the first turn due to thermal loss to the toner and paper. For this reason only rows A and B were used for the quantitative evaluation of the fusing process.

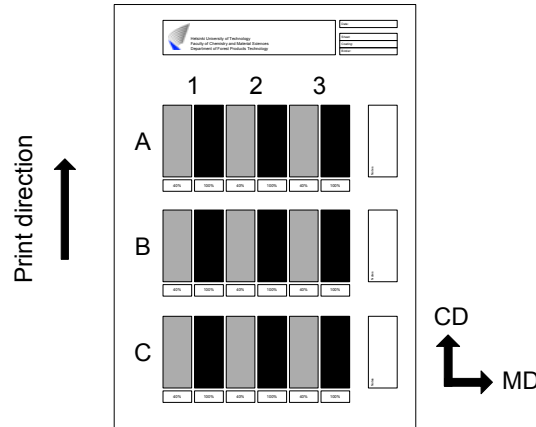


Figure 94. Test pattern used to print the sample sheets. Each test cell consists of a full tone and half tone area. Rows A and B were used for calculation of the toner area fraction. Row C was used for visual evaluation during the printing trial. Arrows indicate MD/CD of the base paper as well as the direction of print. Based on paper [VIII], Figure 2.

For assessing toner adhesion to the surface of the coated paper, a tape peel test (Figure 95) was used. In order to ensure constant angle and speed of the tape removal, a device, as described in ASTM D 1894 (Standard test method for static and kinetic coefficients of friction of plastic film and sheeting), was used. The tape is attached to the printed surface, turned and attached to a carrier. The carrier pulls away the tape at constant speed, while applying constant pressure.

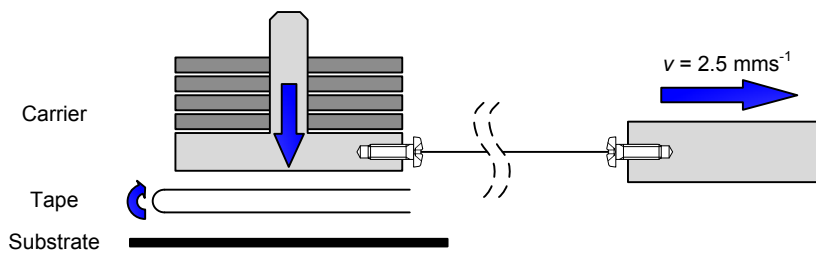


Figure 95. Tape peel test for the measurement of toner adhesion to substrate. Based on [VII], Figure 2.

The toner adhesion ξ_D is calculated by the retained print density:

$$\xi_D = \frac{D_2}{D_1} \cdot 100\% \tag{64}$$

where D_1 is print density before attachment of the tape and D_2 is print density after tape removal. The use of print density to quantify toner adhesion is quite common [79, 81, 83]. As we shall see, the toner adhesion for the fusing process of the commercial laser printer is quite complete, and therefore the print density values are high enough to characterise subtle changes. However, as print density after tape removal can become very low for experimental fusing systems, we distinguish the toner adhesion measurement based on

print density, ζ_D , from the toner adhesion measurement based on the toner area fraction, ζ_A , referring, in turn, to the area of retained toner as observed using image analysis, as used in section 7.5.

7.4.2 Adhesion measurement results

The left side of Figure 96 shows the results of the tape test for toner adhesion on the various coated substrates. As mentioned above, we see that the toner fusing process is quite complete on all substrates. This is because a commercial laser printer was used and these are normally designed to work on a great number of different paper substrates, and thus apply high fusing temperatures and run sufficiently slowly to ensure toner adhesion. The 95 % confidence intervals are narrow enough, however, to discuss differences in toner adhesion. A large part of the variation in the toner adhesion measurement does not come from a variation in toner adhesion itself but from the originally high variation in print density related to uneven printing properties in the experimental setup of the printer used.

In general, we see on the top of Figure 96 that calendering improves toner adhesion on all the given papers, regardless of whether it is on grey (half tone) or black printed areas. However, the extent of the improvement varies significantly. The biggest improvement due to calendering is observed for the MCC coated sheets. Toner adhesion on black printed areas of calendered sheets is very good for all grades, but is distinctly lower on grey printed areas. On the uncalendered grades, toner adhesion on black areas varies more, but is also higher than on grey areas of the corresponding grade. Again the MCC grade shows a large difference, but even more striking is the uncoated base paper.

ELECTROPHOTOGRAPHIC TONER FUSING ON THERMALLY DESIGNED SUBSTRATES

Toner adhesion on coated papers

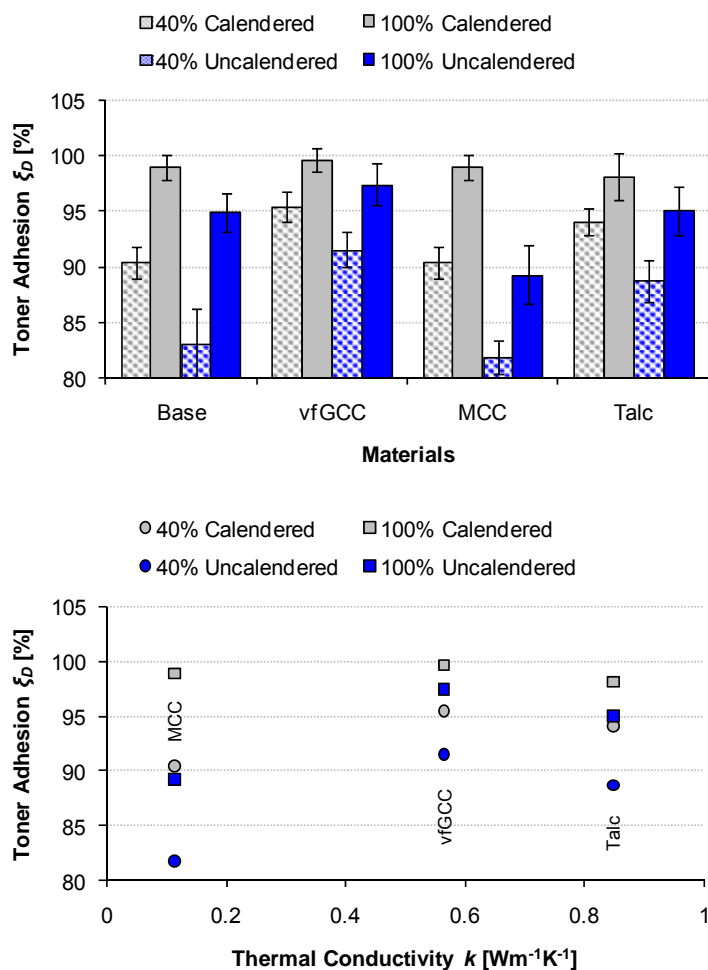


Figure 96. Top: toner adhesion and 95 % confidence intervals for base paper and laboratory coated sheets. Toner adhesion was measured on 40 % black printed areas as well as fully black printed areas for calendered and uncalendered sheets. Bottom: toner adhesion on the coated sheets plotted against thermal conductivity of the coating layer calculated from the diffusivity measurement of the tablet material. Based on paper [VII], Figure 9.

In a visual evaluation, i.e. a before and after comparison of the tape test, three phenomena characterising low toner adhesion could be identified. At first, the interspersed toner “dust” in between the dots is almost completely removed by the tape. The second effect is a reduced dot size or partially broken dots. Thirdly, there are even a few missing dots. These phenomena explain to some extent the generally lower toner adhesion on grey areas. On an evenly black printed area the working surface for the tape is greater per unit force. In contrast, a grey area, where the dots provide additional possibilities for the tape to pull out toner, the pull force is concentrated at the dot-coating interface. Thus, for the full-tone printed area, being a more even layer, any toner pulled out by the tape is more likely to have to overcome cohesive failure in the toner layer before manifesting low toner adhesion to the substrate, i.e. the linear integrity of the continuous toner layer provides for a balance between internal cohesion and adhesion to the surface, where the cohesion can transmit the pulling force away from the weakest points of adhesion. This is analogous to thin film forces, which act for liquids between two planar surfaces providing apparent high adhesion even though there is no potential for surface attraction (non-wetting surface energy criteria).

The bottom of Figure 96 shows the toner adhesion versus thermal conductivity. Although in the medium range of thermal conductivity, the vfGCC coated sheets show generally better toner adhesion, before we can draw any conclusions in relation to thermal properties in practice, we need to consider what we mean by surface roughness more closely.

7.4.3 Surface roughness and surface continuity

Surface roughness was measured with the Parker Print Surf method (ISO 8791-4) for both the calendered and uncalendered sheets. Additionally, the surface micro roughness was measured by confocal laser scanning microscopy (CLSM). The micro roughness is expressed as the root mean square deviation about the mean surface measured along a line of 40 μm length. The out of plane resolution was set to ca. 1 μm , the in plane resolution was ca. 1.6 μm .

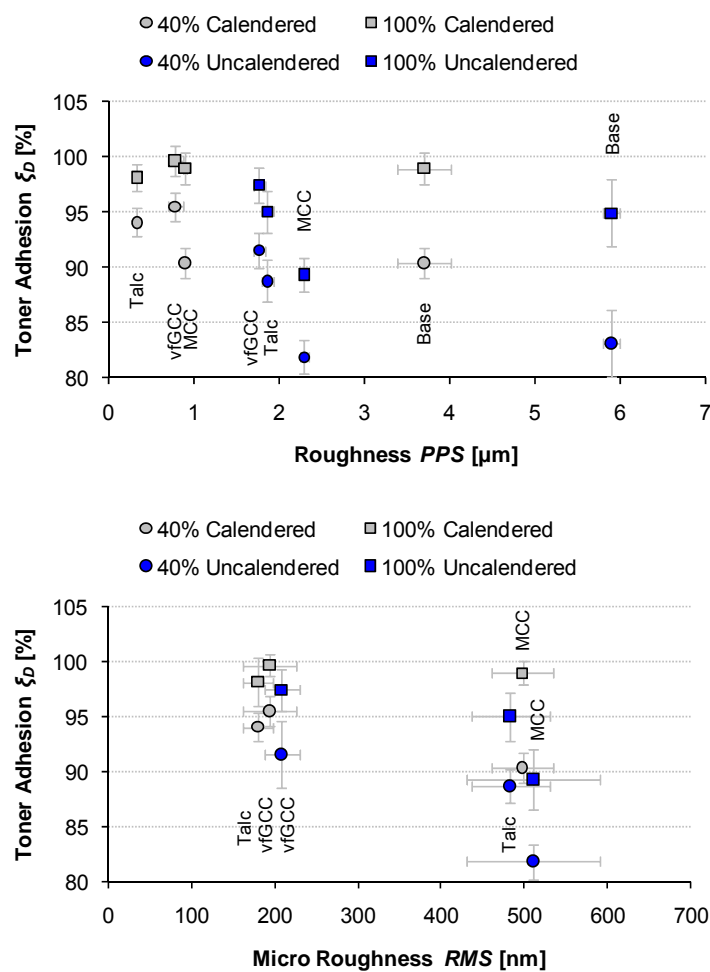


Figure 97. Top: toner adhesion as a function of PPS roughness including 95 % confidence intervals. Bottom: toner adhesion of calendered coated sheets as a function of RMS micro roughness measured by CLSM including 95 % confidence intervals. Based on paper [VII], Figure 11.

Since surface roughness is considered to be an important parameter for toner adhesion, it is necessary here to decouple its effect from surface chemistry but also from thermal conductivity. The uncalendered substrates indeed show greater toner adhesion failure even on black printed areas. Surface roughness measured by PPS is given on the top of Figure 97. For calendered sheets, we see, as discussed before, that toner adhesion on black areas is good even though the PPS roughness varies. The fusing is apparently quite complete and

the closed black surface doesn't allow the tape to pick out toner to the extent that would lead to a measurable print density loss. On grey areas, toner adhesion varies more.

The PPS roughness in Figure 97 (top) indicates no clear trend across the different surfaces. For the coated uncalendered sheets, viewed in isolation, we see that toner adhesion increases more or less linearly with surface smoothness. This is consistent with earlier findings by Sipi /83/ and can explain why the uncalendered MCC coatings, at first sight independent of their insulating thermal behaviour, result in lower toner adhesion (compare Figure 96, bottom). Nonetheless, Figure 97 also indicates that toner adhesion on grey areas of the calendered MCC coated sheets is distinctly lower than that of vfGCC coated sheets, despite having about the same PPS roughness, and even more importantly, the uncoated sheet with much higher PPS roughness and similarly low thermal conductivity (Table 18) displays superior toner adhesion compared to the insulating MCC even for the uncalendered surface in the full tone area. There must, therefore, be other factors at play than surface roughness on the PPS scale and average thermal conductivity.

The bottom of Figure 97 shows that because of the very porous structure of the MCC coating, its surface retains a significantly higher micro roughness after calendering compared to vfGCC, as seen in the CLSM. We see, therefore, that micro roughness, even at high levels does not define the toner adhesion per se. This is logical since it is much finer in scale than both the printed dot (120 μm) and the toner agglomerate particle size itself (~15 μm). The main difference between uncalendered and calendered surface is then the density of the sheet, and thus its micro structural effects on electrical charge and its related thermal conductivity, as predicted by Maxwell /30/, i.e. its continuity.

It is concluded here, therefore, that there is a critical coating density, or better described as surface continuity, independent directly of surface micro roughness, required for good toner adhesion, below which the dielectric and thermal conductive components of the coating are too low. Surface continuity refers to connectivity of all regions across the coating surface. During shrinkage, cracks may form non-connected structures, thus reducing the surface structural continuity. Similarly, any changes in localised compression of the coating, or uneven coat weight distribution will all lead to changes in the continuity of thermal transfer laterally across the surface.

Based on these findings that a thermally insulating coating layer would be beneficial for the fusing behaviour in theory, as long as sufficient surface continuity is provided in practice, one can further develop coating formulations and configurations. A thin, thermally conducting layer could be applied on top of an insulating porous layer to provide material continuity and sufficient lateral thermally conductive continuity in order to achieve better half tone area adhesion. The following section builds on this concept and describes the toner adhesion development for increasing fusing temperatures.

7.5 Toner fusing and improved adhesion development

7.5.1 Coating concepts and their thermal properties

Based on the discussion in 7.4 that introduced the concept of surface continuity, two newly thermally designed coatings are studied. They are comprised of a thermally insulating precoating and a topcoating layer to provide surface continuity. The first concept, henceforth simply referred to as "Mica", uses mica¹⁹ as a precoating pigment together with a fine, narrow particle size distribution ground calcium carbonate topcoating²⁰ (nfGCC). Compared to other minerals, mica has a very low inherent thermal

¹⁹ Mica SFG 40 (Mica), Aspanger

²⁰ Covercarb 75 (nfGCC), Omya AG

conductivity of ca. $0.4 \text{ Wm}^{-1}\text{K}^{-1}$ /42/. This is about a sixth of the inherent thermal conductivity of calcium carbonate.

The second coating concept is based on the porous Modified Calcium Carbonate (MCC) as simulated in 7.3, and also used as a paper coating in 7.4. The MCC pigment alone showed greater thermal insulating behaviour compared to standard calcium carbonate pigments (see Table 18) and even compared to the mica pigment. However, it was found that a precoating consisting of MCC pigment only delaminates easily, for example in the tape test which is used to study toner adhesion. This was observed even at a binder concentration of 15 w/w%. Therefore, to develop better internal cohesion of the MCC coating layer, it was used in blend combination with a broad particle size distribution ground calcium carbonate²¹ (bfGCC).

To avoid changes in surface energy of the paper, the papers had essentially a comparable topcoating formulation applied to the precoats. In general, binder systems, dispersants and polymer additives control surface chemistry to the greatest extent, apart from the hydrophobic case of the talc used in previous discussions. In addition the surface energy of toner can have an effect on spreading and therefore toner adhesion /92/. Therefore, to eliminate the role of surface chemistry change, the same toner was used for all prints. As we shall see later, the differential increase in cohesion versus adhesion plays a significant role in terms of measured toner adhesion using the method applied here. It could be that interface surface energy effects could change this balance in individual cases.

Both the mica and MCC precoating concepts are compared to a reference coating which is a monolayer of a calcium carbonate and clay²² blend. The binders used were a standard medium T_g SA²³ latex and a self-thickening rotogravure latex (SA-R²⁴) to promote the barrier properties in the mica formulation, and to counter the high dewatering tendency of such a coarse pigment on the coating machine. Table 20 provides a summary of the coating formulations and the corresponding coating method used. All the coatings had a similar target coat weight of ca. 12 gm^{-2} per side and were coated on an industrial scale pilot coating machine²⁵ using both the blade coating and film press coating methods. The base paper used was a commercial magazine paper grade with a basis weight of 42 gm^{-2} . After coating, the web was calendered to target gloss of 33-35 % (TAPPI 75°) and cut to A4 sheets for printing.

Table 20. Coating formulations (parts per hundred based on total pigment) and methods used in the pilot scale coating trial

Precoat	Reference	Mica	MCC
Method	Blade	Blade	Film
Pigment(s)	80 nfGCC 20 Clay	100 Mica	80 bfGCC 20 MCC
Binder	11 w/w%, SA	9 w/w%, SA-R	12 w/w%, SA
Topcoat	*	Top I	Top II
Method		Film	Blade
Pigment(s)		100 nfGCC	100 nfGCC
Binder		6 w/w%, SA 4 w/w%, Starch	10 w/w%, SA

*single coating layer

Figure 98 shows the measured thermal conductivities of the coating formulations for both the precoatings and the topcoatings. The formulation “Top I” refers to the nfGCC

²¹ Hydrocarb 90 (bfGCC), Omya AG

²² Hydragloss 90, Huber Engineered Materials

²³ Latexia 203, Ciba

²⁴ Latexia 211, Ciba

²⁵ FPC – Forest Pilot Center Oy, Raisio, Finland

topcoat formulation applied on the mica precoat, whereas “Top II” is the formulation used on top of the MCC base-coating. It can be seen that the conductivities of the reference coating, the MCC formulation as well as the topcoating formulations are very similar. While it was desired to achieve comparable thermal conductivities for the topcoatings and the reference coating, the thermal conductivity of the MCC formulation is higher than initially expected. When using only MCC pigment and a binder amount of 15 w/w%, the thermal conductivity was measured to be $0.12 \text{ Wm}^{-1}\text{K}^{-1}$ (listed in Table 18). However, in the case of the blend of 80 parts bfGCC and 20 parts MCC, the thermal conductivity is raised to ca. $0.54 \text{ Wm}^{-1}\text{K}^{-1}$, due to the increased tablet density (1666 kgm^{-3} for MCC/bfGCC compared to 825 kgm^{-3} for MCC pigment only) and due to increased solid phase connectivity because the bfGCC fills the MCC pore structure to some extent.

Aside from the disadvantageously rather high thermal conductivity of the MCC/bfGCC formulation, Figure 98 shows that the mica formulation exhibits the desired distinctly lower thermal conductivity. Since the binder amount of 9 w/w% is close to the amount used in, say, the Top II formulation, it suggests that the difference in thermal conductivity is in fact largely due to the inherently lower thermal conductivity of the mica pigment.

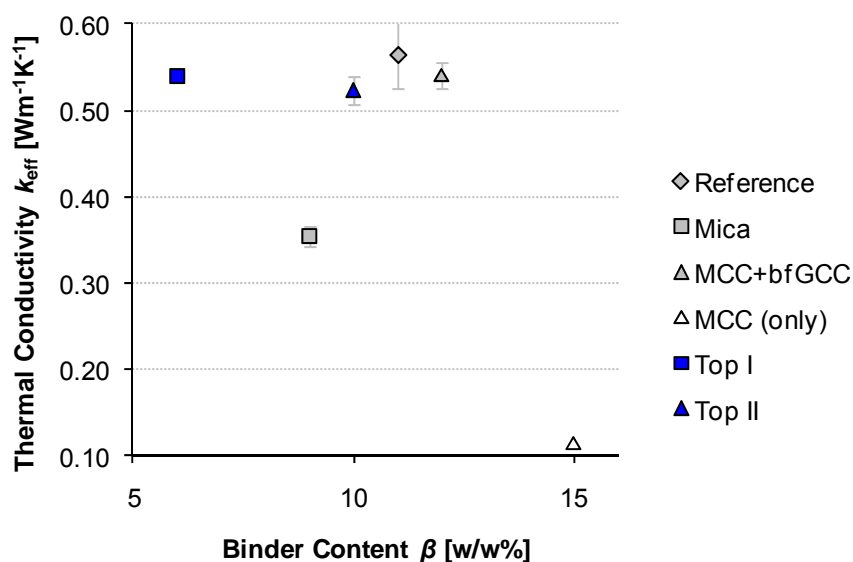


Figure 98. Thermal conductivities of the coating formulations involved. Based on paper [VIII], Figure 5.

7.5.2 Printing

The printing trials were performed on an experimental electrophotography printing system²⁶ (Figure 99). This system allows individual adjustment of the process parameters, such as printing speed, toner transfer voltage and fusing temperatures. Because of its open structure it is also possible to sample in between process steps to evaluate such parameters as toner transfer and fusing.

²⁶ KCL Duplo

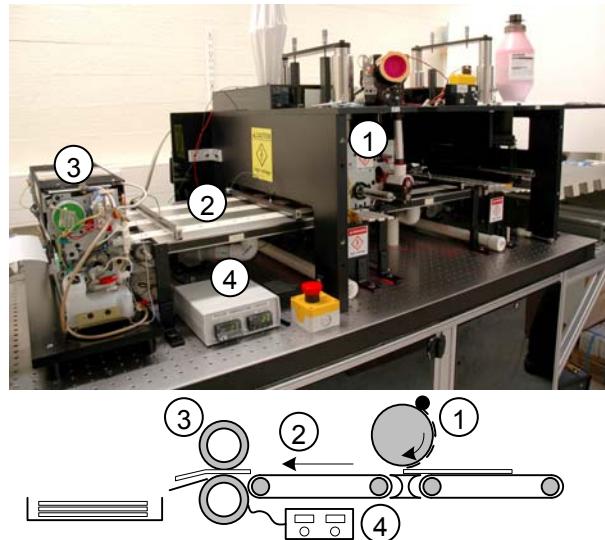


Figure 99. Photo and schematic of the experimental electrophotography printing system.
 1) Toner transfer unit, 2) Transfer belt, 3) Fusing unit, 4) Fusing temperature control.
 Photo courtesy of VTT (previously KCL). Based on paper [VIII], Figure 1.

The sheets were printed with the 1 bit bitmap test pattern shown in Figure 94. For all prints the toner transfer adopted a voltage of 3.8 kV at a speed of 10 cms⁻¹. The toner²⁷ was a traditional melt ground polyester based toner ($T_g = 78\text{ }^\circ\text{C}$, /93/). Sampling of sheets after toner transfer confirmed a complete and even toner transfer. The temperature of the fuser roll was set to temperatures ranging from 130 °C up to 160 °C. The test printing system also allows adjustment of the temperature of the backing roll. This was set constant to the lowest controllable temperature of ca. 90 °C. However, the sample sheets were fixed onto a thick (240 μm) insulating carrier board, in order to minimise temperature fluctuation influences from the backing roll.

7.5.3 Adhesion development

As mentioned previously in 7.4.1, toner adhesion was quantified by the relative loss in optical print density after removal of an adhesive tape. However, print density was found to be unsuitable when it comes to the region of very low toner adhesion as encountered during the build-up of adhesion. Toner adhesion is therefore expressed here as the area fraction ξ_A of toner that remained on the test field after removal of the adhesive tape.

For the evaluation, the test pattern was scanned after performing the tape test at double the resolution of that of the printing (Nyquist sampling theorem). The scanned image was analysed using a custom made image analysis program that calculated the number of black (toner) pixels N_{black} based on the total pixel number:

$$\xi_A = \frac{N_{\text{black}}}{N_{\text{black}} + N_{\text{white}}} \cdot 100\% \quad (65)$$

Due to the use of the 1 bit printing format and scanning, no thresholding was required.

The total cohesion of the multilayer composite consists of the combination of individual cohesion of each of the components γ_i as well as the adhesion defined between the separate layers γ_{ij} . Figure 100 lists the possible adhesion and cohesion energies for the case when the tape is fully covering the toner layer (full tone) or when the tape is also in direct contact with the coating (between the dots of the half tone). The nomenclature given in Figure 100

²⁷ DC 40, Xerox

will be used in the subsequent discussions. Peeling off the adhesive tape will delaminate the structure at the weakest link /94/, i.e. at the point of least cohesion or adhesion. As such, the tape test does not necessarily measure “toner adhesion” (γ_{23}) only. Delamination might occur because of adhesion failure at any of the material interfaces or because of cohesive failure within a material. Since the toner area fraction measurement evaluates the number of black toner pixels per area, the toner area fraction might deviate from recording purely toner adhesion because of cohesive failure of the toner layer (black remains black after the tape test) or because of cohesion or adhesion failures in the lower layers (black turns to white after the tape test even though there was full toner to coating adhesion), i.e. one needs to take into account whether toner is removed by the tape or whether a delamination of coating or base paper occurs. By definition, the maximum toner area fraction is 40 % and 100 % for the half tone and full tone area, respectively. For future discussions, unless pointed out otherwise, any result of a lower toner area fraction will be regarded as low toner adhesion.

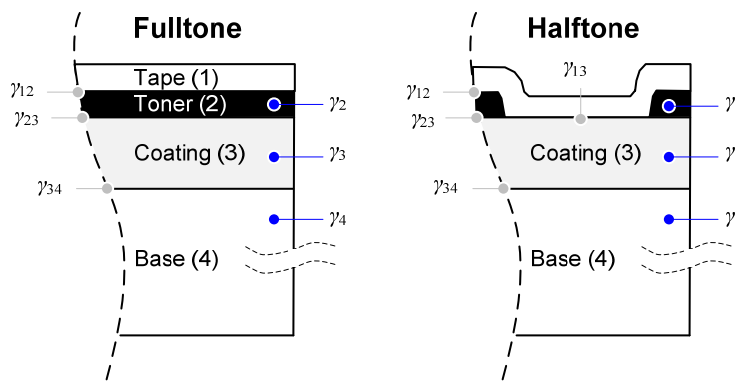


Figure 100. Cohesion (γ_i) and adhesion (γ_{ij}) of the multilayer laminate consisting of tape (1), toner layer (2), coating layer (3) and base paper (4). Left: full tone laminate. Right: half tone laminate with the additional interface of tape to coating layer. Based on paper [VIII], Figure 4.

Surface roughness is generally referred to as being a critical parameter for toner adhesion. Although Sipi /83/ showed that roughness for calendered grades is not the most critical factor, and also the discussion in 7.4.3 could relate neither macro nor micro roughness directly to toner adhesion, PPS roughness shall be included in this discussion to point out the similar surface properties of the coatings. Table 21 shows the PPS roughness, measured on unprinted areas of printed sheets, together with the calendered gloss level. The roughness is slightly less for the mica precoating concept, because of the platy particles providing excellent coverage of the base paper. The MCC precoated paper is slightly smoother than the reference, given the compressibility of the porous structured MCC, but generally all surfaces are at a similar level. In addition to roughness, surface chemistry of the calcium carbonate topcoatings can be regarded as similar.

Table 21. PPS roughness and gloss level (TAPPI 75°) both measured on unprinted area after print.

	PPS [μm]	Gloss level [%]
Reference	1.94	34.5
Mica precoated	1.58	33.2
MCC precoated	1.86	34.4

7.5.4 Full tone adhesion development

Figure 101 shows the measured toner area fraction after the tape test on the full tone area as a function of the fusing roll temperature. First of all, one can see that there is a

rather large standard deviation at the onset of toner adhesion. On the one hand, this refers to the unstable nature of adhesion in the temperature range where toner begins to adhere. However, on the other hand, it was observed that part of this deviation comes from slightly different adhesion levels in the test fields of the print pattern. The fields in row B of the print pattern shown in Figure 94 generally displayed a lower toner adhesion than the fields of row A. The fusing roll temperatures are the temperatures of the fusing roll right before the fusing of the entire sheet. The lower adhesion on fields of row B could, therefore, be as a result of an effective local decrease in the roll temperature during the fusing process.

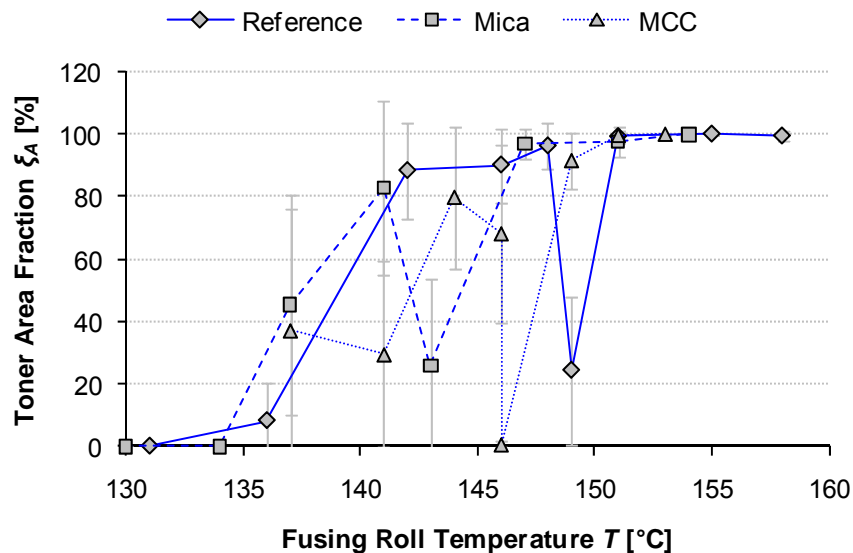


Figure 101. Toner area fraction as a function of the upper fusing roll temperature for full tone areas. Based on paper [VIII], Figure 6.b.

One can see that the temperature of ca. 134 °C is the onset of the measured retained toner area fraction for the reference and the mica precoated sample. The same holds for the MCC precoated sample, even though there is a larger standard deviation. Furthermore, all three coating concepts show the common trend that with increasing fusing temperature the toner area fraction increases as well. However, just before the full toner adhesion is achieved there is a significant drop in the toner area fraction. The toner area fraction subsequently reaches the constant maximum at fusing roll temperatures, respectively, of 147 °C (Mica), 149 °C (MCC) and 151 °C (Reference) on the full tone area. This trend correlates with the measured thermal conductivities. The lowest thermal conductivity of the coating provides the fastest temperature response in the thin more conductive topcoat, and thus highest maximum response temperature to focus more thermal energy on toner fusing.

The behaviour that all the coatings showed in the range of different fusing temperatures for full tone fusing is worth examining in further detail. For the Mica data, which are exemplary for the MCC and reference data as well, Figure 102 shows the trend split into four temperature ranges.

In *range I* no toner adhesion can be observed by the tape test at all. This means that the entire toner layer must have been taken up by the tape removal. To achieve that, the tape to toner adhesion must be higher than the toner to coating adhesion ($\gamma_{12} > \gamma_{23}$), but also the toner cohesion must be higher than the toner to coating adhesion ($\gamma_2 > \gamma_{23}$). Hartus /95/ showed that the initial softening of toner occurs at temperatures above its glass transition temperature. The glass transition temperature of the toner used is $T_g = 78$ °C /93/ and this is well below the threshold temperature of 134 °C. During this initial softening, the

temperature is high enough for toner particles to begin to coalesce and therefore build up cohesion forces. For that reason, the tape test can remove the toner quite effectively in range I.

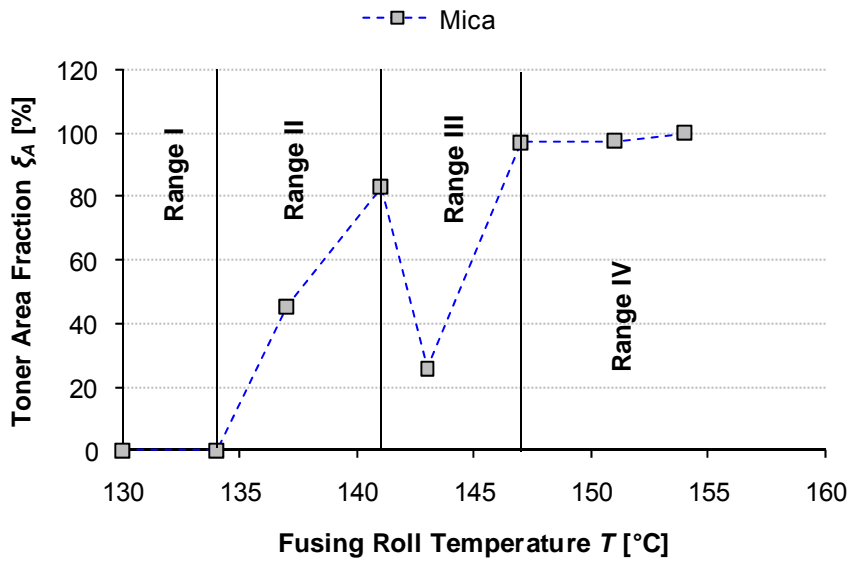


Figure 102. Full tone toner area fraction on the mica precoated paper illustrating the four temperature ranges of the development of a fully cohesive laminate. Based on paper [VIII], Figure 8.

In *range II*, the adhesion between toner and coating begins to build up in addition to the continuing increase of toner cohesion. The tape test cannot exactly quantify the magnitude of toner cohesion versus toner adhesion. However, the fact that this temperature range is characterised by a high variance in the measurement results suggests that there is a competition in delamination between the increase of internal toner cohesion and adhesion to the coating layer and that these forces are within the same order of magnitude ($\gamma_2 \approx \gamma_{23}$). This means that only part of the delamination force is transferred to the toner coating interface. The measurement becomes very susceptible to local variations caused by either the process (cooling of the fusing roll during fusing) or variations within the substrate, such as interface flaws or residual stresses /94/.

The temperature *range III* signifies a critical area for which the cohesion of the toner reaches its maximum while the adhesion to the coating layer is not fully established. The toner to coating adhesion is therefore the weakest link in the delamination process of the tape test. Such a response to delamination has been observed for the adhesion of offset ink on coatings as well, where the build up of cohesion (internal tack) reaches a point where the full delamination force is transmitted to the interface of coating and ink /96/.

For the higher fusing temperatures in *range IV*, both the processes of toner cohesion and adhesion to the coating are complete. The high toner adhesion is observed as the tape test does not show a loss in the toner area fraction. At the same time, the high toner cohesion could be observed by attaching the tape used for testing to a blank sheet of paper. On the white background, no or very little toner on the tape could be identified visually. However, it should be noted that also delamination of the base paper was observed (γ_4 becoming the weakest link). This occurred for all the coating concepts, which is a testimony to the high internal coating strength (γ_3), including that of the MCC concept having the bfGCC blended in.

The discussion above about the four temperature ranges of adhesion/cohesion development focused on the tape test performed on a full tone printed area. The toner area fraction development on a half tone printed surface shown in Figure 103 exhibits a different behaviour. There is a more distinct “jump” to full toner cohesion/adhesion. Furthermore, the full adhesion level for all substrates is reached already at a fusing roll temperature of 137 °C, compared to the fusing roll temperatures of 147 °C (Mica), 149 °C (MCC) and 151 °C (Reference) on the full tone area. The sudden jump to full adhesion can be traced back to the fact that there is the additional tape to coating layer interface (see γ_{13} in Figure 100). The delamination force is almost exclusively transmitted through this interface before there is full toner adhesion: $\gamma_{13} > \gamma_{23}$. That means the tape picks up the half tone dots not because the toner particles fail to coalesce, but, because the toner to coating adhesion is smaller than the tape to coating adhesion, i.e. the toner is removed completely by the tape since there is no longer the long range thin film force derived from the cohesion within a complete full tone layer. This effect is similar to the difference between separating a thin liquid film versus a single droplet, i.e. the surface energy associated with the continuous film dominates the transmission of forces, and is very difficult to break, whereas a droplet is a discrete system with minimised surface energy at the droplet-surface-air interface. Compared to the toner area fraction development on full tone areas, this means that essentially the temperature ranges II and III (the toner cohesion build up) are “skipped” because of the additional tape-coating interface, such that the tape test cannot observe the “competitive build-up” (see discussion in range II above) of toner cohesion and adhesion as was applicable to thin full tone films.

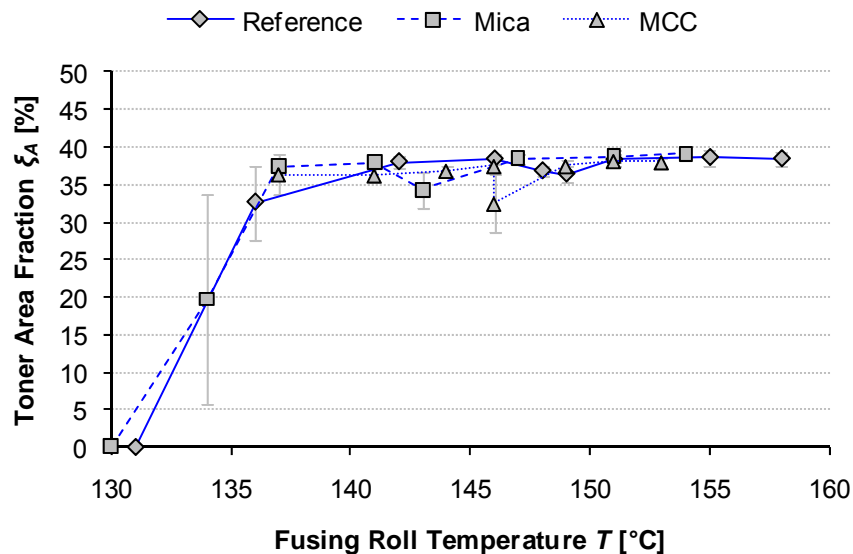


Figure 103. Toner area fraction as a function of the upper fusing roll temperature for half tone areas. Based on paper [VIII], Figure 6.a.

Two reasons come to mind why the toner adhesion in the half tone area is formed at a distinctly lower temperature compared to the full tone. On the one hand, the thickness of a half tone dot might be lower than that of the full tone layer, due to spreading, which would lead to a higher temperature at the interface of toner and coating and also to a faster temperature rise. On the other hand, direct contact of the fusing roll with the coating layer leads to faster temperature rise of the coating layer due to in-plane heat transfer in the continuous topcoat, thus promoting the melting of the toner on its surface. Since all the coatings had comparable topcoating formulation to provide for surface continuity, the latter

reason supports that surface continuity, as stated in 7.4.3, is vital for good half tone toner adhesion.

7.5.5 Print gloss development

No coating would be designed regarding the thermal fusing properties only. Also other print quality parameters should reach desired targets and must therefore be taken into account. Print gloss is considered to be an important print quality parameter in electrophotography. Figure 104 shows the print gloss (TAPPI 75°) on the full tone area as a function of the fusing roll temperature. While it can be seen that a higher fusing roll temperature clearly improves print gloss, it is also visible that at the critical points where full adhesion failure would occur the gloss is reduced to almost the gloss level of the paper.

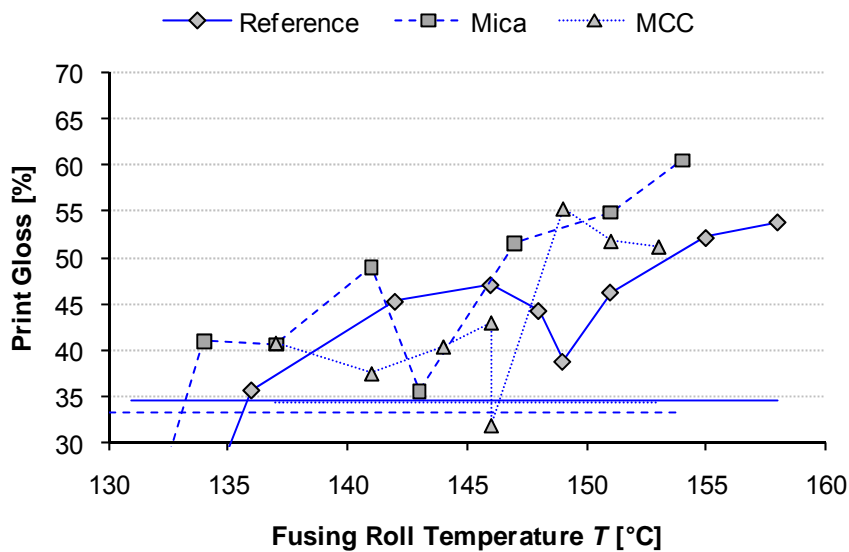


Figure 104. Print gloss as a function of the upper fusing roll temperature. The horizontal lines indicate the paper gloss levels. Based on paper [VII], Figure 9.a.

The graph of print gloss versus toner area fraction (Figure 105, left) shows that there is a somewhat close to linear correlation of measured full tone gloss (before the tape test) and the result in toner area fraction after the tape test. However, this linear correlation holds solely for temperature ranges I to III, before the full adhesion is established. When the maximum toner area fraction is reached, print gloss continues to increase with fusing temperature. Nonetheless, the linear correlation of print gloss and toner area fraction during the build-up of toner adhesion means that the relatively simple measurement of print gloss could be used to anticipate toner adhesion (shown in Figure 105, right) provided the properties of the topcoating are comparable.

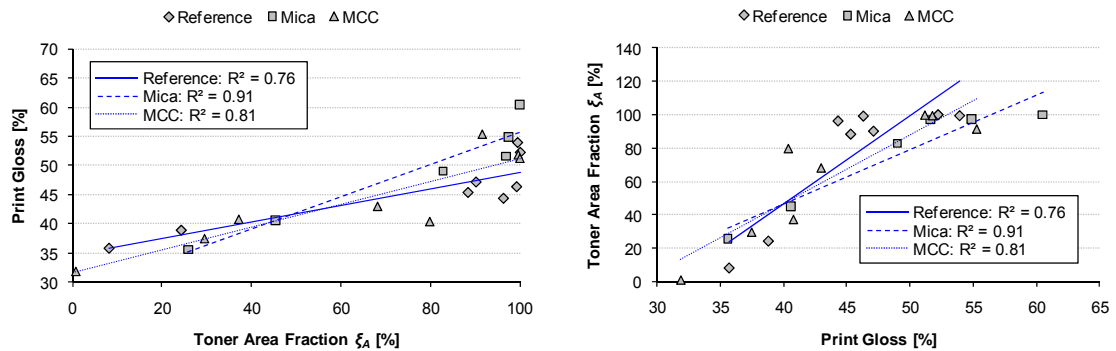


Figure 105. Left: Printed gloss as a function of full tone area fraction after tape test. Right: Toner area fraction as a function of printed gloss. Both include linear trend lines for each substrate. Based on paper [VII], Figure 9.b.

Figure 105 shows that the printed gloss on the mica precoated substrate is slightly higher than that of the MCC precoated or reference coating, while the latter two coatings show very similar print gloss. Although it cannot be stated with absolute certainty that the higher print gloss observed for the mica precoating concept is a direct result of its thermally insulating behaviour and its beneficial fusing temperature development, it is clear that the print quality properties (low surface roughness, high gloss and good toner fusing) are not mutually exclusive, and the combination of these is a clear advantage of the mica precoat formulation.

7.6 Summary

Rising demands in print quality and economy pose the question if and how a thermally designed substrate can contribute to improve these criteria. The finite element method (FEM) simulation of an electrophotography fusing nip showed that the insulating behaviour of an MCC coating layer causes a higher average temperature on top of the coating, while the temperature below the coating rises slower. For toner fusing, this seems to be a desirable behaviour because the thermal energy concentrates on top of the coating, where it is required for the fusing process, and, at the same time, the base paper is shielded. This was reflected in the specific fusing energy demand. Furthermore, it was shown that this shielding effect is due to low thermal conductivity. Low volumetric heat capacity can improve the temperature response as well, but is less effective if the base paper acts as a thermal sink. This contributes on a theoretical level to supporting hypothesis [C].

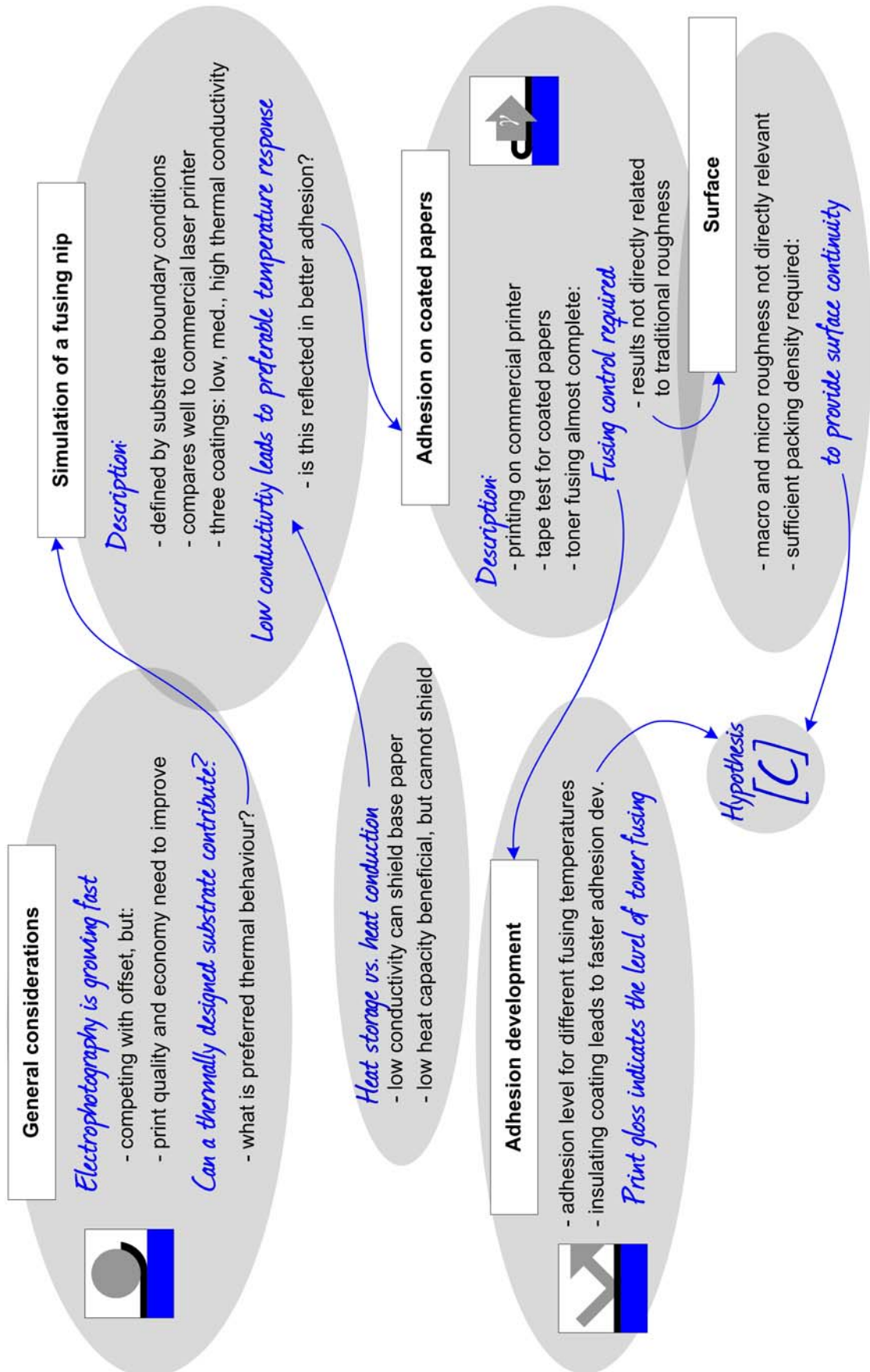
Experimentally, it was seen that neither changes in PPS nor micro roughness can explain the full extent of toner adhesion improvement. However, it was deduced that for good toner adhesion, surface continuity or sufficient packing density is also required. An optimal coating for an electrophotography printing paper should have both a thermally insulating coating layer and sufficient coating pigment packing density. This latter effect can be related primarily to pigment particle size. Calendering the low density insulating MCC coating was shown to suffice in providing the required packing density for good toner adhesion in the full tone areas, but less so in the half tone areas. Additionally, an ultra thin thermally conducting layer could, in principle, be applied on top of such a highly porous insulating layer to provide sufficient lateral thermal continuity for improved half tone area adhesion. This concept was studied using thermal barrier precoatings in combination with a surface continuity providing topcoating layer. The insulating mica thermal barrier precoating, provided complete fusing at the lowest temperature in comparison with comparable, but less insulating concepts. Half tone fusing was measured to be completed at significantly lower temperatures than full tone fusing. In general this

confirms experimentally the earlier fusing nip simulations, and thus hypothesis [C], in that an insulating coating layer will lead to an improved temperature response in the nip and therefore toner adhesion at lower fusing roll temperatures in the case where surface thermal continuity is provided.

The measurement of print gloss on full tone as another print quality parameter showed an increasing print gloss with increasing fusing temperature. In the temperature range where adhesion builds up, and the fusing process takes place, the print gloss correlates very well with assessed adhesion, and could therefore be used to anticipate toner adhesion for coatings with similar surface properties.

- [C] An insulating paper coating having a surface displaying thermally conductive micro-continuity can provide a beneficial effect in terms of the spatial concentration of heating during thermal transfer.

7.7 Electrophotography thread



8 THERMAL EFFECTS IN HEATSET WEB-OFFSET DRYING

8.1 Background

8.1.1 General

Because of the increasing cost pressure as well as gaining focus on sustainable print production, more and more attention is being paid to the specific energy consumption of printed products. In heatset web-offset (HSWO), a significant amount of the total energy consumption is used for drying the printed surface. However, it is known that only ~2 % of the drying energy is utilised for the evaporation of the ink solvent, i.e. contributing to the actual ink setting /97, 98/. This creates an open opportunity for possible improvements in the energy efficiency, and resulting quality control, of the HSWO drying process. In general, the drying process, and, thus, both efficiency and print quality, are defined by the design of four components: the dryer, in particular its hot air nozzles, the substrate, the ink and the fountain solution. Koivumäki and Hellén /99/ showed that all of these components need to be considered to optimise drying. Figure 106 illustrates how each element is part of a “chain” contributing to the efficiency. The work of Gane *et al.* /100/, and Gane and Koivunen /101/ also show the importance of limiting the penetration of liquid components, such as ink oil and fountain solution, if heat transfer to the surface of the coating is to provide maximum drying efficiency.

At first, the dryer is responsible for the transfer of thermal energy to the substrate. Avci and Can /102/ discussed the ink drying process from the perspective of the nozzle design, and evaluated the energy consumption based on the heat transfer coefficient of the dryer. Part of the boundary layer, the stagnant air/vapour film, behaves in a manner so viscous that heat is merely transported by conduction, and thus it forms the main resistance to heat transfer as air itself is a poor conductor of heat. Avci *et al.* /103/ have further shown from a theoretical perspective for the drying of thin films of ink that the coupled effects of heat and mass transfer are a result of jet velocity and temperature and can effectively be influenced by these design criteria. There is also a large number of publications discussing the impingement heat transfer coefficient in hot air dryers, e.g. /104, 105/. It is therefore evident that the dryer design has a significant impact on the overall drying efficiency. This significance is reflected in the continuous development of dryer designs.

As the thermal energy is transported to the substrate, the transient temperature response throughout the material is a result of the effective thermal properties in each layer. It was seen for the simulated temperature responses in 7.3 that a thermally insulating coating layer leads to a faster temperature rise on the surface. It was further observed in section 7.5 that this can result in increased energy efficiency in case of thermally designed coated papers for the toner adhesion development in electrophotography and that print quality, e.g. print gloss, may benefit as well. A similar effect might apply for ink setting in HSWO, even though, in contrast to electrophotography toner fusing, in the offset process liquid transport phenomena in conjunction with heat transport will play a significant role.

Although the final element in the drying “chain” is the ink itself, i.e. the material that is required to be dried, fountain solution, however, is additionally present. It is a water-based component and itself requires latent heat to vaporise before the local temperature can be raised sufficiently to vaporise ink oil components. Limiting its transport into the substrate is, therefore, also an important priority. After the heat has been transferred to the substrate, its thermal properties in combination with the liquids present in its pore structure determine the temperature response. The local temperature rise causes the ink solvent to evaporate. In this process, the vapour pressure range of the solvent used has the main

effect, but also interactions of solvent and binder resin (in the ink layer) as well as solvent and substrate structure (within the substrate) play a role /102, 106, 107/.

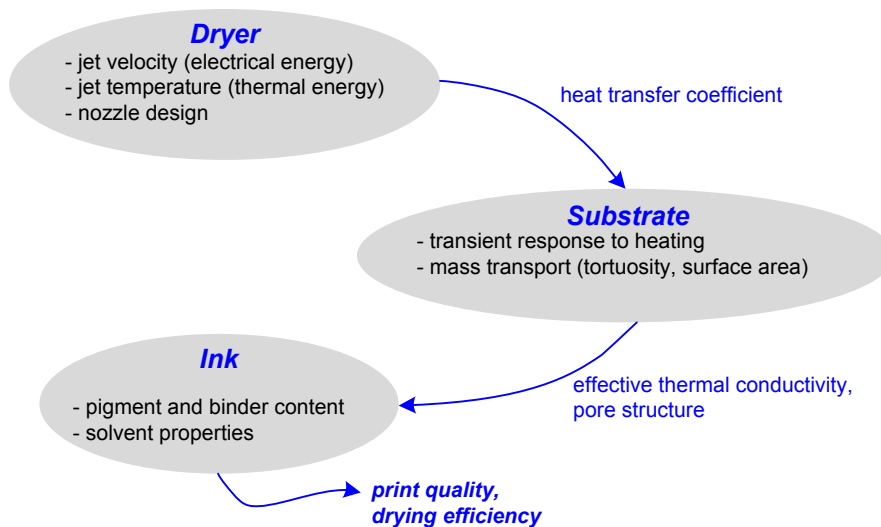


Figure 106. Elements responsible for quality and efficiency in HSWO drying. Based on paper [IX], Figure 1.

This chapter focuses on the effects of the substrate, primarily its coating, on the print quality, and, thus, aims also to improve the overall process efficiency. Printed gloss, roughness and waviness, also known as fluting, are examples of such print quality parameters in HSWO that are related to the thermal response of the substrate in relation to the ink and liquid phase present. Fluting is often a cause for complaints in HSWO printed papers /108/. To outline the aspects of this chapter in more detail, we first take a closer look at theoretical considerations in respect to the possible thermal and liquid transport mechanisms and how they affect print quality and ink setting in a double coated paper.

8.1.2 Theoretical Considerations

On the one hand, waving is considered to be, at least in part, a systematic issue of the web-offset printing process. Due to the strain of the web in the machine direction throughout the press, there is an inevitable cross-dimensional shrinkage. On the other hand, the paper quality itself can have an influence on how susceptible the paper is to waving. For instance, high degrees of fibre orientation lead to more cross-directional shrinkage and thus increase the waving tendency. Low basis weight papers and high initial moisture contents are also known to increase the waving tendency. Furthermore, waving is promoted by an uneven moisture profile caused by printed and unprinted areas (Figure 107.a), i.e. areas poor and rich in fountain solution moisture, respectively. This affects local fibre shrinkage in the dryer and can further increase the waving tendency /108, 109/.

Based on the mechanism that waving is due to the formation of an uneven moisture profile in the base paper expressed during drying of the web, one can introduce a precoating to act as a liquid barrier layer in order to shield the base paper from moisture changes caused by ink and fountain solution and thus help to keep the moisture profile in the base paper even. The topcoating would then be responsible for the printability, i.e. ink absorption. Such a concept, however, would normally make the printing paper more susceptible to blistering. Blistering occurs if the base paper moisture cannot escape fast enough during drying, and thus water vapour pressure causes the base paper structure to rupture (Figure 107.b). It has been found, therefore, that sealing the base paper with a moisture barrier promotes blistering /110/. However, it is here envisaged that if the liquid barrier would at the same time act as a thermal barrier, the base paper would be shielded

from excessive heating. Hence, the temperature would rise slower, thus effectively reducing the risk for blistering whilst also maintaining an even moisture profile in the base paper due to its liquid barrier properties (Figure 107.c).

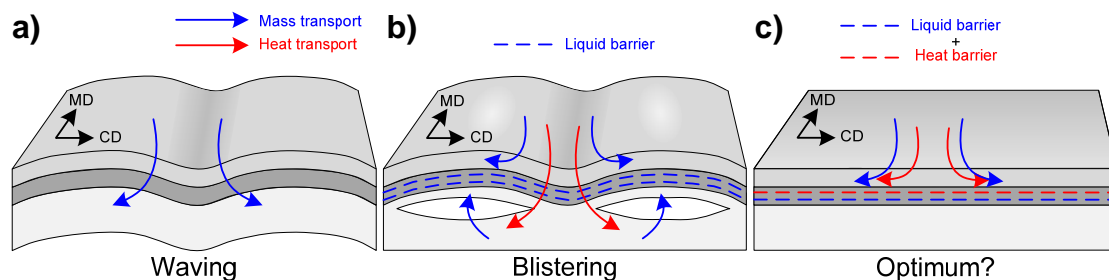


Figure 107. a) Increased waving tendency caused by uneven moisture profile in the base paper. b) A liquid barrier could shield the initially even moisture in the base paper, but alone this would increase the risk of blistering. c) Having a combined liquid and heat barrier could keep the moisture profile even and reduce the risk of blistering. Based on paper [IX], Figure 2.

We now examine the thermal barrier coating concepts as introduced in 7.5.1 in order to study the drying efficiency and minimisation of fluting at the same time. Further studies are then reported, which compare the thermal barrier properties of the mica precoat layer to a commercial calcium carbonate based coating formulation, both having similar topcoatings applied. This enables a discussion regarding the effect of moisture transport and the thermal response of the substrate in the dryer. Print quality parameters will be discussed as well, and thus suggestions for the thermal optimisation of the drying process from the substrate point of view can be formulated.

8.2 Materials and Methods

8.2.1 Materials

At first, the thermally designed coating concepts and the reference paper as described in 7.5.1 are studied. Table 20 provides a summary of the coating formulations and the corresponding coating method used. In a subsequent part, the mica precoat is compared to a commercial coating formulation. The commercial coating colours, both a precoat (Com. A) and topcoat (Com. B), are calcium carbonate based. Like the experimental coatings, the commercial formulations were also coated on the pilot coater for better comparability. Since a high base paper moisture content is known to increase the waving tendency (see 8.1.2), the effect of the substrate moisture content was studied for two different levels of 4.5 % and 6.5 % moisture targeted in the calendering.

The printing of the papers for both parts of this study was done on an HSWO machine²⁸ using standard ink²⁹. In the sampling phase, the machine was running at a speed of 5.6 ms^{-1} . The drying temperatures were adjusted to either low (115 °C) or high web temperatures (130 °C and 150 °C). The length of the dryer was 8 m, which results in a residence time of 1.43 s. Even at low drying temperature, no ink smearing was observed. Table 22 summarises both parts of this study.

²⁸ Heidelberg Web-8

²⁹ Sun Topgloss, Sun Chemical

Table 22. Two parts of the study comparing the objectives and trial parameters.

Objective	Part 1*			Part 2	
	Comparison of thermally designed coatings to that of a reference			Comparison of Mica precoated paper to a commercial formulation	
Coatings					
Precoat	Ref	Mica	MCC + bfGCC ⁺	Com. A	Mica
Topcoat	Ref	Top I	Top II	Com. B	Com. B
Calendering					
Target gloss			33-35 %		40-43 %
Moisture			4.5 %		4.5 % vs. 6.5 %
Printing					
Speed			5.6 ms ⁻¹		5.6 ms ⁻¹
Drying (web-temp.)			115 °C vs. 130 °C		115 °C vs. 150 °C

* see also Table 20 in 7.5.1

⁺ Addition of 80 parts bfGCC to MCC to aid strength

8.2.2 Measurement of waviness

In order to quantify the resultant waviness in the printed paper, without the bias of the human eye in relation to the printed image, a laser scanning method was used to create a three dimensional surface topographic image of the printed sheet. The printed sample is laid out flat on the measurement table (Figure 108.1). A laser scans in the paper cross machine (CD) direction of the sample while moving along in the web (machine) direction (MD) (Figure 108.2) and transfers the data to an acquisition system (Figure 108.3). The measurement is done on a 10 cm x 10 cm green printed area (C100, Y100) of the test pattern. Figure 109 shows such a collected surface topography of a coated paper. The topography data are then transformed into the frequency domain and the amplitude in the 15-30 mm wavelength interval was used to characterise waviness. The camera records the surface height deviations with an in-plane resolution of ca. 100 μm⁻¹ and an out of plane resolution of 50 μm⁻¹.

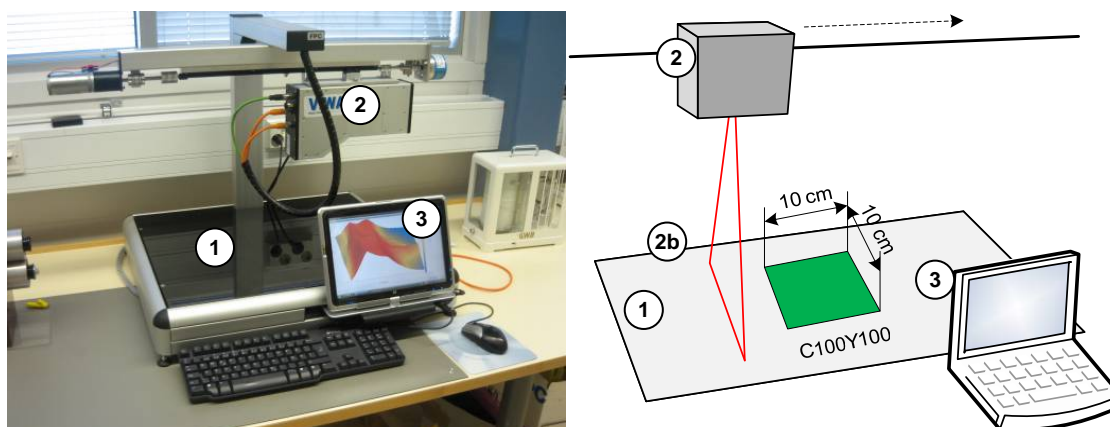


Figure 108. Photo (left) and schematic of the waviness measurement device. 1) Measurement table, the measurement area is a 10 x10 cm green printed area. 2) Laser profilometer. 2b) Scanning laser beam. 3) Data acquisition. Based on paper [IX], Figure 3.

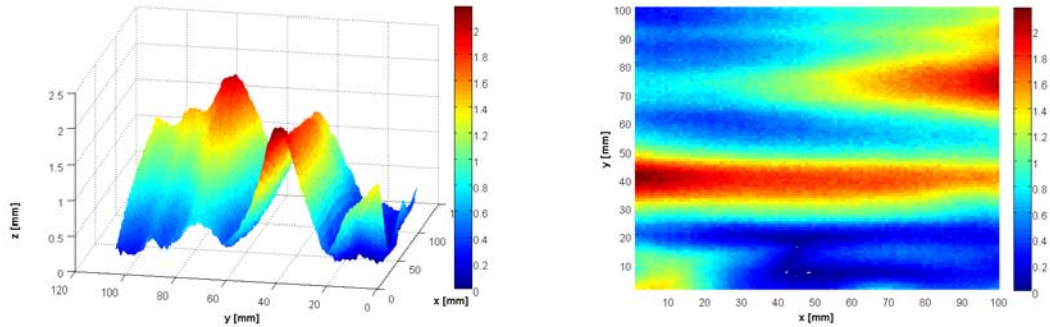


Figure 109. Surface topography of a green (C 100, Y 100) printed area on the print test pattern. The waviness is characterised by the amplitude in the 15-30 mm wavelength region. Based on paper [IX], Figure 4.

8.2.3 Liquid permeability

For the characterisation of the liquid barrier properties, the permeability was measured adopting the method of Ridgway *et al.* [111]. In this method a stack of (ca. 200) small sample sheets is embedded round its edges in resin (Figure 110). An advantage of this technique is, therefore, that it is not susceptible to local defects, e.g. pinholes, in the individual sample sheets. The embedded sample sheets are saturated with hexadecane, which does not interact with either the fibres of the base paper or the binders used in the coating layer(s).

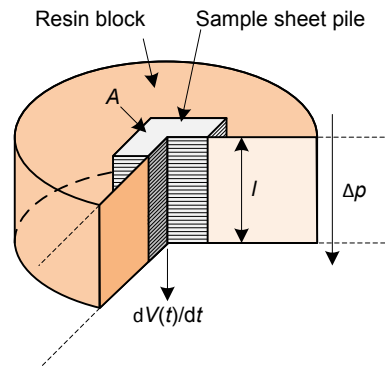


Figure 110. Schematic cut through the resin block with embedded sample sheet pile. Adapted from Ridgway *et al.* [111].

The saturated sample block is then placed in a pressure cell. Gas over-pressure pushes excess hexadecane through the sample stack and an electronic scale records the permeated liquid mass flow rate. For the given density of the hexadecane, the volume flow rate of the hexadecane through the sample pile can be used in the Darcy equation to determine the permeability κ :

$$\frac{dV(t)}{dt} = \frac{-\kappa A \Delta p}{\eta l} \quad (66)$$

where:

V	is the volume of permeated hexadecane,
A	is the cross-sectional permeable area,
Δp	the applied pressure difference,
η	the viscosity of the hexadecane, and
l	the effective pile thickness (calculated by the number of individual sheets of known caliper).

8.2.4 Ink-surface interaction (ISIT)

The ink tack force development was measured with the ISIT apparatus /112/ where a tack disk is brought in contact with the sample a certain time interval after the print. The tack disk pulls away from the printed sample and measures the tack force $F_T(t)$. The tack force development, repeatedly measured, each from a fresh surface of the print as a function of time, can generally be divided into three stages. In the first stage, the tack rises to a maximum. This tack rise time describes the initial ink vehicle imbibition defined by the finest pores. The maximum tack force (second stage) is a measure of the ink cohesion increase in competition with adhesion to the surface, and is a function of surface microsmoothness and the nature of the ink-surface adhesion energy, respectively. In the third stage the tack decays at a rate depending on the available pore volume, its accessibility and surface area, taking part in absorption.

The ink tack development curves help to evaluate whether the experimental barrier coating layer will have a detrimental effect on the ink absorption behaviour, i.e. the printability, in comparison with the commercial coating formulation.

8.3 HSWO printing of thermally designed coated papers

8.3.1 Basic properties

Figure 111 shows the printed gloss (Tappi 75°) and the printed roughness (Parker Print Surf (PPS)) of the two thermally designed formulations as well as for the reference coating. It should be kept in mind that the topcoatings used are comparable to each other. Therefore, the effects will be primarily due to the precoating layer. It can be seen that both in terms of print gloss and, to a lesser extent, also smoothness, the MCC containing concept is favourable. This is because of the compressibility of the porous MCC pigment particles aiding smoothing in the calender. Also the mica precoated paper showed a slightly higher print gloss compared to the reference. This might be related to the platy nature (high aspect ratio) of the mica pigment improving physical base paper coverage.

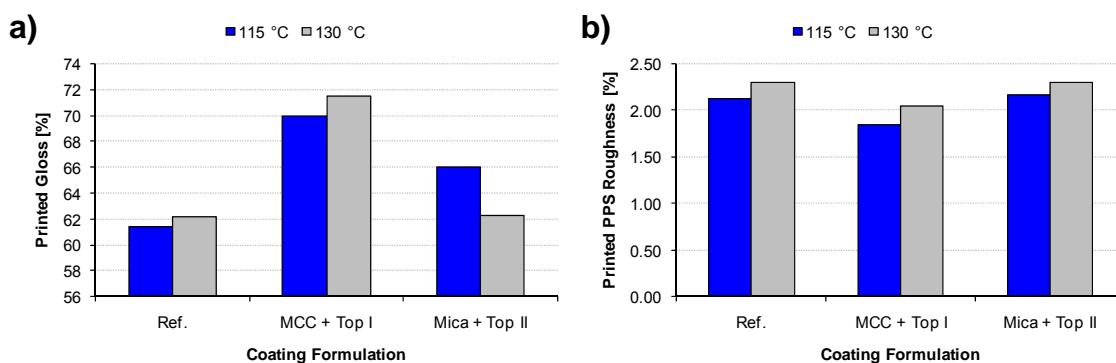


Figure 111. Printed gloss a), and printed PPS roughness b), for the thermally designed coating formulations including MCC containing and Mica experimental precoats, respectively, as well as for the reference coating, observed after low and high temperature drying. Based on paper [IX], Figure 6.

When comparing the mica precoating with the commercial precoating, both using the very same topcoating formulation, one can see that the print gloss level (Figure 112.a) is also distinctly higher, which is a positive side effect of the mica pigment barrier coating. Figure 112.b shows that this is due to the higher delta gloss.

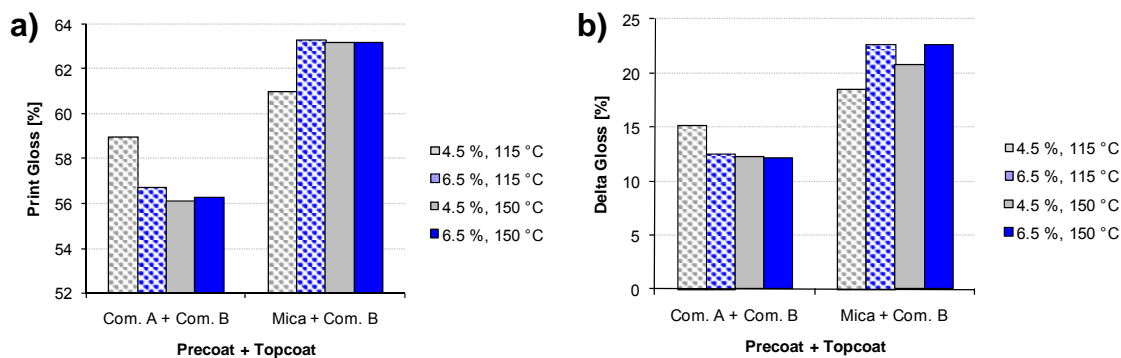


Figure 112. Printed gloss a), and delta gloss b), for the commercial formulations and the formulation with the mica precoat. Based on paper [IX], Figure 7.

However, the lower final ISO brightness of the mica precoated sample studied (85.4 %) compared to calcium carbonate pigment coatings (89.2 %) poses a potential drawback in practice. Further work would, therefore, be needed to develop a higher brightness permeation barrier and insulating layer.

8.3.2 Waving

There is a clear advantage in the result of the waving measurement in the case where the mica precoat is used (Figure 113.a). While it is often difficult to assess waving visually, because of the bias of the human eye to brightness and gloss, nonetheless these results reflect the visual impression of the printed sheets very well.

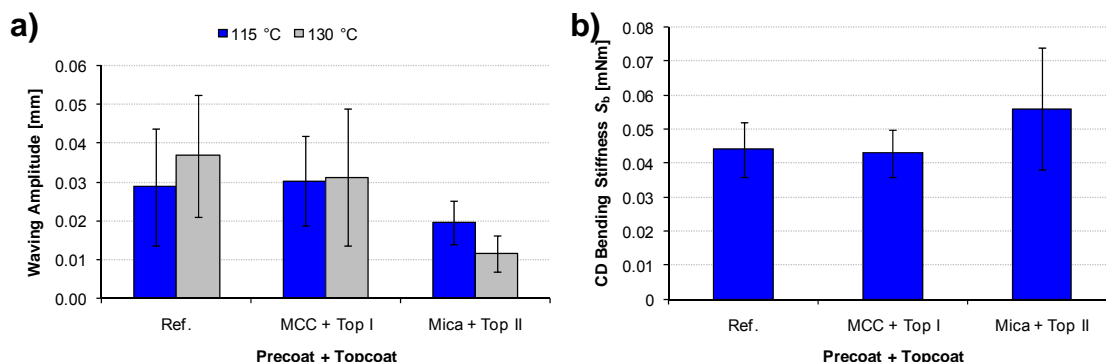


Figure 113. a) Waving for the reference and the thermally designed coatings. b) CD bending stiffness of the unprinted papers. Based on paper [IX], Figure 8.

The advantage of less waving for the mica precoating concept can be at least in part due to the thermal barrier properties of the mica and/or in part due to the liquid/moisture barrier properties because of the platy pigment structure and the self-swelling rotogravure latex used as binder. Additionally, there may be a small stiffness increase associated with the mica precoat adding rigidity to the planar structure (Figure 113.b). However, given the small differences and the standard deviation of the bending stiffness, it is unlikely that it is a decisive factor for the lower waving tendency of the mica. We, therefore, differentiate these mechanisms further by looking at different paper moisture levels, and also study how the mica performs in comparison with the commercial formulation. To do so, the mica precoat formulation is used in combination with the commercial topcoat formulation (Com. B).

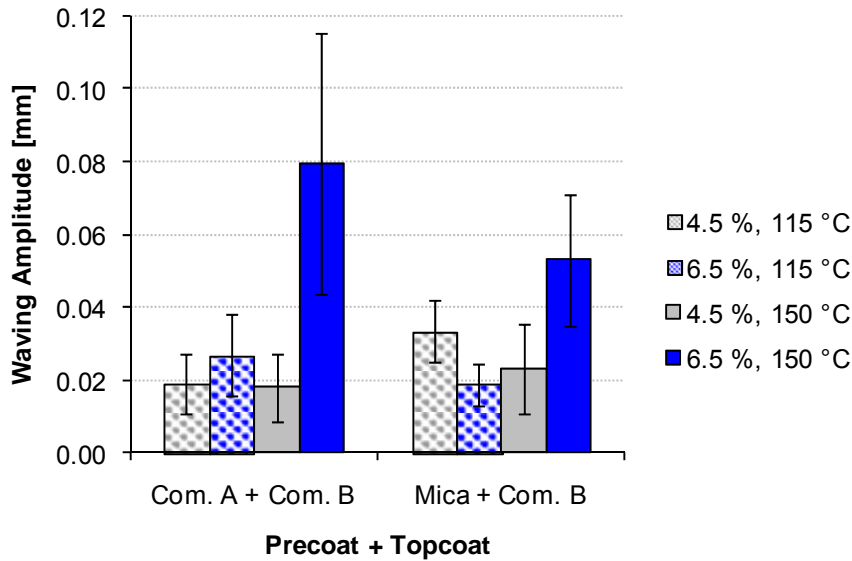


Figure 114. Waving for the commercial formulations in comparison with the mica formulation at different moisture levels and drying temperatures. Based on paper [IX], Figure 9.

Figure 114 shows the waving results from the commercial precoat and topcoat as well as for the mica precoat and commercial topcoat for different moisture levels and different drying temperatures. It can be seen that at low drying temperatures there is generally little waving, even at the high moisture level, and the mica formulation is definitely comparable to the commercial formulation, given the standard deviation in the results. The combination of high moisture content and high drying temperature leads to strong waving. This was to be expected based on the assumed underlying mechanisms of waving [109, 110]. However, the mica precoat continues to show a clear advantage over the commercial formulation under these extreme conditions. As pointed out earlier, this difference could not be directly related to the mechanical property of bending stiffness. The cross-machine directional bending stiffness is 0.07 mNm and 0.06 mNm for the double coated papers with the commercial precoating and the mica precoating, respectively. It is more likely that, despite the high web temperature, the platy and thermally insulating mica can shield the moisture in the base paper to some extent and prevent stronger waving. It was observed that neither the commercial formulation nor the mica formulation showed blistering. The ink level was 200 % and 300 % on each side of the paper, respectively. The absence of blistering could on the one hand indicate that the base paper is largely blister resistant up to the web temperature of 150 °C, but on the other hand it could also support the theory that in addition to the liquid barrier, the mica precoating also creates a thermal barrier that compensates for an increased risk of blistering expected when using a less permeable precoat. The discussion, therefore, now goes on to take a special look at the liquid barrier properties of the mica layer and evaluate whether that has an influence on the printability.

8.3.3 Barrier properties and ink interaction

Figure 115 and Figure 116 show SEM cross-sectional images of the coated papers with the commercial formulation and the mica precoating formulation, respectively. It can be seen in Figure 115 that the commercial precoating (Com. A) is somewhat “coarser” than the topcoating, but there is generally little visual difference between the precoating and the topcoating (Com. B).

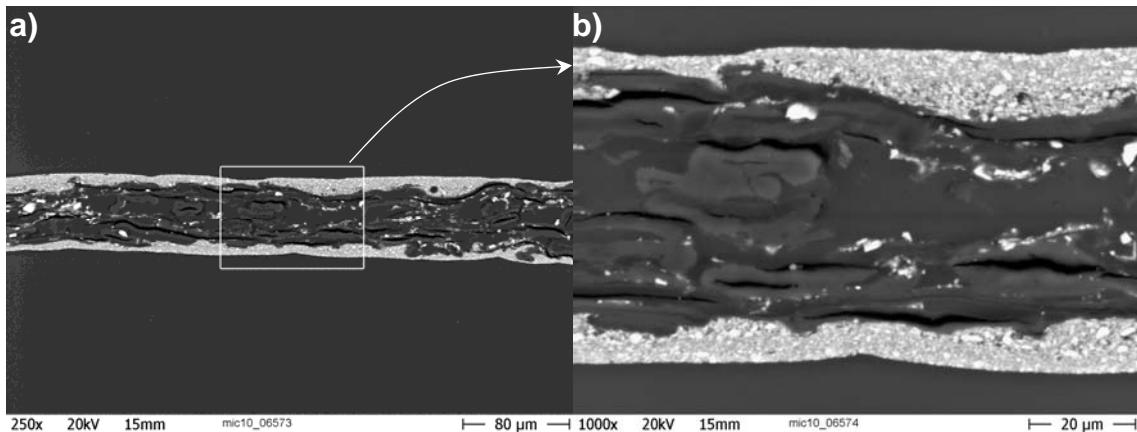


Figure 115. SEM cross-section images of the commercial double coated (Com. A + Com. B) calendered paper. a) 250x and b) 1 000x. Based on paper [IX], Figure 10.

In contrast, Figure 116 shows the mica precoating with the commercial topcoating. The platy mica pigment is readily visible. However, it is questionable to say based on the SEM cross-section how much the mica layer can contribute to forming a liquid barrier. It is, therefore, necessary to quantify the liquid permeability for further discussion.

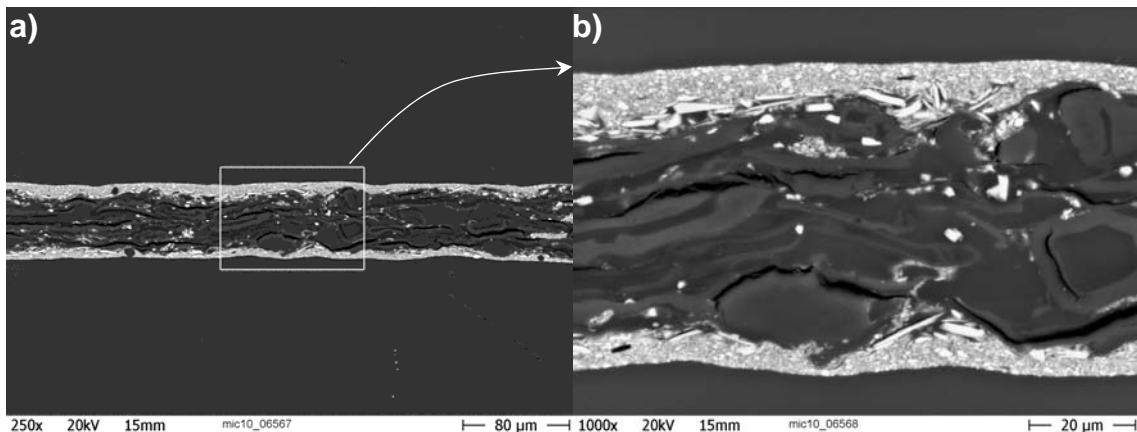


Figure 116. SEM cross-section images of the mica precoated, commercial topcoated (Mica + Com. B), calendered paper. a) 250x and b) 1 000x. Based on paper [IX], Figure 11.

Figure 117.a shows the measured permeabilities for the base paper only and proceeds with the permeabilities of the respective precoated papers, the double coated papers and the calendered papers, respectively. The only difference in the bars of each step in Figure 117.a is the precoating formulation (Mica versus Com. A). In general, it is seen that both coating and calendering reduce the liquid permeability each by roughly one order of magnitude. The difference between the mica precoating and the commercial precoating seems rather small on this logarithmic scale. However, if one takes the actual ratio of both, one can see that for commercial precoating the permeability is in fact more than twice as high. This relation between the two concepts is not notably changed by the application of the identical topcoating or the subsequent calendering, emphasising the dominant role of the mica precoat in reducing permeability. Table 23 summarises the permeability data and also provides the ratios of permeability of commercial versus mica and the calendered grades versus the base paper.

Based on the permeability measurement, it is clear that there is a notable difference in the mass transport rate through the precoating layer. However, for optimum ink setting behaviour some mass transport into the coating is required. The following question arises, therefore, whether the ink setting is affected by the mass transport barrier of the mica layer. This can be studied by looking at the dynamic tack force response.

It is seen (Figure 117.b) that the coatings are comparable in terms if the initial tack increase behaviour. This confirms the identical nature of the top surface microstructure of both papers. However, the tack decrease from the maximum shows a dual porosity step in the curve for the case of the two commercial coating layers, illustrating a potential interlayer phenomenon. The overall tack decrease rate, though, which is describing the available pore volume, can nonetheless be regarded as similar. It is known that the tack response is primarily dependent on the top coating layer /113/. This means, in turn, that the beneficial effect of the mica coating layer in reducing waving (see Figure 114) is not primarily due to the ability to shield the base paper from ink vehicle oil transported by capillarity, but, rather, due to the ability to keep an even moisture profile within the base paper by reduced permeation, as well as its thermally insulating behaviour. This explains the particular advantage of mica in the reduction of waving for high moisture contents in combination with high drying temperatures.

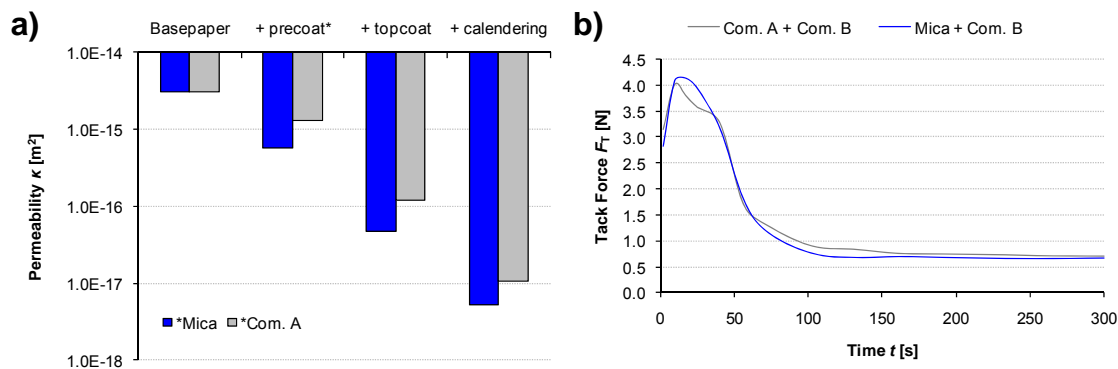


Figure 117. a) Measured permeabilities of the base paper, the precoated papers with Com. A and Mica, respectively, as well as the respective permeabilites of the double coated and the final calendered papers. b) Comparison of the tack force development for the commercial pre- and topcoated paper with the mica precoated and commercial topcoated paper. Both papers have the same topcoating formulation. Based on paper [IX], Figure 12.

Table 23. Coating formulations and methods used for the comparison of thermally engineered layers with a reference.

Permeability κ [m ²]	Com. A*	Mica*	Ratio (Com. vs. Mica)
Base paper	3.04E-15	3.04E-15	
+ precoating	1.32E-15	5.67E-16	2.33
+ topcoating (Com. B)	1.22E-16	4.75E-17	2.56
+ calendering	1.06E-17	5.17E-18	2.06
Ratio (Base vs. Calendered)	285.77	587.33	

*precoating formulation

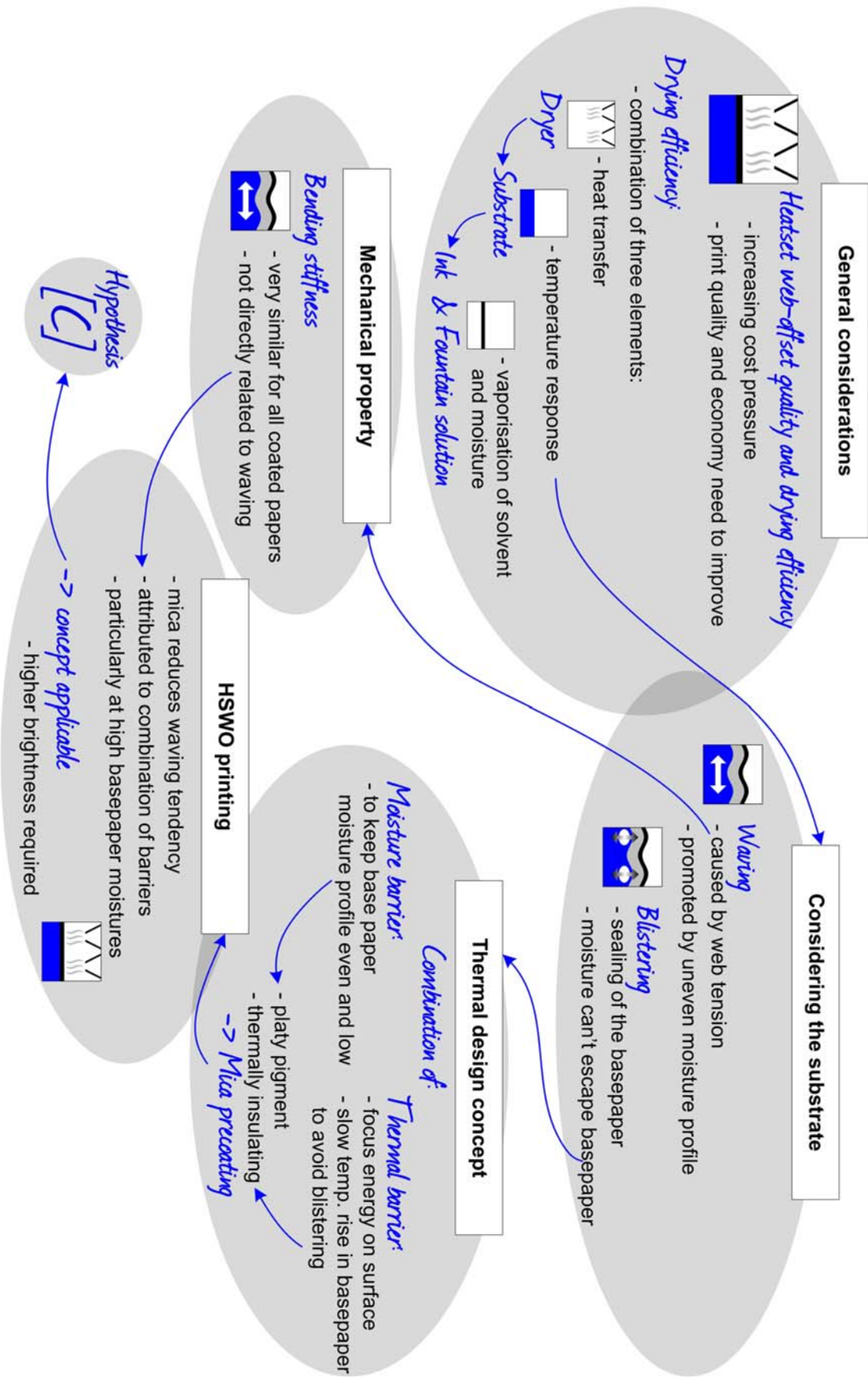
8.4 Summary

Porous MCC and platy mica precoatings were applied in combination with topcoating formulations for studying HSWO printability and fluting tendency. While the MCC coating concept showed high gloss values, a property due to the compressible pigment and its excellent bulking coverage, the mica coating layer showed advantages in terms of a low waving tendency. This was, therefore, further investigated by comparing the mica precoating formulation directly to a commercial formulation, both having the very same topcoat. It was observed that the mica precoating can reduce waving effects particularly present at high moisture contents and high drying temperatures. This reduction was

accounted for by the thermal and/or liquid/moisture barrier properties. To distinguish the barrier effects, the liquid barrier properties were measured by means of permeability. It was shown that the mica precoating reduces the permeability by a factor of two in respect to the commercial formulation. This helps in maintaining an even moisture profile in the base paper. In spite of the increased moisture barrier, no blistering was observed, even at high temperatures, which supports the action of mica in terms of thermal insulation, which results in a slower temperature rise within the base paper as it is hypothesised in [C]. In turn, the thermal energy is more focused on the drying of the ink and moisture removal from the topcoating only. A disadvantage of the mica pigment, seen in this study, is its low brightness. In order to compete successfully with the typically used high brightness carbonate coatings an alternative pigment or pigment beneficiation would have to be found. Nonetheless, this study showed, in principle, that by combining the concept of a liquid barrier and a thermal barrier, both quality and efficiency enhancements in the HSWO process can be achieved.

- [C] An insulating paper coating having a surface displaying thermally conductive micro-continuity can provide a beneficial effect in terms of the spatial concentration of heating during thermal transfer.

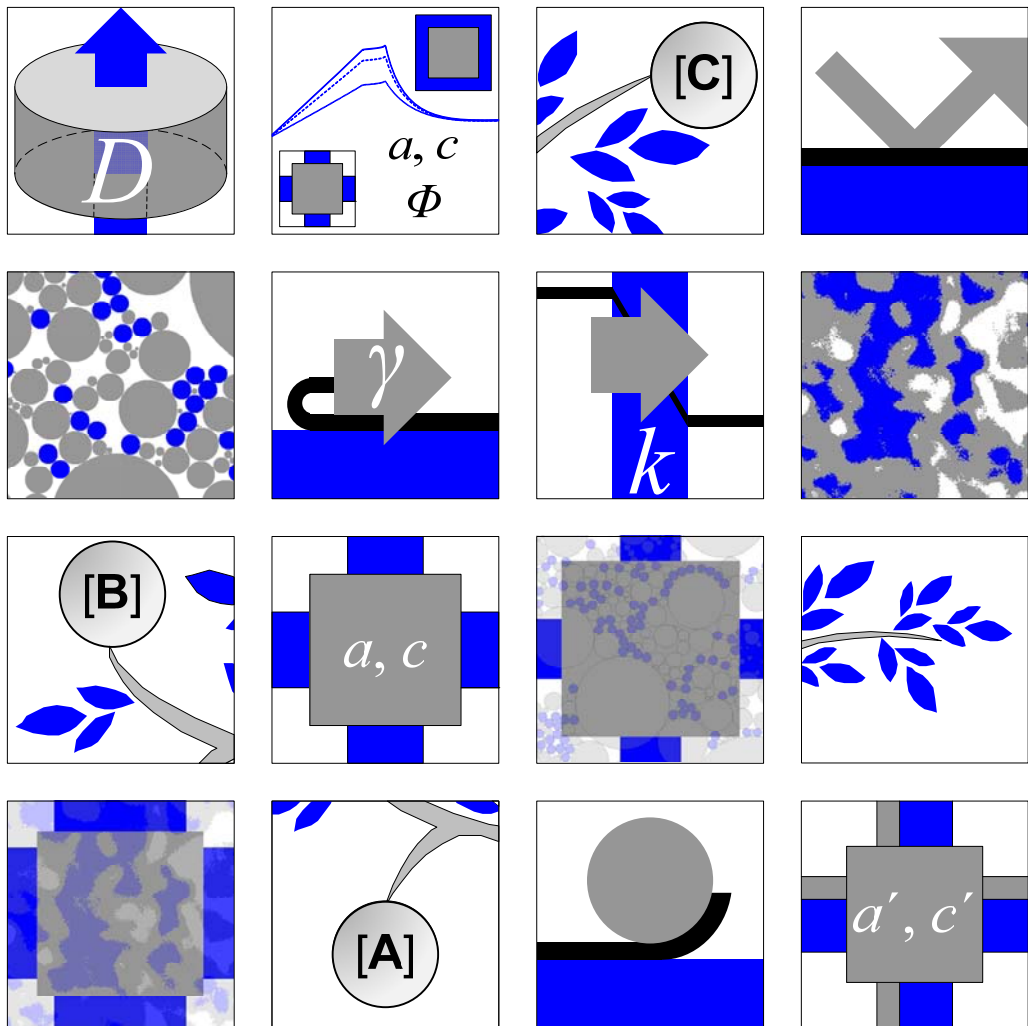
8.5 Offset thread



CONCLUSIONS



OUTLOOK



“Your theory is crazy, the question is whether it's crazy enough to be true.”

Niels Bohr,
Danish Physicist, 1885-1962

9 CONCLUSIONS

For the *methodology* part of this work, both a measurement technique and a model for calculation of effective thermal conductivity were introduced and discussed. The transient method for the measurement of thermal diffusivity was shown to be precise enough to permit analysis of different pigment/binder tablet materials and structures. The pigment/binder tablet material used for the measurements was shown to relate well to the structures as found in heavy weight paper coatings. This method was therefore adopted to measure and discuss thermal diffusivity in the subsequent studies. In addition, a Modified Lumped Parameter Model (LPM) was proposed. A detailed discussion in respect to the individual material parameters and proportions in relation to porosity and volume fractions of the components showed the versatility of such a model approach. Initially, the parameters of the model suggested that it would be favourable to use the binder variable and a pigment volume fraction factor together instead of porosity as the governing parameter. However, because of the structural representation of the LPM, two different modelling approaches, these being parameter modelling and structural modelling, respectively, were followed, depending on whether one starts from a combination of compositional and measured property data, or from compositional and structural information. Both modelling approaches combined can be used to assess the connectivity of pigment binder systems, and, by implication, particulate multiphase systems in general.

Initially, the *basic research* part of this work, applying the Lumped Parameter Model to existing literature values for the thermal conductivity of a packed bed of talcum, showed that the observed behaviour agreed well with the original definition of the model. The maximum thermal conductivity is observed at the critical pigment volume concentration (CPVC) in relation to binder content. The thermal conductivity of a broad size distribution coarse ground calcium carbonate (bcGCC) system with styrene acrylic (SA) latex exhibited similar behaviour in respect to the presence of a maximum. However, in this case, the maximum occurred at binder concentrations well below the CPVC. This indicated that the addition of latex acted to disrupt the packing structure of the bcGCC at low binder concentrations, more so than would have been expected due to physical packing alone. This allowed us to conclude that the observations of Ridgway and Gane /70/, tracing colloidal interactions through to the final coating structure, could be identified via the thermal properties. Both talc and carbonate systems showed that the thermal conductivity cannot be described by either the pore structure or the binder level alone. This, therefore, led to the approach of establishing a link in the model between material components and their role in the structure.

A Monte Carlo simulation-based particle deposition was subsequently applied to create two-dimensional coating structures. Real coating structures in the form of cross-sectional SEM images were also examined. In direct comparison of simulation and real structures it was seen that the connectivity of the simulations, as also the model interpretation of connectivity, is an essential factor. By adopting a particle overlap in the simulation, it could be shown that the soft sphere simulated structures can be regarded as providing equivalency to the microscopy cross-sections. The model parameter of pigment connectivity indicated a lowering in connectivity at the binder concentrations for which a disruption of the pigment packing occurs. Surface and colloid chemistry factors cause binder to accumulate first at pigment nodal points, which causes disruption already at levels up to 8 w/w% binder. It is proposed, therefore, that these methods of imaging, pore structure analysis and thermal conductivity can be used to identify and parameterise subtleties in connectivity in real colloiddally interactive particulate systems, based on deviations between simulations and modelling, and the experimental values.

CONCLUSIONS

The structural modelling displayed the importance of the binder phase in creating solid-solid connectivity. Therefore, to study further the effect of the binder material, different T_g latex binders were analysed in terms of the resulting thermal conductivity, mercury porosimetry and particle packing simulations in combination with the Lumped Parameter Model connectivity. This reconfirmed that a combination of thermal conductivity measurement and pore structure analysis can be used to characterise porous multiphase systems.

After having looked at both solid phases forming the porous medium, the final phase to be discussed was the fluid contained within the pore structure. The effective thermal conductivities of mineral oil and water saturated coating structures were studied and compared to the unsaturated case, where air filled the pores. It was shown that the void filling fluid has a strong impact on the total effective thermal conductivity, thus having implications in drying of printed papers, such as in the heatset web-offset process, in which both water in unprinted areas and mineral oil in the ink are present, in inkjet or flexography, where either water or oil alone are used. In addition, the vaporisation behaviour of liquids saturating the porous structures was studied by means of thermogravimetry. The effect of binder on the coating structure led to observably different vaporisation behaviour for both liquids, principally affected by the confinement of geometry in the case of non-liquid interactive binder, i.e. increased local curvature as pores become finer, and reduced permeability.

The *applied research* part of this work examined how paper coatings that were designed according to their dynamic thermal behaviour can contribute to energy efficiency and print quality improvements in the electrophotography and heatset web-offset processes. At first, a finite element method simulation of an electrophotography fusing nip was utilised to show that an insulating behaviour of the coating layer causes a higher average temperature at the surface of the coating, while the temperature below the coating in the base paper rises slower. This was identified as a desirable behaviour for both the toner fusing in electrophotography and drying in heatset web-offset, as the thermal energy can be concentrated on top of the coating where it is required, thus improving efficiency and print quality.

In general, it was confirmed experimentally that an insulating coating layer will lead to an improved temperature response in the nip, and, therefore, develop toner adhesion at lower fusing roll temperatures. It was further deduced that, for good electrophotographic toner adhesion, surface continuity in respect to thermal conductivity, either adopting a thin conductive layer or by ensuring sufficient packing density, is required in conjunction with the proposed insulating layer effect. An optimal coating for an electrophotography printing paper should, therefore, have a thermally insulating coating layer having sufficient coating pigment packing density on the surface. Alternatively, in place of the high packing density surface, a thermally conducting layer could, in principle, be applied on top of an insulating layer to provide sufficient lateral thermal continuity for improved half tone area adhesion. In heatset web-offset, a similar concept was demonstrated, in which the topcoating layer was additionally optimised for well controlled ink vehicle absorption and sufficient specific surface area to provide optimal ink setting. This concept was studied in pilot scale using thermal barrier precoatings in combination with a surface continuity providing topcoating layer.

In case of heatset web-offset it was additionally proposed that the thermally insulating precoat can reduce the quality problem of waving/fluting effects, which are particularly prevalent at high moisture contents and high drying temperatures. By reducing the permeability of the insulating layer to minimise water transport to the base paper, it was concluded that the combination of thermal and/or liquid/moisture barrier properties, helps

to maintain an even moisture and temperature profile in the base paper. In spite of the increased moisture barrier, no blistering was observed, which supports the action of thermal insulation providing a slower temperature rise in the base paper during passage through the heatset drying oven. In turn, the thermal energy is more focused on the drying of the ink and moisture removal from the topcoating only, and, thus, both quality and efficiency enhancements in the HSWO process could in principle be achieved.

10 FUTURE PROSPECTS

10.1.1 Optimisation and characterisation

Process optimisation can only be achieved by having a detailed knowledge of the process, including the materials involved. The increasing cost of energy and the growing awareness for an effective use of energy will emphasise the need to understand even small scale energy dissipation. This work has shown, on the one hand, that the thermal properties can play an important role in the optimisation of energy efficiency and product quality in processes that deal with the application of heat to porous media. This was exemplified for the printing methods of electrophotography and heatset web-offset. On the other hand, the theoretical discussions showed that the measurement of thermal conductivity in combination with a pore structure analysis can be used in assessing the nature of multiple phases and their interaction in porous media. Both aspects are envisaged to be of importance in future developments. For large scale adaptation of thermally designed materials into existing processes further studies are required regarding the quantitative savings potential in respect to the overall process economy.

For reasons of simplicity, multiphase porous structures are often regarded as two phase (solid-fluid) systems, essentially neglecting differences in two or more of the solid or liquid phases or possible phase interactions. Since thermal conductivity, in combination with pore structure analysis, was shown to be a very sensitive property to describe the micro structural configuration of more than one solid phase, it can be seen as a simple and low cost way to characterise a certain class of porous media. A broader spectrum of materials would help to support this statement.

10.1.2 Homeomorphism

The above stated need to characterise porous media often leads to modelling a three dimensional system by projecting it onto two dimensional structures or using two dimensional equivalents. By doing so in this work, it was observed that this may have drawbacks first of all, although it is driven by practical reasons. The calculation demand for simulations in two dimensions is much lower than tackling the same problem in three dimensions. This holds even for today's high speed computing solutions. Furthermore, a two dimensional system is more tangible and also easier to visualise. However, when trying to express a three dimensional system as a two dimensional one, it is important to examine the equivalence. If a structure could be deemed equivalent in both its 2D and 3D description, and the relationship can be expressed in a mathematical closed form, the description of equivalence itself could contribute to the understanding of the medium more than examining either 2D data or 3D data separately. In addition, it would enable methods that produce two dimensional data to be able to complement three dimensional methods. An example would be, studying a porous medium by cross-sectional SEM images rather than analysing micro/nano-tomography data.

In this work it was found that by adopting the unit cell description, the Lumped Parameter Model can provide a mathematical link between 2D and 3D structures. This link was found to be very effective in describing a talcum particulate system. It is, however, unclear as to what types of porous media qualify for such a relationship, i.e. what the preconditions are for a structure to be deemed homeomorphic.

10.1.3 Skeletal structures

The class of porous media primarily discussed in this work was defined by three phases, for which the thermal conductivity differed by a factor of ten. Due to that, their role in respect to each other, and thus their equivalent in the Lumped Parameter Model, was

clearly defined. However, there is a large number of porous media and composite materials for which the thermal conductivity ratios are within a different order of magnitude, e.g. metal-ceramic sintered materials. This changes the role of the components forming the skeletal structure, i.e. the primary thermal path. The primary thermal path would most likely be defined by a balance of highest thermal conductivity and highest degree of connectivity of a given component. It was shown that the Lumped Parameter Model could adopt different skeletal structures by changing the unit cell mode, i.e. the configuration of phases. Further studies including a wider range of materials would be required to test this hypothesis. This should also investigate the role of the fluid phase in forming the thermal path, leading to the following topic of combined heat and mass transport.

10.1.4 Combined heat and mass transport

When discussing the role of the fluid phase it could be seen that there is a strong effect of absorbed liquid on the effective thermal conductivity of a porous medium, and that the vaporisation behaviour of liquid can differ distinctly according to the local structure geometry and permeability, the effect being related not only to local temperature variations, but also to pore-related structural parameters like curvature or specific surface area. Especially for studies regarding drying efficiency, it is important to understand the combination of heat and mass transport. While this work has examined how structural parameters contribute to the effective thermal conductivity, there needs to be further examination of how heat transmits to the fluid phase and how the transport of the fluid phase in turn transports heat, effectively contributing to a feedback loop.

REFERENCES

1. E.B. Nauman. **Chemical Reactor Design, Optimization and Scaleup**, Chapter 5, Thermal effects and energy balances. McGraw-Hill, New York, 2001.
2. B. Usowicz, J. Kossowski and P. Baranowski. Spatial variability of soil thermal properties in cultivated fields. *Soil Tillage Res.* **39**(1-2):85-100, 1996.
3. Y. Hiraiwa and T. Kasubuchi. Temperature dependence of thermal conductivity of soil over a wide range of temperature (5-75°C). *Eur. J. Soil Sci.* **51**(2):211-218, 2000.
4. R.C. Craig and F.A. Peyton. Thermal conductivity of tooth structure, dental cements and amalgam. *J. Dent. Res.* **40**(3):411-418, 1961.
5. P.A.G. Little, D.J. Wood, N.L. Bubb, S.A Maskill, L.H Mair and C.C Youngson. Thermal conductivity through various restorative lining materials. *J. Dentistry* **33**(7):585-951, 2005.
6. J. Ketolainen, L. Kubičár, V. Boháč, M. Markovič and P. Paronen. Thermophysical properties of some pharmaceutical excipients compressed in tablets. *Pharm Res.* **12**(11):1701-1707, 1995.
7. A. Zavaliangos, S. Galen, J. Cunningham and D. Winstead. Temperature evolution during compaction of pharmaceutical powders. *J. Pharm. Sci.* **97**(8):3291-3304, 2008.
8. J.K. Carson, S.J. Lovatt, D.J. Tanner and A.C. Cleland. Predicting the effective thermal conductivity of unfrozen, porous foods. *J. Food Eng.* **75**(3):297-307, 2006.
9. J. Huang. Thermal parameters for assessing thermal properties of clothing. *J. Therm. Biology.* **31**(6):461-466, 2006.
10. J. Paltakari. **Internal and External Factors Affecting the Paper Drying Process**, Doctoral Thesis, Helsinki University of Technology, Espoo, 2000.
11. R.H. Hestmo and M. Lamvik. Heat Transfer during calendering of paper. *J. Pulp Paper Sci.* **28**(4):128-135, 2002.
12. S. Rousu, T. Grankvist and D. Eklund. The effect of polymers on the final coating structure. In proc. *Tappi 2002 Advanced Coating Fundamental Symposium*, pp. 199-209, San-Diego, CA, USA, Tappi Press, Atlanta, 2001.
13. E. Tsotsas and H. Martin. Thermal conductivity of packed beds: A review, *Chem. Eng. Process.* **22**(1):19-37, 1987.
14. F.P. Incropera and D.P. DeWitt. **Fundamentals of Heat and Mass Transfer**, Fourth Edition, John Wiley and Sons, New York, 1996.
15. D.J. Sanders and R.C. Forsyth. Measurement of thermal conductivity and contact resistance of paper and thin-film materials. *Rev. Sci. Instrum.* **54**(2):238-244, 1983.
16. K. Ofuchi and D. Kunii. Heat transfer characteristics of packed beds with stagnant fluids. *Int. J. Heat Mass Transfer.* **8**(5):749-757, 1965.
17. T.Y.R. Lee and R.E. Taylor. Thermal diffusivity of dispersed materials. *J. Heat Transfer.* **100**(4):720-724, 1978.

REFERENCES

18. M.J. Assael and K. Gialou. A transient hot-wire instrument for the measurement of thermal conductivity of solids up to 590 K. *Int. J. Thermophys.* **24**(3):667-674, 2003.
19. S.E. Gustafsson. Transient plane source techniques for thermal conductivity and thermal diffusivity measurements of solid materials. *Rev. Sci. Instrum.* **62**(3):797-804, 1991.
20. D. Guérin, V. Morin, D. Chaussy and J.L. Auriault. Thermal Conductivity of handsheets, papers and model coating layers. In proc. *12th Fundamental Research Symposium*, Oxford, Fundamental Research Society, Bury, UK, pp. 927-945, 2001.
21. J. Majala, K. Putkisto, R. Pietikäinen and J. Grön. Heat transfer during fixation of coating layers in dry surface treatment. *Nord. Pulp Paper Res. J.* **19**(3):291-299, 2004.
22. P. Rättö and M. Rigdahl. Temperature distributions in a paper sheet subjected to a short pressure pulse from a heated plate. *Nord. Pulp Paper Res. J.* **13**(2):101-106, 1998.
23. W.J. Parker, R.J. Jenkins, C.P. Butler and G.L. Abbot. Flash method of determining thermal diffusivity, heat capacity and thermal conductivity. *J. Appl. Phys.* **32**(9):1679-1684, 1961.
24. S. Zhao and S. Schabel. Measurement of thermal properties of paper by a light flash method. *Int. Paper World.* **5**:34-39, 2006.
25. A. Rosencwaig. **Scanned image microscopy**. Thermal-wave imaging and microscopy. Ed. A. Ash. Academic Press, London, pp. 291-317, 1980.
26. I. Kartovaara, R. Rajala, M. Luukala and K. Sipi. Conduction of heat in paper. In proc. *8th Fundamental Research Symposium*, Oxford, Mechanical Engineering Publications Ltd, London, 1985, pp. 381-412.
27. A. Mandelis, M. Nestoros, A. Othonos and C. Christofides. Thermophysical characterisation of commercial paper by laser infrared radiometry. *J. Pulp Paper Sci.* **23**(3):J108-J112, 1997.
28. D.K. Hale. The physical properties of composite materials. *J. Mater. Sci.* **11**(11):2105-2141, 1976.
29. J.C. Maxwell. **A Treatise on Electricity and Magnetism**, Clarendon Press, Oxford, 1873.
30. J.C.R. Turner. Two-phase conductivity. The electrical conductance of liquid-fluidized beds of spheres. *Chem. Eng. Sci.* **31**(6):487-492, 1976.
31. P. Gerstner. **Heat transfer in paper coatings**. Master's Thesis. Helsinki University of Technology. Espoo, Finland, 2007.
32. P.A.C. Gane, C.J. Ridgway, J. Schölkopf, J. and D.W. Bousfield. Heat transfer through calcium carbonate-based coating structures: observation and model for a thermal fusing process. In proc. *International Printing and Graphic Arts Conference*, Cincinnati, Tappi Press, 2006.
33. C.J. Ridgway, P.A.C. Gane and J. Schölkopf. Modified calcium carbonate coatings with rapid absorption and extensive liquid uptake capacity. *Colloids and Surfaces A.* **236**(1-3): 91-102, 2004.

-
34. Repeatability [online]. IUPAC Compendium of Chemical Terminology, Electronic version, cited November, 2009, available at: <http://goldbook.iupac.org/R05293.html>
 35. Reproducibility [online]. IUPAC Compendium of Chemical Terminology, Electronic version, cited November, 2009, available at: <http://goldbook.iupac.org/R05305.html>
 36. K. Niskanen and S. Simula. Thermal diffusivity of paper. *Nord. Pulp Paper Res. J.* **14**(3):236-242, 1999.
 37. W.M. Lu and K.J. Hwang. Mechanism of cake formation in constant pressure filtrations. *Sep. Technol.* **3**(3):122-132, 1993.
 38. L.M. McDowell-Boyer, J.R. Hunt and N. Sitar. Particle transport through porous media. *Water Resour. Res.* **22**(13):1901-1921, 1986.
 39. C.J. Ridgway and P.A.C. Gane. Bulk density measurement and coating porosity calculation for coated paper samples. *Nord. Pulp Paper Res. J.* **18**(1):24-31, 2003.
 40. P.A.C. Gane, M. Salo, J.P. Kettle and C.J. Ridgway. Comparison of Young-Laplace pore size and microscopic void area distributions in topologically similar structures: a new method for characterising connectivity in pigmented coatings. *J. Mater. Sci.* **44**(2):422-432, 2009.
 41. G.M. Laudone, G.P. Matthews and P.A.C. Gane. Effect of latex volumetric concentration on void structure, particle packing and effective particle size distribution in a pigmented paper coating layer. *Ind. Eng. Chem. Res.* **45**(6):1918-1923, 2006.
 42. Landolt-Börnstein, **Zahlenwerte und Funktionen**, Band IV Technik, 4. Wärmetechnik a, 6. Auflage, Heidelberg, 1980.
 43. J.E. Mark. **Physical Properties of Polymers Handbook**, American Institute of Physics, Woodbury, New York, 1996.
 44. "Simulation", "Model". Encyclopædia Britannica Online, Academic Edition, Merriam-Webster Dictionary & Thesaurus, <http://search.eb.com/> [cited 24.09.2008]
 45. J.F. Hunt and H. Gu. Two-dimensional finite heat transfer model of softwood. Part I. Effective thermal conductivity. *Wood Fiber Sci.* **38**(4):592-598, 2006.
 46. J.F. Hunt, H. Gu and P.K. Lebow. Theoretical thermal conductivity equation for uniform density wood cells. *Wood Fiber Sci.* **40**(2):167-180, 2008.
 47. I. Nozad, R.G. Carbonell and S. Whitaker. Heat conduction in multiphase systems I – Theory and experiment for two-phase systems. *Chem. Eng. Sci.* **40**(5):857-863, 1985.
 48. I. Nozad, R.G. Carbonell and S. Whitaker. Heat conduction in multiphase systems II – Experimental method and results for three phase systems. *Chem. Eng. Sci.* **40**(5):857-863, 1985.
 49. P. Cheng and C.T. Hsu. **Transport Phenomena in Porous Media**, Chapter 3, Heat conduction, D.B. Ingham and I. Pop, Oxford, 1998, pp. 57-76.
 50. R.A. Crane and R.I. Vachon. A Prediction of the Bounds on the Effective Thermal Conductivity of Granular Materials. *Int. J. Heat Mass Transfer.* **20**(7):711-723, 1977.
 51. A.R. Balakrishnan and C.T. Pei. Heat transfer in gas-solid packed bed systems 1. A critical review. *Ind. Eng. Chem. Process Des. Dev.* **18**(1):30-38, 1979.
-

REFERENCES

52. L. Lorenz. Über die Refraktionsconstante. *Ann. Phys. Chem.* **11**(3):70-103, 1880.
53. R.G. Deissler and J.S. Boegli. An investigation of effective thermal conductivities of powders in various gases. *Trans. ASME.* **8**:1417-1425, 1958.
54. N. Wakao and K. Kato. Effective thermal conductivity of packed beds. *J. Chem. Eng. Jpn.* **2**(1):24-33, 1969.
55. R. Krupiczka. Analysis of thermal conductivity in granular materials, *Int. Chem. Eng.* **7**:122-144, 1967.
56. O. Krischer. **Trocknungstechnik Band I**, Die wissenschaftlichen Grundlagen der Trocknungstechnik, Springer Verlag, Berlin, 1978.
57. S. Yagi and D. Kunii. Studies on effective thermal conductivities in packed beds. *Amer. Inst. Chem. Engrs. J.* **3**(3):373-381, 1957.
58. P. Zehner and E.U. Schlünder. Wärmeleitfähigkeit von Schüttungen bei mäßigen Temperaturen. *Chem. Ing. Tech.* **42**(14):933-941, 1970.
59. M. Kaviany. **Principles of Heat Transfer in Porous Media**, Springer-Verlag, New York, 1991.
60. C.T. Hsu, P. Cheng and K.W. Wong. Modified Zehner-Schlünder models for stagnant thermal conductivity of porous media. *Int. J. Heat Mass Transfer.* **37**(17):2751-2759, 1994.
61. C.T. Hsu, P. Cheng and K.W. Wong. A lumped-parameter model for stagnant thermal conductivity of spatially periodic porous media. *J. Heat Transfer.* **117**(2):264-269, 1995.
62. S.C. Cheng and R.I. Vachon. Prediction of thermal conductivity of two and three phase solid heterogeneous mixtures. *Int. J. Heat Mass Transfer.* **12**(3):249-264, 1969.
63. S. Palosaari and H.V. Nordén. Heat transfer in porous media with various moisture contents. *Kemian Teollisuus.* **22**(5):359-364, 1965.
64. D. Vidal, X. Zou and T. Uesaka. Modeling coating structure development using a Monte Carlo deposition method. Part 1: modeling methodology. *Tappi J.* **2**(4):3-8, 2003.
65. T. Pöhler, K. Juvonen and A. Sneck. Coating layer microstructure and location of binder – Results from SEM analysis. In proc. *Tappi 2006 Advanced Coating Fundamentals Symposium*, Turku, Finland, Tappi Press, Atlanta, 2006, pp. 89-100.
66. J.N. Kapur, P.K. Sahoo and A.K.C. Wong. A new method for gray-level picture thresholding using the entropy of the histogram. *Comput. Vision Graphics Image Process.* **29**(3):273-285, 1985.
67. G.M. Laudone, G.P. Matthews and P.A.C. Gane. Modelling the shrinkage in pigmented coatings during drying: A stick-slip mechanism. *J. Colloid Interface Sci.* **304**(1):180-190, 2006.
68. D.R. Lide. **CRC handbook of chemistry and physics**. Fluid properties. 89th ed., CRC Press. Boca Raton, FL, USA. 2008. pp. 6-1 - 6-21.

-
69. Landolt-Börnstein. **Zahlenwerte und Funktionen**. Band IV Technik, 4. Wärmetechnik b, 6. Auflage, Heidelberg, 1980.
70. C.J. Ridgway and P.A.C Gane. Effect of Latex and Pigment Volume Concentrations on Suspension and Consolidated Particle Packing and Coating Strength. *J. Pulp Paper Sci.* **33**(2):71-78, 2007.
71. S. Rousu, M. Lindström, P.A.C. Gane, A. Pfau, V. Schädler, T. Wirth and D. Eklund. Influence of Latex-Oil Interactions on Offset Ink Setting and Component Distribution on Coated Paper. *J. Graphic Technol.* **1**(2):45-56, 2003.
72. P.A.C. Gane and C.J. Ridgway. Moisture pickup in calcium carbonate coating structures: role of surface and pore structure geometry. *Nord. Pulp Paper Res. J.* **24**(3):298-308, 2009.
73. G.C. Lichtenberg. **De nova methodo naturam ac motum fluidi electrici investigandi**. Göttingen, 1778.
74. C.F. Carlson. **Electrophotography**. US Patent No. 2,297,691 Filed: April 4, 1939.
75. W. Sobotka. Schnell und Sauber: Nach dem Offset-Druck wird der Digitaldruck die Technologie für die nächsten Dekaden. *Pap. Österreich.* **2**:12-15, 2009.
76. M.A. Evans, D.E. White and G.F. Peter. Trends in digital printing papers. *Paper360°*, May:10-12, 2007.
77. A.R. Procter. Print-on-demand: A new paradigm for newspaper publication and distribution. *Pulp and Paper Canada.* **102**(8):8, 2001.
78. H. Kipphan. Chapter 5. Printing Technologies without a Printing Plate. **Handbook of Print Media**. Ed. Kipphan, H. Springer-Verlag. Berlin, Germany, p. 689, 2001.
79. T. Maierson, W.H. Mowry and D.M. Potter. **Toner adhesion-enhancing coating for security documents**. US Patent No. 5,045,426 Filed: August 21, 1989.
80. J.L. Johnson. **The Handbook of Non Impact Printing Technology**. Chapter 13. Image Fixing. Palatino Press, Irvine CA, pp. 13-1 – 13-17, 1998.
81. H. Al-Rubaiey and P. Oittinen. Controlling fusing parameters by optical image quality in electrophotographic printing. *Graphic Arts in Finland.* **33**(1):1-5, 2004. [online] cited: 18.02.2010, Available at: http://media.tkk.fi/GTTS/GAiF/GAiF1_2004.htm
82. L.B. Schein. **Electrophotography and Development Physics**. 2nd Edition, Springer-Verlag, Berlin, 1992.
83. K.M. Sipi. Toner layer structure and toner adhesion on coated paper. *In proc. NIP17: international conference on digital printing technologies*, Fort Lauderdale, FL, USA, 2001, pp. 145-150.
84. M.B. Lyne. The effect of digital printing on the demand for communication papers. In proc. *New Printing Technologies Symposium*, Atlanta, GA, TAPPI Press, 1996.
85. H.M. Cody. Coated paper markets post strong rebound. *PaperAge*. Mar/Apr, pp. 18-19, 2005.
86. N.A. Hitchcock. The future of digital substrates. *Electronic Publishing.* **28**(3):36, 2004.
-

REFERENCES

87. C.J. Ridgway, P.A.C. Gane and J. Schoelkopf. Achieving rapid absorption and extensive liquid uptake capacity in porous structures by decoupling capillarity and permeability: Nanoporous modified calcium carbonate. *Transp. Porous Med.* **63**(2):239-259, 2006.
88. T. Mitsuya, T. Kumasaka and S. Fujiwara. Study of toner melting conditions during flash fusing. *Optical Engineering* **30**(1):111-116, 1991.
89. T. Mitsuya and T. Kumasaka. Heat transfer and toner melting in an electrophotographic system, *J. Imaging Sci. Tech.* **36**(1):88-92, 1992.
90. P. Azadi, N. Yan and R. Farnood. Discrete element modeling of the transient heat transfer and toner fusing process in the Xerographic printing of coated papers. *Comput. Chem. Eng.* **32**(12):3238-3245, 2008.
91. J.R. Burnside and R.H. Crotogino. Some thermal properties of newsprint and their variations with bulk. *J. Pulp Paper Sci.* **10**(6):J144-J150, 1984.
92. T. Pettersson and A. Fogden. Spreading of individual toner particles studied using in situ optical microscopy. *J. Colloid Interface Sci.* **287**(1):249-260, 2005.
93. E. Hakola. **Toner Dynamics in Fixing**, Licentiate's Thesis, Helsinki University of Technology, Espoo, Finland, 2007.
94. M.D. Thouless and H.M. Jensen. **Adhesion Measurement of Films and Coatings**, The effect of residual stresses on adhesion measurements, Mittal, K.L. (Ed.), Utrecht, The Netherlands, pp. 95-102, 1995.
95. T. Hartus. Adhesion of electrophotographic toner on paper. *Graphic Arts in Finland.* **30**(3):14-19, 2001. [online] cited: 13.10.2009, Available at: http://media.tkk.fi/GTTS/GAiF/GAiF3_2001.htm
96. C.J. Ridgway, E. Kalela and P.A.C. Gane. Ink-coating adhesion: Factors affecting deposits on the CIC in "satellite" type CSWO (cold-set web offset press) using VAC papers, *J. Graphic Tech.* **1**(1):49-58, 2002.
97. E. Frank. Trocknung im Rollenoffset: Neue technologische und ökologische Erkenntnisse. *Dtsch. Drucker.* **32**(25):w2-w10, 1996.
98. P. Wendt. Trocknung, Abluftentsorgung und Energiekreislauf an Rollenoffsetmaschinen heute. *Dtsch. Drucker.* **18**(4):6-13, 1982.
99. K. Koivumäki and E.K.O. Hellén. **Advances in Printing and Media Technology. Volume 36.** Drying in heatset web offset printing. N. Enlund and M. Lovreček (ed.), Iarigai, Darmstadt, 2009, pp. 267-271.
100. P.A.C. Gane, C.J. Ridgway and J. Schölkopf. Absorption rate and volume dependency on the complexity of the porous network structures. *Transp. Porous Med.* **54**(1):79-106, 2004.
101. P.A.C. Gane and K. Koivunen. Relating liquid location as a function of contact time within a porous coating structure to optical reflectance. *Transp. Porous Med.* In the press, DOI: 10.1007/s11242-009-9523-x
102. A. Avcı and M. Can. The analysis of the drying process on unsteady forced convection in thin films of ink. *Appl. Therm. Eng.* **19**(6):641-657, 1999.
103. A. Avcı, M. Can and A.B. Etemoğlu. Theoretical approach to the drying process of thin film layers. *Appl. Therm. Eng.* **21**(4):465-479, 2001.

-
104. P. Heikkilä and N. Milosavljevic. Investigation of impingement heat transfer coefficient at high temperatures. *Drying Tech.* **20**(1):221-222, 2002.
 105. B.P.E. Dano, J.A. Liburdy and K. Kanokjaruvijit. Flow characteristics and heat transfer of a semi-confined impinging of jets: effect of nozzle geometry. *Int. J. Heat Mass Trans.* **48**(3-4):691-701, 2005.
 106. T. Hartus and P. Oittinen. Characterisation of the drying properties of heatset inks by thermal methods. *Graphic Arts in Finland.* **25**(1):9-15, 1996. Available online at: http://media.tkk.fi/GTTS/GAiF/GAiF_artikkelit/gaif96_1.pdf [cited: 19.05.2010]
 107. S. Rousu, M. Lindstöm, P.A.C. Gane, A. Pfau, V. Schädler, T. Wirth and D. Eklund. Influence of latex-oil interaction on offset ink setting and ink oil distributions in coated paper. *J. Graphic Tech.* **1**(2):45-46, 2002.
 108. C. Weigl and J. Weigl. Mechanismen von Reklamationsfällen durch hohe Trocknungstemperaturen im Heatsetdruck. *Wochenblatt für Papierfabrikation.* **136**(1-2):20-23, 2008.
 109. FOGRA. [online] Wellenbildung im Rollenoffset. Online Fehlerkatalog. Available online at: http://www.fogra.org/DB/_fogra/index.htm [cited: 17.05.2010]
 110. J. Weigl and M. Schachtl. Blasenbildung bei doppelt gestrichenen Rollenoffset-Druckpapieren. *Wochenblatt für Papierfabrikation.* **123**(8):332-345, 1995.
 111. C.J. Ridgway, J. Schoelkopf and P.A.C. Gane. A new method for measuring the liquid permeability of coated and uncoated papers and boards. *Nord. Pulp Paper Res. J.* **18**(4):377-381, 2003.
 112. P.A.C. Gane and E.N. Seyler. Some novel aspects of ink/paper interactions in offset printing. In proc. *International Printing and Graphic Arts Conference*, Halifax, Nova Scotia, TAPPI press, Atlanta, GA, 1994, pp. 209-228.
 113. J. Kosse, P.A.C. Gane, D.C. Spielmann, C. Naydowski and S. Kleeman. Auswirkung der Pigmentfeinheit auf die Porenstruktur der Strichoberfläche. In proc. *Münchner Papier-Seminare*, München, Germany, März 28, 2001.